# THE EFFECT OF CATALYST PORE SIZE ON PRODUCT DISTRIBUTION IN FISCHER TROPSCH SYNTHESIS: EXPERIMENTAL AND MACHINE LEARNING APPROACH

By

**NICHOLAS JIM**

submitted in accordance with the requirements for the

**MASTER OF ENGINEERING**

in the subject of

**CHEMICAL ENGINEERING**

at the

**UNIVERSITY OF SOUTH AFRICA**

**SUPERVISOR**: Linda L Jewell

**CO-SUPERVISOR**: Joshua Gorimbo

November 2025

# Declaration

Name: Nicholas Jim

Student number: 18211135

Degree: Master of Engineering in Chemical Engineering

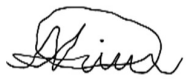
Exact title of the thesis as it appears on the electronic copy submitted for examination:

THE EFFECT OF CATALYST PORE SIZE ON PRODUCT DISTRIBUTION IN FISCHER TROPSCH SYNTHESIS: EXPERIMENTAL AND MACHINE LEARNING APPROACH

I declare that the thesis mentioned above is my own original work and that all the sources that I have indicated and acknowledged by means of complete references, all the sources and resources that I have used in the writing process.

I also declare that I submitted this thesis to an originality-checking software and that it meets the accepted requirements for originality.

Additionally, I declare that I have never submitted this work, or any portion of it, for examination at UNISA for another qualification at any other university.



_____ SIGNATURE

_____15/11/2025_____ DATE

# Acknowledgements

I would like to acknowledge the Institute of Catalysis and Energy Solutions for providing the funds and opportunity to complete this work. I also acknowledge work colleagues Humphrey Mbata, Mandla Mngomezulu and Ntebogang Thibanyane for their aid and support in conducting the experiments.

Special thanks goes to Prof Yao Yali and Dr Liberty Mguni for their contributions in several parts of the project.

Above all, I would like to acknowledge my supervisors Prof Joshua Gorimbo and Prof Linda Jewell for making this project a success through their tremendous contributions and guidance.

# ABSTRACT

In this thesis, the effectiveness of silica-supported cobalt ($Co/SiO_2$) catalysts for Fischer-Tropsch (FT) synthesis, a useful process for the conversion of syngas into clean fuels, was investigated. Emphasis was placed on how the catalyst performance is significantly influenced by the size of silica pores, aiming to decipher the pore size effects on CO conversion and product selectivity in FT synthesis. The Stöber process was used to create the mesoporous silica supports with pores that could be varied from 14 to 28 nm by adjusting the $H_2O$: TEOS: $NH_4OH$: EtOH ratios in the synthesis reaction vessel. The wet impregnation method was used to load 10 wt% cobalt on the silica supports. After loading them with cobalt, 620°C calcination temperature was determined by Thermogravimetric Analysis (TGA) for the calcination of the prepared catalyst samples. The analysis of pore sizes was done using Brunauer–Emmett–Teller **(**BET), morphology was verified by Scanning Electron Microscopy (SEM), Energy-Dispersive X-ray Spectroscopy (EDS), and X-Ray Diffraction (XRD), the available functional groups were examined by Fourier Transform Infrared Spectroscopy (FTIR), reducibility was tested by Temperature-Programmed Reduction (TPR), and dispersion was determined by using $H_2$ chemisorption. The catalyst testing on FT synthesis was done, which involved 150-hour runs at 220°C and 20 bar in a fixed-bed reactor, which resulted in CO conversions of 2–23%. The narrative became evident that the reducibility, product distribution, and CO conversion are all affected by the variation of pore size. Mid-sized pores (15–20 nm) were excellent at maximising CO conversion while minimizing light hydrocarbons ($C_1$-$C_4$). Larger pores (>20 nm) had the highest selectivity for heavy $C_{5+}$ chains, which was up to 88%. Machine learning was used to enhance these results, training CatBoost on 400 data points from 60 research articles covering 79 variables, including loads and temperatures. It supported our laboratory studies and identified 14–18 nm pores as the optimal zone for the production of long-chain hydrocarbons with a good prediction ability ($R^2$ = 0.79). The balance between the catalyst's stability, selectivity, and activity can be strongly influenced by pore structure. This work provides practical ways for synthesizing optimal performing $Co/SiO_2$ catalysts by combining rigorous experimental catalyst testing, characterisation, and implementing machine learning.

# List of publications and presentations

## Publication

1. N. Jim, J. Gorimbo, L. L. Jewell, Y. Yao, X. Liu, and L. L. Mguni, Application of Machine Learning in Analysis of the Effects of $Co/SiO_2$ Catalyst Surface Area on CO Conversion during Fischer Tropsch Synthesis, no. AfrSusEnS 2024. Atlantis Press International BV, 2025. doi: 10.2991/978-94-6463-797-7_3.

## Presentations

1. N. Jim, J. Gorimbo and L. Jewell. Effects of Catalyst Pore Sizes on Fischer-Tropsch Synthesis Product Distribution Models. Fourth International Syngas Convention, 2023, held in Cape Town, South Africa. (Poster)

2. N. Jim, J. Gorimbo and L. Jewell. Effects of Catalyst Pore Sizes on Fischer-Tropsch Synthesis Product Distribution Models. 33rd Annual CATSA Conference, Catalysts Transcending Chemical & Energy Research Frontiers, 5-8 November 2023, Mossel Bay, Western Cape. (Poster).

3. N. Jim, J. Gorimbo, L.L. Mguni, L.L. Jewell, Application of Machine Learning in analysis of the pore size effects on CO conversion during Fischer-Tropsch Synthesis using $CO/SiO_2$ Catalyst. 1st International Symposium of African Sustainable Energy Solutions (AfrSusEnS), Sun City, South Africa, 25 – 28 August 2024. (Oral).

4. N. Jim, J. Gorimbo and L. Jewell. Application of Machine Learning in analysis of the pore size effects on $C_{5+}$ Hydrocarbon production in Fischer-Tropsch Synthesis. CATSA 2024 the 34th Annual National Conference of the Catalysis Society of South Africa: Advancing innovative catalysis, 3-6 November 2024, Champagne Sports Resort, Central Drakensberg. (Poster).

5. N. Jim, J. Gorimbo and L. Jewell. Effects of Catalyst Pore Sizes on the ASF Product Distribution Model in Fischer-Tropsch Synthesis. 11th International conference on Appropriate Technology (ICAT), 25 – 29 Nov 2024, Johannesburg Number : 77. (Poster).

6. N. Jim, J. Gorimbo and L. Jewell. Catalyst Pore Size Effects on the Fischer-Tropsch Synthesis Product Distribution using $Co/SiO_2$. CATSA 2025 the 35rd Annual National Conference of the Catalysis Society of South Africa: Using Catalysis to solve the

UNSDGs, 9-12 November 2025, Emerald Resort & Casino, Van der Bijl Park, South Africa. (Oral).

**Exchange programs**

Visited the Zhejiang University of Technology, China to conduct Fischer-Tropsch experiments.

# TABLE OF CONTENTS


Declaration ..... i

Acknowledgements ..... ii

ABSTRACT ..... iii

List of publications and presentations ..... iv

TABLE OF CONTENTS ..... vi

List of Figures ..... xi

List of Tables ..... xv

List of Abbreviations ..... xvii

CHAPTER 1: INTRODUCTION ..... 1

1.1 Theoretical background and motivation ..... 1

1.2 Research problem statement ..... 3

1.3 Hypothesis ..... 3

1.4 Research aim and objectives ..... 3

1.4.1 Aim ..... 3

1.4.2 Objectives ..... 4

1.5 Research questions ..... 4

1.6 Research description and methodology ..... 5

1.6.1 Literature review ..... 5

1.6.2 Catalyst synthesis ..... 5

1.6.3 Catalyst characterization ..... 5

1.6.4 Catalyst testing ..... 6

1.6.5 Machine learning ..... 6

1.7 Significance of the Study ..... 6

1.8 Thesis Outline ..... 6

1.8.1 Chapter 1 ..... 6

1.8.2 Chapter 2 ..... 6

1.8.3 Chapter 3 ..... 7

1.8.4 Chapter 4 ..... 7
1.8.5 Chapter 5 ..... 7
1.8.6 Chapter 6 ..... 8
1.8.7 Chapter 7 ..... 8
References ..... 9
CHAPTER 2: LITERATURE REVIEW ..... 11
Abstract ..... 11
2.1 Introduction ..... 12
2.2 Factors affecting FT synthesis product distribution ..... 14
2.2.1 Catalyst variables ..... 14
2.2.2 Reaction conditions ..... 17
2.3 Catalyst pore size and pore structure effects in FT synthesis product distribution ..... 18
2.3.1 Role of pore size in FT synthesis ..... 20
2.3.2 Effects on product distribution and on the hydrocarbon chain length ..... 21
2.4 Postulated mechanisms of the FT synthesis ..... 22
2.5 FT synthesis product distribution models ..... 27
2.5.1 Statistical models ..... 27
ASF distribution ..... 30
2.5.2 Mechanistic or Microkinetic models ..... 31
Surface polymerization models ..... 31
2.5.3 Empirical and data-driven models ..... 31
2.6 Application of machine learning in FT synthesis studies ..... 33
2.6.1 Common models used in machine learning ..... 34
2.7 Conclusion ..... 37
References ..... 38
CHAPTER 3: EXPERIMENTAL PROCEDURE ..... 51
3.1 Introduction ..... 51
3.2 Materials and gases ..... 51
3.2.1 Gases ..... 51

3.2.2 Equipment ..... 52
3.3 Catalyst synthesis ..... 52
3.3.1 Reagents ..... 52
3.3.2 Catalyst Synthesis Procedure ..... 53
3.4 Characterization ..... 58
3.4.1 Physisorption analysis ..... 58
3.4.2 Thermogravimetric Analysis ..... 58
3.4.3 Scanning Electron Microscopy ..... 59
3.4.4 Structural Analysis ..... 60
3.4.5 X-ray analysis ..... 61
3.4.6 Temperature Programmed Reduction ..... 62
3.4.7 Hydrogen Chemisorption Studies ..... 63
3.5 Catalyst testing ..... 64
3.5.1 Catalyst reduction ..... 64
3.5.2 Fischer Tropsch Synthesis ..... 65
3.6 Mass balance calculations ..... 67
3.7 Machine learning ..... 70
3.8 Conclusion ..... 70
References ..... 71
CHAPTER 4: VARYING THE PORE SIZE TO DETERMINE THE EFFECT ON SELECTIVITY IN FISCHER-TROPSCH SYNTHESIS FOR SILICA-SUPPORTED COBALT CATALYSTS ..... 73
Abstract ..... 73
4.1 Introduction ..... 74
4.2 Results and discussion ..... 75
4.2.1 TGA ..... 75
4.2.2 Structural analysis ..... 78
4.2.3 XRD analysis ..... 81
4.2.4 SEM and TEM ..... 84
4.2.5 Physisorption analysis ..... 96

4.2.6 Effect of reagent concentration during Stöber synthesis on catalyst and support properties ..... 101
4.2.7 Density studies of the prepared silica samples ..... 110
4.3 Conclusion ..... 114
References ..... 116
CHAPTER 5: CATALYST PORE SIZE EFFECT ON FISCHER-TROPSCH SYNTHESIS ..... 121
Abstract ..... 121
5.1 Introduction ..... 122
5.1.1 Pore Size and Catalyst Structure ..... 122
5.1.2 Controlling the Pore Size via the Stöber Process ..... 123
5.1.3 Effects of Pore Size on FT synthesis Product Selectivity ..... 123
5.1.4 Other factors that influence the product distribution ..... 124
5.1.5 Scope and Chapter Overview ..... 124
5.2 Experimental ..... 125
5.2.1 Catalyst Preparation ..... 125
5.2.2 Catalyst Characterization ..... 125
5.2.3 Catalyst Testing ..... 127
5.3 Results and discussion ..... 128
5.3.1 Catalyst characterization ..... 128
5.3.2 Fischer-Tropsch Synthesis ..... 134
5.4 Conclusion ..... 140
Recommendations ..... 141
References ..... 143
CHAPTER 6: APPLICATION OF MACHINE LEARNING IN STUDYING THE EFFECTS OF CATALYST PORE SIZE ON FISCHER-TROPSCH SYNTHESIS PRODUCTS ..... 148
Abstract ..... 148
6.1 Introduction ..... 148
6.1.1 Application of Machine Learning in Fischer-Tropsch Synthesis and Catalyst Research ..... 149
6.1.2 Advantages and limitations of ML in FT synthesis catalyst modelling ..... 150

6.2 Dataset Sampling and ML Model Choice ..... 151
6.2.1 Sampling Method ..... 151
6.2.2 Model selection ..... 153
6.3 Results and analysis ..... 155
6.3.1 Feature Importance Analysis of the Input Parameters ..... 155
6.3.2 Analysis of the Relative Importance of Catalyst Pore Size Towards the Target Parameters ..... 158
6.3.3 The effects of $Co/SiO_2$ catalyst pore sizes and the five most important parameters on the CO conversion and product distribution. ..... 161
6.4 Conclusion ..... 182
References ..... 184
Bibliography ..... 190
CHAPTER 7: CONCLUSION ..... 196
7.1 Introduction ..... 196
7.2 Conclusions and recommendations ..... 196
7.2.1 Experimental approach ..... 196
7.2.2 Machine learning approach ..... 197
APPENDIX ..... 199

# List of Figures

Figure 2.1. A schematic showing transport phenomena that occur during heterogeneous catalysis with a porous catalyst. Adapted with permission from (García-Sánchez & Baldovino-Medrano (2023) ..... 19
Figure 2.2. Illustration of the relationship between gas diffusivity and catalyst pore size during heterogeneous catalysis. (Adapted with permission from (García-Sánchez & Baldovino-Medrano, (2023) ..... 221
Figure 2.3 A schematic of the carbide mechanism based FT synthesis route (Adapted from Van Santen et al., 2013) ..... 23
Figure 2.4. A schematic showing the CO activation mechanism via the hydroxyl intermediate pathway (Adapted from (Rytter & Holmen (2018)) ..... 244
Figure 2.5. A depiction of the CO- insertion mechanism (Adapted from (Van Santen et al., (2013) ..... 25
Figure 2.6. The Enol Mechanism schematic diagram. Modified from Davis, (2001) ..... 26
Figure 2.7. Illustration of the behaviour of the Flory model on selected alpha values ..... 28
Figure 2.8. A schematic of the Schulz- Flory distribution plot for four different alpha values ..... 29
Figure 2.9. A representation of the ASF distribution for four different alpha parameters (0.2, 0.5, 0.7 and 0.9) ..... 30
Figure 2.10. Depiction of the triangular plot for thermodynamic product distribution of $C_nH_{2n}$, $C_nH_{2n+2}$ and $C_{n+1}H_{2(n+1)}$) (Adapted from (Lu et al.(2012) ..... 332
Figure 2.11. A summary of the steps involved in the ML framework of a study of the catalyst performance on Co- based catalysts. (Adapted with permission from Yuan et al., (2024)) ..... 34
Figure 2.12. A typical sequence of tasks followed when using the Random Forest model (Adapted with permission from Motaev et al. (2023) ..... 35
Figure 3.1. The reflux set up for silica synthesis using the Stöber process ..... 57
Figure 3.2. NOVA 800 Physisorption analyzer used to measure the pore size distribution, the pore volume and the BET surface area of the catalyst samples used in the study. ..... 58
Figure 3.3. Quorum Tech gold coating Instrument used for coating the samples prior to SEM analysis ..... 59
Figure 3.4. Scanning Electron Microscopy Instrument, JEOL, ISM-IT 300 used for the imaging and mapping of the catalyst samples ..... 600
Figure 3.5. PerkinElmer, Spotlight 400 Instrument used in the FTIR experiments ..... 61
Figure 3.6. X-ray diffractometer used in the XRD studies ..... 62

Figure 3.7. CATLAB - PCS Microreactor used to carry out the TPR and Hydrogen chemisorption experiments ..... 63
Figure 3.8. Schematic graph of the temperature profile used for the catalyst reduction ..... 64
Figure 3.9. The temperature controllers of the FT reactors used to set-up and regulate the reactor temperatures ..... 65
Figure 3.10: A typical GC output obtained from the calibration gas ..... 66
Figure 3.11. The FT reactors set up with quartz wool insulation..... 67
Figure 4.1. TGA analysis for the synthesised $Si(OH)_4$ samples ..... 76
Figure 4.2. DTG Analysis of the prepared $Si(OH)_4$ samples ..... 77
Figure 4.3 FTIR analysis for the uncalcined silica support ..... 78
Figure 4.4. FTIR analysis for the calcined silica support samples ..... 79
Figure 4.5. XRD analysis of the 10 synthesized silica supports ..... 82
Figure 4.6. Comparison of the XRD graphs of the support and the cobalt-loaded silica ..... 83
Figure 4.7. Comparison of the XRD graphs of the catalysts from synthesis runs 1 and 7 ..... 84
Figure 4.8. SEM image of the silica sample S1 (TEOS : H2O - 1:1)..... 85
Figure 4.9. SEM image of the silica sample S2. (TEOS: $H_2O$ - 1:1.5)..... 86
Figure 4.10. SEM image of the silica sample S3. (TEOS:$H_2O$ - 1:2)) ..... 866
Figure 4.11. SEM image of the silica sample S4.(TEOS: $H_2O$ - 1:2.5)..... 87
Figure 4.12. SEM image of the silica sample S5. (TEOS:$H_2O$ - 1:5)..... 87
Figure 4.13. SEM image of the silica sample S6. (TEOS: $H_2O$ - 1:10)..... 88
Figure 4.14. SEM image of the silica sample S7. (TEOS:$H_2O$ - 1:12)..... 88
Figure 4.15. SEM image of the silica sample S8. (TEOS:$NH_4OH$ - 1:7)..... 89
Figure 4.16. SEM image of the silica sample S9. (TEOS:$NH_4OH$ - 1: 2.5)..... 89
Figure 4.17. SEM image of the silica sample S10. (TEOS:$NH_4OH$ - 1:5)..... 90
Figure 4.18. EDS Mapping for Co/ $SiO_2$ sample 2 ..... 94
Figure 4.19. EDS elemental mapping for sample CS-9..... 95
Figure 4.20. Nitrogen adsorption-desorption isotherms for the catalysts synthesized with varying water content..... 98
Figure 4.21. Nitrogen adsorption-desorption isotherms for the catalysts synthesized with varying $NH_4OH$ concentrations ..... 100
Figure 4.22. The hysteresis loop types and the corresponding pore shape resemblance (Xu et al., 2020), open access CC BY..... 100
Figure 4.23. Relationship between pore diameter, water/ethanol ratio and water/$NH_4OH$ ratio during the synthesis of the catalyst supports with varying water concentration while keeping other reagent concentrations constant. ..... 102

Figure 4.24. Relationship between the pore diameter, water/ethanol ratio, and water/$NH_4OH$ ratio during the synthesis of the catalyst supports with varying $NH_4OH$ concentration, keeping the rest of the reagents constant ..... 102
Figure 4.25. Relationship between the surface area, water/ethanol ratio, water/$NH_4OH$ ratio during silica synthesis with varying water concentration while keeping other reagent concentrations constant ..... 103
Figure 4.26. Relationship between the surface area, water/ethanol ratio, and water/NH4OH ratio with varying $NH_4OH$ concentration while maintaining the concentrations of the other reagents constant ..... 104
Figure 4.27. Relationship between surface area and pore diameter with $H_2O$ molar ratio ($H_2O$:TEOS=$NH_4OH$) ..... 105
Figure 4.28. Variation of pore volume with the $H_2O$ molar ratio in the reagents ..... 108
Figure 4.29. Relationship between pore diameter and surface area with varying $NH_4OH$ molar ratio ..... 109
Figure 4.30. Relationship between the silica pore volume and $NH_4OH$ molar ratio in the reaction reagents ..... 110
Figure 4.31. Variation of densities across the 10 prepared silica samples ..... 11111
Figure 4.32. Variation of the densities of the silica samples as the $H_2O$ molar ratio increases ..... 113
Figure 4.33. Variation of the density of the prepared silica samples with $NH_4OH$ ratio, as other reagent concentrations remained constant ..... 113
Figure 5.1. A schematic diagram of the setup used to conduct the FT synthesis experiments ..... 127
Figure 5.2. TPR Profiles for Co/$SiO_2$-1, Co/$SiO_2$-3, Co/$SiO_2$-6 and Co/$SiO_2$-9 ..... 129
Figure 5.3. Relationship between pore size, surface area, and $Co_3O_4$ reduction temperature for the four catalysts (Areas of the spheres are proportional to the surface areas) ..... 130
Figure 5.4. Relationship between pore size, surface area, and CoO reduction temperature for the four catalysts (Areas of the spheres are proportional to the surface areas) ..... 132
Figure 5.5 Catalytic performance of Co/$SiO_2$-1. Co/$SiO_2$-3, Co/$SiO_2$-6 and Co/$SiO_2$-9 during FT synthesis over a TOS of 150h ..... 135
Figure 6.1. Two-way partial dependence plot of CO conversion against the top five most influential parameters..... …..…...**Error! Bookmark not defined.**
Figure 6.2. Three-way partial dependence plots of pore sizes and CO conversion against the other top five most influential variables..... ..166
Figure 6.3. Two-way partial dependence plots of $CH_4$ selectivity against the five most influential parameters ..... 168
Figure 6.4. Three-way partial dependence plots of $CH_4$ selectivity and pore size against the other five most influential parameters..... **Error! Bookmark not defined.**

Figure 6.5. Two-way partial dependence plot of $C_2$-$C_4$ selectivity against the five most influential parameters towards $C_2$-$C_4$ selectivity.....173
Figure 6.6. Three-way partial dependence plots of $C_2$-$C_4$ selectivity and pore size against the other five most influential parameters towards $C_2$-$C_4$ selectivity…. .....176
Figure 6.7. Two-way partial dependence plot of $C_{5+}$ selectivity against the five most influential parameters towards $C_{5+}$ selectivity ..... .....178
Figure 6.8 Three-way partial dependence plot of $C_{5+}$ selectivity and pore size against the other five most influential parameters towards $C_{5+}$ selectivity…….....181

Figure A.1. Feature importance towards the CO conversion in the whole population..... 200
Figure A.2. Feature importance towards $C_1$ selectivity in the whole population ..... 20201
Figure A.3. Feature importance towards $C_2$-$C_4$ selectivity in the whole population ..... 202
Figure A.4. Feature importance towards $C_{5+}$ selectivity from the whole population ..... 203
Figure A.5. Feature importance towards CO conversion for the 20 - 60 % CO conversion data set ..... 204
Figure A.6. Feature importance towards $C_1$ selectivity for the 20-60% CO conversion cluster ... 205
Figure A.7. Feature importance towards $C_2$-$C_4$ Selectivity analysis for the 20-60% CO conversion data set ..... 206
Figure A.8. Feature importance towards the $C_{5+}$ selectivity for the 20-60% CO conversion data set ..... 207

# List of Tables

Table 2.1. A summary of the effects of some promoters on the FT synthesis process ..... 15
Table 2.2. A summary of the effects of some supports on the FT synthesis reaction ..... 16
Table 3.1. Composition of the calibration gas used in the FT experiments……..……,,,…….51
Table3.2. Typical ratios of Water/TEOS/$NH_4OH$/ethanol/CTABr and the respective characteristics…….,,,……54
Table 3.3. Different molar ratios of water/TEOS/$NH_4OH$/Ethanol used in the synthesis and the respective volumes mixed…….55
Table 3.4. The notations of the prepared catalysts……...….56
Table 3.5: Response factors of the respective carbon numbers used to extract the data from the GC output……67
Table 4.1. Identification of the peaks from the FTIR results of the silica samples..... 80
Table 4.2. The notations of the prepared catalyst samples..... 81
Table 4.3. EDS Elemental analysis of the prepared silica samples..... 91
Table 4.4. The analysis conditions used in the EDS mapping to determine the elemental layers for sample CS-9 ..... 95
Table 4.5. Physisorption analysis results for the cobalt silica catalysts and the synthesized silica supports ..... 96
Table 4.6. Relationship between the water/$NH_4OH$ ratio, water/ethanol ratio and the silica support properties..... 101
Table 4.7 Variation of water molar ratio across the first seven runs and the respective silica properties..... 105
Table 4.8. Variation of $NH_4OH$ molar ratio across the last three runs and the respective silica properties..... 108
Table 4.9. The variation of densities across the 10 prepared silica supports ..... 111
Table 5.1. Physisorption analysis results ..... 128
Table 5.2. A Summary of the reduction peaks, pore sizes and surface areas of the four catalysts tested ..... 130
Table 5.3. Hydrogen chemisorption results presented with the catalyst pore size..... 134
Table 5.5. A summary of the catalytic performance of the $CO/SiO_2$ catalysts with different pore sizes. (Reaction conditions: Temperature = 220°C, pressure  20 bar, flowrate = 60 mL/min, Time on Stream (TOS) = 150 hours, $H_2/CO$ ratio = 2), average reaction rate = 2.35E-04 (mol CO/g cat./min). ..... 136
Table 6.1. The behaviours of different ML algorithms on the target parameters..... 153

Table 6.2. Metrics for each target variable in the whole population and the 20-60% CO conversion range..... 156
Table 6.3. A summary of the comparison of the impact of pore size on the two different data sets analysed..... 160

**List of Abbreviations**

| | |
|---|---|
| ANN | Artificial Neural Network |
| ANOVA | Analysis of Variants |
| ASF | Anderson – Schulz – Flory |
| BET | Brunauer - Emmet - Teller |
| BJH | Barrett-Joyner-Halenda |
| Cn | Hydrocarbons with carbon number n |
| EDS | Energy-Dispersive X-ray Spectroscopy |
| ETR | Extra Trees Regressor |
| FT | Fischer-Tropsch |
| FTIR | Fourier Transform Infrared Spectroscopy |
| FTO | Fischer-Tropsch to Olefin |
| GBR | Gradient Boosting Regressor |
| GHSV | Gas Hourly Space Velocity |
| HTE | High-throughput experimentation |
| KIT | Korea Advanced Institute of Science and Technology |
| KNN | K-Nearest Neighbour |
| LHHW | Langmuir - Hinshelwood – Hougen – Watson |
| MCM | Mobil Composition of Matter |
| ML | Machine learning |
| Mn | Number of moles of Hydrocarbons with carbon number n |
| N | Maximum size of the hydrocarbon chain length |
| O/P | Oleffin to paraffin ratio |
| P | Pressure |
| PCC | Pearson Correlation Coefficient |
| PINN | Physics-informed machine learning models |

| | |
|---|---|
| RFR | Random Forest Regressor |
| RMSE | Root Mean Squared Error |
| RSM | Response Surface Method |
| SBA | Santa Barbara Amorphous |
| SEM | Scanning Electron Microscopy |
| SF | Schulz- Flory |
| SHAP | SHapley Additive exPlanations |
| SVR | Support Vector Regression |
| T | Temperature |
| TOS | Time on Stream |
| TGA | Thermogravimetric Analysis |
| TPR | Temperature-Programmed Reduction |
| TPD | Temperature-Programmed Desorption |
| Wn | Weight fraction of Hydrocarbons with carbon number n |
| XRD | X-Ray Diffraction |
| $\alpha$ | Chain growth parameter |
| $S_n$ | Selectivity of hydrocarbons with n carbon atoms |

# CHAPTER 1: INTRODUCTION

## 1.1 Theoretical background and motivation

The chemical process known as Fischer-Tropsch (FT) synthesis was first established in 1925 by Franz Fischer and Hans Tröpsch, who were German scientists (Schulz, 1999 ; Pichler, 1952; Fischer , 1930). The process is an alternative route in which liquid fuels are made from a mixture of $H_2$ and CO (syngas) rather than crude oil. Natural gas, biomass, or even coal can be used to produce the syngas feed. The FT synthesis is an alternative supply of hydrocarbon fuels to those obtained from petroleum; moreover, FT synthesis is a source of low-sulphur diesel fuel because any sulphur present is removed from the syngas before the reaction, as it poisons the FT catalysts.

The FT synthesis process is very complex, yielding a diverse range of hydrocarbon products. The products that are typically produced from the FT reaction process include petrol, diesel, jet fuel, light hydrocarbons, naphthalene, and wax. Short-chain hydrocarbons with one to four carbon atoms are the most common type of light hydrocarbons. These gases, which are frequently created as byproducts of the FT process, can be further processed or used as fuel (Schulz, 1999). Longer aliphatic hydrocarbons and hydrocarbons with 5-12 carbon atoms are the most common types found in petrol. The hydrocarbons in the diesel range, which mostly consist of paraffins, olefins, and certain branched hydrocarbons, have 13–18 carbon atoms. These hydrocarbons are appropriate for diesel fuel applications because they have higher boiling points than hydrocarbons in the petrol spectrum. Straight-chain and branched alkanes with 10–16 carbon atoms are among the hydrocarbons that make up the jet fuel component. Usually, long-chain hydrocarbons with 20–100+ carbon atoms make up wax-range hydrocarbons. These hydrocarbons are frequently used to make lubricants, waxes, and other specialty chemicals because of their high melting points (Evans & Smith, 2012).

FT synthesis has been extensively studied to date, with numerous researchers developing mathematical models to illustrate the reaction processes occurring in the reactor system, that is, the rate equations and product selectivity based on various reaction mechanisms and the diffusion processes into and out of the catalyst pellets. The initial model employed to predict and analyze FT product distribution was created by P. J Flory in the early 1930s and was known as the Flory Model (Flory, 1936). Herington (1942) who observed that a probability distribution function may be used to characterise the FT synthesis product distribution, proposed that a geometric progression is followed by the hydrocarbon products from FT synthesis, introducing the concept of a constant chain growth probability. This modification was later named the Schulz-Flory model in

the 1930s (Herrington & Robertson, 1942). The parameters for a particular model are fitted for a specific catalyst system, reactor and operating conditions. To date, there has not been a single FT product distribution model that accurately predicts the product distribution for all cases because of the FT reaction's complexity. The Anderson-Schulz-Flory (ASF) distribution, which has been used in most publications, was modified multiple times to improve its predictive accuracy. The modified, extended ASF models not only had a broad variety of applications and versatility, but they also made it easy to extract the pertinent parameters from the experimental data (Förtsch et al., 2015). Many academics have offered numerous justifications for the deviations from the ideal ASF model, which were generally determined to be caused by a variety of causes, including some experimental artifacts as described by (Gao et al., 2012). However, to increase the selectivity for the production of liquid fuels, these deviations need to be accounted for to achieve the intended outputs.

The chemistry and dynamics present on the catalytic surface during a FT reaction have also been described by a number of reaction mechanisms, hence, one of the key elements influencing the dissemination of the final product is the reaction mechanism. The product distribution in FT synthesis reactions can be engineered by altering the catalyst's physical and chemical properties by using different catalyst supports and relevant promoters (Pardo-Tarifa et al., 2017). The catalyst support type, diffusion limitations, chemisorption, physisorption, and reaction conditions were also reported to affect the distribution of the FT products (Kustov & Tarasov, 2016).

Additionally, a number of scientists have produced a large number of new catalysts for the FT process. These catalysts were designed to increase the hydrocarbon selectivity. The distribution of the product can be significantly impacted by the characteristics of the catalyst. In fact, the diffusion of reactants into the catalyst and products out of the catalyst is greatly influenced by the average size of the support pores, which is why it is an important factor to consider. Thus, in order to maximize conversion efficiency and attain the required product selectivity, catalyst pore size optimization is essential in FT synthesis.

However, it is worth noting that the pore size should not be considered alone but along with other catalytic properties, such as the surface area, metal type, pore volume, crystallite size, particle size, and properties of the support material, to increase the accuracy in modelling the product distribution in the FT process.

Accurate and comprehensive energy and mass balances on the FT reactor system, which are required to have exact information on the reactor operating parameters, are made possible by a thorough understanding of the product distribution.

In this project the influence of several properties of the catalyst on the FT product distributions has been analysed using an experimental and machine learning approach for cobalt supported on silica. In this way, a comprehensive report of the performance of the cobalt supported on silica will be obtained which can be of a great importance in improving the product selectivity of any required hydrocarbon fraction during the industrial FT process. The cobalt on silica system was chosen based on the ease of controlling the average pore size. Silica is relatively inert chemically, avoiding the formation of strong metal support interactions, i.e. cobalt silicates, and it is also thermally stable under the FT reaction conditions (Song & Li, 2006).

## 1.2 Research problem statement

Globally, fossil fuel consumption continues to grow, which is the cause of climate change. Noting that the impacts of climate change are more severe in Africa, recommendations to strengthen energy efficiency and consumption were made (Kwakwa et al., 2018). Carrying out the FT process via alternative feeds, like biomass and natural gas to replace the conventional coal in the gasification processes to produce the syngas can result in the production of carbon-neutral liquid fuels (Aasberg-Petersen et al., 2004). If the product distribution can be controlled more precisely, then gains will be made in the overall process efficiency. In order to do this, accurately predictive models are necessary. Due to the complexity of the FT synthesis no model accurately accounts for the effects of all the variables that determine the product distribution in order to give a prediction of the selectivities and properly optimize the production of the intended hydrocarbons. A number of catalyst supports have been reported in the literature. Cobalt supported on silica is a commonly used FT catalyst and can be further extensively studied in order to come up with a comprehensive understanding of the pore size and surface effects on the catalytic performance and product distribution to maximize the desired hydrocarbon products, and also increase the efficiency of the process.

## 1.3 Hypothesis

Catalyst pore size has a significant effect on FT product distribution with wider catalyst pores favouring different product selectivities than those favoured by more restricted pore sizes because of diffusion limitations and transport effects.

## 1.4 Research aim and objectives

### 1.4.1 Aim

This research aims to be able to analyse the effects of catalyst pore sizes and other catalyst variables on the FT synthesis product distribution and alter the selectivity towards a desired hydrocarbon fraction. In particular, cobalt catalysts supported on silica spheres synthesized using the Stöber process are to be investigated experimentally. By gathering data from the literature, a

machine learning approach was also used to determine the effect of pore size on product selectivity in FT synthesis.

### 1.4.2 Objectives

- The relationship between pore size and product distribution is complex. It is also influenced by various catalyst properties, catalyst pretreatment conditions, and operating conditions such as temperature, pressure, GHSV, and $H_2$/CO ratio. The study will explore the effect of support pore size on the product distribution. Silica supports with different pore size distributions will be synthesized and then used to make Co/$SiO_2$ catalysts for FT synthesis testing.
- A machine learning model can predict FT synthesis product distribution with acceptable accuracy using different process variables as inputs. FT synthesis data over Co/$SiO_2$ catalysts from the reported literature in the last ten years is to be collated and investigated using machine learning techniques. The machine learning model will be able to identify the most important variables controlling CO conversion and product selectivity, and help optimize catalyst design.
- The effect of the following parameters on the FT process performance using Co/$SiO_2$ catalysts was evaluated using experimental and machine learning methods; the analysis of the effects of these parameters is the main objective of this study.

Experimental;

i. Catalyst pore size
ii. Catalyst pore volume
iii. Catalyst BET surface area
iv. Metal dispersion on the catalyst

Machine Learning

i. Catalyst promotion with different types of promoters
ii. Reaction conditions
iii. Catalyst pretreatment conditions

## 1.5 Research questions

1. Can the Stöber method be used to tailor the pore size of a silica support?
2. How is the product distribution in FT synthesis affected by the catalyst pore size and the other more influential parameters, such as pore volume and surface area?

3. How does pore size influence catalyst performance in FT synthesis in terms of conversion, hydrocarbon fractions selectivity, and overall reactor behaviour?
4. Which variables contribute most to product distribution in the machine learning model?
5. Can a machine learning model accurately predict product distribution from catalyst pore size and operating conditions?
6. Can the machine learning approach identify an optimum pore size for desired FT synthesis products?

## 1.6 Research description and methodology

This research project involves the preparation of ten different silica supports with different pore sizes, which were then loaded with 10% cobalt via wet impregnation and characterized. Then four of them were used to carry out the FT experiments. Machine learning was also used to analyze the effects of pore sizes from the $Co/SiO_2$ studies that were published in the last 10 years. The activities in the research project were as follows:

### 1.6.1 Literature review

The literature review was done to address the following objectives:

- To explore prior work done in the field;
- To identify the type of data sources that have been used in the past;
- To get a clear conceptualization of the way the key ideas of the FT process have been defined and measured;
- To evaluate the accuracy of the product distribution models,
- To find reports that could be used to discuss and support the findings in this work.

### 1.6.2 Catalyst synthesis

This was done using the modified Stöber process to prepare 10 different catalysts with different pore sizes and using wet impregnation to load the cobalt metal of 10% loading on to the synthesized support.

### 1.6.3 Catalyst characterization

This was done using various characterization techniques that are described in detail in chapter 3 in order to find the chemical and physical properties of the prepared catalysts

### 1.6.4 Catalyst testing

This was done using an FT synthesis reactor, where the FT experiments were carried out in order to measure the performance of the four catalysts that were selected due to their different pore sizes under the same FT conditions

### 1.6.5 Machine learning

This was done by collecting information from the research literature in the past 10 years on $Co/SiO_2$ based FT synthesis publications and analysing the effects of various parameters on the emerging product distribution during FT synthesis. The analysis using Machine Learning techniques in this study, being based on literature-derived datasets, is intended as a data-driven exploratory tool to identify meaningful patterns and guide future experimental work done using the CatBoost algorithm. One of the key strengths of Machine Learning lies in its ability to analyze complex, heterogeneous datasets and uncover patterns across a wide range of conditions. Rather than being a limitation, this variability allows the model to learn from diverse experimental scenarios, enabling broader comparative insights.

## 1.7 Significance of the Study

This study elucidates the influence of catalyst pore size on product distribution in FT synthesis, thereby informing enhanced catalyst design and optimizing process efficiency. A more precise comprehension of this connection can facilitate the development of catalysts that yield a greater quantity of the desired fuel fractions while minimizing undesirable by-products. At an industrial scale, this is significant as FT synthesis is extensively employed to produce clean fuels and valuable hydrocarbons from syngas. Enhanced selectivity can lower costs, elevate product quality, and enhance the competitiveness of the process.

## 1.8 Thesis Outline

### 1.8.1 Chapter 1

This is the introductory chapter of the work. The background study was outlined, and the research gap, which is the problem statement, was also pointed out, followed by the research aims and objectives. The project justification and the description of the methodology that will be used to carry out the work were provided at the end of the chapter.

### 1.8.2 Chapter 2

The literature review chapter will discuss the historical developments of FT synthesis, focusing on catalyst design, product distribution models, pore size effects, and the influence of internal diffusion on product distribution. Also, it will discuss previous work of cobalt-based catalysis, the functionalities of silica-based porous support as well as impact of the operating condition on

selectivity and performance of the reactor. Furthermore, it will illuminate the remaining research gap in comprehending how pore size governs FT synthesis product distribution and introduce the new components for experimental investigations and machine learning analysis to predict or optimize product distribution.

### 1.8.3 Chapter 3

Here is where you will find a detailed description of the materials and gases such as catalyst precursors, support material that are used in this part of FT testing. Then it will detail a catalyst synthesis protocol by which $Co/SiO_2$ catalysts with varying pore size were prepared, and finally explore the characterization methods used to determine structural and surface properties of these materials. In addition, the chapter will describe the catalyst testing process (reaction conditions and product characterization) as well as the mass balance calculations to confirm the credibility of experimental data. Lastly, it will show the ML method to be applied for analysing the relationship between catalyst pore size, operating conditions, and product distribution.

### 1.8.4 Chapter 4

This chapter mainly focuses on the catalyst synthesis; it will demonstrate and discuss how the silica-supported cobalt catalysts were produced with varying pore diameters. It will first look at the thermal behaviour of the materials using TGA, then go on to structural analysis with XRD to show the crystal characteristics of the catalysts and supports. The chapter will also address the SEM, EDS and TEM characterization data to explain the material's form and particle structure, along with physisorption studies to examine pore size, pore volume, and surface area. In addition, it will examine how adjusting the reagent concentrations during Stöber synthesis changed the catalyst and support properties, and it will close with density tests of the generated silica samples to show how the different synthesis conditions influenced the final structure.

### 1.8.5 Chapter 5

The impact of catalyst pore size on FT synthesis performance is examined in this chapter using four $Co/SiO_2$ catalyst samples. The experimental section begins with an explanation of the catalyst preparation, characterisation, and testing procedures employed for the four selected samples. Before presenting the FT synthesis data, the results and discussion section delves deeper into the catalyst attributes utilizing physisorption studies, temperature programmed reduction, and hydrogen chemisorption. The behaviour of the catalysts, the relationship between dispersion and CO conversion, and the changes in product selectivity that were noted are then covered in the chapter.

### 1.8.6 Chapter 6

The use of machine learning in FT synthesis and catalyst research is introduced in this chapter, which also discusses the preparation of the dataset and the selection of the machine learning model for the study, before delving into how machine learning can aid in understanding the impact of catalyst pore size on FT synthesis products. The significance of the various input variables, the role of catalyst pore size in relation to the other important parameters, and the impact of $Co/SiO_2$ pore size in conjunction with the five most important variables on CO conversion and product distribution are all examined in the findings and analysis section. Before concluding with the key findings from the machine learning research, it also looks at how pore size and the most significant independent variables affect CO conversion, $CH_4$ selectivity, $C_2$-$C_4$ selectivity, and $C_{5+}$ selectivity.

### 1.8.7 Chapter 7

This chapter outlines the main conclusions and recommendations obtained from the experimental and machine learning work that has been done in this research.

## References


Aasberg-Petersen, K., Christensen, T. S., Dybkjær, I., Sehested, J., Østberg, M., Coertzen, R. M., Keyser, M. J., & Steynberg, A. P. (2004). Synthesis gas production for FT synthesis. *Studies in Surface Science and Catalysis*, *152*, 258–405. https://doi.org/10.1016/s0167-2991(04)80461-0

Evans, G., & Smith, C. (2012). Biomass to Liquids Technology. In *Comprehensive Renewable Energy* (Vol. 5). Elsevier Ltd. https://doi.org/10.1016/B978-0-08-087872-0.00515-1

Fischer, F. & Tropsch, H. (1926). Die Erdölsynthese bei gewöhnliehem Druck aus den Vergasungsprodukten der Kohlen. *Brennstoff-Chemie: Zeitschrift für Chemie und Technik* von Kohle, Öl und Gas, Volume 7, p. 97 –116. https://books.google.co.za/books?id=60iZg1A5IBgC&focus=searchwithinvolume&q=Kohlenforschung

Fischer, F. (1930) . Development of the benzene synthesis from carbon monoxide and hydrogen at atmospheric pressure. *Brennst.-Chem.* 1930; 11:489

Flory, P. J. (1936). Molecular Size Distribution in Linear Condensation Polymers. *Journal of the American Chemical Society*, *58*(10), 1877–1885.

Förtsch, D., Pabst, K., & Groß-Hardt, E. (2015). The product distribution in Fischer-Tropsch synthesis: An extension of the ASF model to describe common deviations. *Chemical Engineering Science*, *138*, 333–346. https://doi.org/10.1016/j.ces.2015.07.005

Gao, J., Wu, B., Zhou, L., Yang, Y., Hao, X., Xu, J., Xu, Y., & Li, Y. (2012). Irregularities in product distribution of fischer-tropsch synthesis due to experimental artifact. *Industrial and Engineering Chemistry Research*, *51*(36), 11618–11628. https://doi.org/10.1021/ie201671g

E. F. G. Herrington and A. Robertson, "The influence of reaction mechanism on size distribution in polymers," *Trans. Faraday Soc.*, p. 38,40,490, 1942, doi: doi.org/10.1039/TF9423800490.

Jalama, K., Kabuba, J., Xiong, H., & Jewell, L. L. (2012). Co/TiO 2 Fischer-Tropsch catalyst activation by synthesis gas. *Catalysis Communications*, *17*, 154–159. https://doi.org/10.1016/j.catcom.2011.10.029

Kustov, L. M., & Tarasov, A. L. (2016). Fischer–Tropsch synthesis in a slurry mode using ionic liquids. *Catalysis Communications, 75*, 42–44. https://doi.org/10.1016/j.catcom.2015.12.003

Kwakwa, P. A., Adu, G., & Osei-Fosu, A. K. (2018). A time series analysis of fossil fuel consumption in Sub-Saharan Africa: Evidence from Ghana, Kenya and South Africa. *International Journal of Sustainable Energy Planning and Management*, *17*, 31–44. https://doi.org/10.5278/ijsepm.2018.17.4

Pardo-Tarifa, F., Cabrera, S., Sanchez-Dominguez, M., & Boutonnet, M. (2017). *Ce-promoted $Co/Al_2O_3$ catalysts for Fischer–Tropsch synthesis*. International Journal of Hydrogen Energy,

42(15), 9754–9765. https://doi.org/10.1016/j.ijhydene.2017.01.056

Schulz, H. (1999). Short history and present trends of Fischer-Tropsch synthesis. *Applied Catalysis*, *186*, 3–12. https://doi.org/PII S0926-860-X (99)00160-X

Song, D., & Li, J. (2006). Effect of catalyst pore size on the catalytic performance of silica supported cobalt Fischer-Tropsch catalysts. *Journal of Molecular Catalysis A: Chemical*, *247*(1–2), 206–212. https://doi.org/10.1016/j.molcata.2005.11.021

# CHAPTER 2: LITERATURE REVIEW


## Abstract

FT synthesis is a complex catalytic reaction for forming a wide range of hydrocarbons from syngas. The product distribution, which describes the different selectivities towards preferred fuels like gasoline, diesel, and waxes, is one of the most important components of FT synthesis. Designing catalysts that are suited to particular hydrocarbon product targets requires an understanding of the aspects influencing the distribution of FT synthesis products. A multidisciplinary approach integrating experimental, mechanistic, and data-driven methodologies is necessary to address the interplay between catalyst qualities, support parameters, and reaction conditions. This, therefore, leads to the formation of different fractions which correspond to different fuel product ranges as desired by the production process. The low carbon numbers $C_1$-$C_4$ are gaseous fuels, $C_5$-$C_{11}$ represent the gasoline hydrocarbon range, $C_{12}$-$C_{16}$ hydrocarbons are the diesel and jet fuel products, whereas $C_{17+}$ represents the waxes and lubricants (Schulz, 1999). The most probable product range is the short-chain hydrocarbon range, since cracking tends to take place when the chains become too long. For obtaining a specific product range, the extra processing step incurs extra costs and, thus, needs to be avoided. Therefore, there is a need to produce catalysts that direct the products towards the desired range without further processing.

The catalyst pore size is one of the factors that greatly influence the nature of the products in the FT synthesis process. Generally, the product molecules are much larger than reactants; therefore, there are different diffusion limitations for the product molecules depending on pore size distribution and chain length. If the product molecule is retained in the pore for too long, readsorption occurs, leading to the formation of longer chains.

During FT synthesis, the pore size of the catalyst significantly influences mass transfer resistance, product diffusion and access by the reactants to the active sites. This in turn affects the selectivity, efficiency, and the product distribution formed by the FT synthesis reaction.

This chapter sheds light on the complex relationship between catalyst pore size and product distributions in FT synthesis, in particular, how the dimensions of the pores impact selectivity, the rate of the reactions, and the growth of hydrocarbon chains. The reaction mechanisms through which this happens and the different product distribution models used to describe the resulting products have also been reviewed. An understanding of these effects, will facilitate optimization of catalysts towards the production of more useful hydrocarbons and fuel for industrial purposes. Several studies have been done on the factors that affect the product distribution of the process.

## 2.1 Introduction

Among multiple factors that influence the product distribution in FT synthesis, the catalyst support pore structure – including the average pore size distribution and catalyst loading influences the product distribution by altering the accessibility of the active sites of the catalyst, diffusion of the products and reactants, and the overall catalyst stability (Dry, 2002; Khodakov et al., 2001). The FT synthesis reaction was discovered by Hans Tropsch and Franz Fischer (after whom it is named) in the 1920s (Fischer & Tropsch, 1926, Fischer, 1930; Pichler, 1952) which allowed the production of organic hydrocarbon molecules on an industrial scale. To date, FT synthesis has been extensively studied, with a number of scientists developing mathematical models to illustrate the reaction mechanisms, the diffusion between the products and reactants and the catalyst pellets, and in turn, the distribution of products from the emerging output. Some mechanisms have been put forward that postulate how the FT synthesis reaction occurs on the catalytic surface, in an attempt to account for the subsequent distribution of the products. The distribution of FT synthesis products can be changed by utilizing promoters, catalytic supports, and different catalysts (Pardo-Tarifa et al., 2017). It has also been discovered that other parameters, such as solubility, physisorption and chemisorption, diffusion limitations, and reaction and reduction conditions, affect the outcome of the FT synthesis reaction (Kustov & Tarasov, 2016).

It has been established through experimental studies that materials which are mesoporous, with pore sizes in the range of 2 – 50 nm tend to offer an optimum performance in balancing diffusional control and surface area in Co – based FT synthesis (Bartholomew, 1990; Iglesia, 1997). The work that was done by Iglesia, (1997) managed to show that larger pores (>20 nm) tend to reduce the diffusion limitations within the particles, which would in turn lead to the observation of higher turnover frequencies (TOFs) for long-chain hydrocarbon products. On the other hand, very small sizes of the support pores (<4 nm) were found to cause the entrapment of waxes and eventually restrict the desorption and diffusion of the product, which increases secondary hydrogenation and thereby leads to higher selectivities of the paraffins.

A pore diameter of around 10 nm was found by some researchers to maximize the selectivity of the $C_{5+}$ hydrocarbons over $Co/SiO_2$ (Intarasiri et al., 2018; Chen et al., 2020; Song & Li, 2006) while inhibiting the production of methane. Moreover, very small pores that are less than 6 nm were found to affect the dispersion of the cobalt nanoparticles, which reduces the catalytic efficiency (Xing et al., 2016). Narrower pores have also been associated with higher chain growth probabilities in terms of affecting the hydrocarbon distribution; this could be due to longer intermediate residence times. Moreover, confinement effects, which are caused by mesopores, can

change the olefin/paraffin ratios and even favour the formation of particular oxygenates in some situations (De Deugd et al., 2003).

The FT synthesis process yields a complex hydrocarbon mixture. This necessitates the adoption of a model that can both predict the result when particular input conditions have been applied and facilitate the analysis of the results. Flory published the first model, known as the Flory model, to forecast the distribution of products in the early 1930s (Flory, 1936a). It was subsequently modified multiple times, and further models were created. Due to the process's complexity, no mathematical model has been developed yet that can accurately depict the product distribution in every case. Most models consider only the ideal ASF distribution of the FT synthesis products. Since many of the experimentally fitted product distributions have been found to deviate from this ideal model, the ASF model has undergone a number of modifications. In addition to their flexibility and wide range of applicability, the improved ASF models made it simpler to analyse the experimental data and extract the relevant information (Förtsch et al., 2015).

Where deviations from the ASF predicted product distribution are observed, Gao et al. (2012) attributed this to many factors, including some experimental artifacts. However, in order to be able to determine the product distribution, these variations will need to be evaluated to determine the circumstances that need to be put in place to get the intended products, that is, to increase the selectivity of the hydrocarbons responsible for the production of liquid fuels.

Recently, the use of machine learning (ML) techniques to simulate and forecast the impact of pore size on product distribution has increased due to the growing research which continues to lead to the discovery of further complexity of the catalyst–structure–performance interactions. These techniques overcome the drawbacks of conventional parametric experimental models by enabling the use of large, multi-dimensional datasets for analysis that result in a simpler and clearer understanding of the complex interrelationships (Jablonka et al., 2020), including pore size variations, reaction conditions, and product selectivity. The use of physics-informed machine learning models (PINNs), which integrate data-driven techniques with kinetic models to more accurately forecast the impact of pore size on diffusion-limited regimes, is another new trend. By leveraging computational techniques such as support vector machines (SVMs), artificial neural networks (ANNs) and random forest models, researchers can identify optimal catalyst structures and predict FT synthesis outcomes with greater accuracy (Raissi et al., 2019; Luo et al., 2023).

ML applied to experimental data validates the significance of pore size; combined with additional tools, like generative and Bayesian statistical models, for catalyst design and FT synthesis process optimization. To validate ML predictions, experimental data continues to provide the basis for

mechanistic insight. The combination of these techniques can be effective in designing catalysts of the future with specific porosity for desired hydrocarbon profiles (Kitchin, 2018).

This chapter explores some reported FT synthesis studies with three main foci: the factors which affect the product distribution obtained from the process, the effects of catalyst pore size on the catalyst performance and product selectivities and the mechanisms and product distribution models that are used to describe the observed reaction outcomes. The literature on recent ML studies was also included to comprehensively understand the subject and create a basis for the analysis of the findings of this particular study.

## 2.2 Factors affecting FT synthesis product distribution

Understanding the interactions between these elements is critical for maximizing FT synthesis performance as the niche market for clean synthetic fuels expands. A number of variables, such as catalyst characteristics, reaction conditions, and mechanistic elements, affect this distribution. Some important parameters that control product distribution in FT synthesis are discussed in this section.

### 2.2.1 Catalyst variables

**Active metal**

The choice of the active metal (e.g, ruthenium, cobalt or iron), has an impact on the distribution of products and the probability of the chain growth. Cobalt catalysts favour the production of paraffins with long chains and show poor water-gas shift activity, so that they are often used in low temperature FT synthesis (LTFT) (Dry, 2002; Gorimbo et al., 2018). Iron catalysts, on the other hand, are suitable for syngas with low $H_2$/CO ratios because they are active for the water-gas shift process and encourage the production of olefins. They are also more applicable in high-temperature FT synthesis (HTFT) conditions (Horáček, 2021). However, some studies have reported the use of iron catalysts in LTFT (Jahangiri et al., 2014; Chun et al., 2020). The HTFT process involves the use of temperatures in the range 300 – 350 °C, whereas LTFT incorporates temperatures below 300°C but above 200°C .

**Catalyst promoters**

In order to improve FT synthesis selectivity, the required reduction (activation) temperature must be decreased, catalytic activity, increased and catalyst stability increased, by adding promoters to the catalysts during synthesis (Horáček, 2021). It should be noted that a promoter often favour one outcome while inhibiting another. Table 2.1 lists some of the promoter effects from the previously conducted studies.

Table 2.1. A summary of the effects of some promoters on the FT synthesis process

| **Active metal** | **Support** | **Promoter** | **Effect** | **Reference** |
|---|---|---|---|---|
| Fe | Carbon nanotubes (CNT) | Na, K | Greater stability of the catalyst, reduced catalytic activity | (Xiong et al., 2015) |
| Co | SiC | Na | Acts as an impurity that lowers the selectivity and activity for SIC-supported catalysts | (Blekkan, 2013) |
| Co | $SiO_2$ | K | Increased $C_{5+}$ selectivity for $SiO_2$-supported catalysts | (Khobragade et al., 2012) |
| Fe | Activated carbon | Cu | Higher $C_{5+}$ selectivity, reduced FT synthesis and WGS activity, and easier Fe reduction | (Teimouri et al., 2023) |
| Fe | Unsupported | S | Reduced hydrogen coverage of active particles and increased olefin to paraffin ratios | (Bromfield & Coville, 1999). |
| Fe | $SiO_2$ | Ni | Reduced $C_{5+}$ selectivity and increased activity of the catalyst | (Qian et al., 2014) |
| Co | $SiO_2$ | Mn | Increased CO consumption, decreased $CH_4$ selectivity and increased $C_{5+}$ selectivity | (Dinse et al., 2012) |
| Fe<br>Co | $SiO_2$ | Zr | Enhanced stability due to inhibition of carburization, but also inhibits the extent of reduction extent. Increase C5+ selectivity when Co metal is used | (Qian et al., 2014)<br>(Johnson & Bell, 2016) |

**Catalyst support**

$SiO_2$, $Al_2O_3$, and $TiO_2$ are examples of FT catalyst support materials that affect the dispersion of metals, thermal stability, reducibility, and interaction with metal active sites. Because of its high surface area and irreducibility, silica is frequently employed to promote the uniform metal nanoparticles dispersion. Reducibility and activity can be impacted by the strong interactions of $Al_2O_3$ with metal particles (Gao et al., 2012; Bezemer et al., 2006). While neutral supports like $SiO_2$ favor heavier hydrocarbons, acidic supports tend to encourage cracking and enhance light hydrocarbons (Bartholomew, 2001). Iglesia (1997) concluded that the supports have an impact on the water molecules' adsorption and desorption throughout the reaction, which is important in FT synthesis because water is a significant byproduct. The active phase may oxidize or sinter as a result of inadequate water removal. Table 2.2 lists the effects of some of the well-known supports on the FT process.

Table 2.2. A summary of the effects of some supports on the FT synthesis reaction

| Support Type | Key Support Properties | Impact on FT Synthesis | Reference |
|---|---|---|---|
| Shaped carbon, activated carbon (AC) | High dispersion, sufficient metal-support interaction to result in small particles that are stable. | Useful for particle size studies | (Chen et al., 2021) |
| $ZrO_2$ | Moderate metal-support interaction, thermal stability | Balanced activity and selectivity | (Mosayebi et al., 2019) |
| $TiO_2$ | Redox active, facilitates the spillover effect | Enhanced catalyst reducibility, possible reoxidation | (Atashi et al., 2010) |
| $SiO_2$ | Inert, high surface area, pore size variability, easily reducible | Good dispersion, stable long-chain hydrocarbons | (Barbier et al., 2001; Moazami et al., 2015; Tian et al., 2018; Yaghoobpour et al., 2019) |
| $Al_2O_3$ | Acidic, strong metal-support | Reduced reducibility, methane formation | (Arslan et al., 2023; Riyahin et al., 2020; Shiba et al., 2023) |

| | | | |
|---|---|---|---|
| | interaction | | |
| SiC | High thermal conductivity, with some occurrence of Na and Mg impurities on the active sites | Catalyst sites are at the reaction temperature as the exotherm due to the enthalpy of reaction is mitigated. For supports with low thermal conductivity, the catalytic sites will be at much higher temperatures that the temperature of the surrounding gas and support material | (Blekkan, 2013) |

**Pore Size and Structure**

The catalyst support's pore size and shape affect how reactants and products diffuse, which can either encourage or inhibit secondary reactions like cracking and olefin re-adsorption. Better diffusion is often made possible by mesoporous materials, which results in more selective hydrocarbon dispersion (Li et al., 2016; Mehmood et al., 2017; Kim et al., 2023; Song & Li, 2006).

**Catalyst particle size and dispersion**

The number of active sites per gramme of metal loaded and their electrical characteristics are influenced by the size of the metal particles. Smaller particles may enhance dispersion, but they may also increase methane selectivity or result in unstable catalyst activity due to sintering. An optimal range of particle sizes is required to optimize the synthesis of $C_{5+}$ hydrocarbons (Bezemer et al., 2006).

**2.2.2 Reaction conditions**

Syngas conversion during FT synthesis and the product distribution are significantly impacted by reaction parameters, such as the temperature and pressure, gas hourly space velocity (GHSV), and $H_2$:CO ratios in syngas. The qualitative characteristics of the products, such as alcohols, diesel fraction, $C_2$–$C_4$ olefinic fraction, and naphtha, or $C_{25+}$ waxy compounds, can be the result of the choice of reaction conditions and catalyst type (Horáček, 2021).

**Operating pressure**

Increased residence time of reactants due to higher reaction pressures encourages chain growth and produces heavier hydrocarbons. Because of their poor inherent water-gas shift activity, cobalt-

based catalysts exhibit this effect more strongly (Dry, 2002; Ji et al., 2001; Yang et al., 2017; Farias et al., 2007).

**Gas Hourly Space Velocity**

The GHSV, which can be defined as the gas volumetric flow rate per catalyst volume per hour, has a major impact on the product distribution, particularly the probability and selectivity of chain growth, because it establishes how long the reactants stay in the catalyst bed. Chain propagation reactions are less likely at higher GHSV because reactants move through the catalyst bed more quickly, leading to low selectivities of $C_{5+}$ hydrocarbons (Van Der Laan & Beenackers, 1999). On the other hand, because there is greater time available for sequential CO insertion and product readsorption at lower GHSV, the gas remains in contact with the catalyst for longer periods, increasing the chain growth probability (α). Under these circumstances, high selectivity toward $C_{5+}$ hydrocarbons (diesel and wax range) is also discernible (Iglesia, 1997).

**Temperature of Reaction**

By raising the chain growth probability, lower temperatures are known to promote the synthesis of higher molecular weight hydrocarbons. Conversely, higher temperatures promote the synthesis of olefins and lighter hydrocarbons. The temperature also improves the hydrogenation rate, which in turn enhances the CO conversion (Pandeyet al., 2021). However, generally, every catalyst system has an ideal temperature range for balancing selectivity and activity (Sun et al., 2017; Gorimbo et al., 2018; Niu et al., 2020; Farias et al., 2007).

**Ratio of $H_2$/CO**

The hydrogen-to-carbon monoxide ratio in syngas has a big impact on the final product's makeup. Particularly in iron-catalyzed systems, a low $H_2$/CO ratio favors olefins and oxygenates, whereas a high ratio encourages the synthesis of methane and paraffin (Jess & Kern, 2023). Higher $H_2$/CO ratios also tend to favour the growth of the hydrocarbon chain, suppressing methane production, which enhances selectivity towards long-chain hydrocarbons. This causes the equilibrium of the water gas shift (WGS) to shift towards the consumption of more CO, producing more $H_2$ (Bukur et al., 2016)

## 2.3 Catalyst pore size and pore structure effects in FT synthesis product distribution

In FT synthesis, the movement of products and reactants via catalyst pores has a direct impact on secondary reactions, reaction kinetics, and, consequently, the distribution of the hydrocarbon chain length. Pore engineering has become a crucial design approach in recent years to maximise the

performance of FT synthesis catalysts, especially cobalt-based systems supported by mesoporous supports such as silica or alumina materials. To enhance mass transfer and boost the porosity of the material, additives can be included in the catalyst formulation such as acetic acid, ethanol and triisopropylbenzene as swelling agents resulting in additional pores (Mohammadnasabomran et al., 2021). The support's mechanical strength may decline as a result of these pores. This decline in mechanical qualities, however, causes problems when the reactor is operating. Therefore, a balance must be found between the material's mechanical strength, heat and mass transfer limitations, and the pressure drops. Every stage of the process, including production, the assessment of mechanical, physicochemical, and catalytic properties, typically entails trial and error (García-Sánchez & Baldovino-Medrano, 2023).

The chemical reactions and physical processes that occur in a heterogeneous catalytic reactor at the molecular scale are depicted in Figure 2.1 for cases where the active site of the catalyst is within the pores (Davis & Davis, (2003). The process of external mass transfer involves moving reactants from the fluid's bulk stream to the catalyst's surface as shown in steps 1 and 7 in Figure 2.1, as well as products from the outside of the catalyst body to the bulk fluid stream.

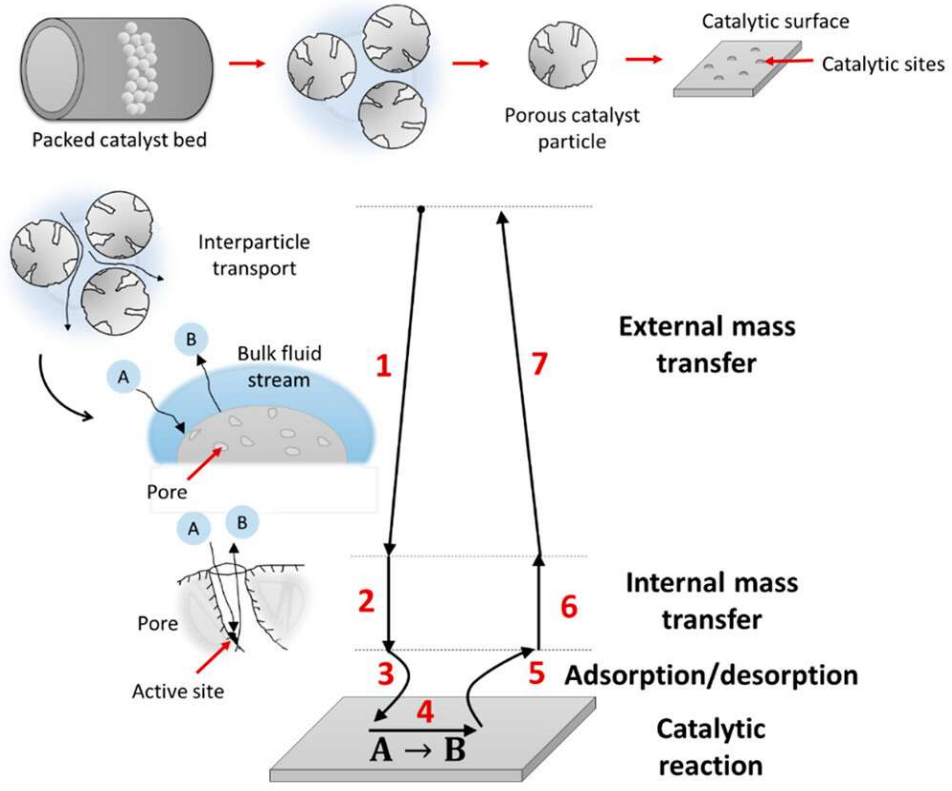



*Figure 2.1. A schematic showing transport phenomena that occur during heterogeneous catalysis with a porous catalyst. Adapted with permission from (García-Sánchez & Baldovino-Medrano (2023)*

### 2.3.1 Role of pore size in FT synthesis

During heterogeneous catalysis, catalyst pores increase the specific surface area available for adsorption and reaction and act as the transport channel for the products and reactants ( Davis & Davis, 2003). As the surface area increases, dispersion also increases, coupled with an increase in the number of active sites available (Kabir et al., 2024; Merino et al., 2016).

Pore size can be classified into:

- Micropores (diameter less than 2 nm): May cause pore blockage and limit mass transfer.
- Mesopores (diameter 2 to 50 nm) are ideal for FT synthesis because they achieve a balance between diffusion and surface area.
- Macropores (diameter greater than 50 nm): Reduce total surface area while improving flow-through.

Understanding the average radial diameters of the pore size is vital in FT synthesis as it also impact the sizes of the product molecules relative to the reactant molecules as the pores influence the diffusion of the reactants and products desorption inside the pores.

Condensation and capillary effects also sometimes take place within the catalyst pores, impacting the catalytic activity. Condensation takes place when the heavier hydrocarbons condense inside the catalyst mesopores, leading to the formation of liquid or semi-solid states in the system which can hinder diffusion. Capillary effects entail the lowering of the vapour pressure inside the smaller catalyst pores at pressures below bulk saturation leading to the formation of liquid. Both of these processes can cause pores to get blocked leading to reduced mass transport of the products and the reactants hence impacting the catalytic efficiency and selectivity of the long chain hydrocarbons (Kruk et al., 1997).

The typical gas phase diffusivity values in relation to pore size are displayed in Figure 2.2. There is a noticeable impact of the pore network's dimension on the diffusivity. When molecular collisions occur more frequently than collisions with walls, in large pores (greater than 17nm) transport by molecular diffusion occurs. Due to the molecules' limited ability to enter the pores, configurational diffusion and additional diffusion constraints occur in the case of small pores.

From Figure 2.2 it can be seen that micropores are associated with configuration diffusion whereas Knudsen diffusion dominates in micropores and partly takes place in some macropores where molecular diffusion is dominant for larger macropores. In general, the most desirable catalyst supports fall in the regime of Knudsen diffusion.

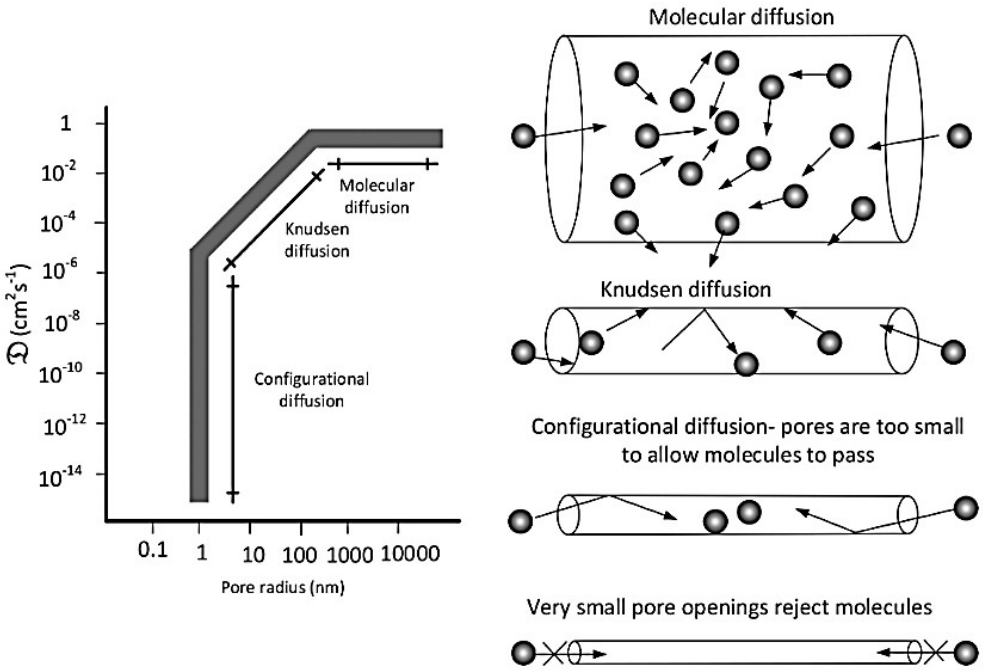



*Figure 2.2. Illustration of the relationship between gas diffusivity and catalyst pore size during heterogeneous catalysis. (Adapted with permission from (García-Sánchez & Baldovino-Medrano, (2023)*

### 2.3.2 Effects on product distribution and on the hydrocarbon chain length

**Secondary reactions and suppression of side reactions**

By promoting the first olefinic products' desorption from the active sites and stopping re-adsorption through diffusion out of the pores, mesoporous supports aid in reducing secondary hydrogenation or isomerisation. This lessens the undesirable production of paraffins from primary olefins (Tsubaki et al., 2001).

Larger mesopore supports have been shown to improve mass transfer, increase CO and $H_2$ residence times, and encourage chain propagation, all of which raise $C_{5+}$ yields. Their catalytic activity is also generally higher (Cheng et al., 2015; Zhang et al., 2010). Methane selectivity is increased by smaller pores since they can restrict the diffusion of larger molecules and facilitate the diffusion of methane product out of the pores, selecting methane as the only product that can desorb from the catalyst surface and diffuse out of its pores. On the other hand, higher $C_{5+}$ selectivities were noted for larger pore diameters of the support (Cheng et al., 2015).

**Coking and catalyst deactivation**

Catalyst pores that are too small (normally < 5 nm) can trap heavy hydrocarbons, which over time can cause pore blockage and coke production, thereby deactivating the catalyst. However, such deactivation mechanisms are less likely to occur in pores that are wider (Bezemer et al., 2006; Cheng et al., 2015).

The Boudouard reaction, which involves carbon deposition on the surface of the catalyst, at elevated temperatures ranging from 400 to 700 °C and high CO partial pressures, is shown in equation 2.0. The reaction commonly occurs in Fe-catalysed FT synthesis reactions due to the higher CO dissociation activity on the Fe catalyst.

$$2CO_{(g)} \rightarrow C_{(s)} + CO_{2\ (g)} \qquad 2.0$$

By obstructing the active sites, the deposited carbon solids may deactivate the catalyst (Liu et al., 2018; W. Chen et al., 2018).

**Improved metal dispersion and reducibility**

Metal dispersion and reducibility, which are essential for high activity and selectivity, are enhanced by supports with optimum pore sizes (usually 6–12 nm), which provide a good trade-off between surface area and metal accessibility (Zhang et al., 2010). When impregnating or depositing the metal during catalyst synthesis, metal precursor species can move more easily and readily through larger pores (5–20 nm) (Zhang et al., 2010). This ensures the availability of high surface areas of active sites and limits cobalt nanoparticle aggregation, resulting in better metal dispersion.

Achieving homogeneous cobalt particle sizes is essential for reliable catalytic performance, and supports with narrow pore size distributions aid in this process (Gnanamani et al., 2016; Intarasiri et al., 2017; Z. Li et al., 2018; Ni et al., 2017; Zhang et al., 2010).

## 2.4 Postulated mechanisms of the FT synthesis

A number of FT synthesis routes were discovered and modelled based on empirical evidence: the surface carbide mechanism, the hydroxyl assisted CO activation, the CO insertion model, and the enol mechanism. The mechanisms are described below:

- According to the surface carbide mechanism, the rate-determining stage of the hydrocarbon synthesis process is dissociative CO adsorption. Carbene species that readily polymerize are created in the scheme as a result of the surface carbide being partially hydrogenated (Van Santen et al., 2013).

  The mechanism is considered to be mechanistically simpler and it is mostly used in iron-catalysed systems. However, the dissociation of CO directly on cobalt on certain surfaces suffers from some kinetic hindrance (Chen et al., 2017). Figure 2.3 shows a schematic display of the mechanism.

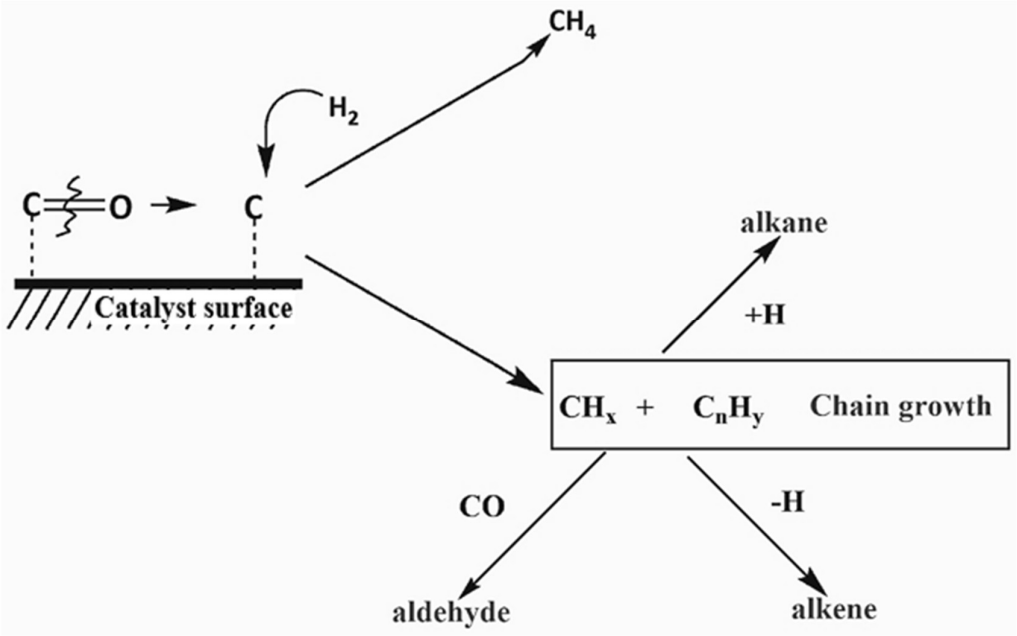



*Figure 2.3 A schematic of the carbide mechanism based FT synthesis route (Adapted from Van Santen et al., 2013).*

Formation of metal carbide intermediates occurs in this mechanism, and it can be considered the most structure-sensitive, as it relies on specific active sites to mediate the dissociation of CO and pave the way for the subsequent chain propagation.

- Hydroxyl-assisted CO activation, also known as hydroxy-polymerization (Rytter & Holmen, 2018). In order to produce -CHOH- like surface intermediates that easily condense to produce hydrocarbon products, the hydroxy-polymerization mechanism assumes that CO will be hydrogenated from H* or $H_2O$* species (Vlasenko & Yuzefovich, 1969). This mechanism is predominantly plausible on hydroxylated or acidic support surfaces. However, it is less effective in highly reduced or dry systems. The mechanism is schematically depicted in Figure 2.4.

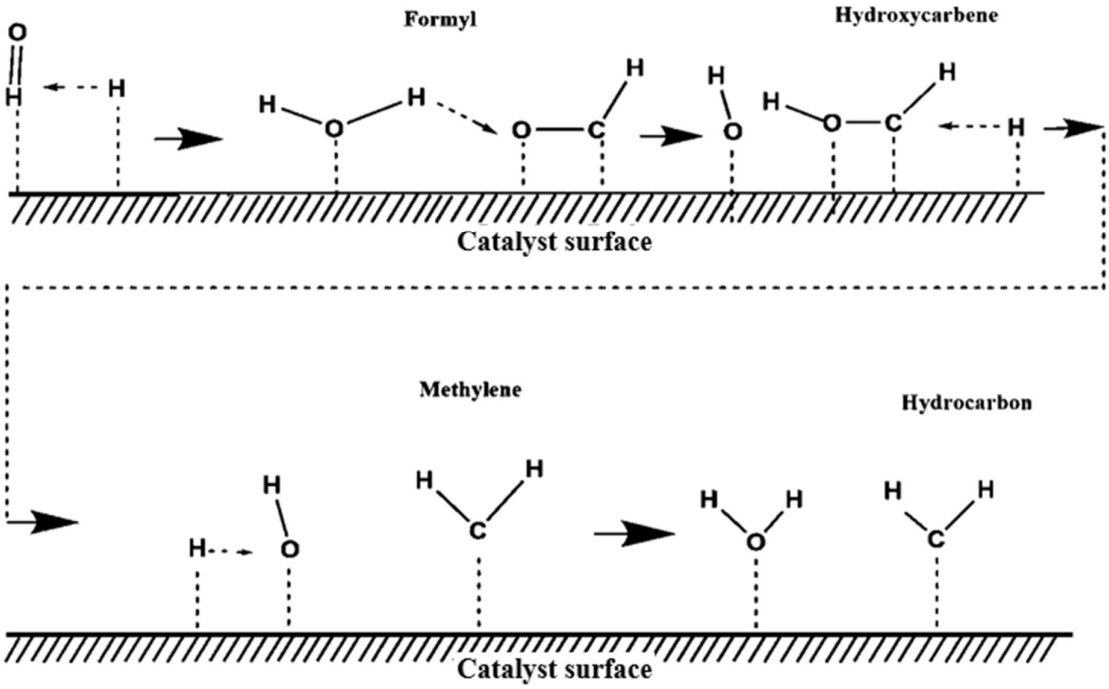



*Figure 2.4. A schematic showing the CO activation mechanism via the hydroxyl intermediate pathway (Adapted from (Rytter & Holmen (2018))*

- The CO insertion mechanism. The Schulz-Flory product distribution model of the FT synthesis served as the basis for the creation of this model. It shows how a chain can grow by inserting CO molecules into an alkyl chain with an adsorbed carbon species. After that, the product is hydrogenated to create alcohol or an olefin., and as shown in Figure 2.5, oxygen can also be removed from the alcohol precursor to create a paraffin. Adsorbed carbene species are also believed to be moved on top of alkyl chains (Biloen et al., 1979; Davis, 2001). The mechanism, however is regarded as more energetically demanding on some catalyst surfaces.

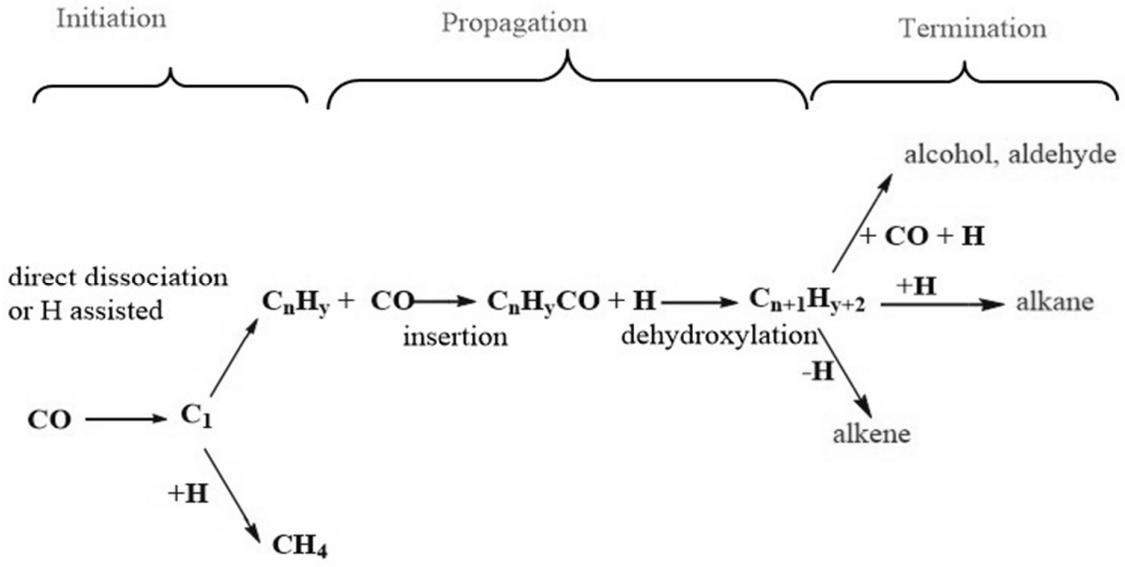



*Figure 2.5. A depiction of the CO- insertion mechanism (Adapted from (Van Santen et al., (2013)*

- The enol mechanism: In this mechanism, CO is chemisorbed and combines with adsorbed hydrogen to produce an enol molecule such as -MCHO*, where M represents the hydrocarbon chain. Then, using nearby groups, this structure expands through a series of water elimination stages (Davis, 2001). The main advantage of this mechanism is to capture the influence of the OH groups at the surface. The mechanism is usually less supported than the CO insertion mechanism, as it requires the pathway to go via the formation of some enol species and stabilization. The mechanism is schematically depicted in Figure 2.6.

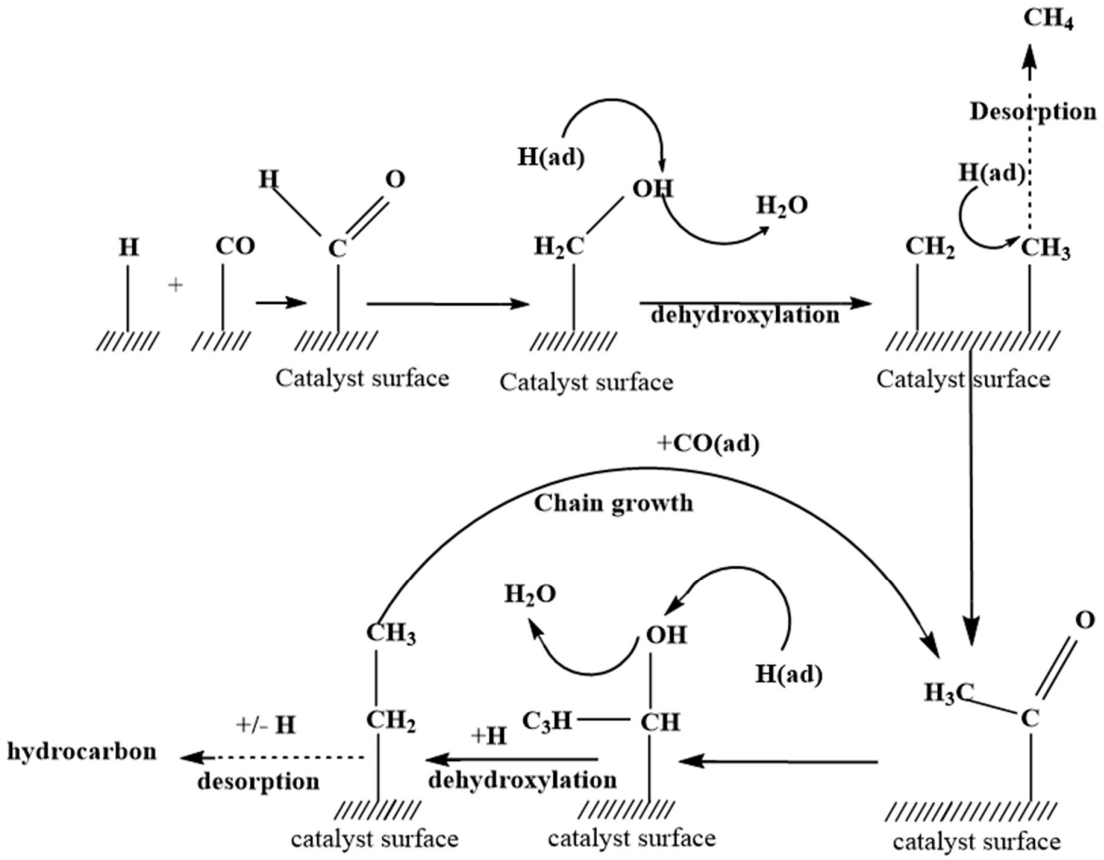



*Figure 2.6. The Enol Mechanism schematic diagram. Modified from Davis, (2001)*

Nijs et al. (1980) discovered that "end-to-end attachment" is the main growth pathway after looking at the product distribution of the reaction using catalysts that are ruthenium-assisted on the addition of 1-olefins (Nijs & Jacobs, 1980). Their work led to a model combining the carbide and CO insertion hypothesis, in addition to the four methods previously mentioned (Nijs et al., 1980).

In contrast, Fe, Co, and Ru were reported to selectively produce FT products when supported on zeolites or alumina in other studies (Vanhove et al., 1979). In these cases, the product spectrum could not be fitted into a Schulz-Flory equation because chain length affected chain growth. It is challenging to visualize and compare the product distributions from these findings to other models because they are usually only displayed in tabular form.

The studies by Nijs and Jacobs suggests that the chain growth probability is always significantly reduced at $C_1$, although it is relatively constant for $C_2$ hydrocarbons over the classical catalysts (e.g., Co promoted on silica) (Nijs & Jacobs, 1980; Nijs et al., 1980) Through a series of meticulously planned tests conducted in settings with high hydrocarbon growth rates, Nijs & Jacob

(1980) showed that induced dipoles (which occur in the presence of water and acid catalysts) encourage chain propagation in FT synthesis because of the ease of attraction between the molecules.

Overall, while the hydroxyl-assisted and enol mechanisms involve CO hydrogenation without full dissociation, the carbide mechanism involves CO cleavage, during the cleavage, direct dissociation of CO into adsorbed carbon (C*) and oxygen species on the catalyst surface occurs. The carbon species will then serve as chain growth sites for hydrocarbon polymerization, this fundamentally differentiates the chain growth initiation and propagation pathways in FT synthesis.

## 2.5 FT synthesis product distribution models

The product distribution of FT synthesis products has been studied since the early 1930s and several models have been put forward to analyse the output from the process. Different models which exist to date can be classified into four main categories which are the statistical, mechanistic or microkinetic, empirical and data driven models, and thermodynamic models. These models are useful in predicting the product distributions from the information obtained from the process conditions, catalyst, and kinetic parameters. However, there are also some hybrid models which combine thermodynamic, statistical and/ or mechanistic models. The widely used statistical models are fully explained below.

### 2.5.1 Statistical models

These models were created based on the chain growth probability, represented by a parameter known as the chain growth parameter (α) or alpha value. Some models use one chain growth parameter and others implement multiple chain growth parameters in the establishment of the models (Förtsch et al., 2015; Hillestad, 2015; Peacock-Lopez & Lindenberg, 1986; Stenger, 1985; Yu et al., 2018). There are three fundamental models that were derived from the early research work found in the literature which are summarised in Table 2.3.

Table 2.3. An overview of the fundamental statistical models

| Model | Equation | Reference |
|---|---|---|
| **Flory** | $W_n = (1-\alpha)\alpha^{(n-1)}$ | (Flory, 1936b) |
| **Schulz-Flory** | $M_n = (1-\alpha)^2\alpha^{(n-1)}$ | (Schulz, 1938) |
| **ASF** | $W_n = n(1-\alpha)^2\alpha^{n-1}$ | (Henrici-Olivé & Olivé, 1976b) |

Flory (1936) found and experimentally demonstrated that the FT synthesis products follow the distribution shown by the following equation:

$$W_n = (1 - \alpha)\alpha^{(n-1)} \quad \text{.....(2.1)}$$

Where α is the chain growth parameter and $W_n$ is the weight fraction of hydrocarbons with n carbon atoms (Flory, 1936a; Huff & Satterfield, 1984; Odian, 2004; Satterfieldand & Huff, 1982).

Generally, the alpha values observed from FT synthesis range from very low values as low as 0.3 as reported by Martínez et al., (2003) up to as high as 0.95 as reported by Kabir et al., (2024). With most of the studies reporting alpha values between 0.5 and 0.9. To cater for the whole range of values, and observe the trends, values of 0.2, 0.3, 0.5 and 0.9 were used in the following section to analyse the behaviour of the various models upon changing the alpha values.

An illustration of the effect of the four alpha values of 0.2, 0.3, 0.5, and 0.9 on the Flory distribution is presented in Figure 2.7. Higher alpha values indicate the formation of longer hydrocarbon chains.

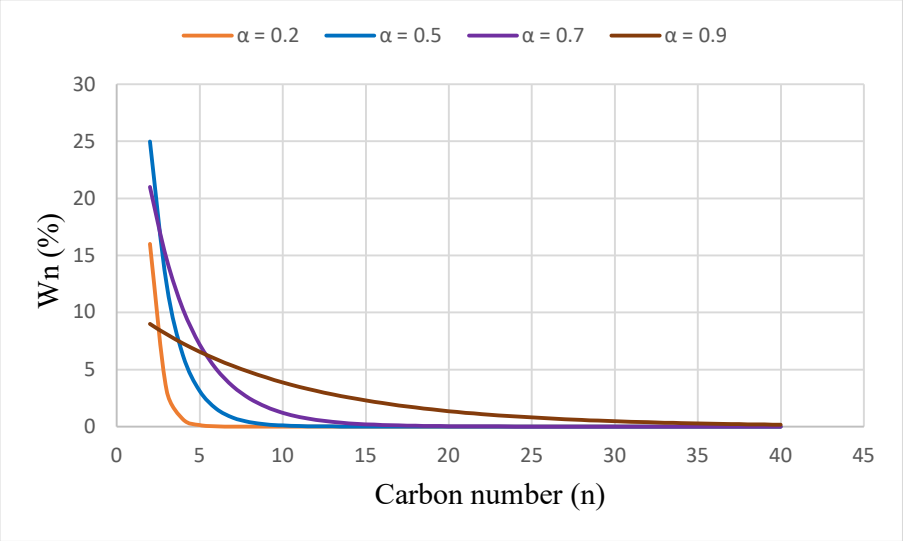



*Figure 2.7. Illustration of the behaviour of the Flory model on selected alpha values*

After this, a separate model was created by Schulz (1938) to show the distribution of the FT products. The model is represented by equation 2.2 below:

$$M_n = (1 - \alpha)^2\alpha^{(n-1)} \quad \text{.....(2.2)}$$

where α has the same definition as mentioned before, and $M_n$ represents the mole fraction of the product for carbon number n (Schulz, 1939). It should be noted that certain publications, such as (Donnelly et al., 1988), refer to equation 2.2 as the Schulz-Flory Model. The same four values of alpha as were used in Figure 2.7 have been used as inputs in equation 2.2 to produce Figure 2.8, to illustrate the outputs of the model.

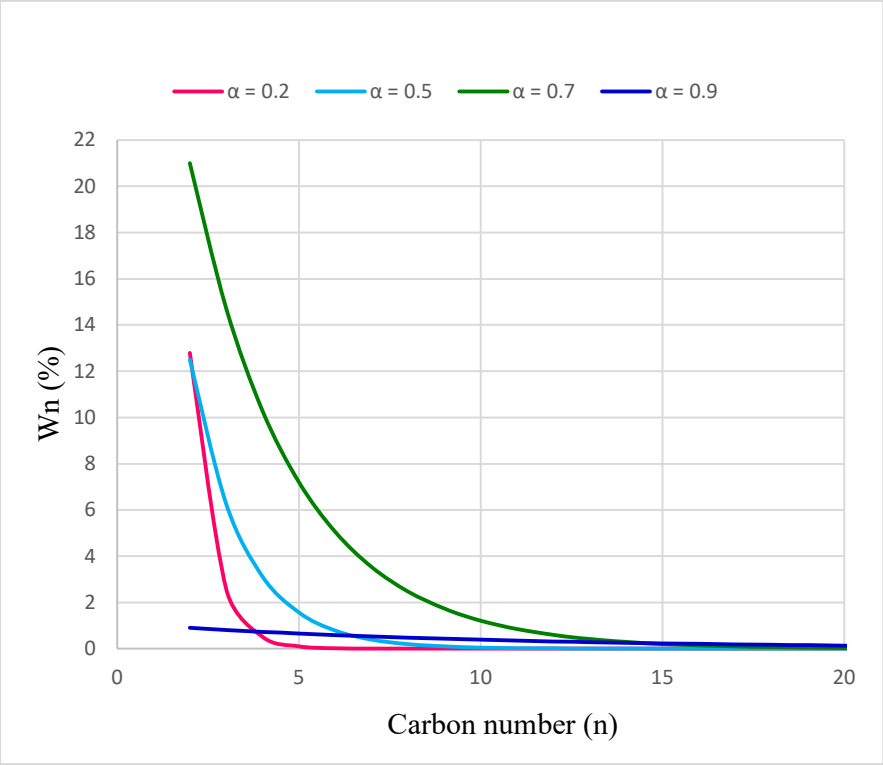



*Figure 2.8. A schematic of the Schulz- Flory distribution plot for four different alpha values*

This model is easy to use because it is simpler, and with a slight modification of the generic Flory model, it represents the product distribution. However, it had some shortcomings that caused the model to be changed in the years that followed:

- Chain transfer and termination reactions can have a substantial impact on the distribution of the molecular weights of the hydrocarbon products, but the model disregards these. The molecular weight distribution may become narrower or wider in actual polymerisation processes as a result of chain transfer and termination; in other words, chain transfer reactions often result in a wider molecular weight distribution since they increase the variety of chain lengths. Termination by combination of some chain transfer processes, on the other hand, which entail the transfer of a developing polymer chain to another molecule, such as transfer to a consistent termination agent, might limit the molecular weight dispersion. (Odian, 2004).
- The Schulz-Flory model ignores the potential for branching in polymer chains by assuming a completely linear polymer structure. Branching can actually happen, resulting in molecular weight distributions that are more intricate (Schulz, 2013).
- The impact of catalyst type, pressure, and temperature on the polymerisation process is also not taken into consideration by the Schulz-Flory model. These elements can significantly affect the molecular weight distribution of the polymer in a variety of real-world situations.

**ASF distribution**

Two stages could be distinguished in the evolution of the ASF distribution model: (1) Chain development through lateral reactions between adsorbed building pieces on the catalyst surface.

(2) Chain expansion by inserting a single building block at a time.

The first model was published by (Craxford & Rideal, (1939). The relatively low branched-chain hydrocarbons percentage observed among the FT synthesis products could not be explained by this mechanism (Storch, 1948). The molar distribution of the products from a synthesis reaction was initially discovered by Herrington and Robertson in 1942, and they introduced the concept of progressive insertion in 1942 (Herrington & Robertson, 1942). The same derivation was later on done independently by Anderson et al. (1951) (Anderson et al., 1951). Henrici-Olivé and Olivé (Henrici-Olivé & Olivé, 1976a) noted this and named it the Anderson-Shulz-Flory (ASF) distribution model. The model shown in Equation 2.3 represents the product distribution:

$$W_n = n(1-\alpha)^2\alpha^{n-1} \quad \text{.....(2.3)}$$

Where Wn, represents the mass fraction and α, and n have the same definition as those in the previous section. The same four values of alpha (viz. 0.2, 0.5, 0.7 and 0.9) are used to illustrate the ASF distribution model in Figure 2.9.

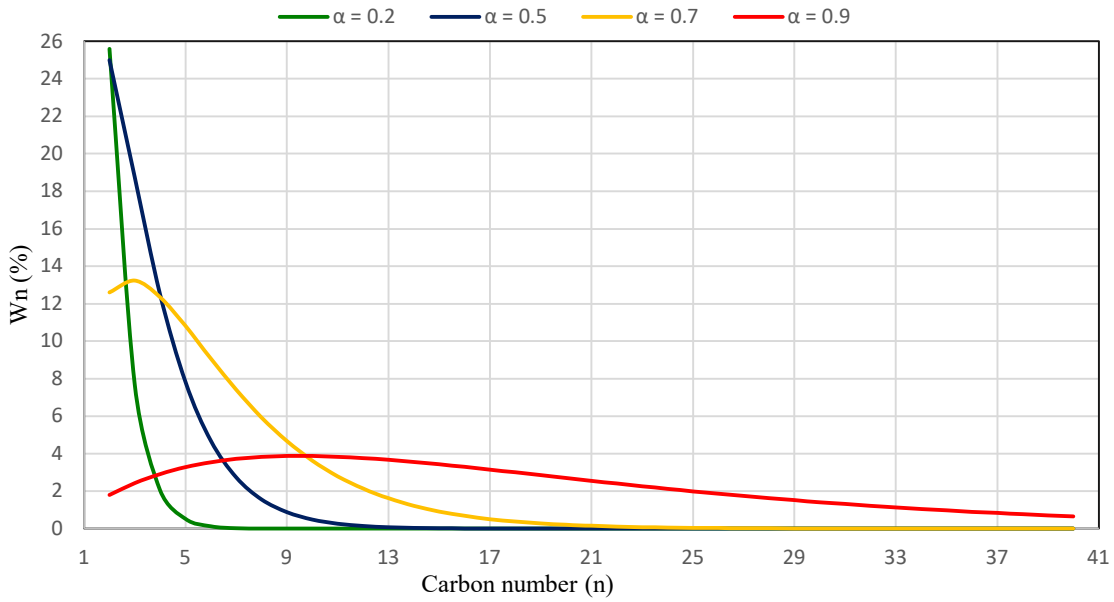



*Figure 2.9. A representation of the ASF distribution for four different alpha parameters (0.2, 0.5, 0.7 and 0.9)*

It is evident from the curves in Figure 2.9 that the higher chain growth probability values favours the creation of long-chain hydrocarbons and vice versa. For any chain growth probability value,

there is a maximum yield associated with a particular chain length. For instance, the highest yield for $C_{10}$ is achieved when $\alpha = 0.9$.

However, there are other approaches that are used to describe and model the FT synthesis product distribution.

### 2.5.2 Mechanistic or Microkinetic models

These models are based on the elementary reaction steps taking place as the reaction progresses, such as CO dissociation, chain termination, and hydrogenation. To formulate the models, a detailed knowledge of the chemical energetics and surface chemistry is required. These fall under two primary categories, which are the Langmuir-Hinshelwood-Hougen-Watson (LHHW) models and the Surface Polymerization models (Todic et al., 2013)

#### LHHW Models

LHHW models examine all facets of the FT synthesis mechanisms, such as chain initiation, propagation, termination, monomer synthesis, and reactant adsorption and incorporate these in rate expressions. They can further explain how the product distribution varies with carbon number using concepts like chain length-dependent olefin desorption and/or 1-olefin readsorption. One notable application for them is in modelling the rates of reaction (Botes, 2007; Todic et al., 2013).

#### Surface polymerization models

These models consider the hydrocarbon chain growth on the metal surfaces as a process similar to polymerisation, with active sites acting as centres of polymerisation used to describe branching behaviour and chain-length distributions (Shao et al., 2015).

### 2.5.3 Empirical and data-driven models

#### Empirical kinetic models

These make use of fitted parameters for the equations that describe the relationships between product yields and operating conditions in the reactor (such as $H_2$/CO ratio, temperature and pressure). Use of them is helpful for process simulations, but less generalisable since it is equipment and catalyst specific (Das et al., 2005; Nakhaei Pour et al., 2013; Pandey, Runningen, et al., 2021; Van Steen & Schulz, 1999; Withers et al., 1990; Yakubovich & Strizhak, 2007).

#### Models for Machine Learning (ML)

ML models utilise large, collated datasets to forecast the distribution of hydrocarbons depending on input variables like reaction conditions and catalyst characteristics (such as pore size and metal

loading) using different ML algorithms. These can perform better on prediction tasks than traditional models, but they require big, high-quality datasets (Patel et al., 2023).

### 2.5.4 Thermodynamic models

These models assume that thermodynamic equilibrium is reflected in product distributions and are usually applied to evaluate limiting behaviour of high-temperature gas-phase FT synthesis. The models primarily incorporate the use of approaches to make the Gibbs free energy a minimum in describing the phase and chemical equilibria of multiphase and multicomponent systems that are involved in FT synthesis (Marques & Guirardello, 2018; Chen & Yang, 2019).

The researchers, Norval and Phillips, showed that the ASF distribution could be formulated on the basis of thermodynamic equilibrium (Norval & Phillips, 1990). Later a complementary but different thermodynamic technique was proposed by Lu et al., (2012). The product distribution was represented as a triangle in the analysis using paraffin to olefin (P/O) ratios. These ternary plots were inspired by residue curve maps that are used in distillation processes. Any position within the triangle represents the normalised mole fraction of the three hydrocarbons under consideration, these are formed by dividing molar amounts of the independent species in the equilibrium by the total molar amounts of all of the species that will be present at equilibrium, which are then arranged clockwise according to their boiling points from low to high. This is the positive mass space. The three sides of the triangle each stand for a pure component of the three hydrocarbons that are being considered.

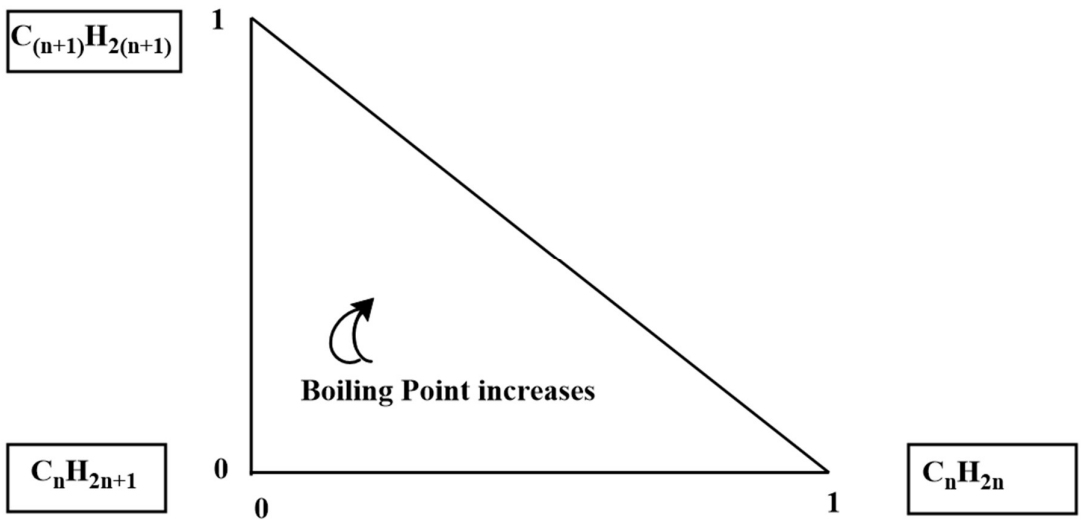



*Figure 2.10. Depiction of the triangular plot for thermodynamic product distribution of $C_nH_{2n}$, $C_nH_{2n+2}$ and $C_{n+1}H_{2(n+1)}$ (Adapted from (Lu et al.(2012).*

From the diagram in Figure 2.10, as we move from $C_nH_{2n} = 1$ towards the origin, i.e. $C_nH_{(2n+2)} = 1$ the reaction that is taking place is olefin hydrogenation as you move from $C_nH_{(2n+2)} = 1$ towards

the $C_{(n+1)}H_{2(n+1)}$ = 1 the chain growth is taking place. Based on experimental data (not shown) a straight line can be fitted between the product composition points for successive hydrocarbon chain lengths. This means that the $C_{n+1}H_{2(n+1)}/C_nH_{2n}$ ratio is constant. The value of the ratio is obtained by reading off the binary composition along the $C_{n+1}H_{2(n+1)}$ $C_nH_{2n}$ axis. The $C_{n+1}H_{2(n+1)}/C_nH_{2n}$ ratio shows a consistent value across the wide variety of experimental conditions and temperatures since the intercepts in the formula are the same for similar carbon numbers. According to Lu et al. (2012), this implies that a reaction equilibrium relationship between the olefin products in the FT synthesis process controls the olefin distribution in the process (Lu et al., 2012).

## 2.6 Application of machine learning in FT synthesis studies

ML has revolutionised catalysis research with its unprecedented capacities for predicting, analysing, and optimising complex chemical processes such as FT synthesis. The FT process has historically been studied using experimental techniques and kinetic modelling. However, because of the wide range of parameters including catalyst composition, structural features, and operating conditions, it is often difficult to compare experimental data from different sources, and therefore it is hard to make sense holistically of the published literature. ML attempts to solve this limitation by enabling data-driven insights that can accelerate catalyst identification and process optimisation. A number of studies have been published in the literature, utilizing this tool in order to predict the performance of catalysts in FT synthesis reactions. Several stages are employed in the application of this method to come up with a clear picture of the product distribution from the collected data. Generating predictive and explanatory hypotheses using data infrastructure, machine learning, statistics, and computational methods, the emerging subfield of "catalysis informatics" combines materials informatics with cheminformatics to solve the unique challenges of complex systems in heterogeneous catalysis (Medford et al., 2018).

FT synthesis is not an outlier in the application of ML, it has been used in a number of energy-related complex systems such as waste to energy projects involving biomass and other solid waste types (Alabdrabalnabi et al., 2022; Li et al., 2021; Yang et al., 2022) demonstrating that ML can be implemented in different types of data analysis in the energy sector.

For FT synthesis, several ML studies have been documented in the literature, which analyse the robust functionality of heterogeneous catalysts (Chakkingal et al., 2022; Garona et al., 2021; Teimouri et al., 2024). The ML methods can be applied to several aspects of the given set of data. ML methods involve data identification and collection, data processing, model selection and engineering, model interpretation and application. Figure 2.11 summarizes these processes from the studies conducted by Teimouri et al. (2024).

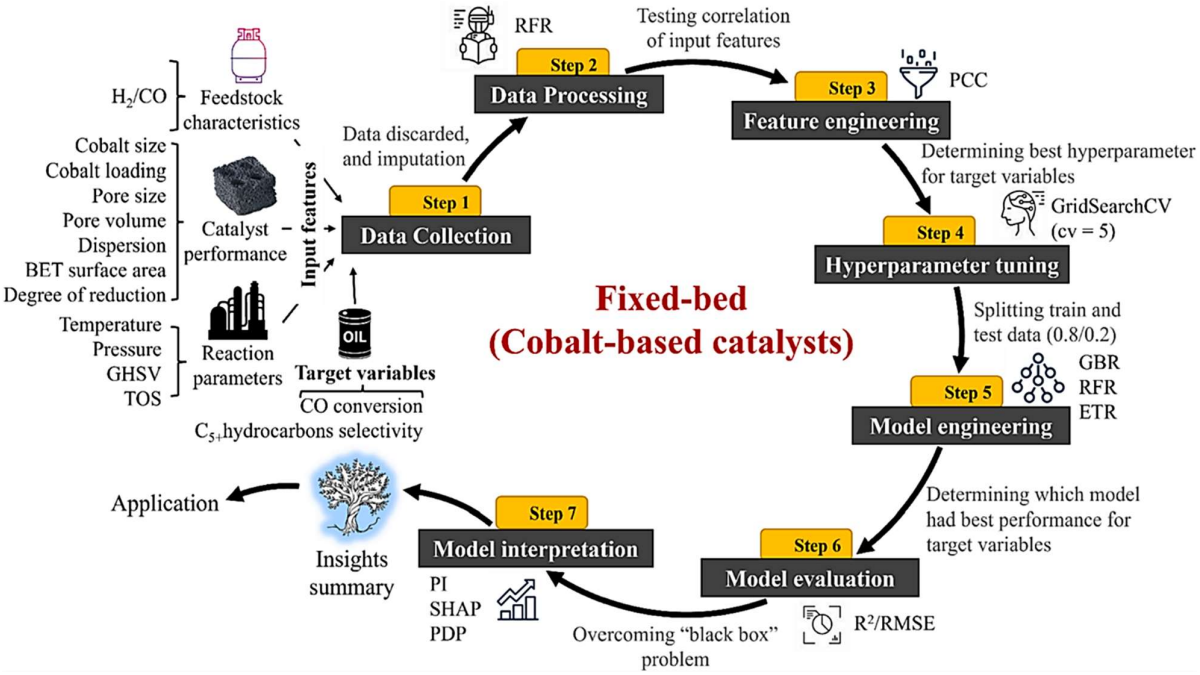



*Figure 2.11. A summary of the steps involved in the ML framework of a study of the catalyst performance on Co- based catalysts. (Adapted with permission from Yuan et al., (2024))*

### 2.6.1 Common models used in machine learning

For multi-output forecasts in general, several machine learning methods are applicable. Decision trees, Lasso Regression, Random Forests, K-Nearest Neighbour regression (KNN), Support Vector Regression (SVR) and Artificial Neural Network (ANN) are the most widely used machine learning techniques for regression (Brownlee, 2014). According to the literature, the machine learning models stated above have a complexity that goes in the order: ANN > SVR > KNN > Lasso> Random Forest. Multi-output regression is directly supported by machine learning techniques including KNN regression, Lasso regression, and ANN, and its implementation is comparable to that of single output (Brownlee, 2014). The Random Forest model was used in this research work and one of the less complex ones to use. For instance, Teimouri et al., (2024) created machine learning models to forecast $C_{5+}$ selectivity using Random Forest approaches.

Figure 2.12 shows the typical steps that are followed when using the Random forest model based on the studies conducted by Motaev et al. (2023) on using ML on Co-catalysed FT synthesis.

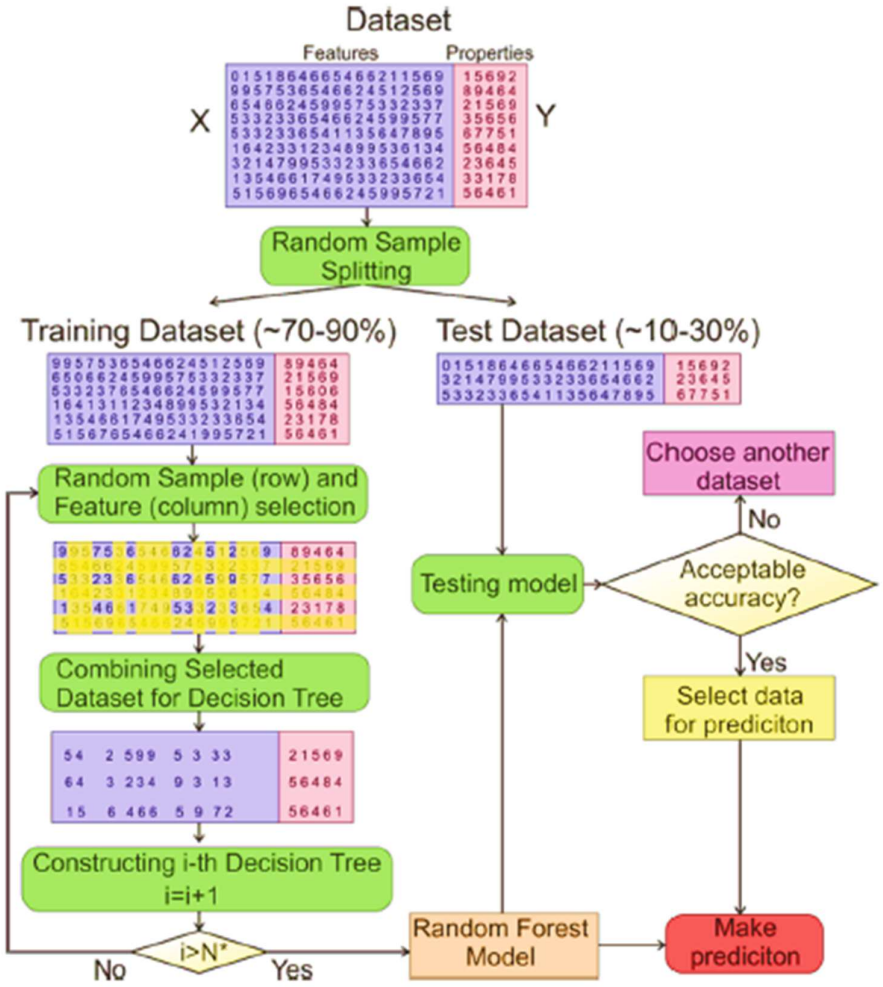



*Figure 2.12. A typical sequence of tasks followed when using the Random Forest model (Adapted with permission from Motaev et al. (2023)*

A list of some highlights of the advantages of using the ML approach is shown below:

**Catalyst Screening and Property Prediction**

Based on characteristics like metal loading, support type, and synthesis parameters, machine learning (ML) models like regression, ANN, and artificial SVR have been used to forecast catalyst stability, selectivity and activity (Jain et al., 2013).

**Use of ML in product distribution modelling**

Using supervised machine learning techniques like gradient boosting and decision trees, the distribution of hydrocarbon products based on variables like temperature, pressure, and $H_2$/CO ratio has been modelled (Patel et al., 2023). These techniques offer versatility beyond the standard ASF model by capturing complex nonlinearities and secondary reactions.

**Reaction conditions optimization**

To determine the ideal reaction conditions for optimising long-chain hydrocarbon production Bayesian optimisation and genetic algorithms are frequently employed (Kitchin, 2018). These techniques enhance process efficiency and drastically lessen the experimental load.

**Significance and interpretability of features**

Increasingly, tree-based models like XGBoost and SHAP (SHapley Additive exPlanations) approaches are being used to understand how different catalyst properties impact performance (Lundberg & Lee, 2017; Dean et al., 2023).

**Automated catalyst design**

Combining automated synthesis, high-throughput experimentation (HTE), and machine learning (ML) enables the speeding up of the catalyst discovery cycles (Jensen, 2017). Furthermore, reinforcement learning (RL)-based autonomous experimentation is being studied.

**Generalization of models and transfer learning**

By improving scalability and minimizing the need for intensive retraining, transfer learning aids in the adaptation of models trained on one catalyst-support system to another (Yamada et al., 2019; Butler et al., 2018).

Generally, ML is becoming a more significant aspect of research on FT synthesis. It improves the interpretation of experimental data, leverages data analytics to support logical design, and facilitates the rapid identification of the optimal catalysts and conditions. As ML methods and catalytic data resources continue to advance, their significance in transforming FT synthesis research will only increase. However, major challenges include process engineering integration, interpretability of the model, and lack of data. These can be addressed via shared datasets and making use of open data from other entities and researchers, available to the public domain as the models work best with a larger amount of data (Himanen et al., 2019).

To prove the usefulness of the ML tool in FT synthesis, studies have been done in the past to test the FT synthesis system behaviour and some experimental data was used to validate the accuracy of the results (Motaev et al., 2023). However, the limitations of the use of ML in FT synthesis studies are found in the fact that the process requires very high volumes of complete, high quality diverse experimental data for the best outcome, without many outliers. It is not feasible to obtain this due to the diverse experimental conditions used in the published literature. The presence of noise and incomplete data reduces the predictive power of the models.

The limitations of machine learning (ML) in Fischer–Tropsch synthesis studies primarily stem from data quality, model interpretability, and generalizability. ML models strongly rely on the

availability of sizable, and diverse experimental datasets, which are of a high quality, incomplete or noisy data can reduce model accuracy and predictive power.

## 2.7 Conclusion

The impact of catalyst pore size on the distribution of products in FT synthesis is complex, combining aspects of secondary reaction suppression, active site accessibility, and mass transfer. By improving metal dispersion and reducing the readsorption of light hydrocarbons that cause secondary reactions, mesoporous supports, especially those with larger pore diameters have been shown in numerous experimental investigations to aid in the production of hydrocarbons with longer chains ($C_{5+}$). Hydrocarbon selectivity, suppression, or promotion of methane production, and catalyst stability are all directly impacted by these physical characteristics. Several product distribution models, such as statistical, mechanistic, empirical data-driven, thermodynamic, and even ML-based models, can be used to simulate the results of these fluctuations.

In addition to the experimental results, ML techniques have been explored for deciphering the intricate relationships between pore structure and product distribution. ML techniques have emerged as useful tools for trying to understand the complex relationships in FT synthesis and can also be applied to study the relationship between hydrocarbon selectivity, operating variables, and pore structure. Furthermore, interpretable, physics-based ML frameworks increase reliability by integrating mechanistic insights into data-driven models. The ML techniques shall be incorporated in this work to study the effects of the catalyst pore sizes on the product distribution.

When combined, these methods offer a thorough comprehension of the relationship between pore size and FT synthesis performance. Continuous integration of ML with high-throughput experimental methods and enhanced characterisation will be necessary to accelerate catalyst development and achieve sustainable synthetic fuel production.

## References


Alabdrabalnabi, A., Gautam, R., & Mani Sarathy, S. (2022). Machine learning to predict biochar and bio-oil yields from co-pyrolysis of biomass and plastics. *Fuel*, *328*(December 2021), 125303. https://doi.org/10.1016/j.fuel.2022.125303

Anderson, R. B., Friedel, R. A., & Storch, H. . (1951). Fischer - Tropsch Reaction Mechanism Involving Stepwise Growth of Carbon Chain. *Journal of Chemical Physics*, *19*, 313–319. https://doi.org/doi.org/10.1063/1.1748201

Arslan, M., Bepari, S., Abrokwah, R., Mohammad, N., Shajahan, J., & Kuila, D. (2023). Effect of Al2O3 Support on Co-Based SiO2 Core–Shell Catalysts for Fischer–Tropsch Synthesis in 3D Printed SS Microchannel Microreactor. *Topics in Catalysis*, *66*(5–8), 477–497. https://doi.org/10.1007/s11244-022-01733-z

Atashi, H., Siami, F., Mirzaei, A. A., & Sarkari, M. (2010). Kinetic study of Fischer-Tropsch process on titania-supported cobalt-manganese catalyst. *Journal of Industrial and Engineering Chemistry*, *16*(6), 952–961. https://doi.org/10.1016/j.jiec.2010.04.005

Barbier, A., Tuel, A., Martin, G. A., Arcon, I., Arcon, I., Kodre, A., & Kodre, A. (2001). Characterization and catalytic behavior of CO/SiO2 catalysts: Influence of dispersion in the Fischer-Tropsch reaction. *Journal of Catalysis*, *200*(1), 106–116. https://doi.org/10.1006/jcat.2001.3204

Bartholomew, C. H. (1990). Recent technological developments in Fischer-Tropsch catalysis. *Catalysis Letters*, *7*, 303–315.

Bartholomew, C. H. (2001). Mechanisms of catalyst deactivation. *Applied Catalysis A: General*, *212*(1–2), 17–60. https://doi.org/10.1016/S0926-860X(00)00843-7

Bezemer, G. L., Bitter, J. H., Kuipers, H. P. C. E., Oosterbeek, H., Holewijn, J. E., Xu, X., Kapteijn, F., Van Diilen, A. J., & De Jong, K. P. (2006). Cobalt particle size effects in the Fischer-Tropsch reaction studied with carbon nanofiber supported catalysts. *Journal of the American Chemical Society*, *128*(12), 3956–3964. https://doi.org/10.1021/ja058282w

Biloen. P., Helle, J.N., & Sachtler, W.M.H. (1979) Incorporation of surface carbon into hydrocarbons during Fischer-Tropsch synthesis: Mechanistic implications, Journal of Catalysis, Volume 58, Issue 1, Pages 95-107, https://doi.org/10.1016/0021-9517(79)90248-3.

Blekkan, E. A. (2013). *Fischer – Tropsch Synthesis on SiC-Supported Cobalt Catalysts*. 730–736. https://doi.org/10.1007/s11244-013-0032-3

Botes, F. . (2007). Proposal of a New Product Characterization Model for the Iron-Based Low-Temperature Fischer−Tropsch Synthesis. *Energy and Fuels*, *21*, 1379–1389.

Bromfield, T. C., & Coville, N. J. (1999). *The effect of sulfide ions on a precipitated iron Fischer – Tropsch catalyst*. *186*, 297–307.

Brownlee, J. (2014). *Machine Learning Mastery*. 1–15. http://machinelearningmastery.com/machine?learning?resources/

Bukur, D. B., Todic, B., & Elbashir, N. (2016). Role of water-gas-shift reaction in Fischer – Tropsch synthesis on iron catalysts : A review. *Catalysis Today*, *275*, 66–75. https://doi.org/10.1016/j.cattod.2015.11.005

Butler, K. T., Davies, D. W., Cartwright, H., Isayev, O., & Walsh, A. (2018). Machine learning for molecular and materials science. *Nature*, *559*(7715), 547–555. https://doi.org/10.1038/s41586-018-0337-2

Chakkingal, A., Janssens, P., Poissonnier, J., Virginie, M., Khodakov, A. Y., & Thybaut, J. W. (2022). Multi-output machine learning models for kinetic data evaluation: A Fischer–Tropsch synthesis case study. *Chemical Engineering Journal*, *446*(P4), 137186. https://doi.org/10.1016/j.cej.2022.137186

Chen, J., & Yang, C. (2019). *Thermodynamic Equilibrium Analysis of Product Distribution in the Fischer − Tropsch Process Under Di ff erent Operating Conditions*. https://doi.org/10.1021/acsomega.9b03707

Chen, W., Kimpel, T. F., Song, Y., Chiang, F., Zijlstra, B., Pestman, R., Wang, P., & Hensen, E. J. M. (2018). *Infl uence of Carbon Deposits on the Cobalt-Catalyzed Fischer − Tropsch Reaction : Evidence of a Two-Site Reaction Model*. https://doi.org/10.1021/acscatal.7b03639

Chen, W., Pestman, R., Zijlstra, B., Filot, I. A. W., & Hensen, E. J. M. (2017). *Mechanism of Cobalt-Catalyzed CO Hydrogenation:1. Methanation*. https://doi.org/10.1021/acscatal.7b02757

Chen, Y., Li, X., Dai, L., Nisa, M. U., Liu, C., Lv, S., Lv, J., & Li, Z. (2020). Controllable synthesis of core-shell Co@C@SiO2 catalysts for enhancing product selectivity in Fischer-Tropsch synthesis by tuning the mass transfer resistance. *Journal of Energy Chemistry*, *51*, 199–206. https://doi.org/10.1016/j.jechem.2020.03.074

Chen, Y., Wei, J., S. Duyar, M., V. Ordomsky, V., Y. Khodakov, A., & Liu, J. (2021). Carbon based catalysts for Fischer–Tropsch synthesis. *Chemical Society Reviews*, *50*(4), 2337. https://doi.org/10.1039/d0cs00905a

Cheng, K., Virginie, M., Ordomsky, V. V, Cordier, C., Chernavskii, P. A., Ivantsov, M. I., Paul, S., Wang, Y., & Khodakov, A. Y. (2015). Pore size effects in high-temperature Fischer – Tropsch synthesis over supported iron catalysts. *Journal of Catalysis*, *328*, 139–150. https://doi.org/10.1016/j.jcat.2014.12.007

Chun, D. H., Bae, G., Min, R., Youn, H., Deviana, D., Eun, J., Ji, L., Park, C., & Jeong, H. (2020). Brief Review of Precipitated Iron-Based Catalysts for Low-Temperature Fischer – Tropsch Synthesis. *Topics in Catalysis*, *63*(9), 793–809. https://doi.org/10.1007/s11244-020-01336-6

Craxford, S. R., & Rideal, E. K. (1939). The mechanism Of the Sythesis of Hydrocarbons from Water Gas. In *Journal of the Chemical Society* (Issue 140). https://doi.org/DOI https://doi.org/10.1039/JR9390001604

Das, T., Conner, W., Li, J., Jacobs, G., Dry, M., & Davis, B. (2005). Fischer−Tropsch synthesis: kinetics and effect of water for a Co/SiO2 catalyst. *Energy Fuel*, *4*(19), 1430–1439. https://doi.org/doi.org/10.1021

Davis, B. H. (2001). Fischer-Tropsch synthesis: Current mechanism and futuristic needs. *Fuel Processing Technology*, *71*(1–3), 157–166. https://doi.org/10.1016/S0378-3820(01)00144-8

Davis, M. E., & Davis, R. J. (2003). Effects of transport limitations on rates of solid-catalyzed reactions. *Fundamentals of Chemical Reaction.McGraw-Hill New York, NY, USA*, 1.

De Deugd, R. M., Kapteijn, F., & Moulijn, J. A. (2003). Using monolithic catalysts for highly selective Fischer-Tropsch synthesis. *Catalysis Today*, *79–80*, 495–501. https://doi.org/10.1016/S0920-5861(03)00073-7

Dean, J., Scheffler, M., Purcell, T. A. R., Barabash, S. V., Bhowmik, R., & Bazhirov, T. (2023). Interpretable machine learning for materials design. *Journal of Materials Research*, *38*(20), 4477–4496. https://doi.org/10.1557/s43578-023-01164-w

Dinse, A., Aigner, M., Ulbrich, M., Johnson, G. R., & Bell, A. T. (2012). *Effects of Mn promotion on the activity and selectivity of Co / SiO 2 for Fischer – Tropsch Synthesis*. *288*, 104–114. https://doi.org/10.1016/j.jcat.2012.01.008

Donnelly, T. J., Yates, I. C., & Charles N Satterfield. (1988). Analysis and Prediction of Product Distributions of the Fischer-Tropsch Synthesis. *Energy and Fuels 2*, *6*, 734–739. https://pubs.acs.org/sharingguidelines

Dry, M. E. (2002). The Fischer-Tropsch process: 1950-2000. *Catalysis Today*, *71*(3–4), 227–241. https://doi.org/10.1016/S0920-5861(01)00453-9

Farias, F. E. M., Silva, F. R. C., Cartaxo, S. J. M., Fernandes, F. A. N., & Sales, F. G. (2007).

Effect of Operating Conditions on Fischer-Tropsch Liquid Products. *287*, 283–287.

Fischer, F. & Tropsch, H. (1926). Die Erdölsynthese bei gewöhnliehem Druck aus den Vergasungsprodukten der Kohlen. *Brennstoff-Chemie: Zeitschrift für Chemie und Technik von Kohle, Öl und Gas*, Volume 7, p. 97-116.

Fischer, F. (1930) . Development of the benzene synthesis from carbon monoxide and hydrogen at atmospheric pressure. *Brennst.-Chem.* 1930; 11:489

Flory, P. J. (1936). Molecular Size Distribution in Linear Condensation Polymers. *Journal of the American Chemical Society*, *58*(10), 1877–1885.

Förtsch, D., Pabst, K., & Groß-Hardt, E. (2015). The product distribution in Fischer-Tropsch synthesis: An extension of the ASF model to describe common deviations. *Chemical Engineering Science*, *138*, 333–346. https://doi.org/10.1016/j.ces.2015.07.005

Gao, J., Wu, B., Zhou, L., Yang, Y., Hao, X., Xu, J., Xu, Y., & Li, Y. (2012). Irregularities in product distribution of fischer-tropsch synthesis due to experimental artifact. *Industrial and Engineering Chemistry Research*, *51*(36), 11618–11628. https://doi.org/10.1021/ie201671g

García-Sánchez, J. T., & Baldovino-Medrano, V. G. (2023). Elements of the Manufacture and Properties of Technical Catalysts. *Industrial & Engineering Chemistry Research*, *20*(62), 7769–7838. https://doi.org/10.1021/acs.iecr.3c00369

Garona, H. A., Cavalcanti, F. M., de Abreu, T. F., Schmal, M., & Alves, R. M. B. (2021). Evaluation of Fischer-Tropsch synthesis to light olefins over Co- and Fe-based catalysts using artificial neural network. *Journal of Cleaner Production*, *321*(December 2020), 129003. https://doi.org/10.1016/j.jclepro.2021.129003

Gnanamani, M. K., Jacobs, G., Pendyala, V. R. R., Graham, U. M., Hopps, S. D., Thomas, G. A., Shafer, W. D., Sparks, D. E., Xiao, Q., Hu, Y., & Davis, B. H. (2016). Fischer-Tropsch synthesis: Anchoring of cobalt particles in phosphorus modified cobalt/silica catalysts. *Applied Catalysis A: General*, *523*, 146–158. https://doi.org/10.1016/j.apcata.2016.05.024

Gorimbo, J., Muleja, A., Liu, X., & Hildebrandt, D. (2018). Fischer–Tropsch synthesis: product distribution, operating conditions, iron catalyst deactivation and catalyst speciation. *International Journal of Industrial Chemistry*, *9*(4), 317–333. https://doi.org/10.1007/s40090-018-0161-4

Henrici-Olivé, G., & Olivé, S. (1976a). Die Fischer-Tropsch-Synthese: Molekulargewichtsverteilung der Primärprodukte und Reaktionsmechanismus. *Angewandte Chemie*, *88*(5), 144–150. https://doi.org/10.1002/ange.19760880503

Henrici-Olivé, G., & Olivé, S. (1976b). The Fischer-Tropsch Synthesis: Molecular Weight Distribution of Primary Products and Reaction Mechanism. *Angewandte Chemie International Edition in English*, *15*(3), 136–141. https://doi.org/10.1002/anie.197601361

Herrington, E. F. G., & Robertson, .A. (1942). Trans. Faraday Society. In *Journal of the Chemical Society* (p. 38,40,490). p. 38,40,490, 1942, doi: doi.org/10.1039/TF9423800490.

Hillestad, M. (2015). Modeling the Fischer-Tropsch Product Distribution and Model Implementation. *Chemical Product and Process Modeling*, *10*(3), 147–159. https://doi.org/10.1515/cppm-2014-0031

Himanen, L., Geurts, A., Foster, A. S., & Rinke, P. (2019). Data-Driven Materials Science: Status, Challenges, and Perspectives. *Advanced Science*, *6*(21). https://doi.org/10.1002/advs.201900808

Horáček, J. (2021). Fischer – Tropsch synthesis , the effect of promoters , catalyst support , and reaction conditions selection. *Monatshefte Für Chemie - Chemical Monthly*, *151*(5), 649–675. https://doi.org/10.1007/s00706-020-02590-w

Huff, G.A., Jr. and Satterfield, C.N., 1984. Evidence for two chain growth probabilities on iron catalysts in the Fischer–Tropsch synthesis. *Journal of Catalysis*, 85(2), pp.370–379. https://doi.org/10.1016/0021-9517(84)90226-4

Iglesia, E. (1997). Design, synthesis, and use of cobalt-based Fischer-Tropsch synthesis catalysts. *Applied Catalysis A: General*, *161*(1–2), 59–78. https://doi.org/10.1016/S0926-860X(97)00186-5

Intarasiri, S., Ratana, T., Sornchamni, T., Phongaksorn, M., & Tungkamani, S. (2017). Effect of pore size diameter of cobalt supported catalyst on gasoline-diesel selectivity. *Energy Procedia*, *138*, 1035–1040. https://doi.org/10.1016/j.egypro.2017.10.090

Intarasiri, S., Tanakorn, R., Sornchamni, T., Tungkamani, S., & Phongaksorn, M. (2018). Pore size effect of mesoporous support on metal particle size of Co/SiO2 catalyst in Fischer-Tropsch synthesis. *International Journal of Avanced and Applied Sciences*, *5*(11), 80–85. https://doi.org/10.21833/ijaas.2018.11.011

Jablonka, K. M., Ongari, D., Moosavi, S. M., & Smit, B. (2020). Big-Data Science in Porous Materials: Materials Genomics and Machine Learning. *Chemical Reviews*, *120*(16), 8066–8129. https://doi.org/10.1021/acs.chemrev.0c00004

Jahangiri, H., Bennett, J., Mahjoubi, P., Wilson, K., & Gu, S. (2014). A review of advanced catalyst development for Fischer-Tropsch synthesis of hydrocarbons from biomass derived

syn-gas. *Catalysis Science and Technology*, *4*(8), 2210–2229. https://doi.org/10.1039/c4cy00327f

Jain, A., Ong, S. P., Hautier, G., Chen, W., Richards, W. D., Dacek, S., Cholia, S., Gunter, D., Skinner, D., Ceder, G., & Persson, K. A. (2013). Commentary: The materials project: A materials genome approach to accelerating materials innovation. *APL Materials*, *1*(1). https://doi.org/10.1063/1.4812323

Jensen, K. F. (2017). Flow Chemistry- Microreaction Technology Comes of Age. *AIChE Journal*, *59*(4), 215–228. https://doi.org/10.1002/aic

Jess, A., & Kern, C. (2023). Significance of Pressure Drop, Changing Molar Flow, and Formation of Steam in the Accurate Modeling of a Multi-Tubular Fischer–Tropsch Reactor with Cobalt as Catalyst. *Processes*, *11*(12). https://doi.org/10.3390/pr11123281

Ji, Y. Y., Xiang, H. W., Yang, J. L., Xu, Y. Y., Li, Y. W., & Zhong, B. (2001). Effect of reaction conditions on the product distribution during Fischer-Tropsch synthesis over an industrial Fe-Mn catalyst. *Applied Catalysis A: General*, *214*(1), 77–86. https://doi.org/10.1016/S0926-860X(01)00480-X

Johnson, G. R., & Bell, A. T. (2016). *Role of ZrO 2 in Promoting the Activity and Selectivity of Co-Based Fischer − Tropsch Synthesis Catalysts*. https://doi.org/10.1021/acscatal.5b02205

Kabir, L. M., Albolkany, M. K., Mohamed, M. M., & El-Moneim, A. A. (2024). Porous Carbon-Supported Cobalt Catalyst for CO Hydrogenation to Gasoline Range Hydrocarbons. *Catalysis Letters*, *0123456789*. https://doi.org/10.1007/s10562-023-04567-w

Khobragade, M., Majhi, S., & Pant, K. K. (2012). Effect of K and CeO 2 promoters on the activity of Co / SiO 2 catalyst for liquid fuel production from syngas. *Applied Energy*, *94*, 385–394. https://doi.org/10.1016/j.apenergy.2012.02.002

Khodakov, A. Y., Griboval-Constant, A., Bechara, R., & Villain, F. (2001). Pore-size control of cobalt dispersion and reducibility in mesoporous silicas. *Journal of Physical Chemistry B*, *105*(40), 9805–9811. https://doi.org/10.1021/jp011989u

Kim, J., Kim, S., Ban, M., Lee, D., Kim, S., Lee, J., & Ha, K. S. (2023). Unravelling the effects of short pore on Fischer-Tropsch synthesis and its role as selectivity controller. *Chemical Engineering Journal*, *475*(September), 146039. https://doi.org/10.1016/j.cej.2023.146039

Kitchin, J. R. (2018). Machine learning in catalysis. *Nature Catalysis*, *1*(4), 230–232. https://doi.org/10.1038/s41929-018-0056-y

Kruk, M., Jaroniec, M., & Sayari, A. (1997). Application of large pore MCM-41 molecular sieves

to improve pore size analysis using nitrogen adsorption measurements. *Langmuir*, *13*(23), 6267–6273. https://doi.org/10.1021/la970776m

Kustov, L. M., & Tarasov, A. L. (2016). Fischer–Tropsch synthesis in a slurry mode using ionic liquids. *Catalysis Communications, 75*, 42–44. https://doi.org/10.1016/j.catcom.2015.12.003

Li, J., Zhu, X., Li, Y., Tong, Y. W., Ok, Y. S., & Wang, X. (2021). Multi-task prediction and optimization of hydrochar properties from high-moisture municipal solid waste: Application of machine learning on waste-to-resource. *Journal of Cleaner Production*, *278*, 123928. https://doi.org/10.1016/j.jclepro.2020.123928

Li, Z., Wu, J., Yu, J., Han, D., Wu, L., & Li, J. (2016). Effect of incorporation manner of Zr on the Co/SBA-15 catalyst for the Fischer–Tropsch synthesis. *Journal of Molecular Catalysis A: Chemical*, *424*, 384–392. https://doi.org/10.1016/j.molcata.2016.09.025

Li, Z., Wu, L., Han, D., & Wu, J. (2018). Characterizations and product distribution of Co-based Fischer-Tropsch catalysts: A comparison of the incorporation manner. *Fuel*, *220*(February), 257–263. https://doi.org/10.1016/j.fuel.2018.02.004

Liu, B., Li, W., Zheng, J., Lin, Q., Zhang, X., Zhang, J., Jiang, F., Xu, Y., & Liu, X. (2018). *Catalysis Science & Technology synthesis over iron-based catalysts : a combined experimental and theoretical study †*. 5288–5301. https://doi.org/10.1039/c8cy01621f

Lu, X., Hildebrandt, D., Liu, X., & Glasser, D. (2012). A thermodynamic approach to olefin product distribution in fischer-tropsch synthesis. *Industrial and Engineering Chemistry Research*, *51*(51), 16544–16551. https://doi.org/10.1021/ie3000453

Lundberg, S. M., & Lee, S. I. (2017). A unified approach to interpreting model predictions. *Advances in Neural Information Processing Systems*, *2017-Decem*(Section 2), 4766–4775.

Luo, G., Li, Z., Liu, Q., Guo, S., Pei, X., Lv, J., Huang, S., Wang, Y., & Ma, X. (2023). Enhanced synthesis of C2+ alcohols from syngas over a Co-Co2C catalyst supported on mesoporous carbon–silica composites. *Chemical Engineering Journal*, *475*(September), 146206. https://doi.org/10.1016/j.cej.2023.146206

Marques, F. H., & Guirardello, R. (2018). Thermodynamic analysis for Fischer–Tropsch synthesis using biomass. *Chemical Engineering Transactions, 65*, 397–402. https://doi.org/10.3303/CET1865067

Martínez, A., López, C., Márquez, F., & Díaz, I. (2003). Fischer-Tropsch synthesis of hydrocarbons over mesoporous Co/SBA-15 catalysts: The influence of metal loading, cobalt precursor, and promoters. *Journal of Catalysis*, *220*(2), 486–499.

https://doi.org/10.1016/S0021-9517(03)00289-6

Medford, A. J., Kunz, M. R., Ewing, S. M., Borders, T., & Fushimi, R. (2018). Extracting Knowledge from Data through Catalysis Informatics. *ACS Catalysis*, *8*(8), 7403–7429. https://doi.org/10.1021/acscatal.8b01708

Mehmood, A., Ghafar, H., Yaqoob, S., Gohar, U. F., & Ahmad, B. (2017). Mesoporous Silica Nanoparticles: A Review. *Journal of Developing Drugs*, *06*(02). https://doi.org/10.4172/2329-6631.1000174

Merino, D., Pérez-Miqueo, I., Sanz, O., & Montes, M. (2016). On the Way to a More Open Porous Network of a Co-Re/Al2O3 Catalyst for Fischer-Tropsch Synthesis: Pore Size and Particle Size Effects on Its Performance. *Topics in Catalysis*, *59*(2–4), 207–218. https://doi.org/10.1007/s11244-015-0436-3

Moazami, N., Mahmoudi, H., Rahbar, K., Panahifar, P., Tsolakis, A., & Wyszynski, M. L. (2015). Catalytic performance of cobalt-silica catalyst for Fischer-Tropsch synthesis: Effects of reaction rates on efficiency of liquid synthesis. *Chemical Engineering Science*, *134*, 374–384. https://doi.org/10.1016/j.ces.2015.05.025

Mohammadnasabomran, S., Márquez-álvarez, C., Pérez-Pariente, J., & Martínez, A. (2021). Short-channel mesoporous SBA-15 silica modified by aluminum grafting as a support for CoRu Fischer–Tropsch synthesis catalysts. *Catalysis Science & Technology*, *11*, 4245–4258. https://doi.org/10.1039/d0cy02418j

Mosayebi, A., Nasabi, M., & Abedini, R. (2019). Evaluation and modeling of Fischer-Tropsch synthesis in presence of a Co/ZrO2 catalyst. *Petroleum Science and Technology*, *37*(23), 2338–2349. https://doi.org/10.1080/10916466.2018.1522339

Motaev, K., Molokeev, M., Sultanov, B., Kharitontsev, V., Matigorov, A., Palianov, M., Azarapin, N., & Elyshev, A. (2023). Application of Machine Learning to Fischer–Tropsch Synthesis for Cobalt Catalysts. *Industrial & Engineering Chemistry Research*, *62*(48), 20658–20666. https://doi.org/10.1021/acs.iecr.3c03147

Nakhaei Pour, A., Khodabandeh, H., Izadyar, M., & Housaindokht, M. R. (2013). Mechanistic double ASF product distribution study of fischer-tropsch synthesis on precipitated iron catalyst. *Journal of Natural Gas Science and Engineering*, *15*, 53–58. https://doi.org/10.1016/j.jngse.2013.09.005

Ni, Z., Kang, S., Bai, J., Li, Y., Huang, Y., Wang, Z., Qin, H., & Li, X. (2017). Uniformity dispersive, anti-coking core@double-shell-structured Co@SiO2@C: Effect of graphitic carbon modified interior pore-walls on C5+ selectivity in Fischer-Tropsch synthesis. *Journal*

*of Colloid and Interface Science*, *505*, 325–331. https://doi.org/10.1016/j.jcis.2017.05.096

Nijs, H. H., & Jacobs', P. A. (1980). Metal Particle Size Distributions and Fischer-Tropsch Selectivity. An Extended Schulz-Flory Model. In *JOURNAL OF CATALYSIS* (Vol. 65).

Nijs, H. H., Jacobs, P. A., Verdonck, J. J., & Uytterhoeven, J. B. (1980). Growth and Properties of Metal Clusters. In J. Bourdon (Ed.), *Studies in Surface Science and Catalysis 4* (p. 479). Elsevier Scientific.

Niu, C., Xia, M., Chen, C., Ma, Z., Jia, L., Hou, B., & Li, D. (2020). Effect of process conditions on the product distribution of Fischer-Tropsch synthesis over an industrial cobalt-based catalyst using a fixed-bed reactor. *Applied Catalysis A: General*, *601*(27), 117630. https://doi.org/10.1016/j.apcata.2020.117630

Norval, G. W., & Phillips, M. J. (1990). Application of Equilibrium Analysis to a Fischer-Tropsch Product. In *Journal of Catalysis* (Vol. 126).

Odian, G. (2004). *Principles of Polymerization* (4th ed.). John Wiley & Sons, Inc. https://doi.org/10.1002/047147875X

Pandey, U., Putta, K. R., Rout, K. R., Rytter, E., Hillestad, M., & Blekkan, E. A. (2021). *Fischer-Tropsch synthesis over an alumina-supported cobalt catalyst in a fixed bed reactor – Effect of process parameters*. *369*(June 2020), 150–157.

Pandey, U., Runningen, A., Gavrilović, L., Jørgensen, E. A., Putta, K. R., Rout, K. R., Rytter, E., Blekkan, E. A., & Hillestad, M. (2021). Modeling Fischer–Tropsch kinetics and product distribution over a cobalt catalyst. *AIChE Journal*, *67*(7), 1–15. https://doi.org/10.1002/aic.17234

Pardo-Tarifa, F., Cabrera, S., Sanchez-Dominguez, M., & et al. (2017). Ce-promoted Co/Al2O3 catalysts for Fischer–Tropsch synthesis. *Int J of Hydrogen Energy*, *42*(10), 9754–9765.

Patel, H., Panda, A., Nikolaienko, T., Jaso, S., & Lopez, A. (2023). *Accurate and Fast Fischer-Tropsch Reaction Microkinetics using PINNs*.

Peacock-Lopez, E., & Lindenberg, K. (1986). The Transient Flory Model and Its Application to Catalytic Polymerization. 2. *Chem. Phys. Lipids*, *90*(16), 1725–1732. https://pubs.acs.org/sharingguidelines

Pichler, H. (1952). *Advances in Catalysis* (W. Frankenburg, E. Rideal, & V. Komarewsky (eds.); Vol IV, p. 271). Academic Press.

Qian, W., Zhang, H., & Sun, Q. (2014). *Effects of Zr and Ni promoters on the activation and*

*deactivation of a precipitated iron-based catalyst*. 293–304. https://doi.org/10.1007/s11144-013-0648-0

Raissi, M., Perdikaris, P., & Karniadakis, G. E. (2019). Physics-informed neural networks: A deep learning framework for solving forward and inverse problems involving nonlinear partial differential equations. *Journal of Computational Physics*, *378*, 686–707. https://doi.org/10.1016/j.jcp.2018.10.045

Riyahin, M., Mohebbi-Kalhori, D., Zohdi-Fasaei, H., Mirzaei, A. A., & Atashi, H. (2020). Proposing innovative modeling for Fischer–Tropsch synthesis product selectivity over Cobalt catalyst and skewness analyzing. *Petroleum Science and Technology*, *38*(4), 411–419. https://doi.org/10.1080/10916466.2019.1705859

Rytter, E., & Holmen, A. (2018). Consorted vinylene mechanism for cobalt Fischer–Tropsch synthesis encompassing water or hydroxyl assisted CO-activation. *Top Catal*, *61(9)*, 1024–1034. https://doi.org/https://doi.org/10. 1007/s11244-018-0932-3

Satterfieldand, C. N., & Huff, G. A. (1982). Carbon Number Distribution of Fischer-Tropsch Products Formed on an Iron Catalyst in a Slurry Reactor. In *JOURNAL OF CATALYSIS* (Vol. 73).

Schulz, G. V. (1938). Über die Abweichung des viscosimetrischen vom mittleren Molekulargewicht bei Stoffen mit einer Molekulargewichtsverteilung nach der GAUSsschen Fehlergleichung. *Zeitschrift für Physikalische Chemie*, *41*(1), 466-468. https://www.degruyterbrill.com/document/doi/10.1515/zpch-1938-4135/html

Schulz, G. V. (1939). Über die Kinetik der Kettenpolymerisationen. *Zeitschrift Für Physikalische Chemie*, *44*(1), 25–46. https://doi.org/doi:10.1515/zpch-1939-4418

Schulz, H. (1999). Short history and present trends of Fischer-Tropsch synthesis. *Applied Catalysis*, *186*, 3–12. https://doi.org/PII S0926-860-X (99)00160-X

Schulz, H. (2013). Principles of Fischer-Tropsch synthesis - Constraints on essential reactions ruling FT-selectivity. *Catalysis Today*, *214*, 140–151. https://doi.org/10.1016/j.cattod.2013.05.009

Shao, M., Li, Y., Chen, J., & Zhang, Y. (2015). Mesoscale Effects on Product Distribution of Fischer-Tropsch Synthesis. In *Advances in Chemical Engineering* (1st ed., Vol. 47). Elsevier Inc. https://doi.org/10.1016/bs.ache.2015.10.002

Shiba, N. C., Liu, X., & Yao, Y. (2023). Insight into the Physicochemical Properties of Co-Based Catalysts in Fischer–Tropsch Synthesis. *Reactions*, *4*(3), 420–431.

https://doi.org/10.3390/reactions4030025

Song, D., & Li, J. (2006). Effect of catalyst pore size on the catalytic performance of silica supported cobalt Fischer-Tropsch catalysts. *Journal of Molecular Catalysis A: Chemical*, *247*(1–2), 206–212. https://doi.org/10.1016/j.molcata.2005.11.021

Stenger, H. G. (1985). Distributed-chain-growth-probabilities-for-the-Fischer-_1985_Journal-of-Cata. *JOURNAL OF CATALYSIS*, *92*, 426–428.

Storch, H. H. (1948). The Fischer-Tropsch and Related Processes for Synthesis of Hydrocarbons by Hydrogenation of Carbon Monoxide. *Advances in Catalysis*, *1*, 115–156. https://doi.org/doi.org/10.1016/S0360-0564(08)60674-4

Sun, C., Zhan, T., Pfeifer, P., & Dittmeyer, R. (2017). Influence of Fischer-Tropsch synthesis ( FTS ) and hydrocracking ( HC ) conditions on the product distribution of an integrated FTS-HC process. *Chemical Engineering Journal*, *310*, 272–281. https://doi.org/10.1016/j.cej.2016.10.118

Teimouri, Z., Abatzoglou, N., & Dalai, A. K. (2023). Green synthesis of Cu-Mo promoted Fe catalyst for production of the gaseous and liquid fuels through Fischer-Tropsch synthesis. *Energy Conversion and Management*, *286*(April), 117079. https://doi.org/10.1016/j.enconman.2023.117079

Teimouri, Z., Abatzoglou, N., & Dalai, A. K. (2024). A novel machine learning framework for designing high-performance catalysts for production of clean liquid fuels through Fischer-Tropsch synthesis. *Energy*, *289*(October 2023), 130061. https://doi.org/10.1016/j.energy.2023.130061

Tian, Z., Wang, C., Si, Z., Wang, Y., Chen, L., Liu, Q., Zhang, Q., Xu, Y., & Ma, L. (2018). Product Distributions of Fischer-Tropsch Synthesis over Core-Shell Catalysts: The Effects of Diverse Shell Thickness. *ChemistrySelect*, *3*(44), 12415–12423. https://doi.org/10.1002/slct.201801515

Todic, B., Ma, W., Jacobs, G., Davis, B. H., & Bukur, D. B. (2014). Effect of process conditions on the product distribution of Fischer – Tropsch synthesis over a Re-promoted cobalt-alumina catalyst using a stirred tank slurry reactor. *Journal of Catalysis*, *311*, 325–338. https://doi.org/10.1016/j.jcat.2013.12.009

Todic, B., Olewski, T., Nikacevic, N., & Bukur, D. B. (2013). Modeling of fischer-tropsch product distribution over Fe-based catalyst. *Chemical Engineering Transactions*, *32*(2007), 793–798. https://doi.org/10.3303/CET1332133

Tsubaki, N., Sun, S., & Fujimoto, K. (2001). *Different Functions of the Noble Metals Added to Cobalt Catalysts for Fischer – Tropsch Synthesis*. *246*, 236–246. https://doi.org/10.1006/jcat.2001.3163

Van Der Laan, G. P., & Beenackers, A. A. C. M. (1999). Kinetics and Selectivity of the Fischer-Tropsch Synthesis: A Literature Review. *Catalysis Reviews - Science and Engineering*, *41*(3–4), 255–318. https://doi.org/10.1081/CR-100101170

Van Santen, R. A., Markvoort, A. J., Filot, I. A. W., Ghouri, M. M., & Hensen, E. J. M. (2013). Mechanism and microkinetics of the Fischer-Tropsch reaction. *Physical Chemistry Chemical Physics*, *15*(40), 17038–17063. https://doi.org/10.1039/c3cp52506f

Van Steen, E., & Schulz, H. (1999). Polymerisation kinetics of the Fischer– Tropsch CO hydrogenation using iron and cobalt based catalysts. *Applied Catalysis A: General*, *1*(186), 309–320. https://doi.org/doi.org/10.1016/S0926- 860X(99)00151-9.

Vanhove, D., Makambo, P., & Blanchard, M. (1979). Selective catalytic synthesis of linear paraffins from CO and H2 over cobalt supported catalysts. *Journal of the Chemical Society, Chemical Communications*, *14*, 605–606. https://doi.org/10.1039/C39790000605

Vlasenko, V. ., & Yuzefovich, G. . (1969). Mechanism of the Catalytic Hydrogenation of Oxides of Carbon. *Russian Chemical Reviews*, *9*(38), 728–739.

Withers, H., Eliezer, K., & Mitchell, J. (1990). Slurry-phase Fischer-Tropsch Synthesis and kinetic studies over supported cobalt carbonyl derived catalysts. *Ind Eng Chem Res*, *9*(29), 1807–1814. https://doi.org/doi.org/ 10.1021/ie00105a011

Xing, C., Ai, P., Zhang, P., Gao, X., Yang, R., Yamane, N., Sun, J., Reubroycharoen, P., & Tsubaki, N. (2016). Fischer–Tropsch synthesis on impregnated cobalt-based catalysts: New insights into the effect of impregnation solutions and pH value. *Journal of Energy Chemistry*, *25*(6), 994–1000. https://doi.org/10.1016/j.jechem.2016.09.008

Xiong, H., Motchelaho, M. A., Moyo, M., Jewell, L. L., & Coville, N. J. (2015). Effect of Group I alkali metal promoters on Fe / CNT catalysts in Fischer – Tropsch synthesis. *FUEL*, *150*, 687–696. https://doi.org/10.1016/j.fuel.2015.02.099

Yaghoobpour, E., Zamani, Y., Zarrinpashne, S., & Zamaniyan, A. (2019). Fischer–Tropsch synthesis: effect of silica on hydrocarbon production over cobalt-based catalysts. *Chemical Papers*, *73*(1), 205–214. https://doi.org/10.1007/s11696-018-0565-9

Yakubovich, M. N., & Strizhak, P. E. (2007). Kinetic models of the molecular mass distribution of the products of the Fischer-Tropsch synthesis at cobalt catalysts. *Theoretical and*

*Experimental Chemistry*, *43*(6), 361–379. https://doi.org/10.1007/s11237-007-0044-9

Yamada, H., Liu, C., Wu, S., Koyama, Y., Ju, S., Shiomi, J., Morikawa, J., & Yoshida, R. (2019). Predicting Materials Properties with Little Data Using Shotgun Transfer Learning. *ACS Central Science*, *5*(10), 1717–1730. https://doi.org/10.1021/acscentsci.9b00804

Yang, K., Wu, K., & Zhang, H. (2022). Machine learning prediction of the yield and oxygen content of bio-oil via biomass characteristics and pyrolysis conditions. *Energy*, *254*, 124320. https://doi.org/10.1016/j.energy.2022.124320

Yang, R., Zhou, L., Gao, J., Hao, X., Wu, B., & Yang, Y. (2017). E ff ects of experimental operations on the Fischer-Tropsch product distribution. *Catalysis Today*, *298*(September 2016), 77–88. https://doi.org/10.1016/j.cattod.2017.05.056

Yu, F., Lin, T., Wang, X., Li, S., Lu, Y., Wang, H., Zhong, L., & Sun, Y. (2018). Highly selective production of olefins from syngas with modified ASF distribution model. *Applied Catalysis A: General*, *563*(July), 146–153. https://doi.org/10.1016/j.apcata.2018.07.006

Yuan, Z., Wang, Y., Zhu, L., Zhang, C., & Sun, Y. (2024). Advancing C5+ hydrocarbons fuels production: An interpretable machine learning framework for Co-catalyzed syngas conversion. *Fuel*, *361*(November 2023), 130658. https://doi.org/10.1016/j.fuel.2023.130658

Zhang, Q., Kang, J., & Wang, Y. (2010). Development of Novel Catalysts for Fischer-Tropsch Synthesis: Tuning the Product Selectivity. In *ChemCatChem* (Vol. 2, Issue 9, pp. 1030–1058). https://doi.org/10.1002/cctc.201000071

# CHAPTER 3: EXPERIMENTAL PROCEDURE

## 3.1 Introduction

This chapter's primary goal is to provide information on the experimental strategies and tactics employed to accomplish the objectives of the research. The equipment, methods, and explanations of the various experiments that were carried out will all be included in this chapter. The experimental part of this project involved the direct synthesis of cobalt nanoparticles supported on silica using a modified Stöber process (Ibrahim et al., 2010; Stober, W; Fink, A; Bohn, 1968). The synthesized silica nanospheres where then characterized by several different techniques and then cobalt nitrate, the precursor of the catalyst's active component, was loaded onto the support using the wet impregnation method. The resulting catalyst was evaluated for CO hydrogenation via Fischer Tropsch Synthesis.

## 3.2 Materials and gases

### 3.2.1 Gases

AFROX (South Africa) supplied all of the high purity gases used in this study. Shown below is an outline of the composition of the gases used.

**Calibration gas composition used in Fisher Tropsch experiments**

The analysis of the output of the FT reactor was done using a 7890 GC-MS Gas Chromatograph (GC) model manufactured by Agilent Technologies. Table 3.1 below shows the molar composition of the gas mixture that was used for the calibration of the GC:

Table 3.1 Composition of the calibration gas used in the FT experiments

| Gas component | Molar percentage (mol %) |
|---|---|
| $H_2$ | 49.99 |
| CO | 31.4 |
| $N_2$ | 10.4 |
| $CO_2$ | 4.9 |
| $CH_4$ | 2.62 |
| $C_2H_4$ | 0.21 |
| $C_2H_6$ | 0.48 |

**Feed gas**

The feed gas for the FT synthesis runs was syngas with an inert component (nitrogen), which contained 10% $N_2$, 22.5% CO, and $H_2$ making up the remainder.

**Nitrogen**

Before beginning the reaction, nitrogen was used to flush and cleanse the system, pressurize it, and check for leaks.

**Carrier gases for Gas Chromatography**

A 99.999% pure Ar was utilised as a carrier gas for a thermal conductivity detector (TCD) that was attached to an Agilent Technologies Carboxen® 1006 column.

Air and $H_2$ (of purity 99.999%) were utilized as flame gases, and $H_2$ also served as the carrier gas for the flame ionization detector (FID), which was attached to a 30-cm, 0.32-mm-diameter fused silica capillary column.

**Gases used as reducing agents:**

10%$H_2$/90%Ar was used for performing Temperature Programmed Reduction (TPR) and Hydrogen Chemisorption experiments.

### 3.2.2 Equipment

A variety of equipment was employed to accomplish this project's experimental goals. Hot plates with magnetic stirrers were used for the preparation of the support in fume cupboards using a reflux set-up. Both the prepared support and the support samples that had been impregnated with a cobalt precursor solution were dried in a drying oven prior to calcination in order to eliminate moisture from the samples. A calcination oven was then used in order to eliminate moisture from both the prepared supports and the impregnated supports and to decompose the metal precursor in the catalyst into its oxide or metallic forms.

A number of characterization tools were used in this investigation and are described in detail in section 3.3 below.

## 3.3 Catalyst synthesis

This section describes the equipment and the procedure used to synthesize the silica nanoparticles which were used as the support, as well as the method for supporting the metal on the silica, namely incipient wetness impregnation.

### 3.3.1 Reagents

Tetraethyl orthosilicate (TEOS 98%) with a density of 0.933 g/mL, ethanol (99.5%) with a density of 0.789 g/mL, ammonia ($NH_3 \cdot H_2O$ 30-33%) with a density of 0.9 g/mL and cobalt (II) nitrate

hexahydrate (98%) were obtained from Sigma Aldrich, USA, and deionized water were used in all of the experiments. The reagents used in the experiments were used in the form they were acquired without further purification.

### 3.3.2 Catalyst Synthesis Procedure

The Stöber process (Stober et al., 1968) was used in the synthesis of the silica supports in this work as it is particularly well-suited for the synthesis of mesoporous silica nanoparticles with controlled size and narrow size distribution. In other studies, as shown in Table 3.2, silica particle sizes using the Stöber process were controlled by adjusting parameters such as the concentration of silica precursor, water content, reaction temperature, pH, and reaction time. In the work of Vazquez et al (Vazquez et al., 2017), different particle sizes were produced from varying concentrations of the reactants and also yielded different pore sizes. Therefore, the pore sizes can also be varied by varying the concentrations of the reagents. Equation 3.1 shows the reaction that happens between the TEOS and water in the presence of $NH_3.H_20$ catalyst.

$$Si(OC_2H_5)_{4(l)} + 4\,H_2O_{(l)} \overset{NH_{3\,(aq)}}{\rightleftharpoons} Si(OH)_{4(aq)} + 4\,C_2H_5OH_{(l)} \qquad \text{eqn (3.1)}$$

In the reaction, the hydrolysis of TEOS produces silanol groups, which then go through condensation reactions to create siloxane (Si-O-Si) linkages and develop into silica nanoparticles. The condensation reactions involve the loss of water molecules, resulting in the formation of covalent bonds between silicon atoms.

The condensation reaction can be represented as follows:

$$Si(OH)_{4(aq)} \rightarrow SiO_{2(s)} + 2\,H_2O_{(l)} \qquad \text{eqn (3.2)}$$

Different pore sizes of the $SiO_2$ support will be obtained from the reaction. The table below shows some of the different ratios of TEOS, water, ethanol and aqueous ammonia used in the literature for silica synthesis and the support characteristics obtained. In some cases, cetyltrimethylammonium bromide (CTABr), was used as a template for controlling the morphology and structure of the silica nanoparticles (Vazquez et al., 2017).

Table 3.2: Typical ratios of Water/TEOS/$NH_4OH$/ethanol/CTABr and the respective characteristics

| RATIOS | | | | | Particle diameter(nm) | Pore volume (cm^3/g) | Pore Diameter (nm) | Reference |
|---|---|---|---|---|---|---|---|---|
| Water | TEOS | NH4OH | Ethanol | CTABr | | | | |
| 144 | 1 | 11 | 58 | 0,3 | | 0,757 | 3,3 | Zola et al., 2016 |
| 1,1 | 1 | 0,2 | 16,2 | | 185 | | | Zola et al., 2016 |
| 10,2 | 1 | 2,0 | 79,5 | | 230 | | | Chen et al., 2018 |
| 6,8 | 1 | 1,3 | 52,7 | | 270 | | | Chen et al., 2018 |
| 2,9 | 1 | 0,6 | 21,7 | | 291 | | | Chen et al., 2018 |
| 5,6 | 1 | 0,4 | 13,3 | | 360 | | | Walther & Brühwiler, 2024 |
| 81 | 1 | 1,76 | 24 | | | 0,085 | | Walther & Brühwiler, 2024 |
| 81 | 1 | 6,15 | 24 | | | 0,091 | | Walther & Brühwiler, 2024 |
| 81 | 1 | 16,3 | 24 | | | 0,093 | | Walther & Brühwiler, 2024 |
| 1 | 4 | 6 | 6 | | 98 | | | Singho & Johan, 2012 |
| 1 | 4 | 6 | 24 | | 56 | | | Singho & Johan, 2012 |
| 45,6 | 1 | 10,4 | 20 | | 700-800 | 0,01 | | Vazquez et al., 2017 |
| 45,6 | 1 | 10,4 | 20 | 0,1 | 600-700 | 0,21 | 2,9 | Vazquez et al., 2017 |
| 45,6 | 1 | 10,4 | 20 | 0,3 | 600-700 | 0,49 | 2,7 | Vazquez et al., 2017 |
| 600 | 1 | 10,4 | 20 | 0,3 | 380 | 0,6 | 2,5 | Vazquez et al., 2017 |
| 1200 | 1 | 10,4 | 20 | 0,3 | 270 | 0,6 | 2,8 | Vazquez et al., 2017 |

In this work, a similar approach was adopted, varying molar ratios of water, TEOS, aqueous ammonia, and ethanol to yield the different silica pore sizes. Ten different runs with different reactant ratios were used, using variations of the ratios which were reported by Singho & Johan, (2012) as the basis.

During synthesis, firstly, deionized water and ammonia were mixed in a flat-bottomed flask. Then, ethanol was poured into the prepared solution of water and aqueous ammonia. A corresponding amount of TEOS was then mixed into the water/ethanol/ammonia solution and the mixture was vigorously hand stirred for approximately 10s in a fume cupboard. The volumes required were calculated by using the concentrations and the densities of the respective substances using the equation below:

$$\text{Volume} = \frac{(\%\, concentation)(moles)(Molar\ mass)}{density(g/ml)} \qquad \text{eqn (3.3)}$$

Table 3.3 shows the ratios for 10 different supports created, varying the amounts of water while keeping the rest constant and also varying the amounts of ammonia while keeping the others constant.

Table 3.3. Different molar ratios of water/TEOS/NH4OH/Ethanol used in the synthesis and the respective volumes mixed

| Run | | Water | TEOS | $NH_4OH$ | Ethanol | Water/Ethanol Ratio | Water/$NH_4OH$ Ratio |
|---|---|---|---|---|---|---|---|
| 1 | Molar Ratio | 1 | 1 | 1 | 2.5 | 0.4 | 1 |
| | Moles | 0.3 | 0.3 | 0.3 | 0.75 | | |
| | Volumes (mL) | 5.4 | 65.647 | 3.505 | 43.573 | | |
| | | | | | | | |
| 2 | Molar Ratio | 1.5 | 1 | 1 | 2.5 | 0.6 | 1.5 |
| | Moles | 0.45 | 0.3 | 0.3 | 0.75 | | |
| | Volumes (mL) | 8.1 | 65.647 | 3.505 | 43.573 | | |
| | | | | | | | |
| 3 | Molar Ratio | 2 | 1 | 1 | 2.5 | 0.8 | 2 |
| | Moles | 0.8 | 0.4 | 0.4 | 1 | | |
| | Volumes (mL) | 14.4 | 87.529 | 4.673 | 58.098 | | |
| | | | | | | | |
| 4 | Molar Ratio | 2.5 | 1 | 1 | 2.5 | 1 | 2.5 |
| | Moles | 1 | 0.4 | 0.4 | 1 | | |
| | Volumes (mL) | 18 | 87.529 | 4.673 | 58.098 | | |
| | | | | | | | |
| 5 | Molar Ratio | 5 | 1 | 1 | 2.5 | 2 | 5 |
| | Moles | 2 | 0.4 | 0.4 | 1 | | |
| | Volumes (mL) | 36 | 87.529 | 4.673 | 58.098 | | |
| | | | | | | | |
| 6 | Molar Ratio | 10 | 1 | 1 | 2.5 | 4 | 10 |
| | Moles | 4 | 0.4 | 0.4 | 1 | | |
| | Volumes (mL) | 72 | 87.529 | 4.673 | 58.098 | | |
| | | | | | | | |
| 7 | Molar Ratio | 12 | 1 | 1 | 2.5 | 4.8 | 12 |
| | Moles | 3.6 | 0.3 | 0.3 | 1 | | |
| | Volumes (mL) | 64.8 | 65.647 | 3.505 | 43.573 | | |
| | | | | | | | |
| 8 | Molar Ratio | 15 | 1 | 7 | 2.5 | 6 | 2.14 |
| | Moles | 6 | 0.4 | 2.8 | 1 | | |
| | Volumes | 108 | 87.529 | 32.711 | 58.098 | | |

| | | | | | | | |
|---|---|---|---|---|---|---|---|
| | (mL) | | | | | | |
| | | | | | | | |
| 9 | Molar Ratio | 15 | 1 | 2.5 | 2.5 | 6 | 6 |
| | Moles | 4.5 | 0.3 | 0.75 | 0.75 | | |
| | Volumes (mL) | 81 | 65.647 | 8.7625 | 43.573 | | |
| | | | | | | | |
| 10 | Molar Ratio | 15 | 1 | 5 | 2.5 | 6 | 3 |
| | Moles | 6 | 0.4 | 2 | 1 | | |
| | Volumes (mL) | 108 | 87.529 | 23.367 | 58.098 | | |
| | | | | | | | |

The mixture was placed in a reflux setup in a fume cupboard and left to react in an oil bath at 60˚C, magnetically stirring at 400 rpm for 4 hours, after which a white precipitate was observed in the reaction flask. The precipitate was filtered under room temperature conditions and solid silica powder was obtained and was then dried in an oven for 24 hours at 60°C. Figure 3.1 shows the laboratory set-up used, with the white precipitate of silica observed at the end of the reaction inside the round-bottomed flask.

The prepared catalysts were labelled using the notation shown in Table 3.4 which involves introducing a prefix number to denote the run involving the ratios of the reagents used to prepare the support from Table 3.3.

Table 3.4: The notations of the prepared catalysts

| Run | Notation | |
|---|---|---|
| | Loaded support | Silica Support |
| 1 | 1-Co/$SiO_2$ | S1 |
| 2 | 2-Co/$SiO_2$ | S2 |
| 3 | 3-Co/$SiO_2$ | S3 |
| 4 | 4-Co/$SiO_2$ | S4 |
| 5 | 5-Co/$SiO_2$ | S5 |
| 6 | 6-Co/$SiO_2$ | S6 |
| 7 | 7-Co/$SiO_2$ | S7 |
| 8 | 8-Co/$SiO_2$ | S8 |
| 9 | 9-Co/$SiO_2$ | S9 |
| 10 | 10-Co/$SiO_2$ | S10 |



*Figure 3.13. The reflux set up for silica synthesis using the Stöber process*

The prepared white silica powder was then calcined at 300˚C to drive off the water, facilitating the reaction in Equation 3.1 above. Cobalt (II) nitrate hexahydrate was used as the source of cobalt metal and 10 wt% was loaded onto the synthesized mesoporous $SiO_2$ support using incipient wetness impregnation. During impregnation, a solution of the required amount of cobalt (II) nitrate hexahydrate was added to a corresponding amount of $SiO_2$, and the mixture was mixed in a sonicator for 5 minutes at 40 ˚C, afterward, the mixture was dried for 24 hours at 75 °C in an oven. After drying, the prepared cobalt-loaded samples were then separated into two groups of five corresponding to the different water/TEOS/$NH_4OH$/ethanol ratios, the first one was calcined at 500 ˚C at 5 ˚C/min ramping rate and the second batch was calcined at 700 ˚C using a ramping rate of 10˚C/min.

## 3.4 Characterization

### 3.4.1 Physisorption analysis

The pore characteristics and surface area were analyzed using an Anton Paar, NOVA 800 physisorption analyzer instrument using the Brunauer - Emmett -Teller method. The 6 mm cells were used and were calibrated using the filler rods after which the filler rods for the particular cells were labelled. Nitrogen was chosen as the gas to be used in the analysis as the adsorbate and the run was made using a standard sample's pellets calibration profile from which the results were found to be within the standard sample characteristic range.

The samples were then weighed to be within the range of 0.15 g to 0.2 g and degassed using a vacuum degassing profile customized for the silica powdered sample with a runtime of 12 hours at 180 ˚C and custom crossover pressure of 5 Torr. After degassing the cells with the samples loaded, thee samples were reweighed to determine the actual amounts of the sample remaining. The samples were put in four stations of the analysing chamber and the running profiles for each of the samples were created using the software's analysis profile manager selecting the $N_2$ full isotherm profile with a run-time of 8 hours. Figure 3.2 shows an images of the set up that was used for degassing and analysis.




*Figure 3.14. NOVA 800 Physisorption analyzer used to measure the pore size distribution, the pore volume and the BET surface area of the catalyst samples used in the study.*

### 3.4.2 Thermogravimetric Analysis

Thermogravimetric Analysis (TGA) was done using a SETARAM Labsys TG-DTA12 instrument. Six samples of the synthesized silica supports were heated at 900 ºC in argon in alumina crucibles

at a 10ºC/min ramping rate in order to determine the thermal decomposition profile to be used in obtaining the appropriate calcination temperatures.

### 3.4.3 Scanning Electron Microscopy

The particle sizes and morphology of the prepared silica samples were determined by Scanning Electron Microscopy. A small pinch of the prepared samples was soaked in 8 mL of water in 16 mL polytop glass vials, then stirred and placed in an ultrasonic bath for 5 minutes at 40˚C in order to obtain a uniformly dispersed monolayer of the silica samples for the analysis of the support. After 5 minutes the sample vials were taken out and three regions of the sedimented silica particles could be observed in the vial, a dropper was used to extract the liquid from the middle section, which was then dropped on a carbon tape and dried in an oven for four hours at 50˚C from which a very thin layer of a white stain of silica remained on the carbon tape. For the analysis of the support loaded with cobalt, the powdery sample was loaded directly onto the carbon tape.

The prepared samples were coated by an 8nm gold layer using a Quorum Tech Q150RES Carbon/Gold Sputter Coater shown in Figure 3.3 in preparation for SEM imaging.




*Figure 3.15. Quorum Tech gold coating Instrument used for coating the samples prior to SEM analysis*

The coated samples were then taken for SEM analysis and analysed using JOEL, ISM IT300, JOEL (Tokyo, Japan) shown in Figure 3.4 below . At a magnification of 10.36 kX at 1µm and a working voltage of 15 kV and a working distance of 12.5nm. Energy Dispersive X-Ray (EDX)

elementary analysis and mapping was also done using the same instrument and the distribution of the elements within the $Co/SiO_2$ composite was determined.

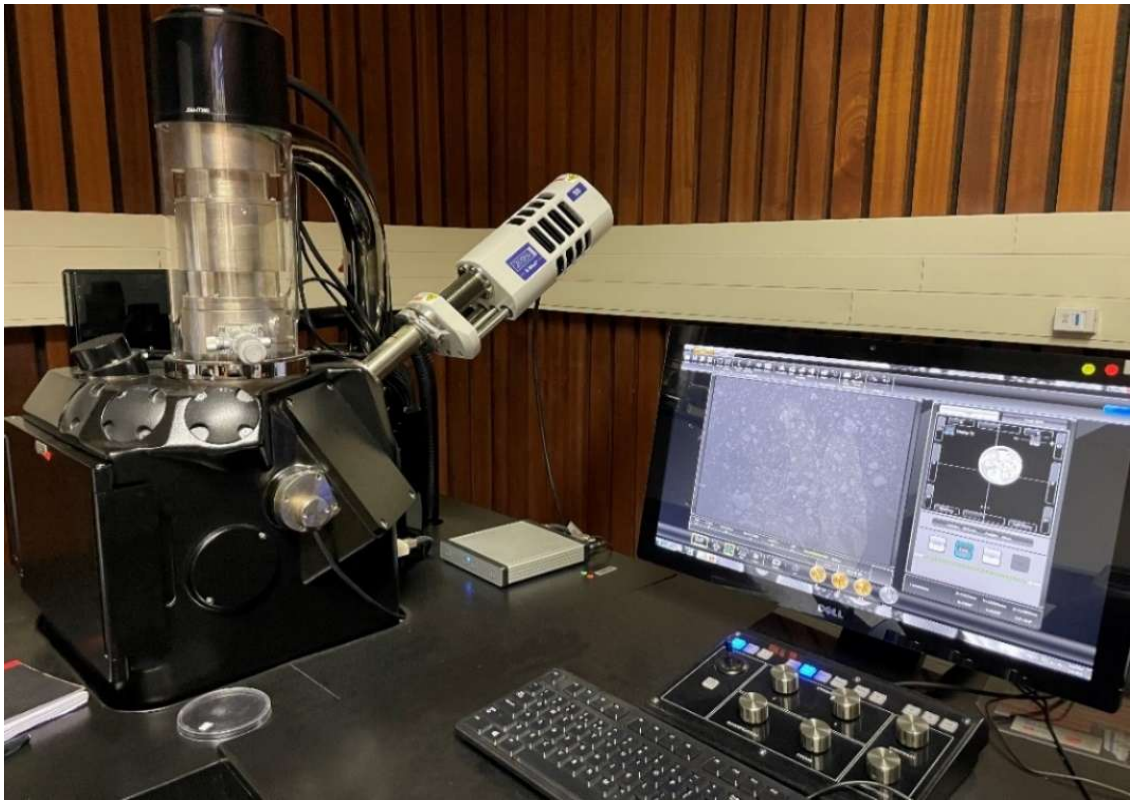


*Figure 3.16. Scanning Electron Microscopy Instrument, JEOL, ISM-IT 300 used for the imaging and mapping of the catalyst samples*

### 3.4.4 Structural Analysis

The functional groups of the calcined and the uncalcined silica supports were identified by the use of the PerkinElmer Fourier Transform Infrared Spectroscope (FT-IR), Spotlight 400 instrument (Germany), using a 0.2cm/s scan rate. Before analysis, the silica samples were mixed and ground with KBr then pelletized into thin semi-transparent pellets containing the minute sample particles spread across the pellet to enable the analysis. The pellet samples were then scanned within a wavenumber range of 400 to 4000 $cm^{-1}$ in transmittance mode. Figure 3.5 below shows an image of the instrument.




*Figure 3.17. PerkinElmer, Spotlight 400 Instrument used in the FTIR experiments*

### 3.4.5 X-ray analysis

X-ray fluorescence (XRF) and X-ray diffraction analysis was done on the samples to further analyse the composition and structure of the prepared samples.

**X-ray Florescence**

XRF was done using a PANalytical MagiX PRO instrument to determine the exact elemental composition of the prepared samples. This analysis method involves irradiating a sample with X-rays, causing some characteristic fluorescent X-rays to be emitted by the atoms that reveal the sample's elemental composition.

During the sample preparation, the silica was pressed into a fine transparent pellet which was then sealed with a thin paper film to prevent contamination before being placed in a sample cup for analysis. The analysis was then done for an hour before obtaining the results.

**X-Ray Diffraction**

The X-ray diffraction technique was used to characterize and determine the crystal structure and phases present in the support samples and the metal-loaded samples. The experiments were conducted at the Council for Scientific and Industrial Research (CSIR), South Africa. A PANalytical X'pert PRO instrument manufactured by PANalytical in the Netherlands was used. The instrument was used fitted with a Cu Kα ($\lambda$ = 0.154 nm) radiation source to analyze the samples over a 2θ range of 5 degrees to 90 degrees using 40 kV and 40 mA at room temperature. The samples were ground until they reached an ultra-fine state and exposed to X-Rays in the

instrument for 15 minutes. An image of the X-ray diffractometer used for the XRD investigations is presented in Figure 3.6.




*Figure 3.18. X-ray diffractometer used in the XRD studies*

### 3.4.6 Temperature Programmed Reduction

$H_2$ Temperature-Programmed Reduction ($H_2$-TPR) was conducted using a CATLAB-PCS Microreactor manufactured by Hidden Analytical in Germany. During the process, 0.2 g of the sample was weighed and loaded into a glass tube which acts as the reactor, and a small plug of quartz wool was put on top of the catalyst bed and placed into the microreactor column. Generally, prior to the actual TPR measurements, the 0.2 g samples were treated in a constant $N_2$ flow for 1 h to remove trace amounts of impurities and moisture before cooling to the reaction temperature. Argon was then introduced into the system at 100 mL/min for 1 hour at room temperature followed by the gas mixture of 5% $H_2/N_2$ at a flow rate of 30 mL/min until a stable baseline was established in the system. The TPR measurements were set to be recorded for 2 h using the Faraday detector where the $H_2$ TPR curve was obtained from 50 to 800 ◦C at a heating rate of 10 ◦C $min^{-1}$. The reduction temperature for the catalyst for the FT process was deduced from the peaks obtained from the TPR results which were plotted after baseline correction. Analysis of $H_2$ consumption data was used to obtain the reducibility of the $Co/SiO_2$ catalysts. Figure 3.7 shows the set-up of the apparatus used for the TPR experiments.

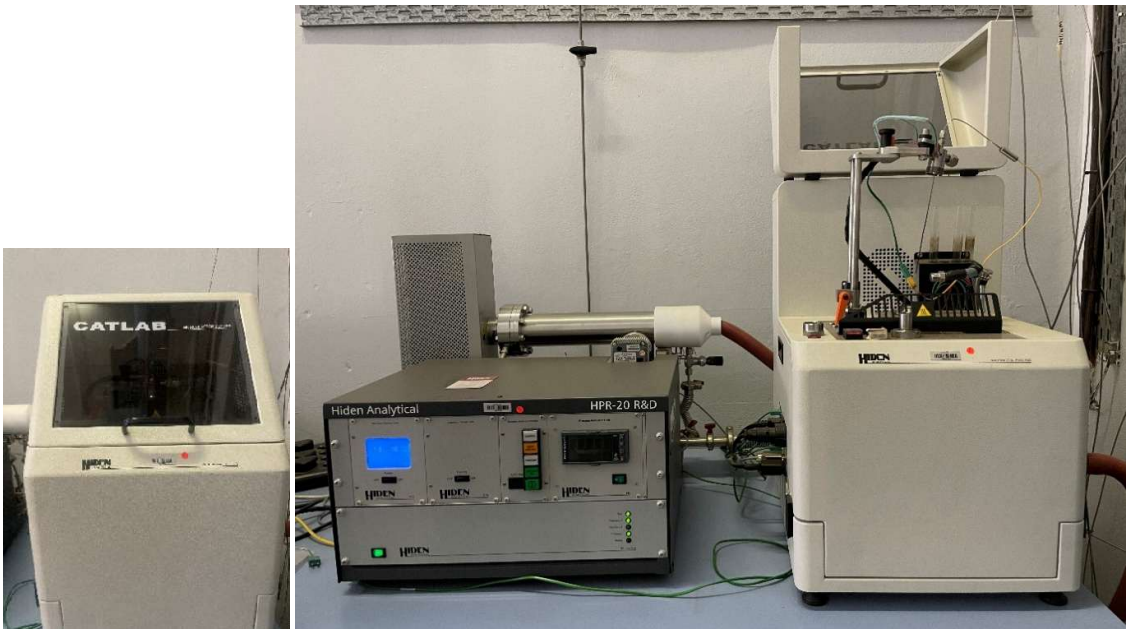



*Figure 3.19. CATLAB - PCS Microreactor used to carry out the TPR and Hydrogen chemisorption experiments*

### 3.4.7 Hydrogen Chemisorption Studies

Hydrogen Chemisorption was conducted for the catalyst samples using the same CATLAB-PCS Microreactor described in section 3.4.6. A catalyst sample with a mass of 0.2 g was prepared and added to the microreactor column. During the first stage, the whole system was first purged with 100 % Argon at 200 ˚C for 1.5 h using a ramp rate of 10 ˚C/min. In the second stage, reduction of the the catalyst was done at 400 ˚C which was the temperature that had been deemed suitable for the catalyst from the TPR studies for 10 h, using a ramp rate of 10 ˚C/min and a gas mixture of 10 % $H_2$/90 % Ar using a flowrate of 60 L/min. In the third stage, the system was evacuated using Ar (100%) at 300 ˚C for 1 h. During the fourth stage, the whole microreactor system was cooled for 90 mintes to the chemisorption temperature which was set at 35˚C. The fifth and last stage involved $H_2$ Chemisorption with a pulse rate of 35/second using a 250SEM MID detector. The hydrogen uptake, active catalyst surface areas and cobalt dispersion were then determined from the experiment as given by the instrument.

The dispersion is given by equation 3.3 below (Jacobs et al., 2002):

$$\text{Co dispersion} = \frac{100 \times \text{Number of Co atoms on the surface}}{\text{Total number of Co atoms in the sample}} \qquad \text{eqn (3.4)}$$

This was calculated taking note of the following assumptions:

- The active metal is uniformly distributed across the surface of the catalyst support
- There are no metal–support interactions that inhibit the $H_2$ adsorption process

- Only surface metal atoms are considered to be active and contribute to the catalysis
- The surface particle shape is assumed to be spherical in the calculations, although in reality it may not be the case
- Fixed oxidation states of cobalt $Co^{2+}$ and $Co^{3+}$ state, although sometimes there will be variation of the states
- No particle agglomeration and sintering
- Constant geometric surface atoms is also assumed to be existing, i.e, a constant surface to total atom ratios throughout the sample (Rytter & Holmen, 2016; Bezemer et al., 2006).

## 3.5 Catalyst testing

### 3.5.1 Catalyst reduction

Three reactors were loaded with the catalyst at the same time and the nitrogen gas was filled in the line at 20 bar and room temperature for 24 h to flush the system. Leak testing was also done during this step. After 24 h the gas was changed from $N_2$ to $H_2$. Temperature controllers were loaded with a sequence that entailed raising the temperature from room temperature to 150 ˚C in 40 minutes then maintaining the temperature at 150 ˚C for 1 h, then raising the temperature from 150 ˚C to 350 ˚C in 1 h 40 min then keeping the temperature at 350 ˚C for 16 h before stopping the heating and bringing it back to room temperature in 2 h; Figure 3.8 illustrates this temperature profile using a schematic graph. The reduction of the catalyst was performed *in situ* using a flowrate of 60 L/min. Figure 3.9 shows the temperature control system that was used in the experiments.

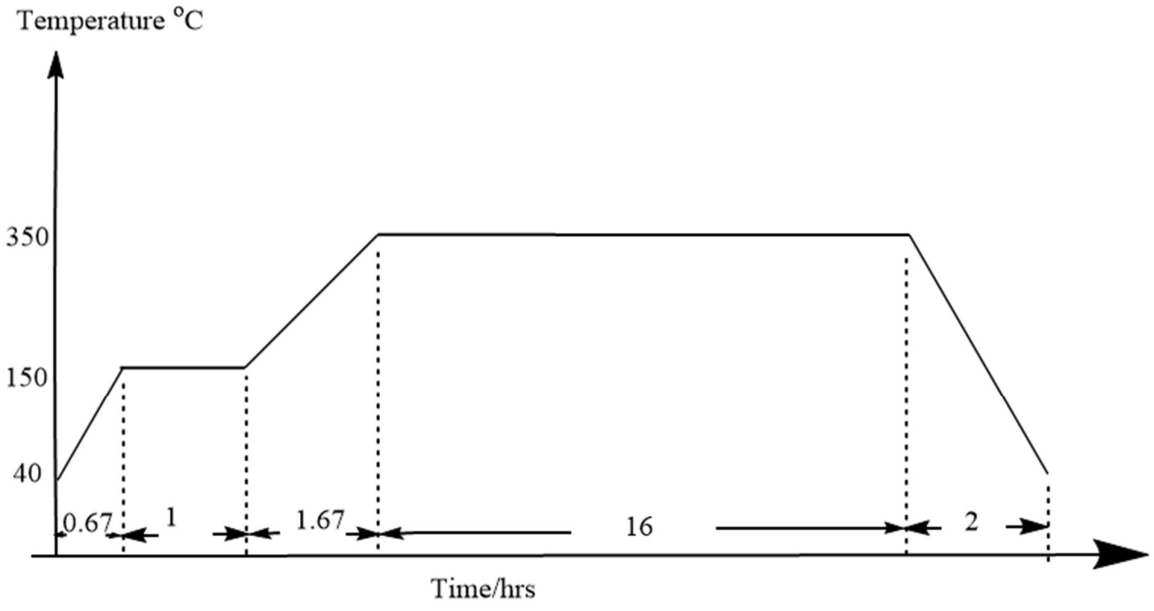



*Figure 3.20. Schematic graph of the temperature profile used for the catalyst reduction*



*Figure 3.21. The temperature controllers of the FT reactors used to set-up and regulate the reactor temperatures*

### 3.5.2 Fischer Tropsch Synthesis

After the catalyst was reduced, a 1g sample of the catalyst was prepared and then loaded into the reactor, the catalyst bed had a length of 3 cm inside the reactor. FT synthesis experiments were conducted in a stainless steel fixed bed reactor which was kept at a temperature of 220°C, a syngas gas input with a composition of $H_2$:CO:$N_2$ ratio of 6:3:1 was passed through the system at 20 bar and a flowrate of 60 L/min for a time-on-stream sufficient to reach the steady state for the CO conversion. An Agilent gas chromatograph (GC) was used to analyse the hydrocarbon products.

Calibration of the GC was done using a premixed calibration gas containing $H_2$, CO, $H_2$, $N_2$, $CO_2$, $C_2H_6$, $C_2H_4$ and $CH_4$ whose compositions are given in Table 3.1. For the calibration of other specific carbon numbers in the gas phase, the RF (Response Factor) values of $C_2$ which is provided on the calibration gas and is known, hence used as the standard, were extrapolated and used to determine the unknown RF values for the hydrocarbons, however, for $C_1$ and $C_2$ hydrocarbons the values were just taken directly from the calibration gas mixture as they were already part of the contents.

Figure 3.10 shows the typical output obtained from the front and the back end of the GC during calibration

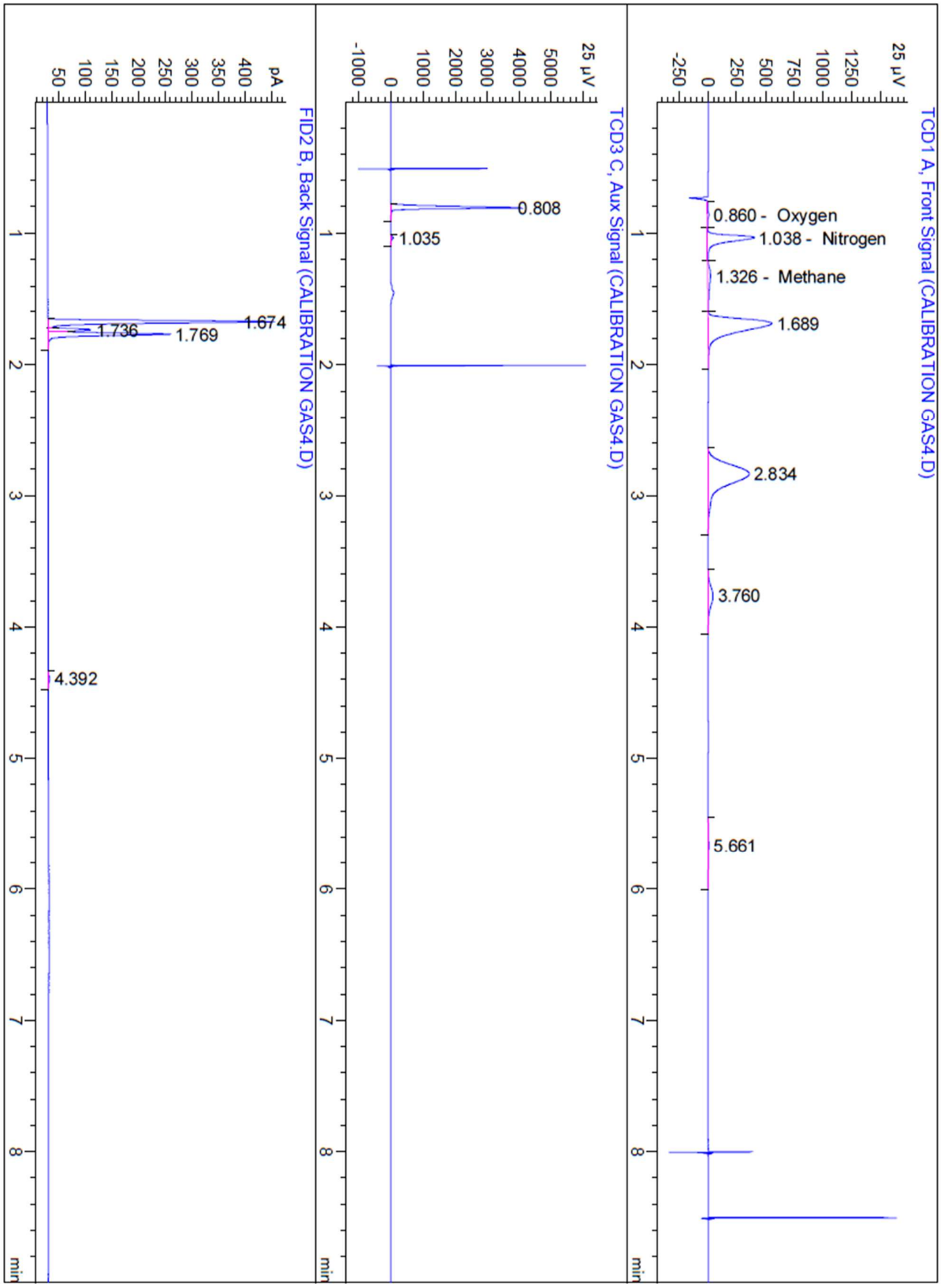



*Figure 3.22: A typical GC output obtained from the calibration gas*

The syngas was passed through the reactor system after calibration, and some peaks were obtained from the GC at 15-minute intervals until steady state was reached. The hydrocarbon peaks occurred at the known retention times, and the areas were calculated from the results to determine

the measured amount of each hydrocarbon. Table 3.5 shows the RF values of the hydrocarbons which were used to identify the obtained peaks during the FT experiments and Figure 3.11 shows the general set up of the three reactors in series that were used for the FT runs.

Table 3.5: Response factors of the respective carbon numbers used to extract the data from the GC output

| Carbon number | Olefin RF Value | Paraffin RF value |
|---|---|---|
| 1 | | 1.62 |
| 2 | 1.73 | 1.76 |
| 3 | 1.95 | 1.98 |
| 4 | 2.63 | 2.74 |
| 5 | 4.22 | 4.46 |
| 6 | 6.56 | 6.83 |



*Figure 3.23. The FT reactors set up with quartz wool insulation*

## 3.6 Mass balance calculations

The experimental setup used in this work can be used to determine the volumetric flow rate of the inlet gas, which can be used to compute the output flow rate. For precise CO conversion calculations, $N_2$ (10%) was incorporated as an internal reference into the reaction

feed.

Equation 3.5 shows the $N_2$ balance.

$$\dot{n}_{T_{in}} \times X_{N_2,\,in} = \dot{n}_{T_{out}} \times X_{N_2,\,out} \qquad \text{eqn (3.5)}$$

Where $\dot{n}_{T_{in}}$ and $\dot{n}_{T_{out}}$ indicate the total molar flow rates that enter (in) and exit (out) the reactor, respectively and $X_{N_2,\,in}$ and $X_{N_2,\,out}$ are the $N_2$ mole fractions flowing in and out of the reactor, respectively as determined from the GC analysis.

The CO molar flow rates entering and exiting the reactor are expressed as follows:

$$\dot{n}_{CO\,in} = \dot{n}_{Tin} \times X_{CO\,in} \qquad \text{eqn (3.7)}$$

$$\dot{n}_{CO\,out} = \dot{n}_{Tout} \times X_{CO\,out} \qquad \text{eqn (3.8)}$$

The percentage CO conversion can then be determined using the following equation:

$$\%_{CO} = \frac{\dot{n}_{CO\,reacted}}{\dot{n}_{CO\,in}} \times 100 = \frac{\dot{n}_{T\,in}\,X_{co\,in} - \dot{n}_{T\,in}\,X_{CO\,out}}{\dot{n}_{T\,in}\;X_{CO\,in}} \times 100 \qquad \text{eqn (3.9)}$$

Assuming that the plug flow reactor bed is small so that the reactor behaves like a differential reactor, which operates at sufficiently low conversion for the rate of reaction not to change down the length of the reactor, the rate of formation for CO mol/(min·gcat) was then determined as follows:

$$r_{CO} = \frac{-\dot{n}_{Tin} \times \%\,CO/100}{m_{cat}} \qquad \text{eqn (3.10)}$$

Where $m_{cat}$ is the mass in grammes of the catalyst utilized in the reaction.

Equation 3.12 below was used to calculate the rate of $CH_4$ production.

$$r_{CH_4} = \dot{n}_{Tout} \times \frac{X\,CH_{4out}}{m_{cat}} \qquad \text{eqn (3.11)}$$

The instantaneous $CH_4$ selectivity is then given by:

$$S_{CH_4} = \frac{r_{CH_4}}{-r_{CO}} \qquad \text{eqn (3.12)}$$

The hydrocarbon product's formation rate, obtaining the mole fraction of the product, $X\,C_{n,out}$ from the GC is given by:

$$r_{C_n} = \dot{n}_{Tout} \times \frac{X\ C_{n,out}}{m_{cat}}$$ eqn (3.13)

The instantaneous selectivity of the $C_n$ hydrocarbons was then generally determined using equation 3.14, which is expressed as:

$$S_{C_n} = \frac{[(rC_nH_{n+1} + rC_nH_{n+2}) \times n]}{-rCO}$$ eqn (3.14)

The number of carbon atoms is denoted by n in the equation.

The selectivity of $C_{5+}$ hydrocarbons was then determined as follows:

$$S_{C_{5+}} = 100\% - S_{CH_4} - (S_{C_2} + S_{C_3} + S_{C_4})$$ eqn (3.15)

The $C_{5+}$ and $CH_4$ yield fractions were obtained by equations 3.16 and 3.17 below:

$$Y_{C_{5+}} = X_{CO} \times S_{C_{5+}} \times 100$$ eqn (3.16)

$$Y_{CH_4} = X_{CO} \times S_{CH_4} \times 100$$ eqn (3.17)

## 3.7 Machine learning

The experimental results based on work done on cobalt catalyst supported on silica over the past ten years were compiled, 410 data points and 40 descriptors were collected from the literature and used to determine the influence of Co supported on silica on the FT product distribution. After analysing their importance, their relative contribution to affecting the CO conversion and the hydrocarbon selectivities was investigated. This was done in order to determine and establish, using the machine learning method, what range of silica surface area values and pore size distribution during FT synthesis and the composition of the catalyst itself will be optimal for the maximum CO conversion and $C_1$, $C_2$-$C_4$ and $C_{5+}$ selectivities in this work. The use of silica support as the basis for the study had some advantages because it can be synthesised in a number of ways (including hydrothermal and sol-gel), enabling researchers to methodically investigate the relationship between surface area and catalytic activity and selectivity (Bezemer et al., 2006). The prediction tool used in this specific investigation was the random forest method.

## 3.8 Conclusion

The experimental protocols described in this chapter and the thorough characterization of the cobalt-based catalysts have given the researcher a strong basis for comprehending the structure and performance relationships in FT synthesis. SEM, TPR, XRD, TGA, BET surface area analysis, and hydrogen chemisorption measurements were among the analytical methods used to precisely ascertain the catalysts' physicochemical characteristics. Particle size, reducibility, metal-support interactions, and cobalt dispersion were all precisely assessed thanks to these characterization techniques.

Additionally, the FT synthesis parameters were selected to mirror parameters that are regarded as optimal in industry, allowing for comparison of catalyst performance evaluations. The robustness and representativeness of the catalytic results are guaranteed by the design of the experimental protocols, which include temperature, pressure, syngas feed composition, and catalyst physical and chemical parameters. To make insightful deductions regarding catalyst activity, selectivity, and stability in the forthcoming chapters, this rigorous study is essential.

## References


Bezemer, G. L., Bitter, J. H., Kuipers, H. P. C. E., Oosterbeek, H., Holewijn, J. E., Xu, X., Kapteijn, F., Van Diilen, A. J., & De Jong, K. P. (2006). Cobalt particle size effects in the Fischer-Tropsch reaction studied with carbon nanofiber supported catalysts. *Journal of the American Chemical Society*, *128*(12), 3956–3964. https://doi.org/10.1021/ja058282w

Chen, Y., Zhang, C., Zheng, Q., & Chen, Y. (2018). Separation-cooperated assembly of liquid photonic crystals from polydisperse particles. *Chemical Communications*, *54*(99), 13937–13940. https://doi.org/10.1039/c8cc06499g

Ibrahim, I. a. M., Zikry, a. a. F., & Sharaf, M. a. (2010). Preparation of spherical silica nanoparticles: Stober silica. *Journal of American Science*, *6*(11), 985–989.

Jacobs, G., Das, T. K., Zhang, Y., Li, J., Racoillet, G., & Davis, B. H. (2002). Fischer-Tropsch synthesis: Support, loading, and promoter effects on the reducibility of cobalt catalysts. *Applied Catalysis A: General*, *233*(1–2), 263–281. https://doi.org/10.1016/S0926-860X(02)00195-3

Rytter, E., & Holmen, A. (2016). On the support in cobalt Fischer–Tropsch Synthesis—emphasis on alumina and aluminates. *Catalysts Today*, *275*, 11–19. https://doi.org/doi.org/10.1016/j

Singho, N. D., & Johan, M. R. (2012). Complex impedance spectroscopy study of silica nanoparticles via sol-gel method. *International Journal of Electrochemical Science*, *7*(6), 5604–5615. https://doi.org/10.1016/s1452-3981(23)19647-7

Stober, W., Fink, A., & Bohn, E. (1968). Controlled Growth of Monodisperse Silica Spheres in the Micron Size Range. *Journal of Colloid and Interface Science*, *26*(1), 62–69. https://doi.org/10.1589/jpts.29.112

Tian, Z., Wang, C., Si, Z., Wang, Y., Chen, L., Liu, Q., Zhang, Q., Xu, Y., & Ma, L. (2018). Product Distributions of Fischer-Tropsch Synthesis over Core-Shell Catalysts: The Effects of Diverse Shell Thickness. *ChemistrySelect*, *3*(44), 12415–12423. https://doi.org/10.1002/slct.201801515

Vazquez, N. I., Gonzalez, Z., Ferrari, B., & Castro, Y. (2017). Synthesis of mesoporous silica nanoparticles by sol-gel as nanocontainer for future drug delivery applications. *Boletin*

*de La Sociedad Espanola de Ceramica y Vidrio*, *56*(3), 139–145. https://doi.org/10.1016/j.bsecv.2017.03.002

Walther, F., & Brühwiler, D. (2024). Investigation of silica particle growth by incorporation of a pyrene fluorescent probe. *Colloids and Surfaces A: Physicochemical and Engineering Aspects*, *685*(October 2023). https://doi.org/10.1016/j.colsurfa.2024.133234

Zola, A. S., Da Silva, L. S., Moretti, A. L., Do Couto Fraga, A., Sousa-Aguiar, E. F., & Arroyo, P. A. (2016). Effect of Silylation and Support Porosity of Co/MCM-41 and Co/SiO2 Catalysts in Fischer-Tropsch Synthesis. *Topics in Catalysis*, *59*(2–4), 219–229. https://doi.org/10.1007/s11244-015-0446-1

# CHAPTER 4: VARYING THE PORE SIZE TO DETERMINE THE EFFECT ON SELECTIVITY IN FISCHER-TROPSCH SYNTHESIS FOR SILICA-SUPPORTED COBALT CATALYSTS


## Abstract

The catalyst pore diameter and surface morphology have a significant effect on how well the catalyst performs in the FT reaction. The Stöber process was used to synthesize the mesoporous silica nanoparticles that serve as the supports for cobalt-based FT synthesis catalysts, incorporating tetraethyl orthosilicate (TEOS) as the silica precursor. TEOS was hydrolysed in the presence of ethanol during the synthesis procedure, using ammonium hydroxide as the catalyst. Different ratios of water : TEOS : $NH_4OH$ : ethanol were used to form mesoporous silica with different pore sizes by varying the water and $NH_4OH$ molar ratios while keeping the other reagents constant. The effects of ammonium hydroxide concentration and water content in the mixture on the synthesized support's physical properties are presented in this chapter. Based on thermogravimetric analysis (TGA), a calcination temperature of 620˚C was chosen. All of the prepared catalysts had a 10 wt% cobalt loading. BET analysis was then done for each catalyst sample to determine the pore size, surface area, and pore volume of the catalysts. The nitrogen adsorption-desorption isotherms from the physisorption studies were used to determine the pore type and structures of the prepared catalyst samples. SEM, EDS, FTIR, and XRD were also used in the characterization of the synthesized catalysts. The findings in this chapter demonstrate a way of systematically tailoring the silica pore sizes using variable ratios of the above-mentioned reagents, which gives a range of concentrations that can be used to achieve the required pore diameter in FT Synthesis applications. Pore diameters in the 14-28 nm range were obtained for the silica supports that were synthesized, this also corresponded to the formation of different surface areas for the resulting catalysts which had values ranging from 17 – 152 $m^2/g$.

## 4.1 Introduction

Because of their high activity, stability under different reaction conditions, and long-chain hydrocarbon selectivity, cobalt-based catalysts are especially preferred in FT synthesis (Dry, 2002). The type of support material greatly affects how well these catalysts work, and silica ($SiO_2$) is one of the most widely used supports (Bartholomew, 2001) to disperse active metal particles and preserve catalyst integrity during FT synthesis. Silica supports are well known for their large surface area, thermal stability, and chemical inertness (Gates et al., 1979). Therefore, the focus of this chapter is to explore the development of an effective catalyst support for which the properties of the support can be enhanced and tailored using different reagent ratios in order to achieve a certain desired outcome for application under different FT synthesis conditions.

The Stöber process is a synthesis method that can be used to systematically control the silica support structure during the silica synthesis because it can create monodispersed, spherical silica particles with regulated diameters ranging from nanometres to micrometers. Ammonia catalyzes the reaction in this process which involves the hydrolysis and condensation of TEOS in an alcoholic solution, which results in the creation of homogeneous silica spheres. By adjusting the silica particles' diameter, the length of the path for diffusion of reagents into and products out of the particles, can be modified. Because of this control over several parameters which can be varied independently, this procedure stands out among the different techniques available for synthesizing silica supports ( Stöber, Fink and Bohn, 1968).

By changing variables like reagent concentrations, solvent ratios, and reaction time, the Stöber method's adaptability enables exact control over particle size and shape (van Blaaderen and Vrij, 1993; Zhuravlev, 2000). This affects the dispersion and interaction between the support and the active metal species, this degree of control is essential when creating catalysts with particular characteristics. Additionally, the Stöber-synthesised silica particles are perfect for supporting cobalt nanoparticles in FT Synthesis applications due to their homogeneity and purity (Rahman and Padavettan, 2012). Cobalt has been successfully incorporated into Stöber-derived silica supports in recent investigations, producing catalysts with improved activity and selectivity in FT synthesis (Fernandes et al., 2019; Smarzaro et al., 2021; Walther and Brühwiler, 2024). For example, the dispersion of cobalt nanoparticles is facilitated by the silica spheres' high surface area and consistent pore structure. Consequently, the reaction will have more active sites available (Bartholomew, 2001).

Furthermore, strong metal-support interactions that may otherwise result in the creation of inactive species are reduced by the inert nature of silica (Gates et al., 1979).

Our goal in this chapter is to create cobalt-supported silica catalysts by preparing the silica support using the Stöber technique. We plan to examine the effects on catalyst shape and pore structure, cobalt dispersion, and overall performance in FT synthesis by methodically altering the concentrations of the synthesis reagents and explicitly analysing the effect on the resulting physical properties of the silica such as densities and pore structure creating a template method for future synthesis of FT-based catalysts. This extends the existing literature on the Stöber process which currently does not provide further information on the effects of different reagent ratios on the pore shape and density. This method will help create more effective FT synthesis catalysts by shedding light on the connection between catalyst characteristics and the ratios of the reagents used in the preparation of the support. During the synthesis of the support, four reagents, namely water, TEOS, aqueous ammonia and ethanol, were used as described in Chapter 3. Here, the impact of the $H_2O$ ratio, and $NH_4OH$ ratio (while keeping the ratios of the other components in the reaction mixture constant) on the pore size, pore volume and surface area of the resulting silica support is reported on. We also investigated the characteristics of the resulting catalysts after loading with the cobalt metal using XRD, EDS, SEM, FTIR, and physisorption analysis techniques.

## 4.2 Results and discussion

### 4.2.1 TGA

The supports that were synthesized using the Stöber process, as explained in Chapter 3, were then named as shown in Table 3.4. At this point, the supports were still in the hydroxide form and therefore they needed to be calcined first to eliminate the water molecules, leaving behind the desired $SiO_2$ according to equation 3.2. To determine the calcination temperature, the TGA analysis was done in air on six of the synthesized $Si(OH)_4$ white powder samples, and Figure 4.1 displays the outcomes.

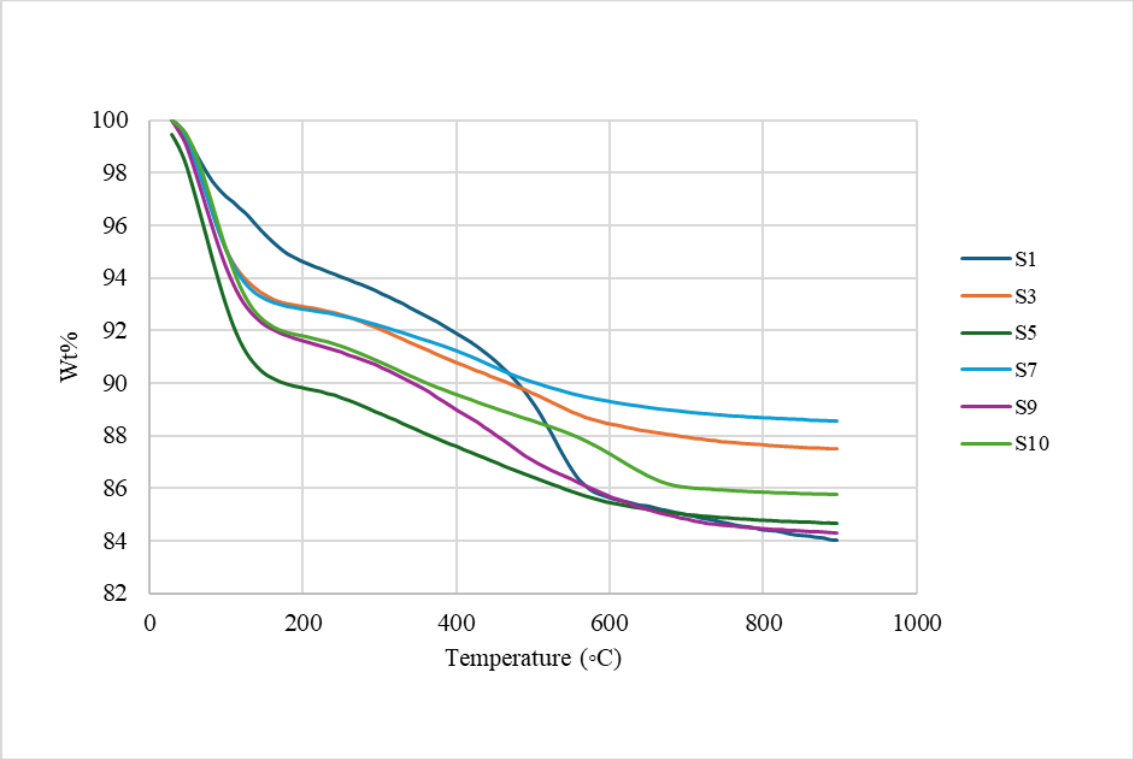



*Figure 4.24. TGA analysis for the synthesised $Si(OH)_4$ samples*

From the graphs, there is a decrease in the weight of the silica samples due to the loss of material from the sample. In the range below 150°C, the samples show a rapid weight loss, which corresponds to the desorption of the adsorbed water molecules that will be weakly bound at the $Si(OH)_4$ particles' surface (Mueller et al., 2003; Rahman and Padavettan, 2012).

Intermediate weight loss continued to occur between 150 and 280°C; in this temperature range, condensation of the present silanol (Si–OH) groups begins to occur, this causes a sharper weight loss for most of the samples as the temperature rises. Water is released as siloxane (Si–O–Si) linkages are formed as a result of this condensation. This phase marks the change from a surface that is hydroxylated to a silica network that is more compact. The increase in density of silanol groups in the sample can be inferred from the extent of this weight loss (Odlyha, Scott and Simpson, 1993).

When temperatures rise to the region above 300°C, the remaining hydroxyl groups will then start to dehydroxylate, causing further weight loss. The silica matrix contains stronger bonds between these hydroxyls. When they are eliminated, the silica framework will be formed and become even more structurally dense and thermally stabilized (Shioji et al., 1998). In samples

with a higher hydroxyl content or inadequate condensation during synthesis, this stage is more noticeable. From the graph it shows that a more gradual or steady decrease starts between 580 and 620°C among the samples. To obtain a clearer picture and locate the temperature which can be appropriate to calcine these samples, derivatives of the points used to plot the graph in Figure 4.1 were taken and plotted against the temperature to obtain the DTG analysis. Figure 4.2 shows the resulting derivative curves from the samples.

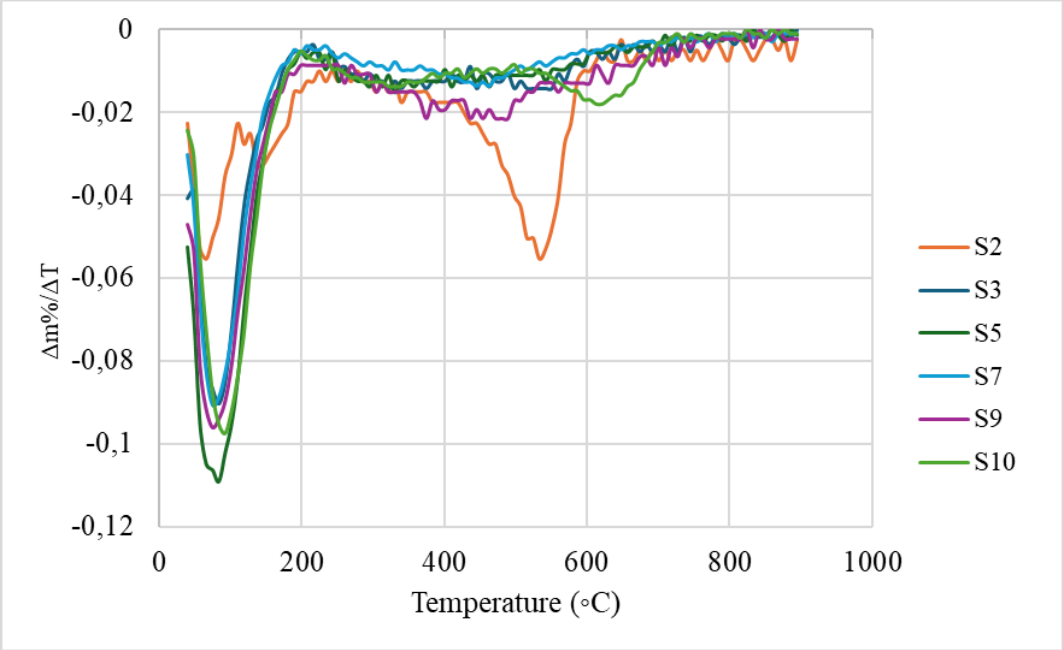



*Figure 4.25. DTG Analysis of the prepared $Si(OH)_4$ samples*

The gradients of the curves depicted in Figure 4.1 are displayed on the graph in Figure 4.2, a more significant minimum representing a greater extent of the change in the slope of the TGA graph. The first minimum at around 150°C corresponds to the loss of the adsorbed water in the sample while the second one, which occurs in the range from 400°C to 620°C corresponds to the condensation and elimination of the silanol groups as explained above. There is no significant peak that corresponds to the intermediate weight loss in the DTG graph, as the rate of change in this zone is small, making the derivative almost constant. The most pure $SiO_2$ is therefore found after all the silanol groups have been removed, which is after 620°C. The sample S10 is associated with this maximum decomposition temperature; therefore, all of the samples were calcined at 620°C in order to obtain the silica support. Each sample was then divided into two portions; one portion was kept for further characterisation of the support, and the second portion was loaded with 10% cobalt by mass. The 20 samples

were taken for physisorption analysis to obtain the pore size, surface area, and pore volume distribution.

### 4.2.2 Structural analysis

The functional groups of the calcined and the uncalcined silica supports were determined using a PerkinEelmer® (USA) Fourier Transform Infrared (FTIR) Spectrometer. Before analysis, the silica samples were pelletized into thin circular pellets of about 1mm thick. The pellet samples were then scanned within a wavenumber in the 400 to 4000 $cm^{-1}$ range in transmission mode. Figures 4.3 and 4.4 show the graphs of the results that were obtained from the FTIR studies for silica samples 1, 4 and 7.

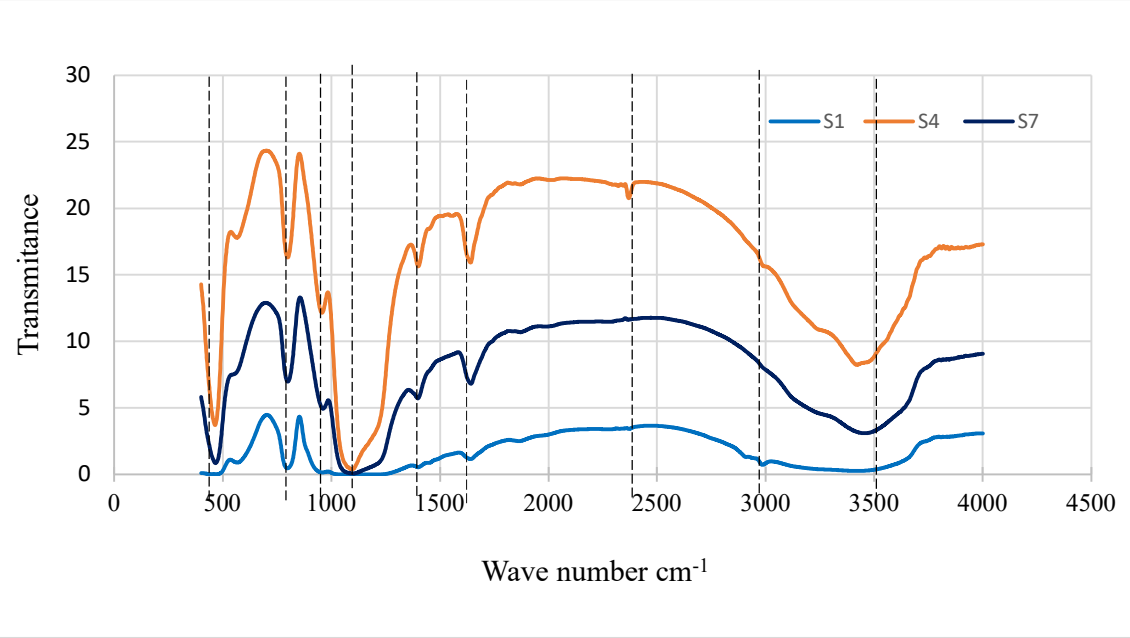



*Figure 4.26 FTIR analysis for the uncalcined silica support*

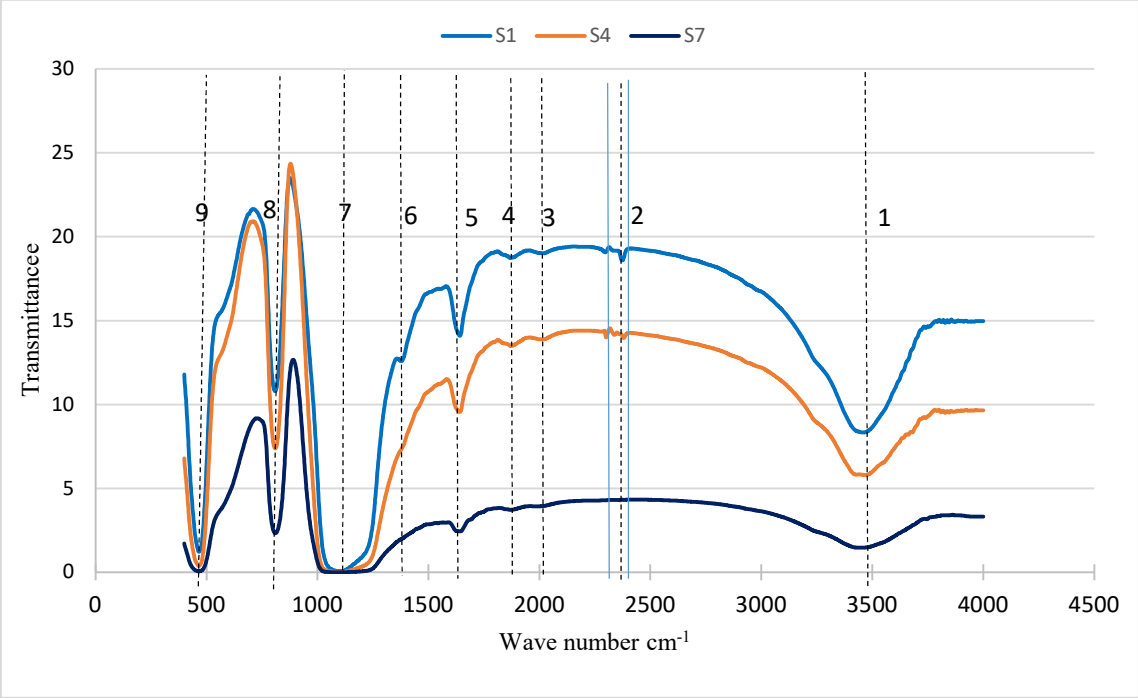



*Figure 4.27. FTIR analysis for the calcined silica support samples*

**Peak identification for the uncalcined silica support**

From Figures 4.3 and 4.4, noticeable differences were obtained, which showed significant differences in the peaks between the samples created with different molar ratios of the reagents during the silica synthesis.

In the two graphs, the first peak was observed at a wavenumber of 3500 $cm^{-1}$ with an assigned functional group of broad O-H bonding from the adsorbed water molecules. The next small peaks correspond to a wavenumber of 2980 $cm^{-1,}$ which corresponds to C-H asymmetric stretching, which appear in the uncalcined samples but do not appear n the calcined samples of Figure 4.4. There are small peaks observed in the wavenumber range of 1900 $cm^{-1}$ to 2400 $cm^{-1}$ which are not so dominant but have been reported in the literature to be some water-related absorption maxima (Efimov and Pogareva, 2006). However, strangely, they seem to be more visible in silica samples 1 and 4 but do not appear in sample 7, where the water molar ratio was higher. There also appears a next peak at 1640-1650 $cm^{-1}$h in the calcined and uncalcined samples, which is assigned to be caused by the Si-O weak overtone. The next peak was found at 1380-1400 $cm^{-1}$ which corresponds to the existence of C-H bending associated with alkyl chains from unreacted or partially hydrolyzed TEOS, these are more prevalent in the uncalcined samples, showing that calcination helped to remove the hydrocarbon residues. The next dominant peak in both the uncalcined and calcined samples is

found at a wavenumber of 1090 $cm^{-1}$ which relates to the asymmetric stretching of Si–O–Si. The peaks at a wavenumber of 780-820 $cm^{-1}$ which only occur in uncalcined samples, can be assigned to a Si-O-C stretching functional group caused by the binding of some remaining organic groups (from TEOS) to the silicon atom (Efimov and Pogareva, 2006). The last peak on both the calcined and uncalcined silica samples was found at 470-500 $cm^{-1}$ which represents the Si–O bending.

Table 4.1 gives a summary of the peaks that were found in the FTIR analysis of the silica samples that were calcined and those that were not.

Table 4.1. Identification of the peaks from the FTIR results of the silica samples

| **Wavenumber ($cm^{-1}$)** | **Assignmnent** | **Explanation** |
|---|---|---|
| 3450 – 3500 | Broad O-H stretching | From adsorbed $H_2O$ molecules through hydrogen bonds and silanol (Si-OH) (Brinker and Scherer, 1990) |
| 2974 | C-H asymmetric stretching –($CH_3$) | This is from unreacted ethoxy groups from the TEOS. |
| 2892-2886 | C-H symmetric stretching | Part of the residual ethoxy groups from ethanol or TEOS hydrolysis (Méndez-Vivar and Mendoza-Bandala, 2000). |
| 1655-1648 | Si-O weak overtone | This results from a lack of harmony in the vibrational potential. |
| 1380-1460 | C-H bending | Also linked to alkyl chains from unreacted or partially hydrolyzed TEOS (Méndez-Vivar and Mendoza-Bandala, 2000). |
| 1080 -1190 | Asymmetric Si–O–Si stretching | Due to the broadening of the main skeletal vibration of the forming silica network (Méndez-Vivar and Mendoza-Bandala, 2000) |
| 800 – 900 | Symmetric Si–O–Si stretching | The tetrahedral network formation is supported by these (Méndez-Vivar and Mendoza-Bandala, 2000). |
| 798 -794 | Si-O-C stretching | Observed in uncalcined silica samples where alkoxy silanes will be binding some remaining organic groups (from TEOS) to the silicon atom (Efimov and Pogareva, 2006). |
| 460 – 470 | Si–O bending | Formed when the bridging oxygen atom in the Si–O–Si bond gets involved in an out-of-plane bending (also referred to as ‘rocking’) (Méndez-Vivar and Mendoza-Bandala, 2000). |

| | | |
|---|---|---|

### 4.2.3 XRD analysis

The prepared $Co/SiO_2$ catalysts were labelled using the following notation, which involves introducing a prefix number to denote the run involving the reagent ratios used to prepare the support from the synthesis procedure explained in the previous chapter. After loading the samples with the cobalt metal, the loaded samples were calcined again at 400 °C. The notations of the prepared samples are given in Table 4.2

Table 4.2. The notations of the prepared catalyst samples

| Notation | Catalyst loading (%) | $H_2O$: TEOS: $NH_4OH$: EtOH Ratio |
|---|---|---|
| 1-$Co/SiO_2$ | 10 | 1 : 1 : 1 : 2.5 |
| 2-$Co/SiO_2$ | 10 | 1.5:1: 1 : 2.5 |
| 3-$Co/SiO_2$ | 10 | 2 : 1 : 1 : 2.5 |
| 4-$Co/SiO_2$ | 10 | 2.5:1: 1 : 2.5 |
| 5-$Co/SiO_2$ | 10 | 5 : 1 : 1 : 2.5 |
| 6-$Co/SiO_2$ | 10 | 10:1 : 1 : 2.5 |
| 7-$Co/SiO_2$ | 10 | 12:1 : 1 : 2.5 |
| 8-$Co/SiO_2$ | 10 | 15:1 : 7 : 2.5 |
| 9-$Co/SiO_2$ | 10 | 15:1 : 2.5 :2.5 |
| 10-$Co/SiO_2$ | 10 | 15:1 : 5 : 2.5 |

The diffractograms of the analyzed silica nanoparticles are displayed in Figure 4.5 and show that only amorphous silica is present, which can be identified by the presence of a single wide peak, which is present in all 10 of the samples prior to loading with cobalt (Rovani et al., 2019). These broad peaks occur at 22° 2θ for all the samples. The density results, which are approximately 2.2 $g/cm^3$ also confirm to the presence of amorphous silica.

Unlike in crystalline silica, amorphous silica, generally contains a higher concentration of silanol groups, which increases the surface hydroxylation and, in turn, the extent of the anchoring of the Co precursor leading to higher dispersion. Crystalline silica contains fewer sites for anchoring the Co atoms due to a well-ordered surface, which is less hydroxylated. Moreover, the differences in these structures enable the amorphous silica forms to be more easily reducible than the highly crystalline types (Jacobs et al., 2002; Bezemer et al., 2006; Yamane et al., 2017).

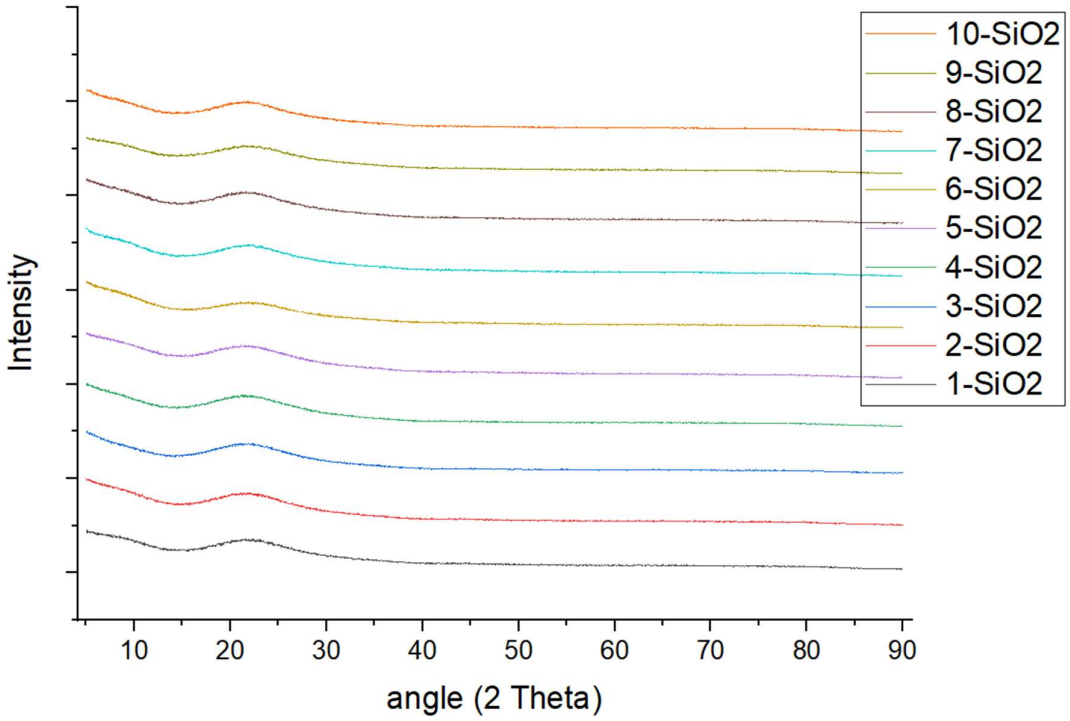



*Figure 4.28. XRD analysis of the 10 synthesized silica supports*

XRD analysis of the cobalt-loaded silica samples was also conducted and the curves are shown in Figure 4.6 for comparison between the pure unloaded amorphous silica and the sample with 10% cobalt loading. The $Co/SiO_2$ graph exhibits peaks at 2θ values of 31.14°, 36.76°, 44.8°, 59.3° and 65.25° on top of the hump at 22° which shows the existence of the amorphous silica in the sample which indicates the existence of the $Co_3O_4$ phase after calcination (Khodakov et al., 1997; Riva et al., 2000; Jozwiak et al., 2004).

Figure 4.7 shows the comparisons of the XRD graphs of samples 1 and 7, from which it was observed that there were no significant differences between the existing peaks when the water molar ratio was varied during the synthesis of the supports of the samples. The same peaks as those observed on 1-$Co/SiO_2$ can be seen, also indicating the presence of the $Co_3O_4$ phase in the samples that have been calcined.

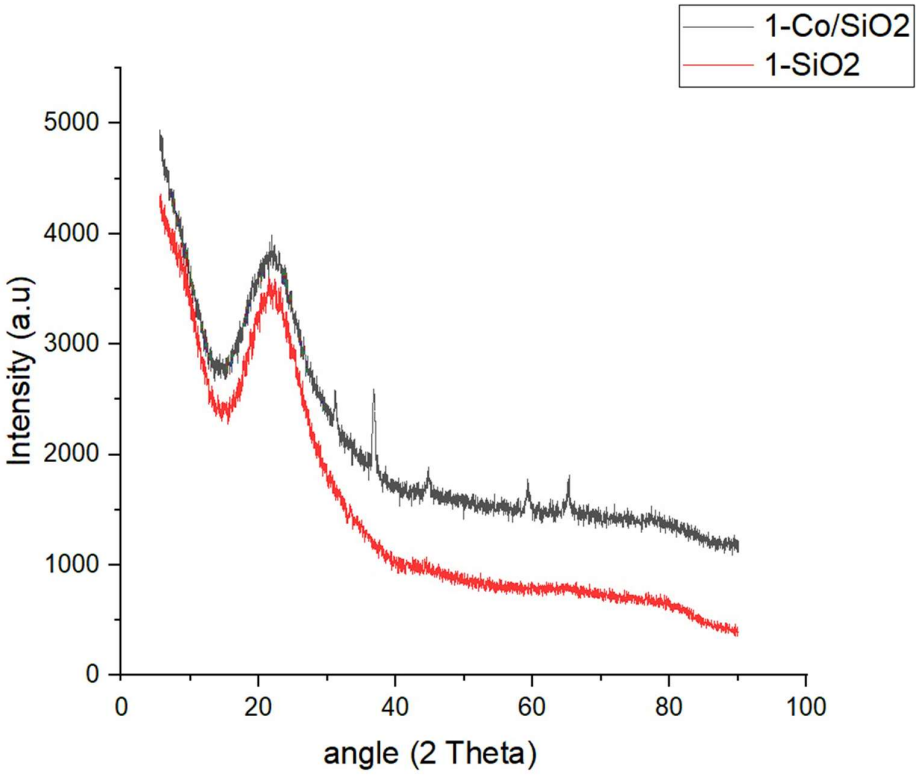



*Figure 4.29. Comparison of the XRD graphs of the support and the cobalt-loaded silica*

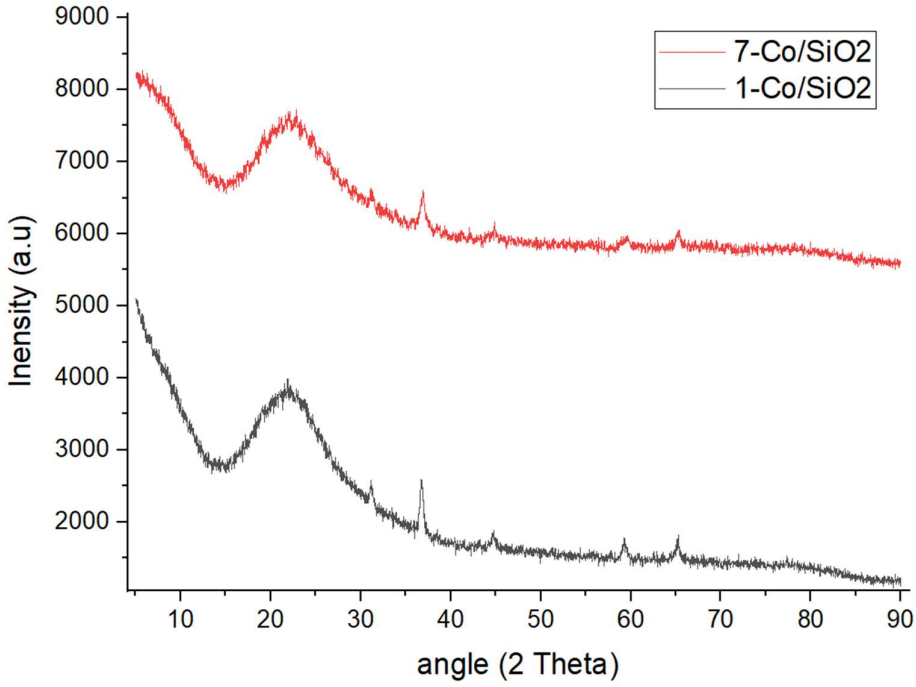



*Figure 4.30. Comparison of the XRD graphs of the catalysts from synthesis runs 1 and 7*

### 4.2.4 SEM and TEM

SEM analysis was used to analyze the dispersion, particle size, and surface morphology of the silica samples. Regarding the various synthesis conditions, all samples displayed a spherical shape with differing levels of monodispersity and particle size. Figures 4.8 to 4.17 show the SEM analysis images of the silica samples, with Figure 4.8 to 4.14 showing samples obtained from varying the water content during synthesis and Figures 4.15 to 4.17 showing samples synthesised by varying $NH_4OH$. All of the samples were imaged in the range of 10 – 11K magnification, 1µm, using Secondary Electron Signal Imaging (SESI signal) and an Electron High Tension (EHT) of 10- 15 kV to accelerate the electrons.

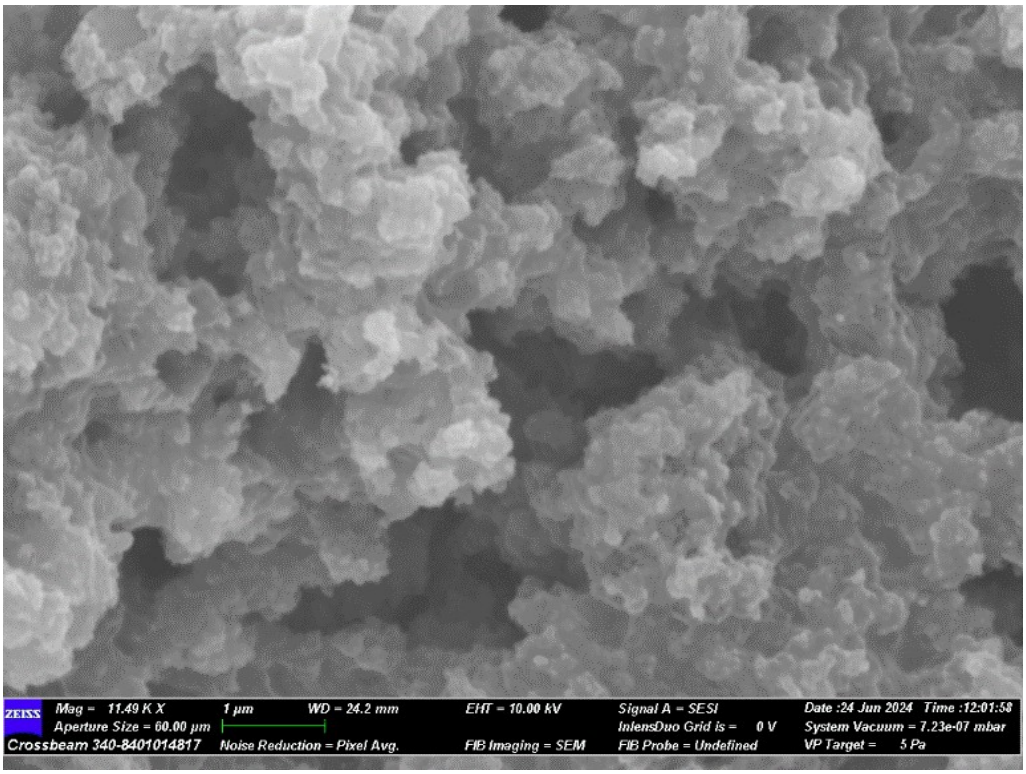



*Figure 4.31. SEM image of the silica sample S1 (TEOS : H2O - 1:1)*

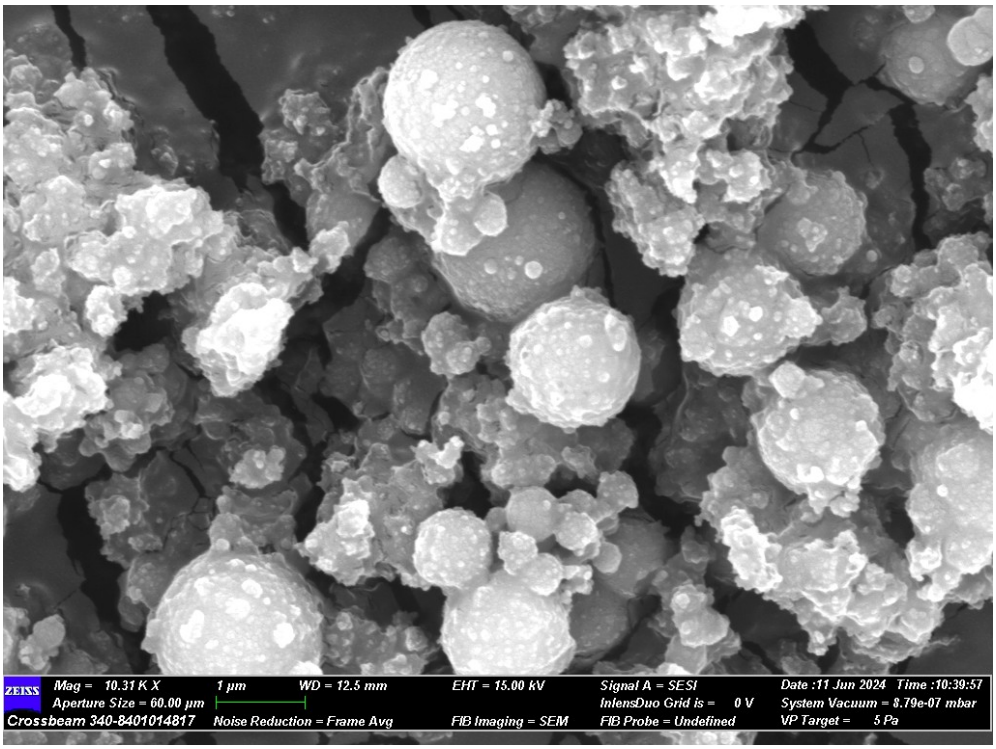



*Figure 4.32. SEM image of the silica sample S2. (TEOS: $H_2O$ - 1:1.5)*

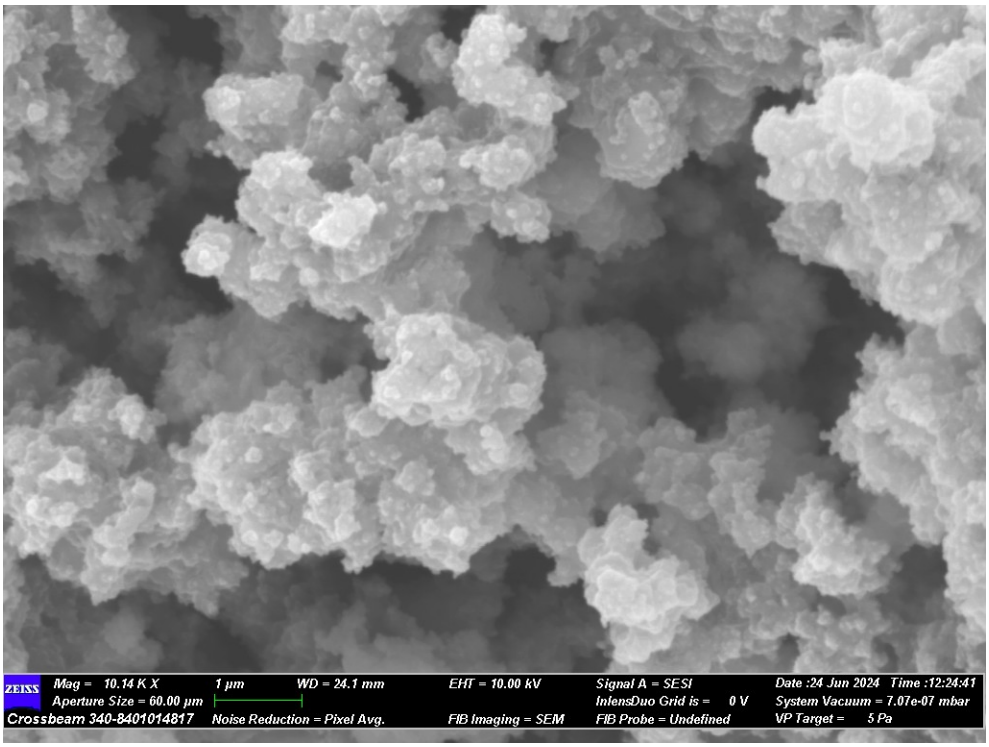



*Figure 4.33. SEM image of the silica sample S3. (TEOS:$H_2O$ - 1:2))*

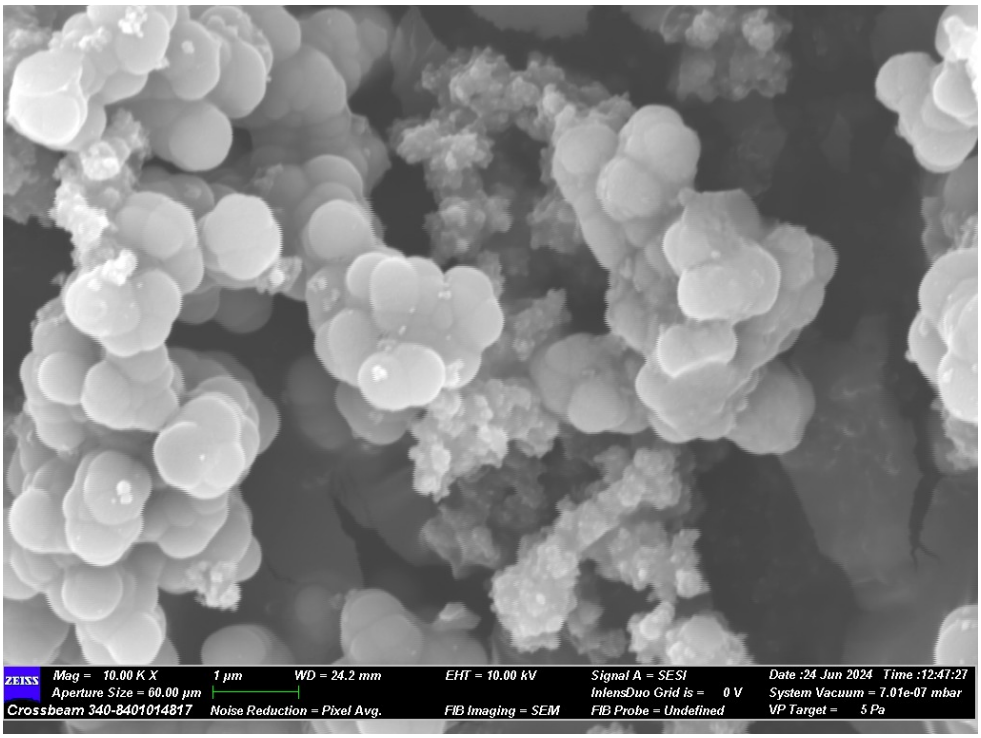



*Figure 4.34. SEM image of the silica sample S4.(TEOS: $H_2O$ - 1:2.5)*

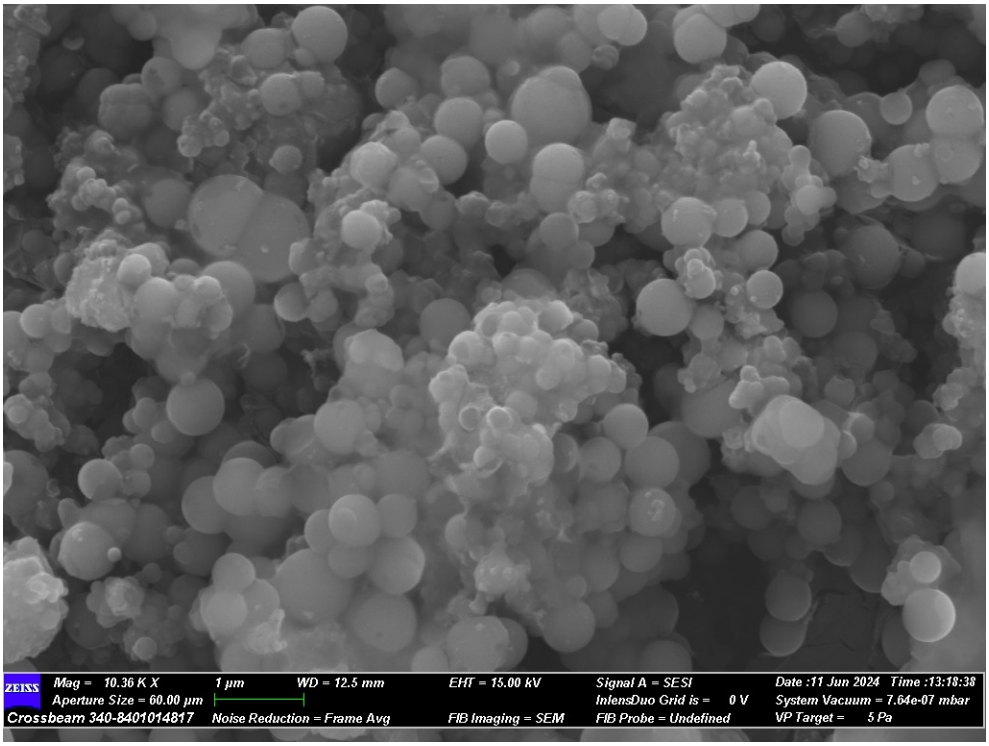



*Figure 4.35. SEM image of the silica sample S5. (TEOS:$H_2O$ - 1:5)*

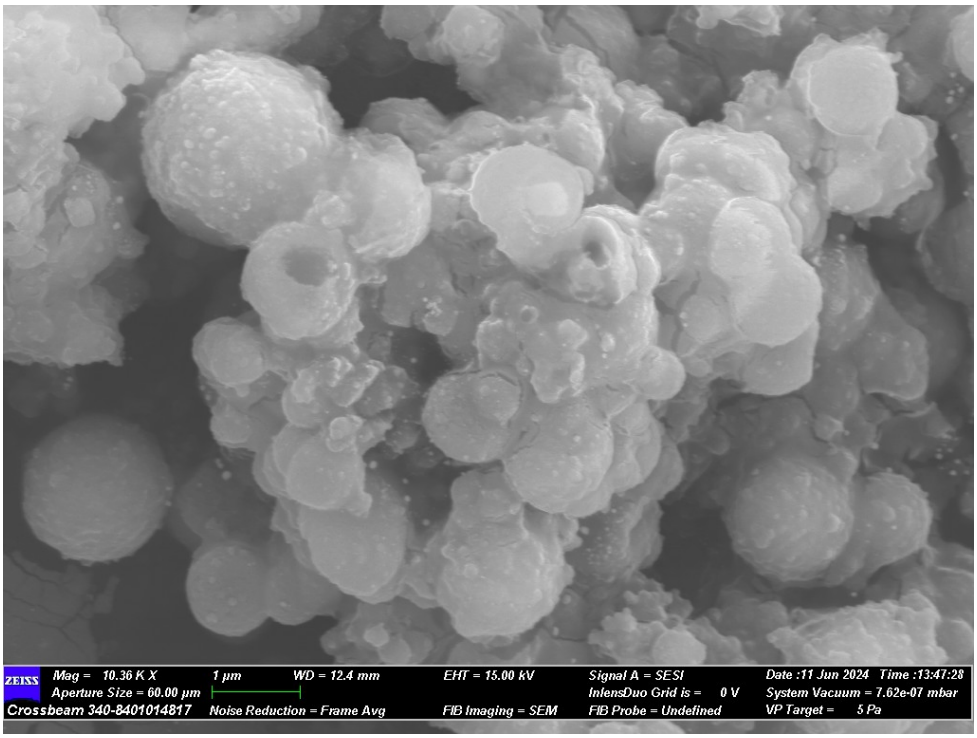



*Figure 4.36. SEM image of the silica sample S6. (TEOS: $H_2O$ - 1:10)*

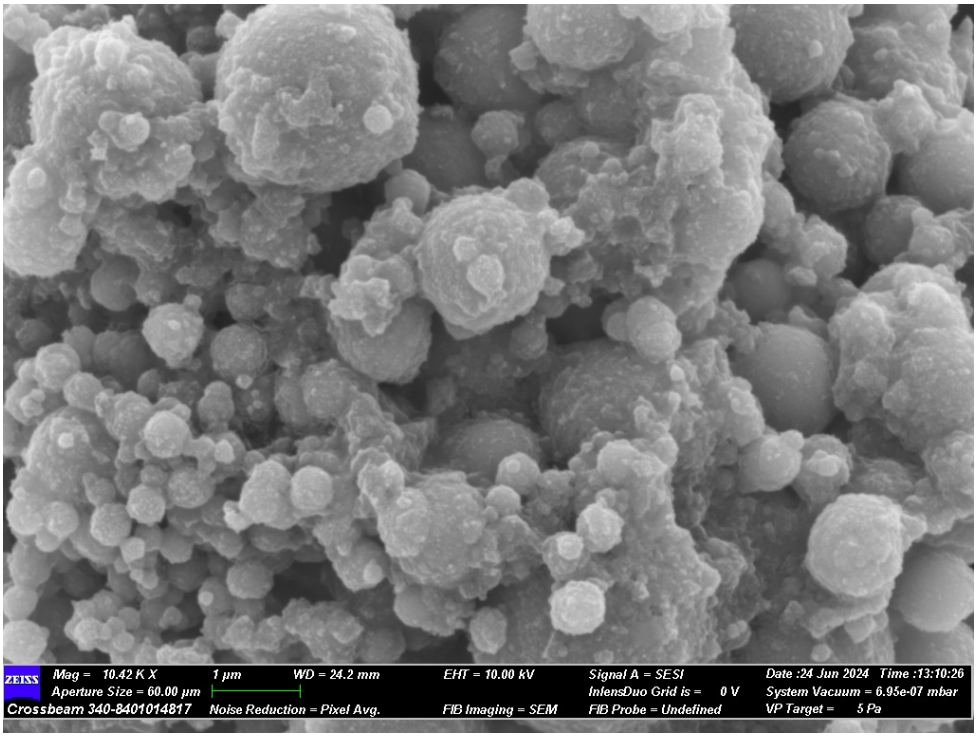



*Figure 4.37. SEM image of the silica sample S7. (TEOS:$H_2O$ - 1:12)*

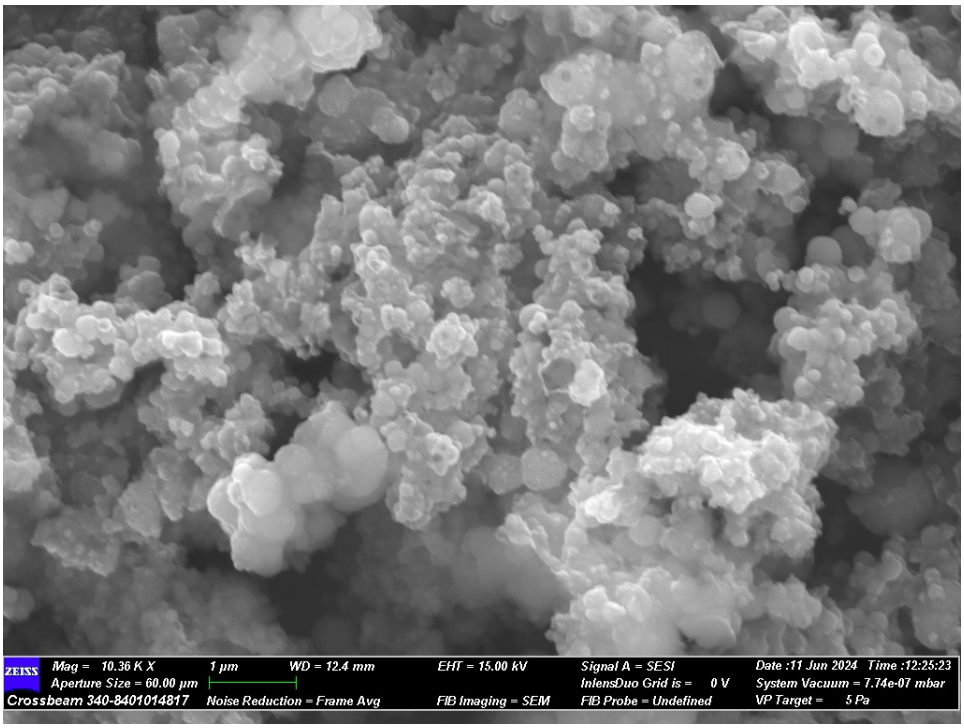



*Figure 4.38. SEM image of the silica sample S8. (TEOS:$NH_4OH$ - 1:7)*

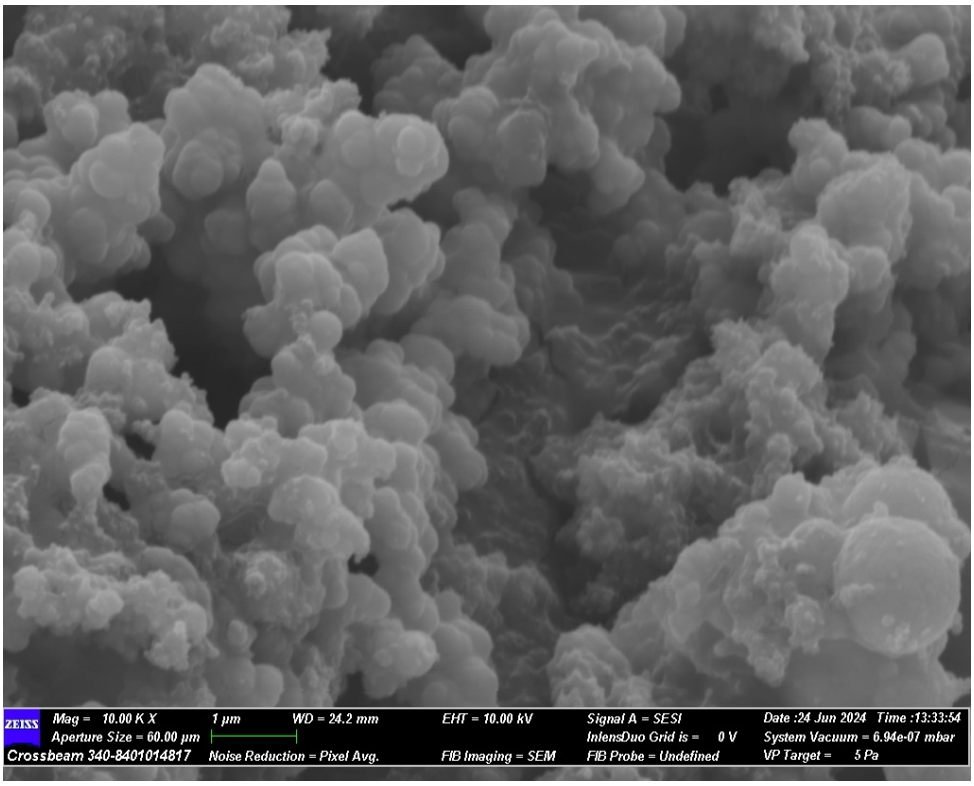



*Figure 4.39. SEM image of the silica sample S9. (TEOS:$NH_4OH$ - 1: 2.5)*

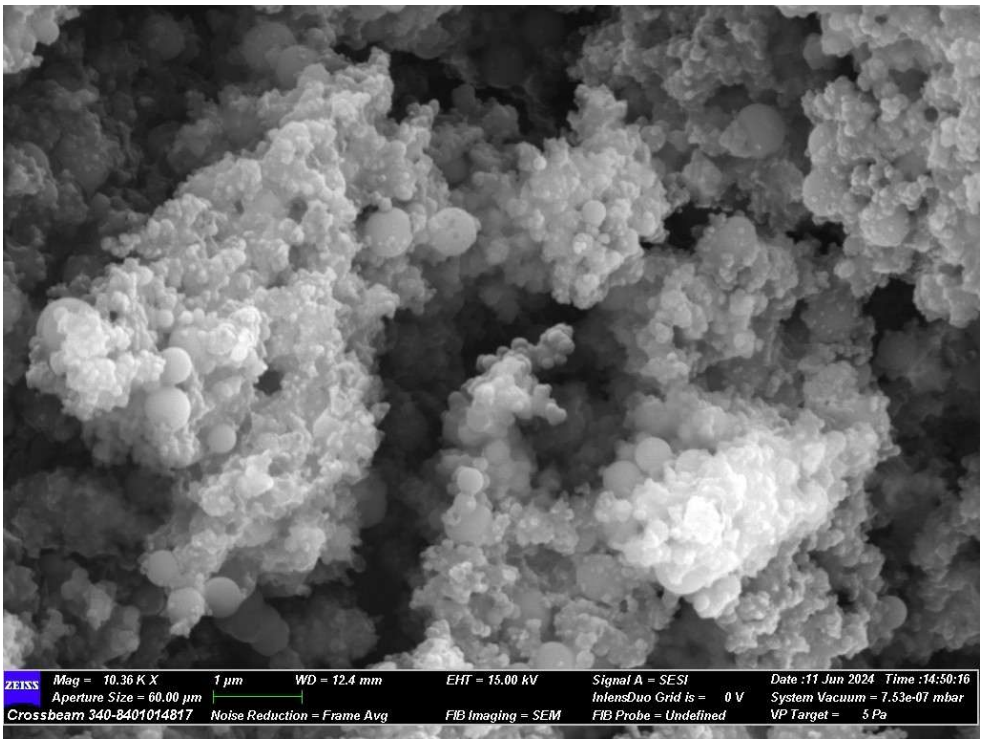



*Figure 4.40. SEM image of the silica sample S10. (TEOS:$NH_4OH$ - 1:5)*

From the SEM images, it was observed that samples S1 to S3 did not have well-defined spherical shaped particles while samples S4 to S7 produced more defined spheres. In terms of particle size, generally, the samples S1 to S3 which were synthesised with water molar ratios of 1, 1.5 and 2 repsectively, had smaller particle sizes, however, the sizes became much bigger in the middle range samples from sample S4 to S6 before they dropped again on sample S7 upon further addition of water during the synthesis. On samples S8 to S10, a general decrease in the particle sizes could be observed upon increasing the $NH_4OH$ molar ratio from 2.5 to 5, and to 7 during the silica synthesis.

In general, a higher water content accelerates the rate of hydration of the TEOS, which results in the creation of additional silanol groups. The presence of more silanol groups in the reaction vessel also accelerates the condensation reaction, which happens according to equation 4.1 below:

$$Si\text{-}OH + Si\text{-}OH \rightarrow Si\text{-}O\text{-}Si + H_2O \quad \text{.....eqn (4.1)}$$

Which reaction results in the formation of silica particles?

A further increase in the water content raises the nucleation rate, which typically results in the creation of many nuclei. These numerous nuclei will then compete strongly for the available silica species, leading to a decrease in the resulting particle sizes due to the limitation in the time for the particles to grow (Bogush, Tracy and Zukoski IV, 1988). This explains the observed increase and later decrease in the particle sizes of samples S1 to S7 as the water molar ratio increased.

The variation in the pore diameters of the silica species is also significantly influenced by this change in particle size. Larger pore diameters may result from a less dense and more open silica network caused by the faster rates of hydrolysis and condensation at higher water contents. Conversely, smaller pore sizes are usually realized as a result of a lower water content, a denser silica network with fewer and smaller pores mostly results from slower reaction rates, although too much water has also been found to cause a dip in the average pore sizes as explained in section 4.2.3 above (Stöber, Fink and Bohn, 1968; Bogush, Tracy and Zukoski IV, 1988; Brinker and Scherer, 1990).

Energy-Dispersive X-Ray Spectroscopy **(**EDS) analysis was done on the synthesized silica samples to determine the amounts of the elements found in selected samples 4 and 7, where three runs per sample were made to determine the range of the compositions of oxygen and silica. Tables 4.3 (a) to (f) shows the breakdown of the EDS elemental analysis done on the two samples. Sample 4 had an average of 63.2 % O; 36.7 % by mass Si and a trace amount of Al which constituted 0.12 % while sample 7 had an average of 65.7 % O; 34.2 % by mass Si and 0.08 % trace amounts of Al in the samples. No plausible explanation for the presence of the trace amount of Al has been found, but it is suggested that this may be due to the presence of Al in the water, in spite of de-ionized water being used throughout the experiments.

*Table 4.3. EDS Elemental analysis of the prepared silica samples*

a) Sample S4-1

| Formula | mass % | Atom % | Sigma | K ratio Line |
|---|---|---|---|---|
| O | 62.0 | 74.1 | 0.18 | 0.0408762 K |
| Al* | 0.14 | 0.10 | 0.08 | 0.0003020 K |
| Si | 37.8 | 25.8 | 0.19 | 0.0339120 K |

| | | | | |
|---|---|---|---|---|
| Total | 100 | 100 | | |

b) Sample S4-2

| Formula | mass % | Atom % | Sigma | K ratio Line |
|---|---|---|---|---|
| O | 61.8 | 74.0 | 0.18 | 0.0371712 K |
| Al* | 0.13 | 0.09 | 0.07 | 0.0002379 K |
| Si | 38.1 | 26.0 | 0.18 | 0.0312352 K |
| Total | 100 | 100 | | |

c) Sample S4-3

| Formula | mass % | Atom % | Sigma | K ratio Line |
|---|---|---|---|---|
| O | 65.83 | 77.05 | 0.18 | 0.0405824 K |
| Al* | 0.08 | 0.14 | 0.07 | 0.0003109 K |
| Si | 34.09 | 22.81 | 0.18 | 0.0265504 K |
| Total | 100.00 | 100.00 | | |

d) Sample S7-1

| Formula | mass % | Atom % | Sigma | K ratio Line |
|---|---|---|---|---|
| O | 65.88 | 77.18 | 0.19 | 0.0371153 K |
| Al* | 0.09 | 0.01 | 0.09 | 0.0005658 K |
| Si | 34.03 | 22.81 | 0.19 | 0.0243778 K |
| Total | 100.00 | 100.00 | | |

e) Sample S7-2

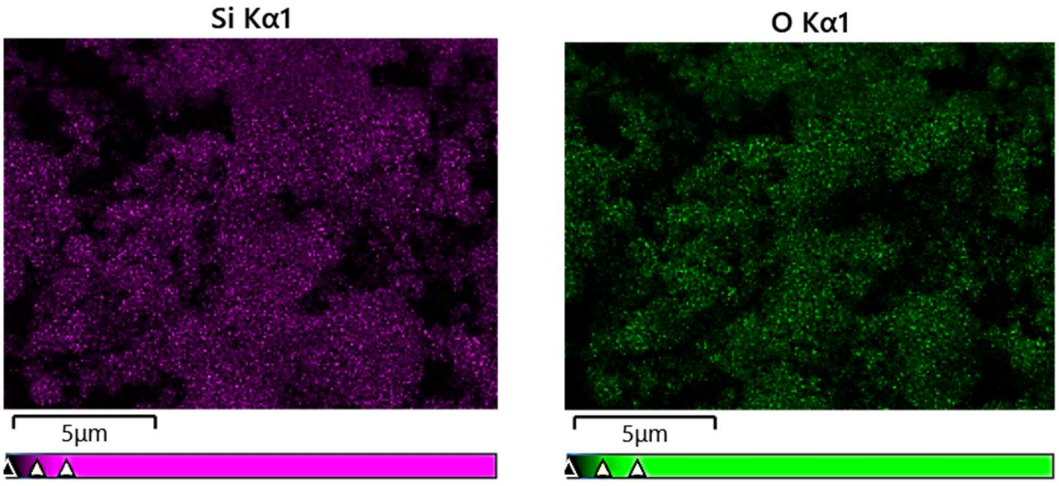
| Formula | mass % | Atom % | Sigma | K ratio Line |
|---|---|---|---|---|
| O | 64.86 | 76.32 | 0.21 | 0.0390776 K |
| Al* | 0.08 | 0.02 | 0.10 | 0.0008224 K |
| Si | 35.06 | 23.66 | 0.21 | 0.0275846 K |
| Total | 100.00 | 100.00 | | |

f) Sample S7-3

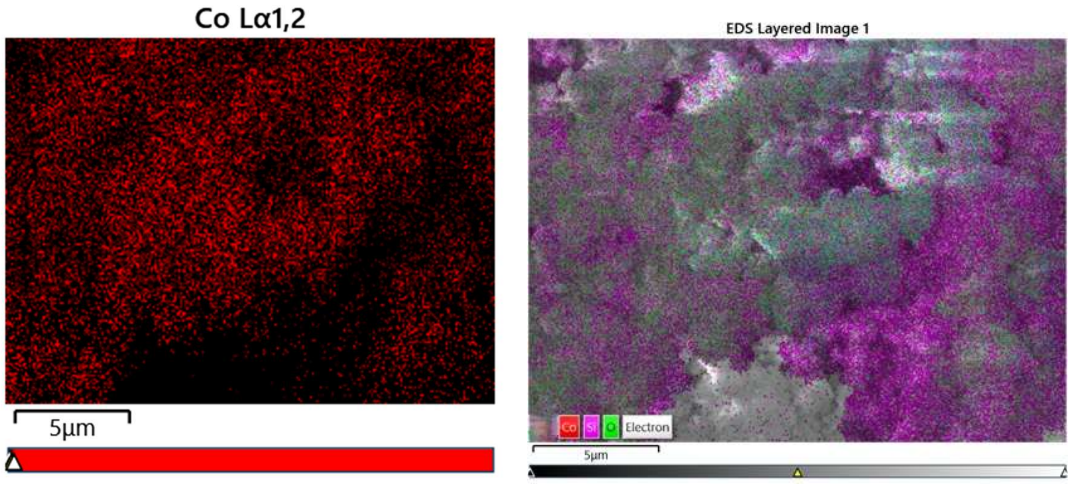
| Formula | mass % | Atom % | Sigma | K ratio Line |
|---|---|---|---|---|
| O | 66.37 | 77.55 | 0.18 | 0.0392930 K |
| Al* | 0.05 | 0.03 | 0.09 | 0.0003365 K |
| Si | 33.58 | 22.42 | 0.18 | 0.0248950 K |
| Total | 100.00 | 100.00 | | |

**EDS Mapping of the prepared catalysts**

The cobalt-loaded $Co/SiO_2$ samples were taken for EDS elemental composition mapping to determine vital information about the loading uniformity, dispersion and localization of the cobalt species on the surface of the silica support. EDS mapping is a potent analytical method that is used in combination with SEM to ascertain the elemental distribution within a sample. Figure 4.18 shows the elemental layers obtained from $Co/SiO_2$ sample 2 (CS-2), and by looking at Figure 4.18(c) it can be seen that there was monodispersion in the loading of cobalt in the sample when wet impregnation was implemented. The same is observed with sample CS-9

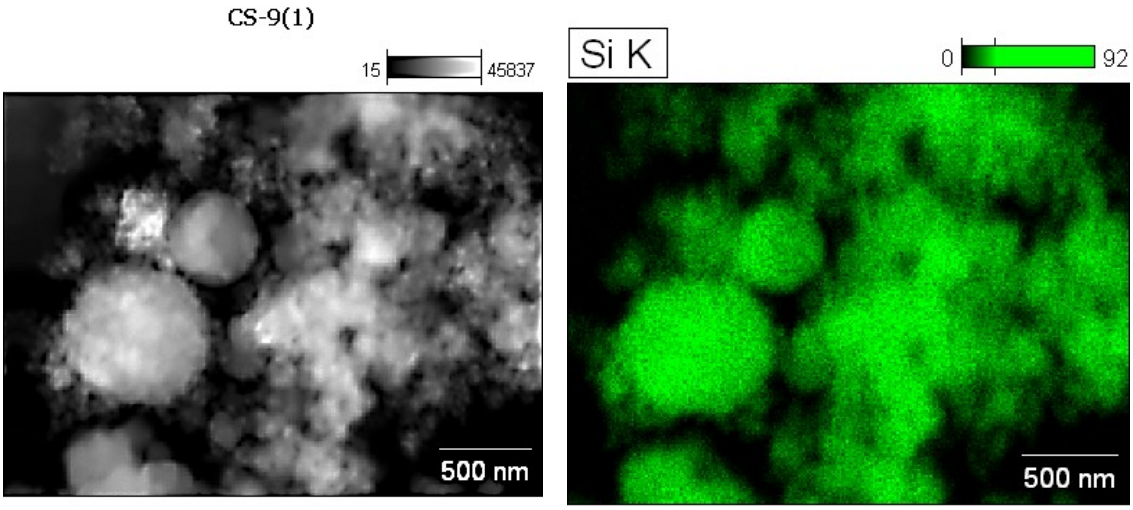



a) b)

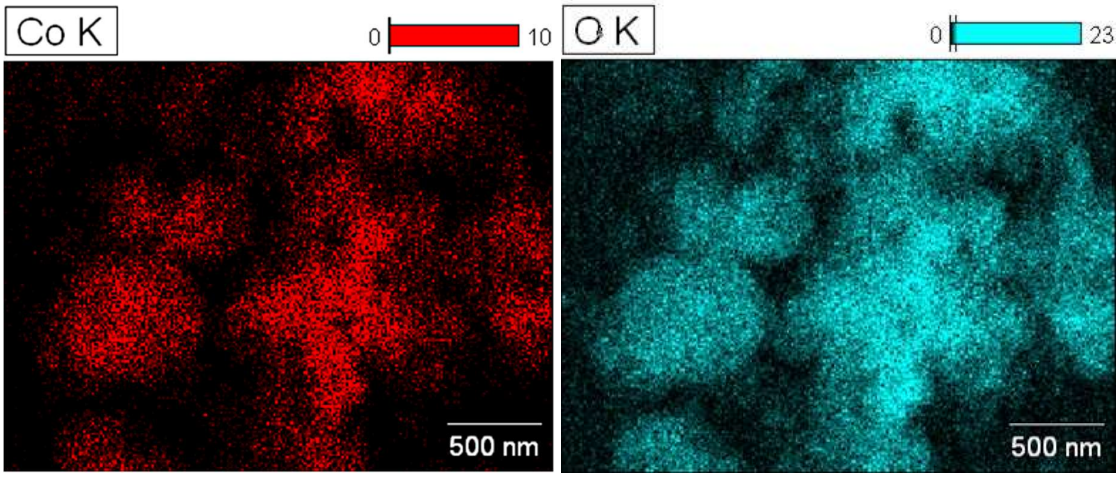



c) d)

*Figure 4.41. EDS Mapping for Co/ $SiO_2$ sample 2*




a) b)




c) d)

*Figure 4.42. EDS elemental mapping for sample CS-9*

The conditions that were used to carry out the EDS analysis for this sample are listed in Table 4.4. Figure 4.19 (a) shows the SEM image that was used to generate the elemental layers. From Figure 4.19 (c) a uniform coverage with the cobalt layer can be clearly seen showing that the cobalt metal could not clog or cluster in some parts, as no intense clustering was observed. This shows that there was a uniform dispersion in both catalytic samples.

Table 4.4. The analysis conditions used in the EDS mapping to determine the elemental layers for sample CS-9

| | |
|---|---|
| Data Type: | Counts |
| Image Resolution: | 512 by 384 |
| Image Pixel Size: | 0.01 µm |
| Map Resolution: | 256 by 192 |
| Map Pixel Size: | 0.01 µm |
| Acc. Voltage: | 200.0 kV |
| Magnification | 40000 |

### 4.2.5 Physisorption analysis

The pore diameter, pore volume, and BET surface area data for the supports and the cobalt-loaded supports were compiled as shown in Table 4.5 for the two calcination conditions. The pore size distributions were obtained using the Barrett-Joyner-Halenda (BJH) method and the surface areas and pore volume were determined using the BET technique. It can be seen that varying the ratios of water/TEOS/ $NH_4OH$/ethanol resulted in changes in the catalyst pore diameters, surface areas and pore volumes. The synthesis method yielded relatively low surface areas in the range 17.518 - 152.266 $m^2/g$ as compared to other silica supports, such as MCM-3, KIT-6 and SBA-15, which can go as high as 1500 $m^2/g$ (Beck et al., 1992; Zhao, Feng, et al., 1998, 1998; Kleitz, Choi and Ryoo, 2003). Table 4.5 shows the results for the textural characteristics of the produced catalysts and supports.

Table 4.5. Physisorption analysis results for the cobalt silica catalysts and the synthesized silica supports

| Sample | BJH Pore Diameter (nm) | BJH Pore Volume ($cm^3/g$) | BET Surface Area ($m^2/g$) | Average particle size (nm) |
|---|---|---|---|---|
| 1-Co/$SiO_2$ | 14.985 | 0.241 | 117.179 | 51.204 |
| 2-Co/$SiO_2$ | 18.311 | 0.139 | 50.007 | 119.983 |
| 3-Co/$SiO_2$ | 20.548 | 0.075 | 24.073 | 249.248 |
| 4-Co/$SiO_2$ | 25.754 | 0.066 | 18.967 | 316.337 |
| 5-Co/$SiO_2$ | 22.179 | 0.057 | 19.355 | 309.900 |
| 6-Co/$SiO_2$ | 19.604 | 0.588 | 121.025 | 54.042 |
| 7-Co/$SiO_2$ | 10.202 | 0.426 | 152.266 | 39.405 |
| 8-Co/$SiO_2$ | 28.543 | 0.133 | 25.585 | 234.515 |
| 9-Co/$SiO_2$ | 30.147 | 0.156 | 31.730 | 189.095 |
| 10-Co/$SiO_2$ | 28.908 | 0.087 | 17.975 | 333.789 |
| | | | | |
| 1-$SiO_2$ | 13.921 | 0.233 | 128.979 | 46.519 |
| 2-$SiO_2$ | 14.119 | 0.128 | 56.729 | 105.767 |
| 3-$SiO_2$ | 19.079 | 0.066 | 23.041 | 260.401 |
| 4-$SiO_2$ | 25.006 | 0.054 | 16.549 | 362.564 |
| 5-$SiO_2$ | 21.785 | 0.049 | 23.284 | 257.690 |
| 6-$SiO_2$ | 19.976 | 0.614 | 125.268 | 47.897 |
| 7-$SiO_2$ | 10.944 | 0.443 | 151.066 | 39.718 |
| 8-$SiO_2$ | 28.345 | 0.076 | 18.809 | 28.345 |
| 9-$SiO_2$ | 25.612 | 0.123 | 32.807 | 182.888 |
| 10-$SiO_2$ | 25.846 | 0.070 | 17.518 | 342.514 |

It can also be seen that the pore volumes and pore diameters of the catalysts generally increased with increasing surface area making the catalysts with larger pore diameters more

suitable for obtaining higher selectivities in FT synthesis. The addition of cobalt metal onto the support led to a minor increase in the pore diameters and volumes of the support. Generally, the addition of the cobalt metal is expected to result in lower pore volumes and surface areas when the pores become blocked. This unexpected result can be explained as follows:

- The silica support may develop interparticle mesoporosity as a result of the incorporation of cobalt atoms. This may happen because cobalt species affect how silica particles aggregate during synthesis. The material's ability for catalytic applications can be improved by this interparticle porosity, which helps to increase the overall pore volume and size (Popova et al., 2014).
- Co atoms may replace some Si atoms when the cobalt metal is loaded onto the silica matrix, forming some Si–O–Co bonds. Because the cobalt ion has a larger ionic radius than silicon, this rearrangement may result in an increase in pore size and pore volumes (Al-Obaidi et al., 2021).
- The cobalt-silica system may also undergo some structural reorganization as a result of calcination. Larger cobalt oxide clusters and new mesoporous structures may arise as a result of this reorganization, which would further increase the sizes and volumes of the pores (Khodakov et al., 2001).

It has also been found that the cobalt loading percentage determines how it will influence the pore sizes and pore volumes with very low loading percentages and very high percentages having different impacts. Pore sizes remain open at very low cobalt loadings while excessive loadings lead to pore blockage and diffusion limitations (Koirala et al., 2018). A 10% loading falls in the middle of the range, which makes the availability of the active sites maximum (Venezia *et al.*, 2012). Nitrogen adsorption-desorption isotherms from the BET analysis for the catalysts calcined at 400°C are shown in Figure 4.20 and Figure 4.21. The results showed the formation of type IV isotherms, indicating that the catalysts were mesoporous with a relatively uniform pore size distribution. The isotherms show an H2-type hysteresis loop at a relative pressure of around 0.8; based on the categorisation provided by (Cychosz and Thommes, 2018) this shows that some capillary condensation is taking place at higher relative pressures within the mesopores. From the shape of the nitrogen adsorption-desorption isotherms, which is generally H2-type hysteresis, it can be deduced that the mesopores have an ink-bottle shape (Yang *et al.*, 2022). The hysteresis types and the corresponding pore shapes are shown in Figure 4.22.

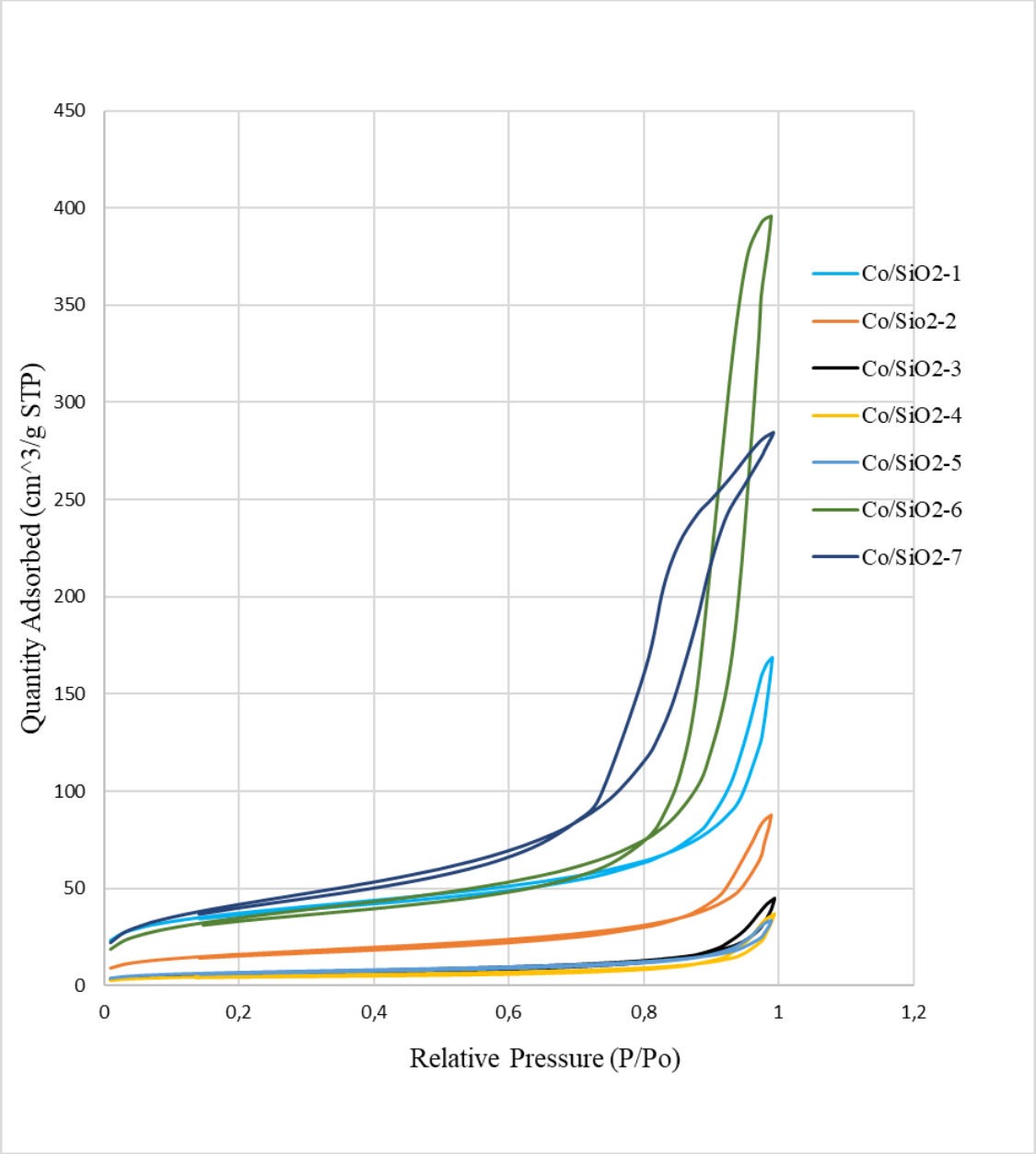



*Figure 4.43. Nitrogen adsorption-desorption isotherms for the catalysts synthesized with varying water content*

From the graphs, it can be seen that the samples produced from runs 1, 2, 3, 4, and 5 had relatively lower areas inside the hysteresis loop, while there is an increase in the area for the samples from runs 6 and 7 and a big decrease from runs 8 to10, as shown in the relatively smaller areas shown in Figure 4.21. This can be explained by the complexity and uniformity of the pore structures of the samples.

Complex pore configurations, including ink-bottle-shaped pores or interconnected mesoporous networks, are frequently indicated by a greater hysteresis loop area in $Co/SiO_2$ BET isotherms. Because of pore blocking effects, which occur when narrower pore necks prevent the release of adsorbed nitrogen gas during desorption, these structures may cause delayed desorption. Materials displaying pore blocking and percolation effects are linked to this phenomenon, which produces a noticeable hysteresis loop, usually of the H2-type (Thommes et al., 2015). Furthermore, capillary condensation within mesopores may be the cause of increased hysteresis regions. The observed hysteresis is caused by nitrogen condensing in these holes when relative pressure rises and the delayed evaporation of the condensed nitrogen upon desorption (Thommes and Cychosz, 2014).

Conversely, the smaller hysteresis loops such as those from runs 1-5 and 8-10, indicate that the structures are more homogeneous with interconnected mesopores; this structure therefore enables easy desorption of the nitrogen gas during the BET analysis. Sing et al. (1985) suggested that the materials that show these smaller hysteresis loops are often associated with H1-type loops, which is a sign of cylindrical-shaped pore structures with narrow size distributions and minimum pore blockage from the diagram in Figure 4.22.

In some $Co/SiO_2$ systems with lower cobalt loadings, the cobalt species will be evenly distributed throughout the silica matrix; this may lead to reduced areas of the hysteresis zones while the homogeneity of the pore structure is maintained. The decrease in hysteresis loop area reflects the more reversible adsorption–desorption processes made possible by the existence of this homogeneity (Kruk, Jaroniec and Sayari, 1997).

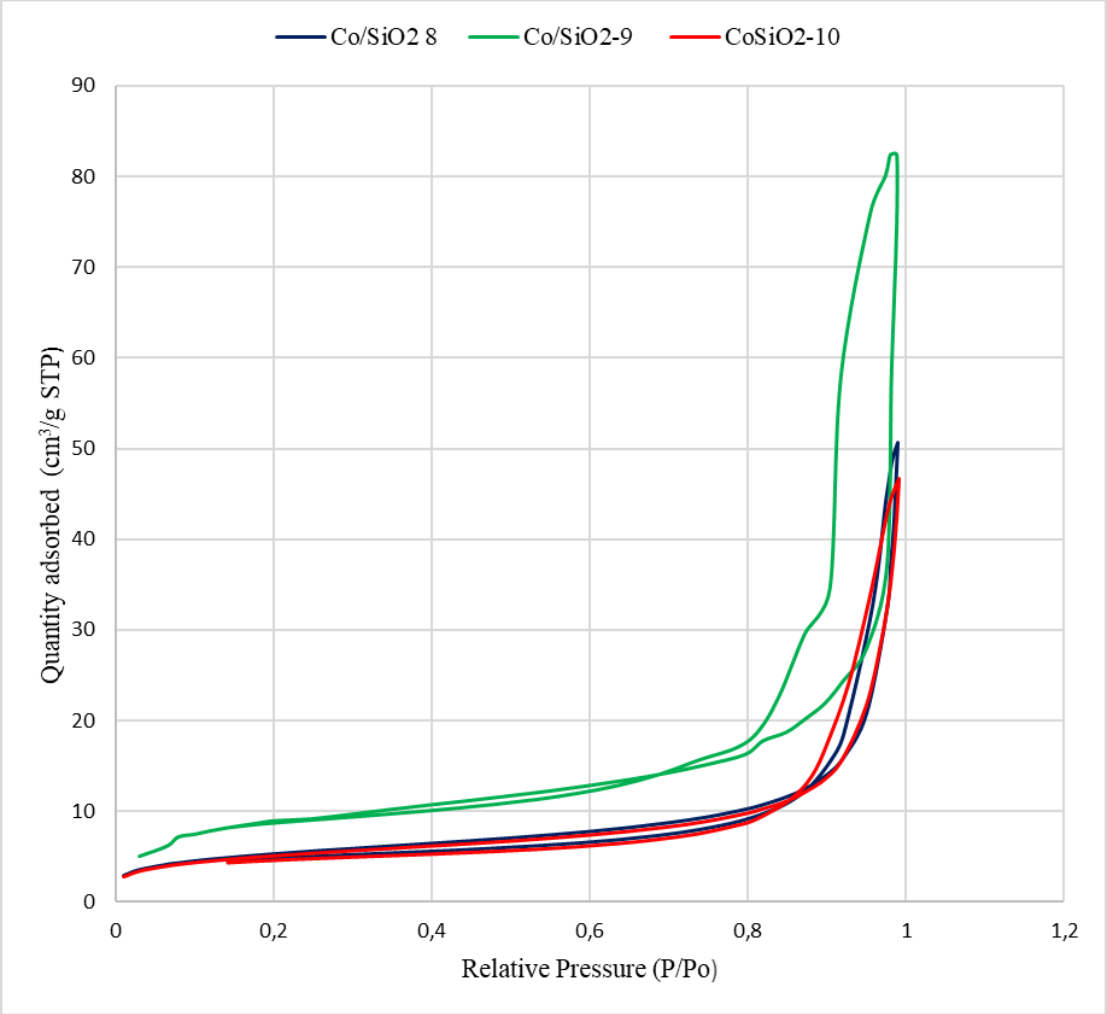



*Figure 4.44. Nitrogen adsorption-desorption isotherms for the catalysts synthesized with varying $NH_4OH$ concentrations*

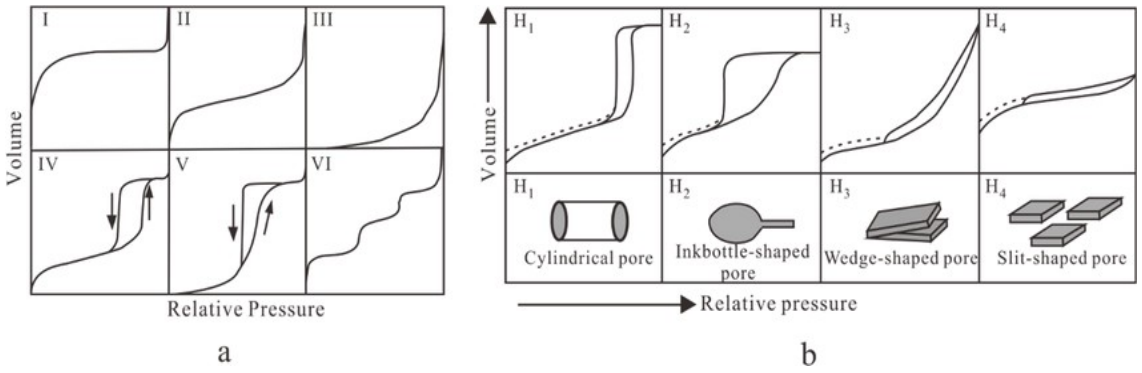



*Figure 4.45. The hysteresis loop types and the corresponding pore shape resemblance* (Xu *et al.*, 2020)*, open access CC BY.*

### 4.2.6 Effect of reagent concentration during Stöber synthesis on catalyst and support properties

The variation of the concentrations of the $H_2O$, TEOS, $NH_4OH$ and $C_2H_5OH$ was found to cause a considerable difference in the characteristics of the silica support that was synthesized using the Stöber method. Table 4.6 shows the ratios used and the corresponding catalyst physical properties obtained from the physisorption analysis results.

Table 4.6. Relationship between the water/$NH_4OH$ ratio, water/ethanol ratio and the silica support properties

| Sample | $H_2O$ : TEOS: $NH_4OH$ : EtOH | Water/Ethanol Ratio | Water/$NH_4OH$ Ratio | Pore Diameter (nm) | Surface Area ($m^2/g$) | Pore Volume ($cm^3/g$) |
|---|---|---|---|---|---|---|
| $SiO_2$-1 | 1 : 1 : 1 : 2.5 | 0.4 | 1 | 13.92 | 128.98 | 0.230 |
| $SiO_2$-2 | 1.5:1: 1 : 2.5 | 0.6 | 1.5 | 14.12 | 56.730 | 0.130 |
| $SiO_2$-3 | 2 : 1 : 1 : 2.5 | 0.8 | 2 | 19.08 | 23.040 | 0.066 |
| $SiO_2$-4 | 2.5:1: 1 : 2.5 | 1 | 2.5 | 25.00 | 16.550 | 0.054 |
| $SiO_2$-5 | 5 : 1 : 1 : 2.5 | 2 | 5 | 21.76 | 23.280 | 0.049 |
| $SiO_2$-6 | 10:1 : 1 : 2.5 | 4 | 10 | 19.96 | 125.27 | 0.610 |
| $SiO_2$-7 | 12:1 : 1 : 2.5 | 4.8 | 12 | 10.94 | 151.07 | 0.440 |
| $SiO_2$-8 | 15:1 : 7 : 2.5 | 6 | 2.14 | 28.34 | 18.810 | 0.076 |
| $SiO_2$-10 | 15:1 : 5 : 2.5 | 6 | 3 | 25.85 | 17.520 | 0.070 |
| SiO2-9 | 15:1 : 2.5: 2.5 | 6 | 6 | 25.61 | 32.810 | 0.120 |

A general representation of the trends in the water/ethanol ratio and water/ ammonium hydroxide ratios with the resulting silica support pore sizes across all of the 10 synthesized samples is shown in Figure 4.23 and 4.24. From the graphs in Figure 4.23 it can be clearly observed that there was an effect of the value of water/ethanol ratio and the water/$NH_4OH$ ratio on the resulting pore sizes of the silica samples. There is a general increase in the pore sizes from sample 1 to sample 4 at which a peak is observed, then a decrease thereafter from sample 4 to the sample corresponding to run 7 as the water/ethanol and the water/$NH_4OH$ ratio is increasing. From samples 8-10, the amount of $NH_4OH$ in the samples was varied while all the other reagents were kept constant, and the resulting trend is shown in Figure 4.24.

The variation of the surface area under the same conditions across the 10 silica samples is shown in Figure 4.25 and 4.26. In Figure 4.25 the graphs generally show an opposite trend to that of the distribution of the pore sizes shown in Figure 4.23, as the water content was being

increased, keeping all of the other reagent concentrations constant for samples 1-7. Figure 4.26 shows the results of the surface areas obtained when varying the $NH_4OH$ concentrations, keeping the other ratios constant. A more detailed explanation is provided in the following paragraphs using a proportional horizontal axis to explain the trends.

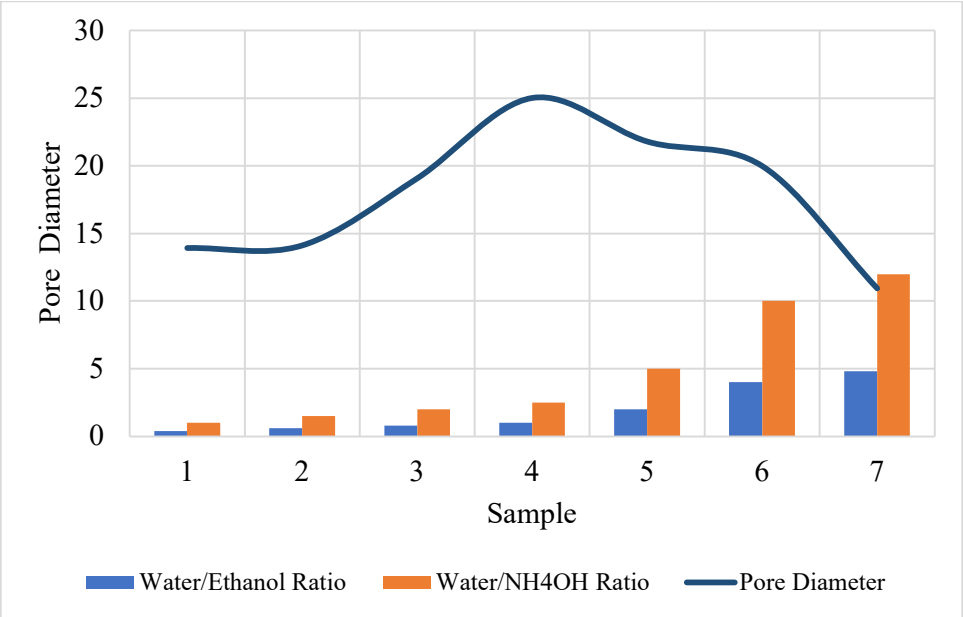



*Figure 4.46. Relationship between pore diameter, water/ethanol ratio and water/$NH_4OH$ ratio during the synthesis of the catalyst supports with varying water concentration while keeping other reagent concentrations constant.*

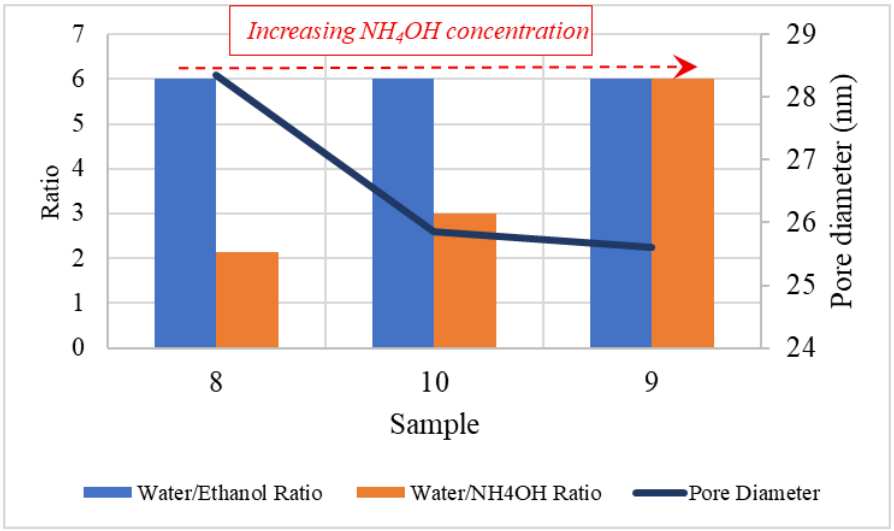



*Figure 4.47. Relationship between the pore diameter, water/ethanol ratio, and water/$NH_4OH$ ratio during the synthesis of the catalyst supports with varying $NH_4OH$ concentration, keeping the rest of the reagents constant*

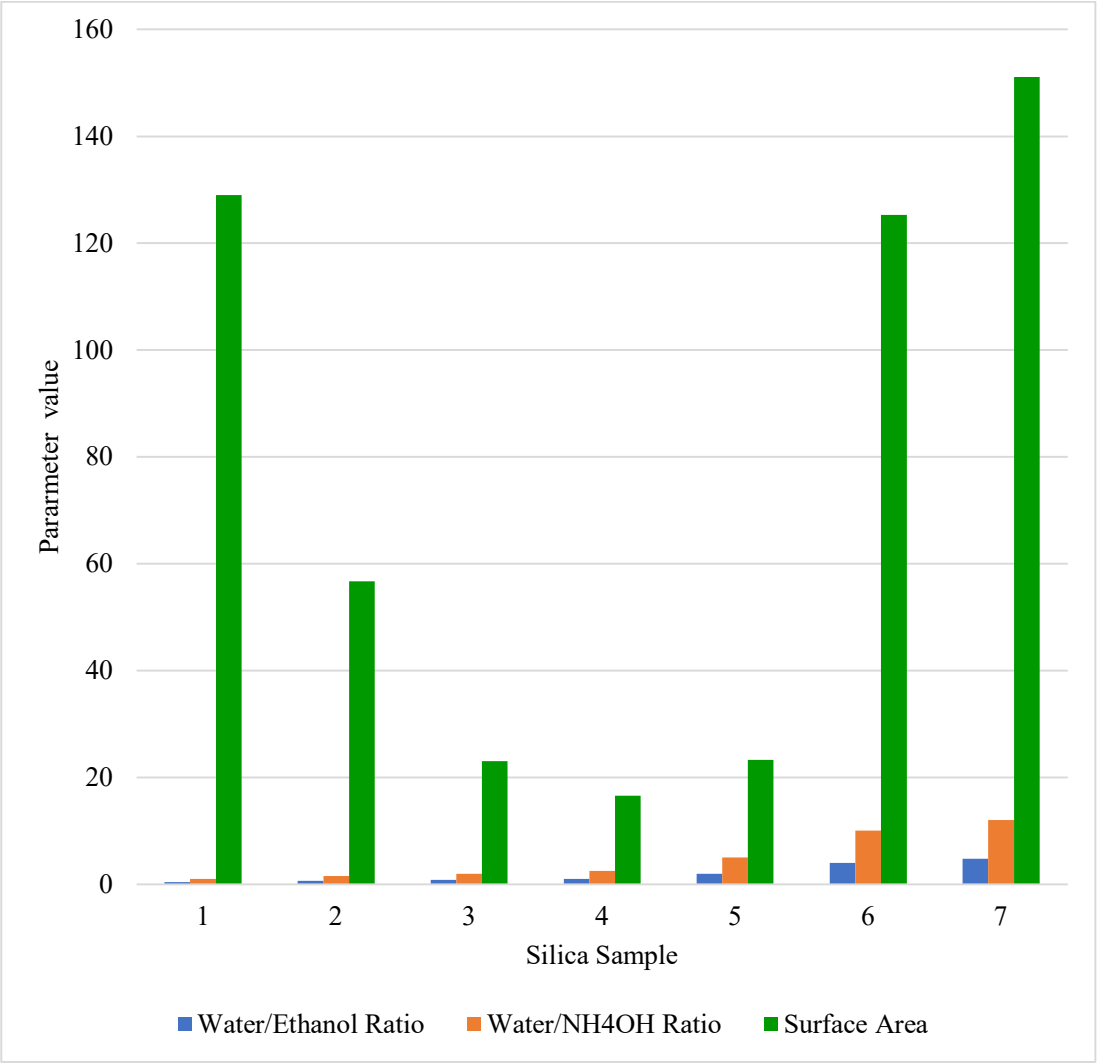



*Figure 4.48. Relationship between the surface area, water/ethanol ratio, water/$NH_4OH$ ratio during silica synthesis with varying water concentration while keeping other reagent concentrations constant*

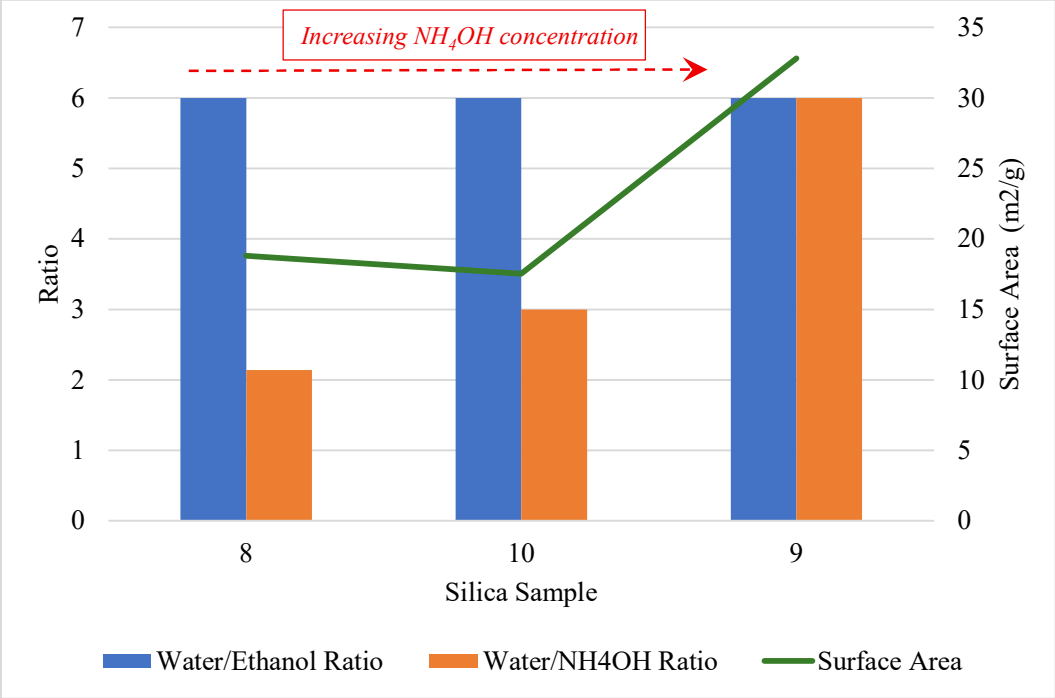



*Figure 4.49. Relationship between the surface area, water/ethanol ratio, and water/NH4OH ratio with varying $NH_4OH$ concentration while maintaining the concentrations of the other reagents constant*

Separating the samples into two groups to analyse the variation of pore diameter, surface area and pore volume with water and $NH_4OH$ throughout the experiments, Tables 4.7 and 4.8 were formulated, showing the actual ratios of the water and $NH_4OH$ implemented in the experiments. For samples 1-7, the amount of water was being increased, keeping the other three constant, the data is shown in Table 4.7. For samples 8, 9, and 10, the amount of $NH_4OH$, which acted as a catalyst, was being varied, keeping the ratios of the other reagents constant, and the data is displayed in Table 4.8.

**Effects of water content on the pore structure and surface area**

The effects of varying the ratio of water in the mixture were investigated from the data provided in Table 4.7, from which graphs were plotted on a proportional horizontal axis representing the molar ratio of the water that was used.

Table 4.7 Variation of water molar ratio across the first seven runs and the respective silica properties

| Run | $H_2O$ molar ratio | TEOS molar ratio | $NH_4OH$ molar ratio | $C_2H_5OH$ molar ratio | Pore Diameter (nm) | Surface Area ($m^2/g$) | Pore Volume ($cm^3/g$) |
|---|---|---|---|---|---|---|---|
| 1 | 1 | 1 | 1 | 2.5 | 13.92 | 128.98 | 0.230 |
| 2 | 1.5 | 1 | 1 | 2.5 | 14.12 | 56.730 | 0.130 |
| 3 | 2 | 1 | 1 | 2.5 | 19.08 | 23.040 | 0.066 |
| 4 | 2.5 | 1 | 1 | 2.5 | 25.00 | 16.550 | 0.054 |
| 5 | 5 | 1 | 1 | 2.5 | 21.76 | 23.280 | 0.049 |
| 6 | 10 | 1 | 1 | 2.5 | 19.96 | 125.27 | 0.610 |
| 7 | 12 | 1 | 1 | 2.5 | 10.94 | 151.07 | 0.440 |

Figure 4.27 shows the variation of the pore sizes as the amount of water was increased in the sample across the first seven runs.

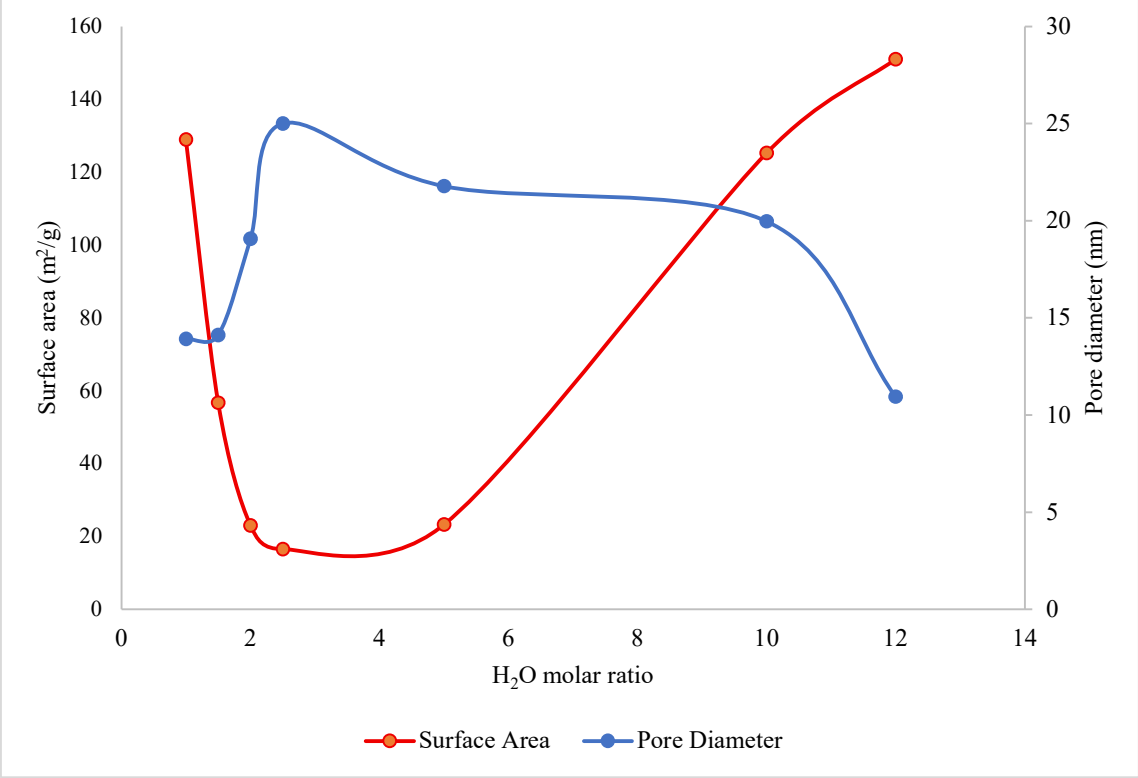



*Figure 4.50. Relationship between surface area and pore diameter with $H_2O$ molar ratio ($H_2O$:TEOS=$NH_4OH$)*

In general, there is an increase in the pore size to a maximum and then a gradual decrease as the water ratio is increased, as shown in Figure 4.27. At first, there was no considerable

change in the pore size when the water ratio was increased from 1 to 1.5, recording pore sizes of 13.9 and 14.1 nm, respectively, in the first and second runs; however, there was a significant increase from 14.1 nm to 19.1 nm when a water molar ratio of 2 was used. The graph indicates a maximum pore size at 25 nm, which appears at the fourth sample when the $H_2O$ ratio in the reagents is 2.5, and a gradual decrease was then observed when a further increase in the water content was done. The maximum pore diameter coincides with the ratio of $H_2O$: TEOS: $NH_4OH$: $C_2H_5OH$ is 2.5:1:1:2.5 after which there is a decrease to 21.8 nm when the water molar ratio is doubled and a slight decrease to 20 nm at a molar ratio of 10 which is not a significant difference from 21.8 nm since the percentage difference is less than 10% (The NOVA 800 physisorption analyzer regards a difference in pore size greater than 10% between samples to be considered as different classes). After this slight drop there was a steep decrease to a minimum pore size of 11 nm.

The hydrolysis reaction and formation of the silica framework are mainly dependent on the speed of reaction of equation 3.1 where the reaction's water to TEOS stoichiometric ratio is 4:1. The rate of hydrolysis is slow at low water: TEOS ratios because of the scarcity of water molecules to react with the TEOS. This limitation leads to the formation of fewer silanol groups that should be available for condensation, which results in denser and smaller particles with smaller pore sizes (Brinker and Scherer, 1990). This can also be confirmed by the smaller values of the average particle sizes for the first three samples, as shown in Table 4.2.

As the water ratio is increased to an intermediate range, which is close to the stoichiometric ratio, it is no longer limiting and so rapid condensation becomes possible due to an increase in the efficiency of the hydrolysis. This leads to a rise in the interparticle voids and promotes the formation of the mesoporous structure. The optimum between the hydrolysis and condensation therefore, results in a maximum silica pore size formation (Rahman and Padavettan, 2012).

However, as the water/TEOS ratio increases further, this leads to the dominance of hydrolysis over condensation. In this case, there will be a large number of nuclei formed rapidly, leading to a larger number of smaller particles to be formed. These smaller particles will be packed more tightly, which results in a reduction in the pore size again due to the dense packing and reduction in the intraparticle voids (Yang, Coombs and Ozin, 1997). Brinker and Scherer (1990) also alluded to this phenomenon and added that the presence of high water content

causes the dilution of the alcohol byproducts, which affects the solubility and the dynamics of the reaction, favouring the formation of smaller structures (Brinker and Scherer, 1990).

The red curve in Figure 4.27 shows the variation of the surface areas as the water ratio is increased in the reagents. Generally, an opposite trend to that observed with the pore diameters was observed. At lower water/TEOS ratios, higher surface areas were observed, and they decrease to a minimum at a water/TEOS ratio of around 4 which is the reaction stoichiometric relation. Afterwards there was a marked (almost linear) increase in the surface area with water/TEOS ratio.

This is explained by the presence of a larger total internal structure when more numerous small pores are present in the structure. At intermediate water content, a faster rate of hydrolysis leads to the creation of many nucleation sites, producing larger particles that loosely aggregate with larger interparticle voids, which will be fewer in number, resulting in smaller surface area per gram of the material (Sing et al., 1985). The larger particles therefore possess smaller surface areas compared to that which is evident for the large numbers of small particles in the samples prepared at high water ratios.

In Figure 4.28, generally, the variation of the pore volume tends to show a downward trend at lower water content and a direct relationship with the water molar ratio as the amount of water in the reagents is increased. This is because when more pores are introduced in smaller particles, the total pore volume increases as compared to the larger particles with a lesser number of pores hence, this is mainly dependent on the overall porosity of the structure. However, there is an anomaly that occurred at a sample from run 6, which had a water/TEOS ratio of 10, this shows that there is a maximum occurring at a water ratio of around 10.5. The alteration in the sample's pore structure at this water/TEOS ratio can account for this, by looking at Figure 4.20 it can be seen from the nitrogen adsorption – desorption isotherm that the sample’s isotherm has got the highest area inside the hysteresis loop, moreover the shape of the loop according to Figure 4.22 signifies that at this point, the pores were more cylindrically shaped and this led to a higher volume inside the pores.

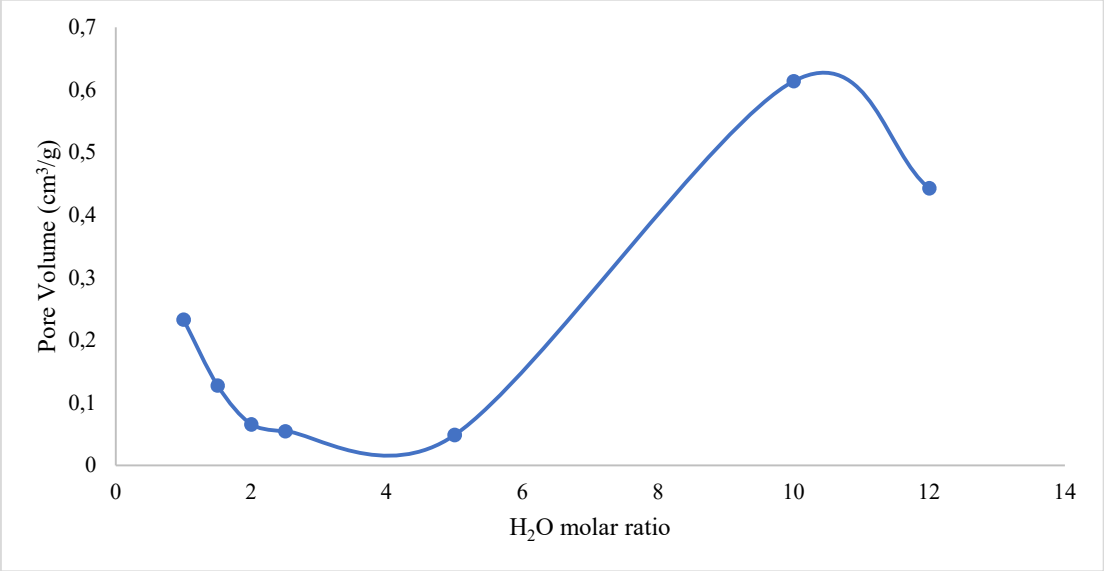



*Figure 4.51. Variation of pore volume with the $H_2O$ molar ratio in the reagents*

**Effects of the $NH_4OH$ concentration on the pore structure and surface area**

The amount of $NH_4OH$ was varied, maintaining constant concentrations of all other reagents. In this reaction, $NH_4OH$ acts as a catalyst, further speeding the rate of the reaction at higher $NH_4OH$ concentrations. Figure 4.29 shows the variation of pore diameter as the molar ratio of $NH_4OH$ was increased.

Table 4.8. Variation of $NH_4OH$ molar ratio across the last three runs and the respective silica properties.

| Run | $H_2O$ molar ratio | TEOS molar ratio | $NH_4OH$ molar ratio | $C_2H_5OH$ molar ratio | Pore Diameter | Surface Area | Pore Volume |
|---|---|---|---|---|---|---|---|
| 9 | 15 | 1 | 2.5 | 2.5 | 25.61 | 32.810 | 0.120 |
| 10 | 15 | 1 | 5 | 2.5 | 25.85 | 17.520 | 0.070 |
| 8 | 15 | 1 | 7 | 2.5 | 28.34 | 18.810 | 0.076 |

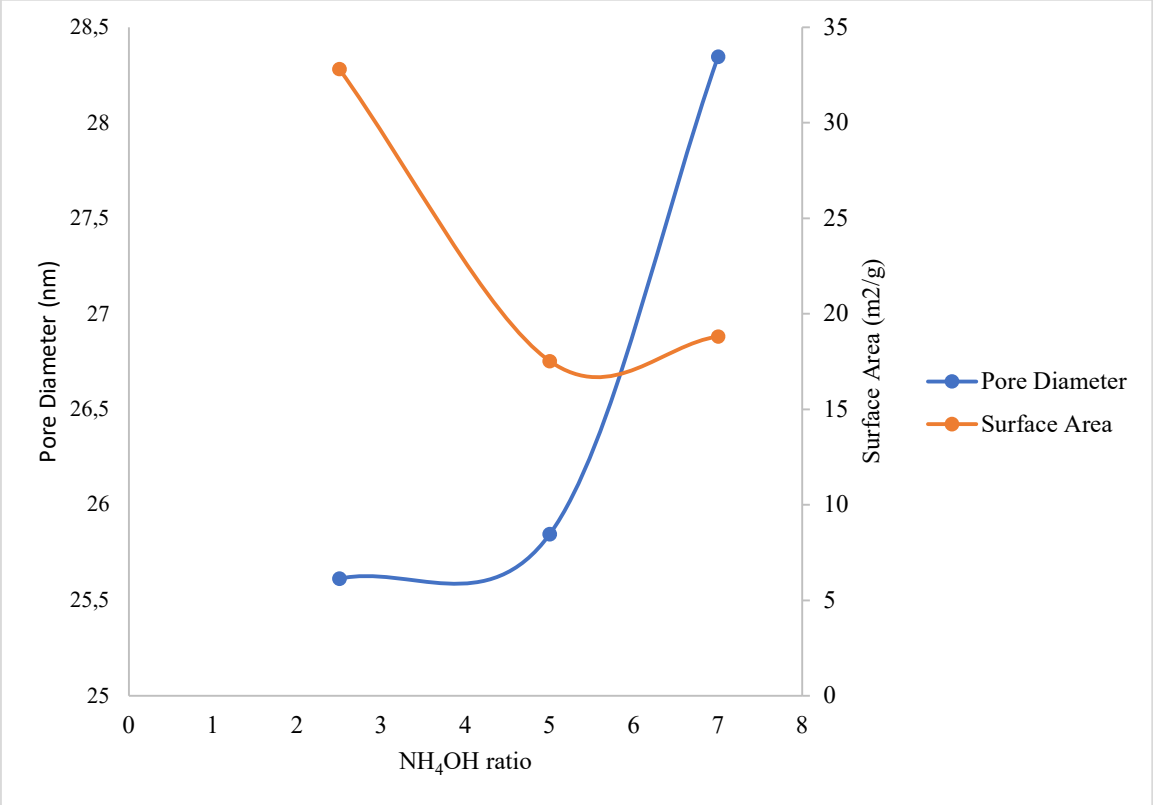



*Figure 4.52. Relationship between pore diameter and surface area with varying $NH_4OH$ molar ratio*

From Figure 4.29, there is a general increase in the pore diameter upon increasing the $NH_4OH$ molar ratio. A slight reduction in the pore diameter occurred when the $NH_4OH$ molar ratio is doubled from 2.5 to 5, and then a steep increase was observed from a molar ratio of 5 to 7.

This trend occurs since $NH_4OH$ acts as a catalyst in the reaction. At low $NH_4OH$ concentration, the rate of hydrolysis will be slow, which leads to the formation of densely packed, smaller silica particles, resulting in reduced porosity. Moderately increasing the $NH_4OH$ concentration results in faster condensation rates, which causes more porous and looser silica particles to develop. However, it was reported that at very high concentrations, the reaction happens too fast, causing the formation of non-uniform particles and irregular pores due to over condensation or structural collapse (Bogush, Tracy and Zukoski IV, 1988;Yang, Coombs and Ozin, 1997; Stöber, Fink and Bohn, 1968).

The orange graph in Figure 4.29 clarifies the relationship between the $NH_4OH$ concentration and the resulting surface area of the silica. As expected, an inverse relationship exists between the trend of the pore sizes to that of the surface area, similar to what was observed

when the amount of water increased. The reason for this inverse relationship is explained in the previous section.

Figure 4.30 shows the variation of pore volume with the $NH_4OH$ ratio in the reagents. There is a general decrease in the pore volume upon increasing the concentration of $NH_4OH$ with the reasons being the same as those explained in the preceding section when increasing the amount of water. However, the graph shows a dip or a minimum when the $NH_4OH$ ratio of 5 was used, which was caused by a slight increase in the surface area upon using an $NH_4OH$ ratio of 7. This can be explained by the distortion of the pore structure that occurs at very fast rates, leading to the existence of collapsed or irregular pores, as explained in the paragraph above.

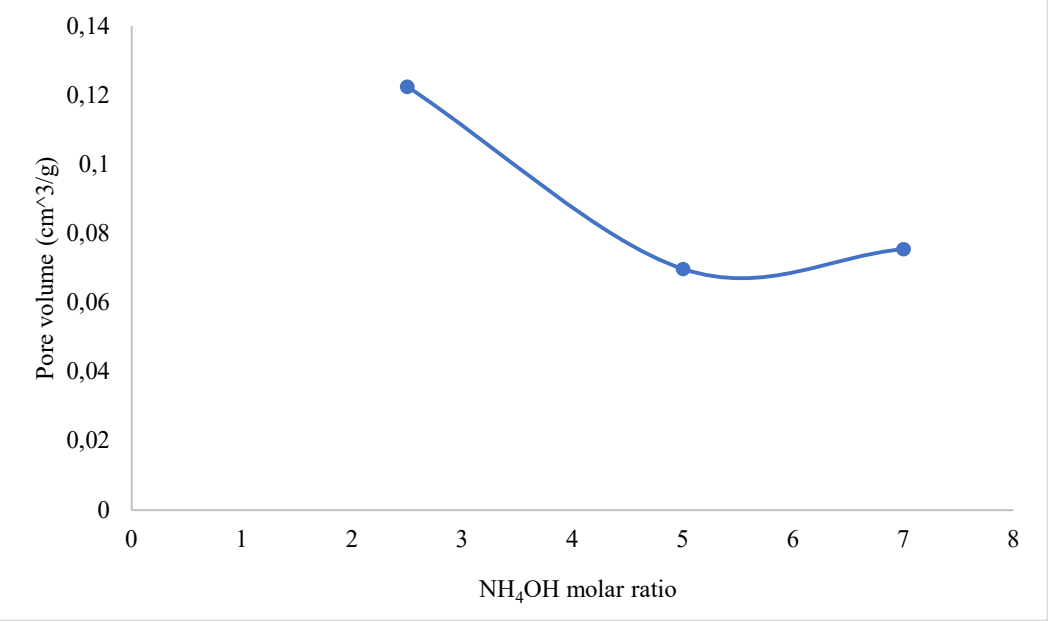



*Figure 4.53. Relationship between the silica pore volume and $NH_4OH$ molar ratio in the reaction reagents*

To verify these findings, the analysis of the densities of the 10 silica samples was conducted using a high-precision gas displacement pycnometer designed to determine the true (skeletal) density of solids and slurries, supplied by Anton Paar.

### 4.2.7 Density studies of the prepared silica samples

The densities of the samples were measured with a repeatability of four cycles per run to obtain the true average skeletal density of the samples at 20 °C. Table 4.9 shows the results obtained during the density measurements.

Table 4.9. The variation of densities across the 10 prepared silica supports

| Sample | Mass | $H_2O$ Molar Ratio | $NH_4OH$ Molar Ratio | Density |
|---|---|---|---|---|
| 1 | 1.175 | 1.0 | 1.0 | 2.199 |
| 2 | 1.545 | 1.5 | 1.0 | 2.206 |
| 3 | 1.342 | 2.0 | 1.0 | 2.209 |
| 4 | 1.386 | 2.5 | 1.0 | 2.233 |
| 5 | 2.999 | 5.0 | 1.0 | 2.221 |
| 6 | 3.878 | 10 | 1.0 | 2.190 |
| 7 | 4.952 | 12 | 1.0 | 2.163 |
| 9 | 1.915 | 6.0 | 2.5 | 2.190 |
| 10 | 3.753 | 6.0 | 5.0 | 2.145 |
| 8 | 3.592 | 6.0 | 7 | 2.157 |

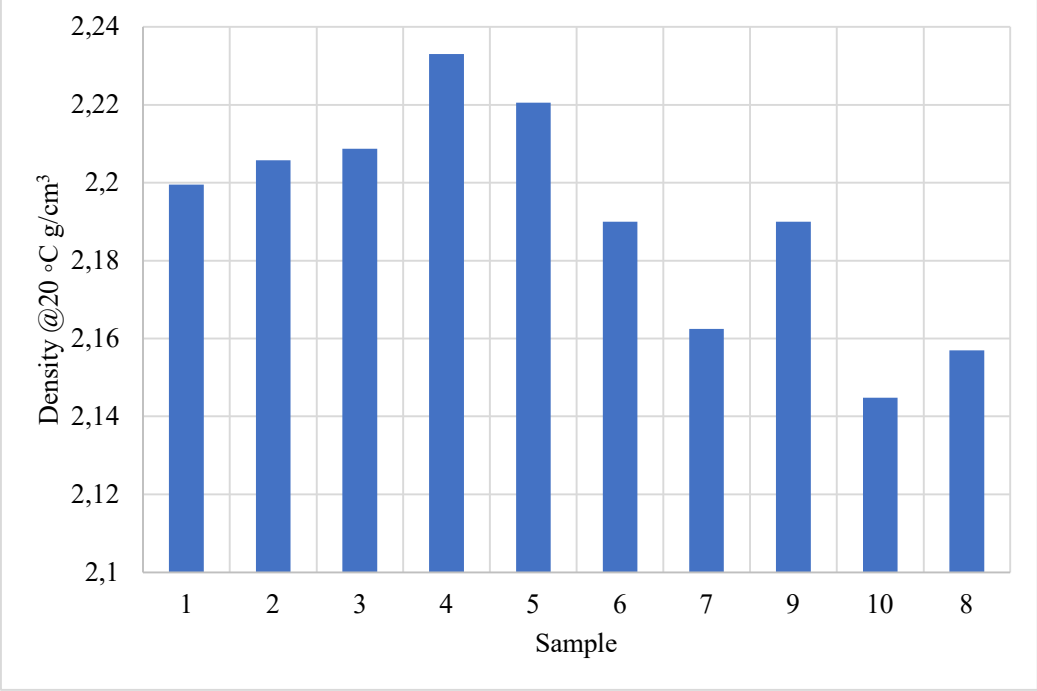



*Figure 4.54. Variation of densities across the 10 prepared silica samples*

Generally, the distribution of the bar graphs of the densities in Figure 4.31 resembles that of the pore sizes previously shown in Figure 4.31 .It can be noted that generally, the densities of

the samples where the amount of $NH_4OH$ was increased, from samples 8-10 have relatively lower densities than those in samples 1-7, where the less $NH_4OH$ was present.

From the equation:

$$\text{Porosity} = 1 - \frac{\text{Bulk density}}{\text{Skeletal density}} \quad \text{eqn (4.1)}$$

Figures 4.32 and 4.33 show the variation of the sample skeletal densities as the water and $NH_4OH$ ratios in the reagents were increased, respectively. From Figure 4.32 in which the water ratios were varied, at lower water ratios, there were generally lower densities, which increased to a maximum of 2.2330 $g/cm^3$ at sample 4, after which there was a steady decrease in the density values to the lowest at a water molar ratio of 12. Upon varying the amounts of $NH_4OH$ while keeping the other reagents constant, the variation of density across the samples is shown in Figure 4.33. It can be noticed that there was also a maximum density of 2.19 observed at an $NH_4OH$ molar ratio of 4.9 and lower densities at either side of this ratio, showing that too little and too much of the catalyst would lead to the lower observed densities, the key being to determine the optimum reaction rate, that would yield the desired results.

Generally, one would expect the skeletal density to decrease as the pore size increases, however, this was not always the case with these samples. Zhao et al. (1998) explained this phenomenon in which the increase in the skeletal density upon an increase in the pore size is caused by an increase in the wall thickness, integrating more material into the wall in order to support the larger pores.

The other reason for the notable increase in the skeletal density of the material is that, by increasing the pore size, the total number of pores may decrease as the larger pores will be formed instead of the smaller ones. The net result will therefore be the formation of a denser silica framework surrounding the larger pores (Rahman and Padavettan, 2012). The opposite is also true upon the decrease in pore size. Brinker and Scherer (1990) also pointed out that a complete condensation, which involves the formation of more Si-O-Si network species can occur under the larger pore sizes, favouring conditions such that there is an optimum amount of water in the experiment. However, in this study, the variation of the density outlined above was mainly studied based on the ratios of the reagents mixed and their impact on the resulting pore sizes and densities.

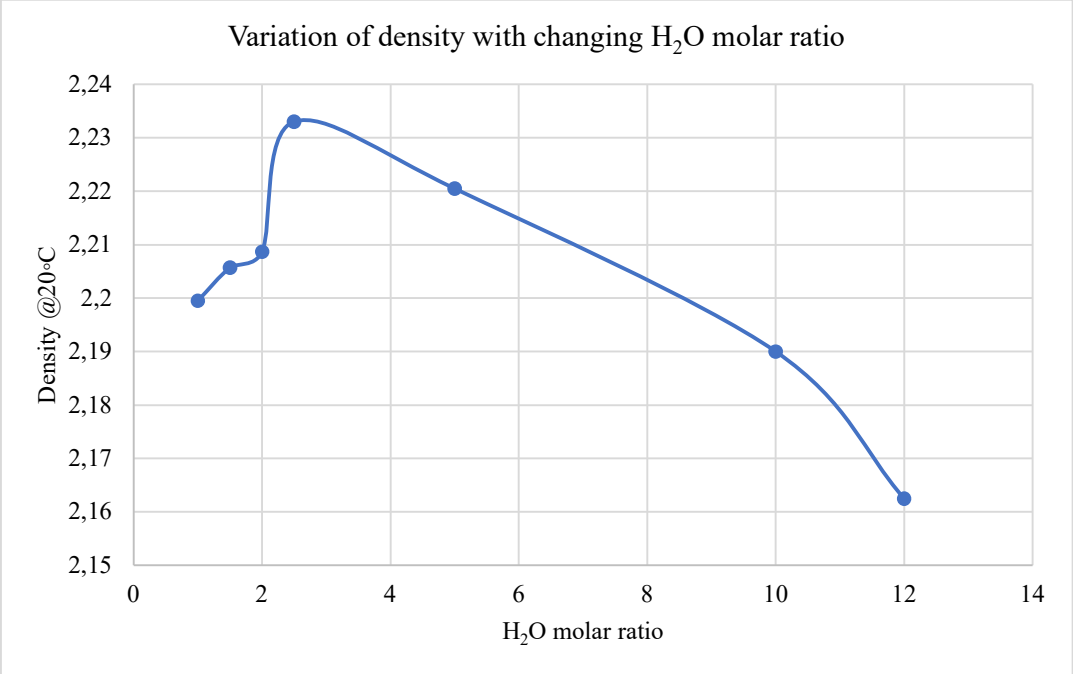



*Figure 4.55. Variation of the densities of the silica samples as the $H_2O$ molar ratio increases*

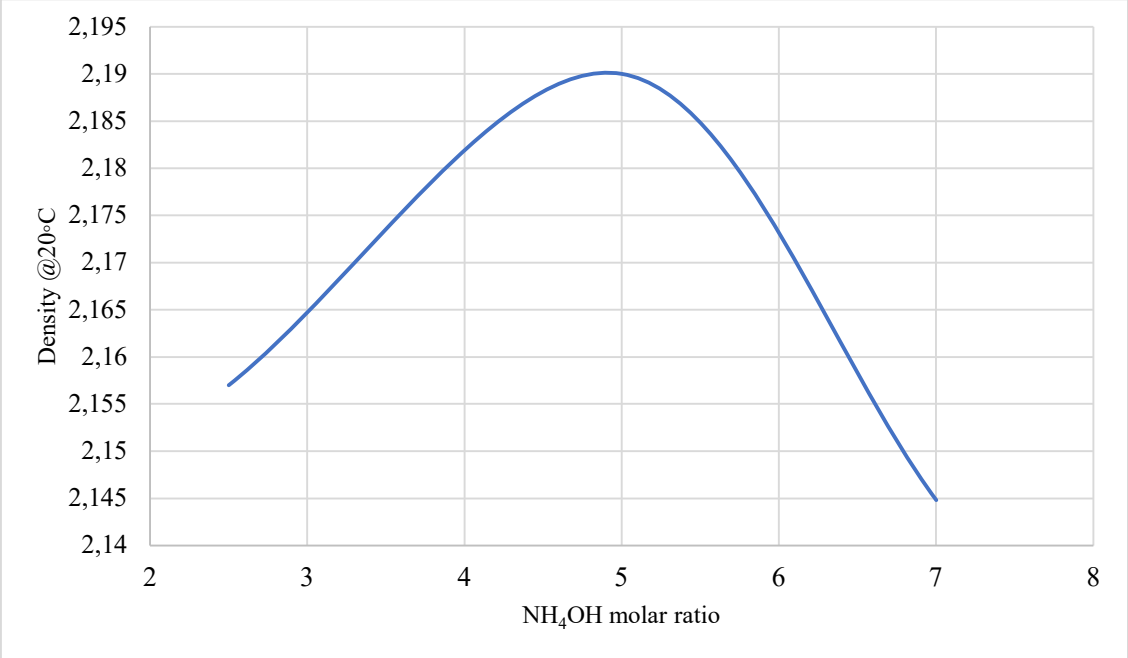



*Figure 4.56. Variation of the density of the prepared silica samples with $NH_4OH$ ratio, as other reagent concentrations remained constant*

## 4.3 Conclusion

The study in this chapter demonstrated successfully the effects of varying the amounts of water content and $NH_4OH$ in the synthesis of silica nanoparticles for creating $Co/SiO_2$ catalysts for implementation in FT Synthesis using the Stöber process; catalyst pore sizes can be varied by changing the ratios of the reagents' concentration ratios. The matrix created by the aforementioned method enabled the creation of an effective support matrix for cobalt loading whose pore diameter, surface area, and pore volume can be engineered for the specific catalytic application. Scientists and engineers can tailor the pore size, surface area, and pore volumes of the silica samples by adjusting the ratios of the reagents: $H_2O$: TEOS: $NH_4OH$: EtOH. The customized catalysts can also be used in various applications other than FT synthesis, such as drug delivery and material science, fine-tuning the catalyst's physical properties to maximize catalytic efficiency.

Characterization of the silica matrix using TGA followed by FTIR confirmed the presence of a robust siloxane matrix and revealed proof that the synthetic silica contained silanol groups. TGA confirmed the characteristic weight losses that occurred due to the presence of the adsorbed water, hydroxyl groups and the residual organic species. The calcination temperature of 620 °C was also determined during this analysis. XRD studies confirmed the predominant amorphous silica matrix in the samples and the presence of $Co_3O_4$ peaks was revealed at 2θ values of 31.14°, 36.76°, 44.8°, 59.3° and 65.25°. SEM analysis was further conducted and lastly the physisorption analysis was done and the results also confirmed the trends observed on the SEM findings, expounding the information on the surface morphology, size and distribution of the particles produced during the Stöber process. Skeletal density measurements were also conducted corresponded with the results obtained during the physisorption studies. EDS analysis conducted in conjunction with SEM, further provided the information confirming the successful addition of Co metal onto the silica support via wet impregnation, as the element layer maps indicated a uniform cobalt dispersion.

Collectively, the findings in this chapter showed that the Stöber process is a versatile and effective way to synthesize specific silica-based catalysts with controlled physical properties and composition. The various characterization techniques provided a comprehensive insight into the $Co/SiO_2$ system's physicochemical properties. This knowledge is crucial in tailoring the catalysts for FT synthesis, environmental remediation, selective oxidation and

nanoparticle manufacturing. Future work may be done to optimize the cobalt loading levels and investigate of the catalytic behaviour of the synthesized materials for different industrial applications.

## References


Bartholomew, C.H. (2001) 'Mechanisms of catalyst deactivation', *Applied Catalysis A: General*, 212(1–2), pp. 17–60. Available at: https://doi.org/10.1016/S0926-860X(00)00843-7.

Beck, J.S., Vartuli, J.C., Roth, W.J., Leonowicz, M.E., Kresge, C.T., Schmitt, K.D., Chu, C.T.W., Olson, D.H., Sheppard, E.W., McCullen, S.B., Higgins, J.B. and Schlenker, J.L., 1992. A new family of mesoporous molecular sieves prepared with liquid crystal templates. Journal of the American Chemical Society, 114(27), pp.10834–10843. https://doi.org/10.1021/ja00053a020.

Bezemer, G. L., Bitter, Johannes H., Kuipers, H.P.C.E., Oosterbeek, H., Holewijn, J. E., Xu, X., Kapteijn, F., Van Diilen, A. J., De Jong, K. P. (2006) 'Cobalt particle size effects in the Fischer-Tropsch reaction studied with carbon nanofiber supported catalysts', *Journal of the American Chemical Society*, 128(12), pp. 3956–3964. Available at: https://doi.org/10.1021/ja058282w.

Blaaderen, A. and Vrij, A. (1993) 'Synthesis and characterization of monodisperse colloidal organo-silica spheres', *Journal of Colloid And Interface Science*, pp. 1–18. Available at: https://doi.org/10.1006/jcis.1993.1073.

Bogush, G.., Tracy, M.. and Zukoski IV, C.. (1988) 'Preperation of monodisperse silica particles: Control of size and mass fraction', *Journal of non - crystaline solids*, 104(1), pp. 95–106. Available at: https://doi.org/https://doi.org/10.1016/0022-3093(88)90187-1.

Brinker, J.C. and Scherer, G.W. (1990) *Sol-Gel Science: The Physics and Chemistry of Sol - Gel Processing*. San Diego: Academic Press.

Cychosz, K.A. and Thommes, M. (2018) 'Progress in the Physisorption Characterization of Nanoporous Gas Storage Materials', *Engineering*, 4(4), pp. 559–566. Available at: https://doi.org/10.1016/j.eng.2018.06.001.

Dry, M.E. (2002) 'The Fischer-Tropsch process: 1950-2000', *Catalysis Today*, 71(3–4), pp. 227–241. Available at: https://doi.org/10.1016/S0920-5861(01)00453-9.

Efimov, A.M. and Pogareva, V.G. (2006) 'IR absorption spectra of vitreous silica and silicate glasses: The nature of bands in the 1300 to 5000 cm- 1 region', *Chemical Geology*, 229(1–3),

pp. 198–217. Available at: https://doi.org/10.1016/j.chemgeo.2006.01.022.

Fernandes, R.S., Raimundo, I.M. and Pimentel, M.F. (2019) 'Revising the synthesis of Stöber silica nanoparticles: A multivariate assessment study on the effects of reaction parameters on the particle size', *Colloids and Surfaces A: Physicochemical and Engineering Aspects*, 577(May), pp. 1–7. Available at: https://doi.org/10.1016/j.colsurfa.2019.05.053.

Gates, C, B., Katzer, Robert, J. and Schuilt, George, C, A. (1979) *Chemistry of catalytic processes*. New York: McGraw-Hill. Available at: https://lccn.loc.gov/77016112.

Jacobs, G., Das, T. K., Zhang, Y., Li, J., Racoillet, G., & Davis, B. H. (2002) 'Fischer-Tropsch synthesis: Support, loading, and promoter effects on the reducibility of cobalt catalysts', *Applied Catalysis A: General*, 233(1–2), pp. 263–281. Available at: https://doi.org/10.1016/S0926-860X(02)00195-3.

Jozwiak, W. K., Szubiakiewicz, E., Góralski, J., Klonkowski, A., & Paryjczak, T. (2004) 'Physico-chemical and catalytic study of the $Co/SiO_2$ catalysts', *Kinetics and Catalysis*, 45(2), pp. 247–255. Available at: https://doi.org/10.1023/B:KICA.0000023799.93711.58.

Khodakov, A. Y., Lynch, J., Bazin, D., Rebours, B., Zanier, N., Moisson, B., & Chaumette. (1997) 'Reducibility of cobalt species in silica-supported Fischer-Tropsch catalysts', *Journal of Catalysis*, 168(1), pp. 16–25. Available at: https://doi.org/10.1006/jcat.1997.1573.

Khodakov, A. Y., Griboval-Constant, A., Bechara, R., & Villain, F. (2001) 'Pore-size control of cobalt dispersion and reducibility in mesoporous silicas', *Journal of Physical Chemistry B*, 105(40), pp. 9805–9811. Available at: https://doi.org/10.1021/jp011989u.

Kleitz, F., Choi, S.H. and Ryoo, R. (2003) 'Cubic Ia3d large mesoporous silica: Synthesis and replication to platinum nanowires, carbon nanorods and carbon nanotubes', *Chemical Communications*, 3(17), pp. 2136–2137. Available at: https://doi.org/10.1039/b306504a.

Koirala, R., Chen, L., Liu, Y., Zhang, J., & Wang, H. (2018) 'Effect of cobalt loading on structure and catalytic behavior of CoOx/SiO2 in CO2-assisted dehydrogenation of ethane', *Applied Catalysis A: General*, 552(October 2017), pp. 77–85. Available at: https://doi.org/10.1016/j.apcata.2017.12.025.

Kruk, M., Jaroniec, M. and Sayari, A. (1997) 'Application of large pore MCM-41 molecular sieves to improve pore size analysis using nitrogen adsorption measurements', *Langmuir*, 13(23), pp. 6267–6273. Available at: https://doi.org/10.1021/la970776m.

Méndez-Vivar, J. and Mendoza-Bandala, A. (2000) 'Spectroscopic study on the early stages of the polymerization of hybrid TEOS-RSi (OR′)3 sols', *Journal of Non-Crystalline Solids*, 261(1), pp. 127–136. Available at: https://doi.org/10.1016/S0022-3093(99)00605-5.

Mueller, R., Kammler, H. K., Wegner, K., & Pratsinis, S. E. (2003) 'OH surface density of SiO2 and TiO2 by thermogravimetric analysis', *Langmuir*, 19(1), pp. 160–165. Available at: https://doi.org/10.1021/la025785w.

Odlyha, M., Scott, R.P.W. and Simpson, C.F. (1993) 'The hydroxyl content of silica gel', *Journal of Thermal Analysis*, 40(3), pp. 1197–1212. Available at: https://doi.org/10.1007/BF02546883.

Popova, M., Spassova, M., & Jiríčková, A. (2014) 'Design of cobalt functionalized silica with interparticle mesoporosity as a promising catalyst for VOCs decomposition', *Catalysis Letters*, 144(6), pp. 1096–1100. Available at: https://doi.org/10.1007/s10562-014-1246-0.

Rahman, I.A. and Padavettan, V. (2012) 'Synthesis of Silica nanoparticles by Sol-Gel: Size-dependent properties, surface modification, and applications in silica-polymer nanocompositesa review', *Journal of Nanomaterials*, 2012. Available at: https://doi.org/10.1155/2012/132424.

Riva, R., Miessner, H., Vitali, R., Del Piero, G. (2000) 'Metal-support interaction in Co/SiO2 and Co/$TiO_2$', *Applied Catalysis A: General*, 196(1), pp. 111–123. Available at: https://doi.org/10.1016/S0926-860X(99)00460-3.

Rovani, S., Santos, J. J., Corio, P., Fungaro, D. A. (2019) 'An alternative and simple method for the preparation of bare silica nanoparticles using sugarcane waste ash, an abundant and despised residue in the Brazilian industry', *Journal of the Brazilian Chemical Society*, 30 (7), pp. 1524–1533. Available at: https://doi.org/10.21577/0103-5053.20190049.

Shioji, S., Kawaguchi, M., Yasuhiro, H., Kenjiro, T., Hideo, Y. (1998) 'A study of the hydroxyl determination of silica', in *Journal of the Society of Power Technology*. 35(2). Tokyo, pp. 98–105. Available at: https://doi.org/https://doi.org/10.4164/sptj.35.98.

Sing, K.S.W., Everett, D.H., Haul, R.A.W., Moscou, L., Pierotti, R.A., Rouquerol, J., Siemieniewska, T. (1985) 'Reporting physisorption data for gas/solid Systems with Special Reference to the Determination of Surface Area and Porosity', *Pure and Applied Chemistry*, 57(4), pp. 603–619. Available at: https://doi.org/https://doi.org/10.1351/pac198557040603.

Smarzaro, J. L., Baldanza, M. A. S., De Almeida, A. J., Caytuero, A., Salim, V. M. M., Passos, F. B., Teixeira Da Silva, V. (2021) 'Effect of Silica Encapsulation on Cobalt-Based Catalysts for Fischer-Tropsch Synthesis under Different Reaction Conditions', *Industrial and Engineering Chemistry Research*, 60(32), pp. 11942–11953. Available at: https://doi.org/10.1021/acs.iecr.1c01940.

Stober, W., Fink, A. and Bohn, E. (1968) 'Controlled Growth of Monodisperse Silica Spheres in the Micron Size Range', *Journal of Colloid and Interface Science*, 26(1), pp. 62–69. Available at: https://doi.org/10.1589/jpts.29.112.

Thommes, M., Kaneko, K., Neimark, A. V., Olivier, J. P., Rodriguez-Reinoso, F., Rouquerol, J., & Sing, K. S. W. (2015) 'Physisorption of gases, with special reference to the evaluation of surface area and pore size distribution (IUPAC Technical Report)', *Pure and Applied Chemistry*, 87(9–10), pp. 1051–1069. Available at: https://doi.org/10.1515/pac-2014-1117.

Thommes, M. and Cychosz, K.A. (2014) 'Physical adsorption characterization of nanoporous materials: Progress and challenges', *Adsorption*, 20(2–3), pp. 233–250. Available at: https://doi.org/10.1007/s10450-014-9606-z.

Venezia, A. M., La Parola, V., Liotta, L. F, Pantaleo, G., Lualdi, M., Boutonnet, M., Järås, S. (2012) 'Co/$SiO_2$ catalysts for Fischer-Tropsch synthesis; Effect of Co loading and support modification by $TiO_2$', *Catalysis Today*, 197(1), pp. 18–23. Available at: https://doi.org/10.1016/j.cattod.2012.05.042.

Walther, F. and Brühwiler, D. (2024) 'Investigation of silica particle growth by incorporation of a pyrene fluorescent probe', *Colloids and Surfaces A: Physicochemical and Engineering Aspects*, 685(October 2023). Available at: https://doi.org/10.1016/j.colsurfa.2024.133234.

Xu, L., Zhang, J., Ding, J., Liu, T., Shi, G., Li, X., Dang, W., Cheng, Y.(2020) 'Pore structure and fractal characteristics of different shale lithofacies in the dalong formation in the western area of the lower yangtze platform', *Minerals*, 10(1). Available at: https://doi.org/10.3390/min10010072.

Yamane, N., Suzuki, K., Tan, M., Tsubaki, N. (2017) 'Influence of Co Precursor and Pt Additive on Catalytic Performance of Highly Active Co/SiO2-based Fischer-Tropsch Synthesis Catalysts', *Journal of the Japan Institute of Energy*, 96(7), pp. 250–254. Available at: https://doi.org/10.3775/jie.96.250.

Yang, H., Coombs, N. and Ozin, G.. (1997) ‘Ordered mesoporous silica synthesized from surfactant-silicate liquid-crystal precursors’, *Nature*, 386(6624), pp. 692–695.

Yang, Y., Zhang, J., Xu, L., Li, P., Liu, Y., Dang, W. (2022) ‘Pore Structure and Fractal Characteristics of Deep Shale: A Case Study from Permian Shanxi Formation Shale, from the Ordos Basin’, *ACS Omega*, 7(11), pp. 9229–9243. Available at: https://doi.org/10.1021/acsomega.1c05779.

Zhao, D., Huo, Q., Feng, J., Melosh, N., Fredrickson, G. H., Chmelka, B. F., & Stucky, G. D. (1998). Nonionic triblock and star diblock copolymer and oligomeric surfactant syntheses of highly ordered, hydrothermally stable, mesoporous silica structures. *Journal of the American Chemical Society, 120*(24), 6024–6036. https://doi.org/10.1021/ja974025i

Zhuravlev, L.T. (2000) ‘The surface chemistry of amorphous silica. Zhuravlev model’, *Colloids and Surfaces A: Physicochemical and Engineering Aspects*, 173(1–3), pp. 1–38. Available at: https://doi.org/10.1016/S0927-7757(00)00556-2.

# CHAPTER 5: CATALYST PORE SIZE EFFECT ON FISCHER-TROPSCH SYNTHESIS


## Abstract

This chapter explores how the catalyst pore size affects the product output during FT synthesis. Four cobalt-based catalysts, all supported on silica with different pore sizes, were implemented in the study while keeping the reaction conditions and catalyst loading constant. Techniques such as Temperature-Programmed Reduction (TPR) and Hydrogen Chemisorption were used to gain insight into the differences and activity and dispersion of the different catalysts. Mesoporous catalysts of a pore size range of 14 – 30nm were then tested for 150 hours, at 220℃ and 20 bar in a fixed-bed reactor, where the CO conversion was found to be between 2% and 23%.

The results showed a clear link between pore size and the product distribution. The catalyst with the largest pore size produced the most long-chain hydrocarbons ($C_5^+$), with selectivity up to 88%. Smaller pores tended to generally produce more methane and short-chain hydrocarbons ($C_2$–$C_4$), likely due to restricted diffusion and more side reactions. Larger pores made cobalt easier to activate but resulted in less long-chain product over time, possibly because of lower chain growth and catalyst degradation. The variation of carbon monoxide conversion and product selectivity over time was also deduced, which showed that the pore structure plays a key role in maintaining active sites and controlling the product mix.

This study highlights how tailoring the pore size in cobalt catalysts is crucial for maximizing the production of valuable long-chain hydrocarbons in FT synthesis using $CO/SiO_2$ catalysts. It also sheds light on how the catalyst's structure and properties interact to affect its performance throughout the reaction.

## 5.1 Introduction

FT synthesis using cobalt-based catalysts remains one of the most used processes for converting synthesis gas (a mixture of CO and $H_2$) into hydrocarbons, which are valuable as clean fuels and chemical intermediates (Jahangiri et al., 2014). The physical properties of the catalyst support, including the pore size, have a substantial influence on catalyst performance by affecting cobalt dispersion, reducibility, and internal mass transport. These factors together dictate the activity, selectivity, and stability of the catalyst, which in turn influences the nature of the product distribution from the FT process (Khodakov et al., 2007; Zhang et al., 2010).

Pioneering work by Khodakov and co-workers (Khodakov et al., 1997), researchers highlighted that supports with pore diameters exceeding 3 nm enable a higher degree of cobalt reduction and larger cobalt crystallites, leading to significantly enhanced reaction rates and improved selectivity toward desirable long-chain hydrocarbons (Merino et al., 2016; Song & Li, 2006) . Notably, cobalt catalysts supported on silica with pore sizes between 6 and 10 nm consistently outperform those with narrower pores in both activity and $C_5^+$ yield (Song & Li, 2006).

### 5.1.1 Pore Size and Catalyst Structure

The pore structure is a critical factor that influences more than just cobalt particle size; it also affects how readily cobalt oxides are reduced to their metallic state and the ease of accessibility of the active catalyst sites. Studies by Intarasiri and co-workers, (Intarasiri et al., 2017; Intarasiri et al, 2018) have shown that catalysts with larger mesopores facilitate the formation of well-dispersed, easily reducible cobalt particles, which translate into higher turnover frequencies. However, increasing pore size often comes hand-in-hand with increases in pore volume and surface area, which significantly complicates efforts to clearly distinguish between these effects. Adjustments in synthesis parameters to increase pore size generally lead to subsequent increases in surface area, which promote cobalt dispersion and particle size reduction. These overlapping changes can modulate the catalytic properties in unexpected ways, sometimes even reversing trends expected solely from pore size considerations. Thus, comprehensive characterization and analysis are essential to isolate and understand the distinct contributions of pore size to catalytic behaviour (Song & Li, 2006). This difficulty has also been observed in this particular study. Techniques like TPR, Temperature Programmed Desorption (TPD), Temperature Programmed Surface Reaction (TPSR), and hydrogen chemisorption are instrumental in characterizing these catalysts. TPR

provides insights into the reducibility profiles of cobalt species, while hydrogen chemisorption enables quantification of cobalt dispersion and the density of active metal sites, thereby helping to differentiate the influence of pore morphology from particle size or metal loading effects (Gnanamani et al., 2015; Jacobs et al., 2002; Okoye-Chine et al., 2023). Detailed TPR analysis reveals that catalysts supported on materials with narrow pores tend to require higher temperatures for cobalt oxide reduction, indicating stronger metal-support interactions and less reducible cobalt species. In contrast, wider pore supports typically feature more prominent reduction peaks at lower temperatures, highlighting enhanced reducibility. When combined with hydrogen chemisorption measurements, these techniques allow for precise evaluation of the cobalt active site population and dispersion, which are key parameters influencing overall catalytic activity and selectivity (Gnanamani et al., 2015; Li et al., 2015).

### 5.1.2 Controlling the Pore Size via the Stöber Process

To systematically evaluate pore size effects in the FT synthesis process, the Stöber synthesis method offers a reliable pathway to prepare uniform silica supports with finely tunable pore sizes and narrow distributions, as shown in Chapter 4. By carefully adjusting surfactant and template concentrations, one can prepare supports with controllable porosity, ensuring reproducibility and consistency in textural properties. This methodology facilitates isolating the impact of pore diameter on catalyst performance, though variations in surface area inherently occur and must be taken into account (Stober et al., 1968).

### 5.1.3 Effects of Pore Size on FT synthesis Product Selectivity

An evident correlation emerges between pore diameter and product selectivity: larger pores promote greater selectivity toward heavier hydrocarbons ($C_5^+$), while suppressing undesired methane and lighter hydrocarbons ($C_2$–$C_4$). This effect is attributed to improved molecular diffusion within larger pores, which mitigates secondary hydrogenolysis and facilitates chain propagation during FT Synthesis (Mehmood et al., 2017; Tian et al., 2018; Wei et al., 2016). Validation studies by Song and Li (2006) (Li et al., 2006; Song & Li, 2006) support these findings, showing enhanced CO conversions and selectivities for catalysts with pores in the 6–10 nm range.

Nevertheless, when evaluating turnover frequencies, Beer et al. (2014) demonstrated that active cobalt surface area more directly governs catalytic activity than nominal pore size alone, emphasizing the interplay of multiple structural parameters. Moreover, incomplete

reduction states or the presence of residual small cobalt particles have been found to necessitate careful interpretation of chemisorption and TPR data for accurate structure-activity relationships (Beer et al., 2014; Karaca et al., 2011).

### 5.1.4 Other factors that influence the product distribution

A number of factors, other than catalyst physical properties, influence the nature and distribution of products in the FT synthesis process. The catalyst type, support type, reaction conditions, reduction conditions, catalyst preparation conditions, types of promoters, GHSV, feed composition and the reactor types are among the top variables that also influence the nature of the product distribution (Munirathinam et al., 2018; Schulz, 1999; Satterfield et al., 1982; Glebov & Kliger, 1994)

Emerging research highlights the influence of support materials beyond silica. Carbon-based materials, such as activated carbons and carbon nanotubes, offer unique tuneable porosity and electronic environments that can enhance cobalt reducibility and catalytic stability. Promoters like manganese and titanium have been shown to regulate particle size and improve product selectivity, particularly towards long-chain hydrocarbons (Maximov et al., 2020; Chen et al., 2021).

The reactor feed and reaction conditions, such as $H_2/CO$ ratio, temperature, pressure, and space velocity all have a direct impact on product selectivity. Higher temperatures, for instance, typically improve methane selectivity, whereas heavier hydrocarbon ($C_{5}^{+}$) production is favoured by higher pressures and appropriate $H_2/CO$ ratios.

### 5.1.5 Scope and Chapter Overview

Within this chapter, a series of four $Co/SiO_2$ catalysts prepared by modified Stöber synthesis with systematically varied pore diameters, while maintaining a constant cobalt loading of 10% were studied. To clarify variations in cobalt dispersion, metal surface area, and reducibility, the author used a wide range of characterisation methods, such as BET surface area, pore volume, TPR, X-ray diffraction, and hydrogen chemisorption. With CO conversions ranging from 2% to 23%, the catalytic performance during FT synthesis was investigated for 150 hours time-on-stream (TOS). Quantitative analysis of product distributions covering methane, light hydrocarbons ($C_2$–$C_4$), and heavier hydrocarbons ($C_{5}^{+}$) yielded maximum selectivities of about 88% towards $C_{5}^{+}$ hydrocarbons.

This study intends to elucidate the impact of mesopore diameter on cobalt active sites and selectivity by combining catalytic results with physicochemical data, highlighting the difficulties in distinguishing these effects from the accompanying changes in surface area and particle size.

## 5.2 Experimental

### 5.2.1 Catalyst Preparation

To carry out the investigations of the effects of the silica pore size on the FT product distribution, ten different catalysts were prepared using the Stöber process (fully described in the Chapter 4) and incipient wetness impregnation. A mixture of water, TEOS $NH_4OH$ and ethanol was reacted in a round-bottomed flask with varying ratios at 60°C for 4 hours, leaving a white precipitate after four hours, which was later on filtered and dried at 80°C for 24 hours, then calcined at 620°C to obtain the $SiO_2$ samples. The variation of the ratios of the reagents led to different rates of the reaction in the round-bottomed flask, therefore, leading to the formation of different mesopores of the silica product. A metal loading of 10 wt% was used on all the catalyst samples to add the cobalt metal on the prepared $SiO_2$ samples using $Co(NO_3)_2.6H_2O$ as the metal precursor, and the resulting mixture was dried at 75°C for 24 hours in an oven before calcination in an aerated environment at 400°C for 4 hours in a muffle furnace and the resulting catalysts were named $Co/SiO_2$-1 to $Co/SiO_2$-10. From which four catalysts $Co/SiO_2$-1, $Co/SiO_2$-3, $Co/SiO_2$-6 and $Co/SiO_2$-9 were selected for the pore size studies based on their different pore sizes and grouped surface areas, with a pair of $Co/SiO_2$-1 and $Co/SiO_2$-3 and the pair of $Co/SiO_2$-6 and $Co/SiO_2$-9 having almost similar surface areas.

### 5.2.2 Catalyst Characterization

The reducibility of the catalysts was studied using $H_2$-TPR for all of the four catalysts in a CATLAB-PCS Microreactor. During the experiments, a small piece of quartz glass wool was placed on top of the catalyst bed and put into the microreactor column in order to prevent the powdered catalyst particles from moving away during the gas flow and to also evenly distribute the feed gas within the reactor. Afterwards, 0.2g of each catalyst sample was weighed and deposited into a glass tube that served as the microreactor vessel. Prior to the reaction, the 0.2g catalyst samples were treated in a continuous argon flow for an hour at ambient temperature to eliminate moisture and trace contaminants before cooling to the reaction temperature in preparation for the actual TPR measurements. After an hour of room

temperature argon introduction, the system was then filled with a 5% $H_2/N_2$ gas mixture at a flow rate of 30 mL/min until a stable baseline was reached. Two hours were allotted for recording the TPR measures utilising the TCD at a heating rate of 10°C $min^{-1}$ from 50°C to 800°C

A NOVA-800 Anton Paar physisorption analyser was used to study the pore characteristics and the surface area of the prepared catalysts and the supports. The BJH method was used to obtain the pore sizes and BET was used to find the surface areas. The $Co/SiO_2$ samples were first degassed for 8 hours at 180°C before the analysis was conducted for 12 hours to obtain a full nitrogen isotherm.

TEM was used to analyse the morphology of the cobalt particles at a mesoscopic level. The samples were prepared by putting the powdered samples in a sonicator to evenly distribute them for the ease of formation of a monolayer when adsorbed onto the carbon taped stubs. The stubs were then coated with 8 nm of gold before analysing using JOEL, ISM IT300, instrument at 10.36 kX magnification, 12.5 nm working distance and a working voltage of 15 kV.

X- Ray diffraction (XRD) experiments were conducted in situ using a PANalytical X'pert PRO instrument.

Hydrogen chemisorption studies were also done using the CATLAB-PCS microreactor. Catalyst samples weighing 0.2 g samples were prepared and inserted into the microreactor and the system was purged at 200 °C at a ramp rate of 10 °C/min for 2 hours followed by the catalyst reduction using a flow mixture of 10% hydrogen and 90% argon at 350°C, as per the catalysts TPR results for 10 hours. The reduction was then followed by the evacuation which was conducted at 250 °C for 1 hour after which temperature was then decreased to the chemisorption temperature of 35°C in 90 minutes. The $H_2$ chemisorption was then conducted at this point using 10:90% $H_2$/Ar gas flow with a pulse delay of 120 s, and 35 pulses per second, a load time of 60 s and a dosing time of 60 s incorporating a Faraday detector for the analysis.

### 5.2.3 Catalyst Testing

To evaluate the performance of the catalysts, pressure testing was conducted prior to reduction, to check for gas leaks. The catalysts were simultaneously loaded into three reactors, and the nitrogen gas was run through the line for 24 hours at room temperature at 20 bar. Reduction was then carried out by flowing $H_2$ gas for 16 hours at 350°C in situ using a flow rate of 60 mL/min.

After reduction, FT synthesis was carried out in a fixed- bed reactor where 1g of each sample was loaded into each reactor in series and After the catalyst was reduced, a 1g sample of the catalyst was prepared and then loaded into the reactor, and syngas with a $H_2$:CO ratio of 2:1 was introduced into the system at 220°C and 20 bar for 150 hours. Figure 5.1 shows a schematic of the set up of the reactor system that was used for the catalyst testing.

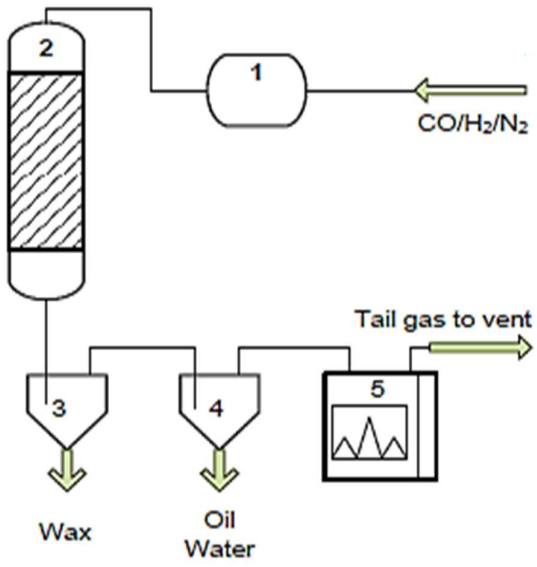



*Figure 5.57. A schematic diagram of the setup used to conduct the FT synthesis experiments*

1- Inlet gas mixer

2- Fixed bed reactor

3- Hot product trap

4- Cold condensable product trap

5- Online GC.

## 5.3 Results and discussion

### 5.3.1 Catalyst characterization

#### Physisorption Analysis

Table 5.1 shows a summary of the results that were obtained from the physisorption analysis. The 10 catalysts that were prepared successfully showed different pore sizes. However, the synthesis method did give rise to some variations in the surface areas and pore volumes of the catalysts as well.

Table 5.4. Physisorption analysis results

| Sample | BJH Pore Diameter (nm) | BJH Pore Volume ($cm^3/g$) | BET Surface Area ($m^2/g$) | Average particle size (nm) |
|---|---|---|---|---|
| 1-Co/$SiO_2$ | 14.98 | 0.241 | 117.19 | 51.20 |
| 2-Co/$SiO_2$ | 18.31 | 0.139 | 50.01 | 119.98 |
| 3-Co/$SiO_2$ | 20.55 | 0.075 | 24.08 | 249.25 |
| 4-Co/$SiO_2$ | 25.75 | 0.066 | 18.97 | 316.34 |
| 5-Co/$SiO_2$ | 22.18 | 0.057 | 19.35 | 309.90 |
| 6-Co/$SiO_2$ | 19.60 | 0.588 | 121.02 | 54.04 |
| 7-Co/$SiO_2$ | 10.20 | 0.426 | 152.27 | 39.40 |
| 8-Co/$SiO_2$ | 28.54 | 0.133 | 25.58 | 234.52 |
| 9-Co/$SiO_2$ | 30.15 | 0.156 | 31.73 | 189.10 |
| 10-Co/$SiO_2$ | 28.91 | 0.087 | 17.98 | 333.79 |

#### Temperature Programmed Reduction

TPR studies were used to investigate the reducibility of four synthesized Co/$SiO_2$ catalysts, and the resulting TPR profiles are shown in Figure 5.2. The profiles of all four catalysts revealed two distinct reduction peaks with different maxima, the first being the smaller in all

the cases. The first observed reduction peak in the range 250 – 351°C corresponds to the first stage in the reduction pathway of $Co_3O_4$, which is represented by the equation 5.1:

$$Co_3O_{4(s)} + H_{2(g)} \rightarrow 3CoO_{(s)} + H_2O_{(g)} \quad \text{.....5.1}$$

Whereas the second reduction peak found in the temperature range of in the range of 340 – 430°C is attributed to the next stage of reduction of the Co (II) to the metallic cobalt ($Co^0$), according to the reaction in equation 5.2 (Gorimbo et al., 2020).

$$CoO_{(s)} + H_{2(g)} \rightarrow Co^0{}_{(s)} + H_2O_{(g)} \quad \text{.....5.2}$$

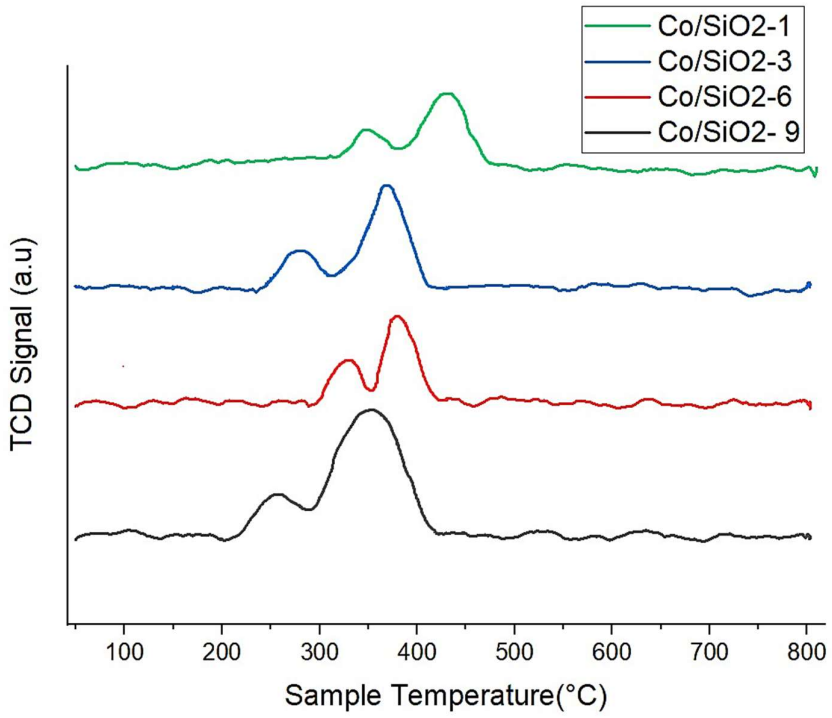



*Figure 5.58. TPR Profiles for Co/$SiO_2$-1, Co/$SiO_2$-3, Co/$SiO_2$-6 and Co/$SiO_2$-9*

The notable variations in peak temperatures and hydrogen consumption among the different catalysts indicate that the customised pore structures and surface areas do affect the cobalt dispersion and metal-support interaction. From Figure 5.2, the first peak of Co/$SiO_2$-1 appears at 350.35 °C and the second one is at 429.21°C, for Co/$SiO_2$-3, the first one is at 279.23°C and the second at 368.55°C, for Co/$SiO_2$-6 the first occurs at 332.27 °C and the second peak at 377.82°C and Co/$SiO_2$-9 has the first and second peaks at 254.77°C and 348.85°C

respectively. Generally, the trend that is observed in the peak temperatures corresponds to the nature of the catalyst pore sizes and surface areas of the catalysts. Table 5.2 shows the values of the pore sizes and surface areas of the catalysts and the corresponding reduction temperatures. The relationship between these parameters is shown in Figures 5.3 and 5.4 with the areas of the spheres represented as proportional to the surface areas.

Table 5.5. A Summary of the reduction peaks, pore sizes and surface areas of the four catalysts tested

| Catalyst | Pore Size (nm) | Surface Area ($m^2/g$) | $Co_3O_4$ Reduction Temperature(°C ) | CoO Reduction Temperature (°C ) |
|---|---|---|---|---|
| $Co/SiO_2$-1 | 14.9848 | 117.1788 | 350.35 | 429.21 |
| $Co/SiO_2$-6 | 19.6037 | 121.0245 | 332.27 | 377.82 |
| $Co/SiO_2$-3 | 20.548 | 24.0725 | 279.23 | 368.55 |
| $Co/SiO_2$-9 | 30.1472 | 31.7301 | 254.77 | 348.85 |

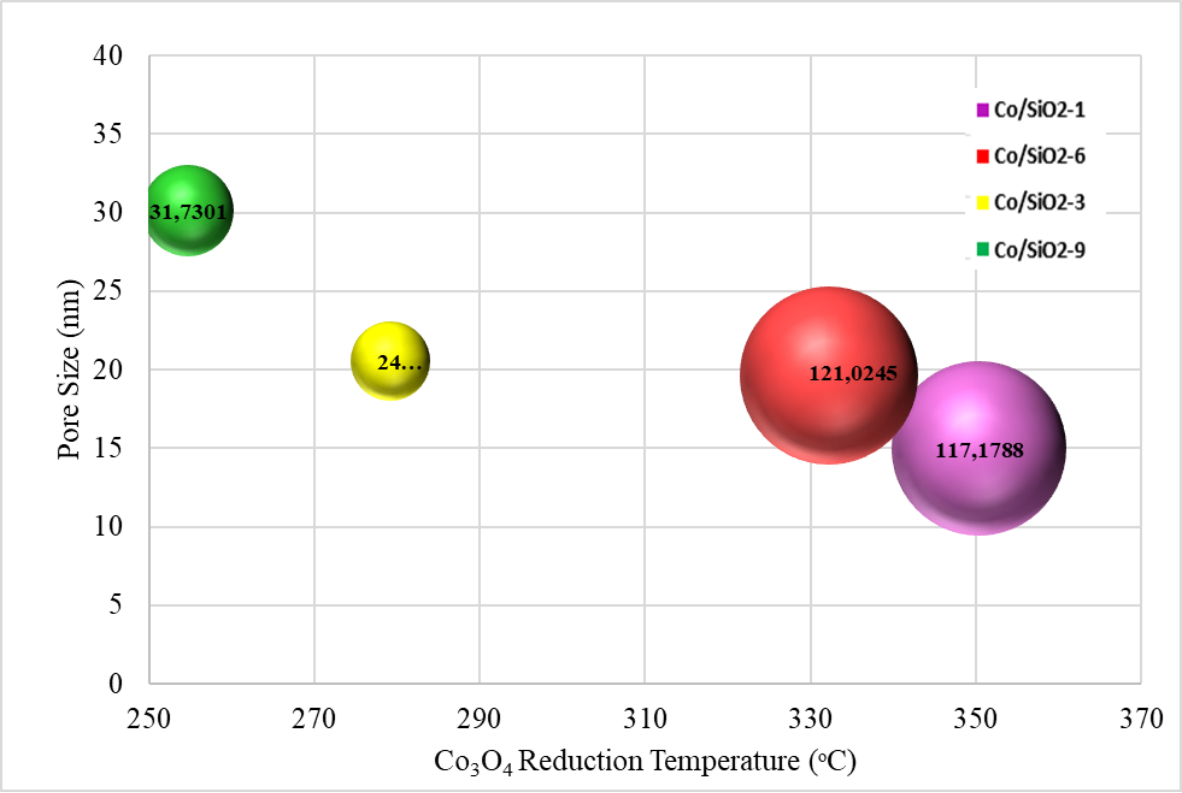



*Figure 5.59. Relationship between pore size, surface area, and $Co_3O_4$ reduction temperature for the four catalysts (Areas of the spheres are proportional to the surface areas)*

From Figure 5.3, generally, there is an observed increase in the reduction temperature of the $Co_3O_4$ phase as the pore sizes decrease, indicating increasing difficulty in the reduction of the $Co_3O_4$ to CoO. There is also a marked observation that there are lower reduction temperatures for the catalysts with smaller surface areas, suggesting more readily reducible cobalt species for the catalysts with lower surface areas and a difficulty for those with high surface areas.

Looking more closely, it can be noted that the pore sizes and surface areas play a part in affecting the reducibility of the catalysts. The $Co/SiO_2$-9 and $Co/SiO_2$-3 with larger pores and smaller surface areas were easier to reduce while $Co/SiO_2$-1 and $Co/SiO_2$-6 which have larger surface areas and smaller pore sizes were more difficult to reduce hence they could only be reduced at higher temperatures. This showed the interrelationship between pore sizes and surface areas in affecting the reducibility.

Intarasari et al. (2018) observed that the larger pore sizes are often associated with an improvement in the cobalt dispersion throughout the catalyst, the larger pore sizes are thought to prevent the encapsulation or entrapment of the cobalt species in micropores (Intarasiri et al., 2018). The larger pores also reduce the $Co\text{-}SiO_2$ interaction (metal-support interaction) leading to the formation of larger cobalt crystallites within the pores, making reduction easier and therefore leading to lower reduction temperatures (Ghampson et al., 2010). Conversely, the smaller pore sizes tend to form stronger metal support interactions and therefore a lower overall hydrogen consumption, leading to higher reduction temperatures due to the increased difficulty (Ghampson et al., 2010; Intarasiri et al., 2017). Higher surface areas increase the interaction with the silanol groups on the silica to form the Co-silicate-like species, hence also enhancing the metal-support interaction (MSI); however, there is also a notable improvement in the dispersion of the cobalt particles that can be observed in them. Lower surface areas, conversely, lead to a reduced dispersion of the cobalt particles, leading to more pronounced agglomeration and formation of larger particles, hence a shift towards the lower reducing temperatures (Ning et al., 2015).

The pore sizes of the silica used in this study are generally considered larger (in the range 15-30 nm) synthesized from the Stöber process, and a relatively higher cobalt loading of 10% was used in all the samples. The larger pores often lead to a more uniform impregnation of the $Co(NO_3)_2$ precursor, forming more of the crystalline $Co_3O_4$ upon calcination, leading to

the more prominent first peak hence a characteristic larger first peak and a smaller second peak on all the catalysts (Bambal et al., 2013).

Figure 5.4 shows the trend observed upon the reduction of the second phase which shows a similar general trend as that observed on the $Co_3O_4$ reduction. The difference is that this is now occurring at higher temperatures as it signifies the second phase of the reduction process after obtaining the CoO particles from the first reduction step. Table 5.2 shows the exact temperatures at which each of the catalysts was reduced.

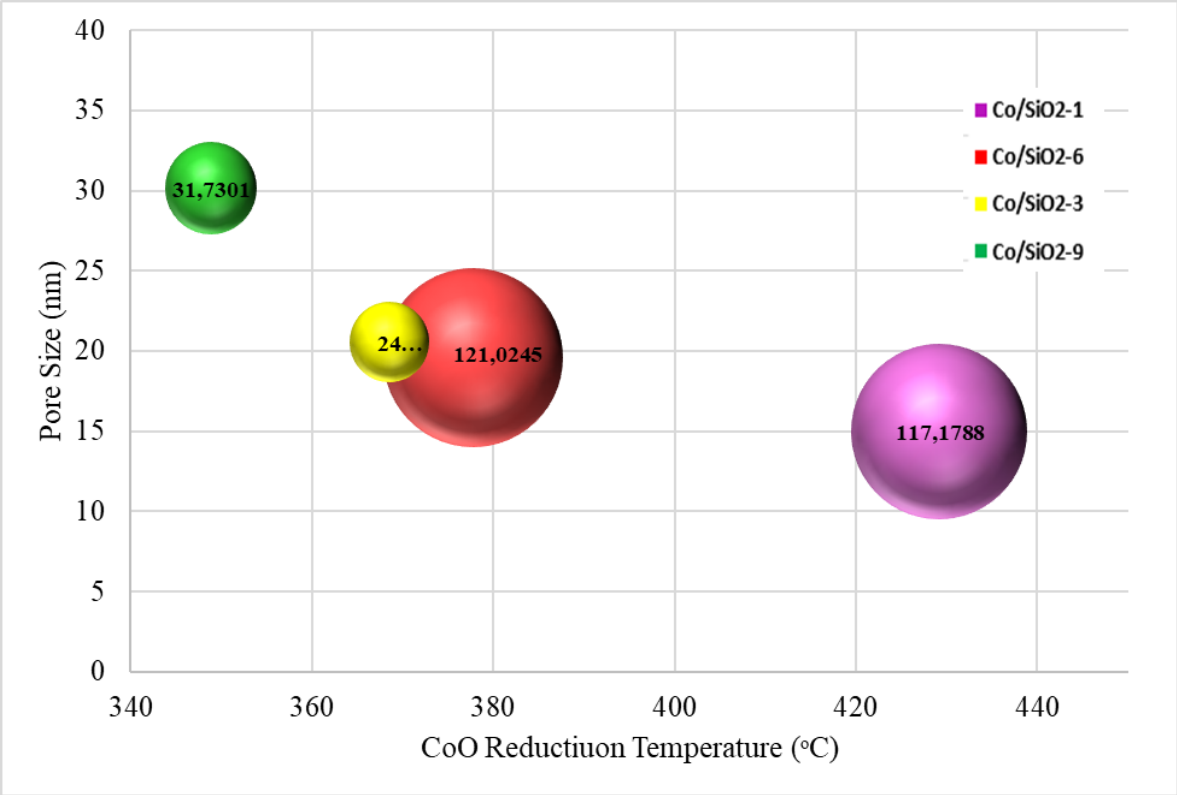



*Figure 5.60. Relationship between pore size, surface area, and CoO reduction temperature for the four catalysts (Areas of the spheres are proportional to the surface areas)*

**Hydrogen Chemisorption**

Hydrogen chemisorption experiments were carried out on all four catalysts to determine the dispersion and the cobalt surface area after the reduction process. Table 5.3 shows a summary of the results obtained and the corresponding catalyst pore sizes.

Generally, there is a clear increase in metal surface area, $H_2$ uptake, and dispersion with increasing pore size. Where the catalysts with larger pores exhibited greater hydrogen uptake, and consequently, higher dispersion, suggesting an increased metallic surface area and improved cobalt accessibility. As expected $Co/SiO_2$-1, which has a smaller pore diameter of 14.948 nm, also has a lower dispersion because of more pronounced encapsulation of the cobalt particles in the smaller pores, leading to a decreased reducibility and the lowest hydrogen uptake and dispersion of 3.596E-6 moles/g and 0.353% respectively. This can also be confirmed by the TPR results which showed the highest reduction temperature for the catalyst. $Co/SiO_2$-3 has a pore size of 20.548 nm but was found to have a very small metal surface area of 0.2637$m^2$/g, a hydrogen uptake of 4.394E-6 moles/g and second lowest dispersion of 0.37% among the four catalysts, this could have been attributed to the amorphous nature of the support as shown on the SEM results in Chapter 4 which led to the formation uneven pores resulting in pore blockage. The TPR results also show that it was relatively easy to reduce the catalyst. $Co/SiO_2$-6 had a very large surface area and an intermediate pore size which led to a good dispersion on a metallic surface area of 2.859 $m^2$/g due to weaker MSI, as explained in the previous section. The result also corresponds with what was observed during the TPR studies. The catalyst had a relatively higher $H_2$ uptake of 4.765E-5 moles/g and a dispersion of 2.806%. Catalyst $Co/SiO_2$-9 had the largest average pore size of 30 nm and a relatively smaller catalyst surface area, from the TPR graph, the catalyst was the easiest to reduce, this being due to the weak metal-support interactions in the sample. These are attributed to the ease of access of the metal crystallites and formation of larger crystallites which are easier to reduce hence faster reduction. The catalyst has the highest hydrogen uptake of 1.635E-4 moles/g and a dispersion of 9.632%.

Overall, the findings show that larger pores encourage the development of a more accessible cobalt metal surface, most likely as a result of larger or better-exposed cobalt crystallites and decreased confinement. Better reducibility and dispersion are reflected in the enhanced $H_2$ absorption, which is correlated with more active metallic sites available to absorb hydrogen.

Although it varies greatly, the BET surface area (i.e. support surface area) does not vary with dispersion in a straightforward way. $Co/SiO_2$-6 has a moderate dispersion (2.8%) and a very high BET area (~121 $m^2$/g). The BET areas of $Co/SiO_2$-3 and $Co/SiO_2$-9 are lower (~24–32 $m^2$/g), while their dispersions differ significantly (0.37% vs. 9.63%), while $Co/SiO_2$-1 with a surface area of ~117 $m^2$/g had the lowest dispersion of 0.35%. This demonstrates that the

there is no direct correlation between the interaction of accessibility, cobalt particle distribution, support structure and metal dispersion.

Table 5.6. Hydrogen chemisorption results presented with the catalyst pore size

| Catalyst | Pore size (nm) | Metal Surface Area ($m^2/g$) | $H_2$ Uptake (moles/g) | Dispersion (%) |
|---|---|---|---|---|
| $Co/SiO_2$-1 | 14.985 | 0.216 | 3.596E-6 | 0.353 |
| $Co/SiO_2$-6 | 19.604 | 2.859 | 4.765E-5 | 2.806 |
| $Co/SiO_2$-3 | 20.548 | 0.264 | 4.394E-6 | 0.370 |
| $Co/SiO_2$-9 | 30.147 | 9.812 | 1.635E-4 | 9.632 |

Limited reactant accessibility in more constrained structures may counteract these results, which may suggest a trade-off between diffusional and dispersion constraints.

The combined TPR and $H_2$ chemisorption data give a comprehensive understanding of the activation behaviour of cobalt in relation to pore architecture. These findings form the basis for the relationship between catalyst structure and FT synthesis performance trends, as discussed in the following section.

### 5.3.2 Fischer-Tropsch Synthesis

The catalysts were tested under consistent FT synthesis conditions over 150 hours on stream, capturing how product selectivity evolved over time. Special focus was placed on $C_5^+$ selectivity, which signals the formation of heavier hydrocarbons valuable for liquid fuels, along with the distribution of lighter products such as methane ($CH_4$) and $C_2$–$C_4$ hydrocarbons. The experiments spanned a CO conversion range from 2% to 23%, enabling a robust comparison of selectivities, so that the relationship between structural characteristics and catalytic function could be understood. Table 5.4 shows a summary of the results obtained from the FT synthesis experiments which were conducted at 220°C, 20 bar and a flowrate of 60 mL/min.

**Catalytic behaviour**

FT synthesis measurements for the four catalysts $Co/SiO_2$ -1, $Co/SiO_2$-3, $Co/SiO_2$-6 and $Co/SiO_2$-9 were made in a fixed - bed reactor and assessed over a period of 150 hours. Figure 5.5 shows the catalyst behaviour of the catalysts towards CO conversion over the 150-hour period.

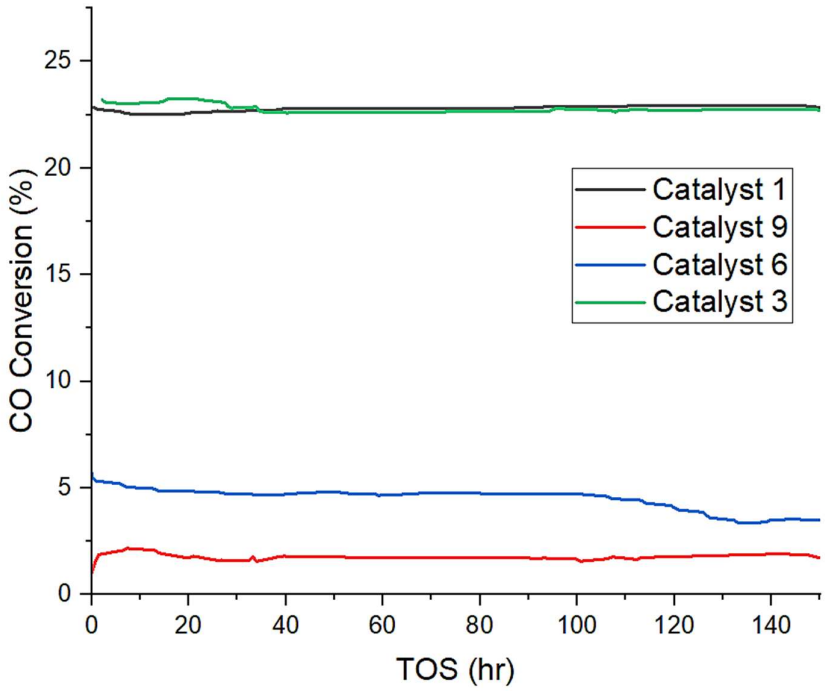



*Figure 61.5 Catalytic performance of $Co/SiO_2$-1. $Co/SiO_2$-3, $Co/SiO_2$-6 and $Co/SiO_2$-9 during FT synthesis over a TOS of 150h*

Many authors in the literature report short (3-12 hours) to moderate (12-40 hours) periods, for the Co based catalyst in FT synthesis to stabilize with the time; this is largely influenced by the pretreatment conditions of the catalyst (Bambal et al., 2013; Kord-Tamandani et al., 2023; Mochizuki, 2018; Widiatmika, 2015; Zeng et al., 2014). Notably in one instance the catalyst took 78 hours to stabilize (Jakub & Ochodek, 2023). In this study, it can be seen from Figure 5.5 that the stability of the catalysts was reached at around 40 hours. This is moderate in comparison to the catalysts in the literature but enhanced pretreatment methods would reduce the time. Of the four catalysts, $Co/SiO_2$-1, $Co/SiO_2$-3 and $Co/SiO_2$-9 remained stable over the whole 150 hours while $Co/SiO_2$-6 deactivated after 110 hours. This could have been caused by the presence of a cobalt phase which is oxidised thereby causing higher hydrogen consumption at that point leading to the build up of more water in the catalyst as explained by

Barbier et al (Barbier et al., 2001). The average CO conversions and selectivities for all the four catalysts were therefore determined between 40 – 100 hours and the summary is shown in Table 5.5.

Table 5.7. A summary of the catalytic performance of the $CO/SiO_2$ catalysts with different pore sizes. (Reaction conditions: Temperature = 220°C, pressure 20 bar, flowrate = 60 mL/min, Time on Stream (TOS) = 150 hours, $H_2/CO$ ratio = 2), average reaction rate = 2.35E-04 (mol CO/g cat./min).

| Catalyst | Pore Size (nm) | CO Conversion (%) | Hydrocarbon Selectivity (%) | | |
|---|---|---|---|---|---|
| | | | $CH_4$ | $C_2$-$C_4$ | $C_{5+}$ |
| $Co/SiO_2$-1 | 14.985 | 22.875 | 15.394 | 7.355 | 77.251 |
| $Co/SiO_2$-6 | 19.604 | 4.242 | 14.456 | 10.748 | 74.796 |
| $Co/SiO_2$-3 | 20.548 | 22.763 | 15.080 | 8.450 | 76.469 |
| $Co/SiO_2$-9 | 30.147 | 1.732 | 6.416 | 5.148 | 88.435 |

**Relationship between the dispersion and CO conversion**

The catalysts with different pore diameters do show a general trend with respect to the dispersion and the associated CO conversion. The relationship between dispersion and CO conversion has been shown in Figure 5.6 as a bar graph. The graph was plotted with the corresponding standard deviations indicated in black on top of the bars from the average CO conversions obtained during the reaction between 40 and 100 hours. According to the experimental data, trend between CO conversion and dispersion generally shows an inverse relationship. It can be deduced that the catalysts with lower dispersion ($Co/SiO_2$-1 and $Co/SiO_2$-3) exhibit much better CO conversions (22.9 and 22.8 %) than the catalysts with the higher dispersion, $Co/SiO_2$-6 and $Co/SiO_2$-9 which only converts 4.2 and 1.7% respectively. These results show that for $Co/SiO_2$-6, even if it was easily reduced and with a higher dispersion, the active sites were not easily accessible.

The impact of dispersion suggests that factors other than pore size may affect activity, such as the catalyst reducibility and dispersion (Barbier et al., 2001). Even though they had reduced metal surface area and cobalt dispersion, the catalysts with moderate pore sizes of about 15 to 20.5 nm ($Co/SiO_2$-1 and $Co/SiO_2$-3) showed the highest CO conversions, at roughly 22.8%.

This implies that catalytic activity is significantly influenced by variables other than the amount of active cobalt surface, such as an ideal cobalt particle size and increased catalytic turnover frequency (Intarasiri et al., 2018).

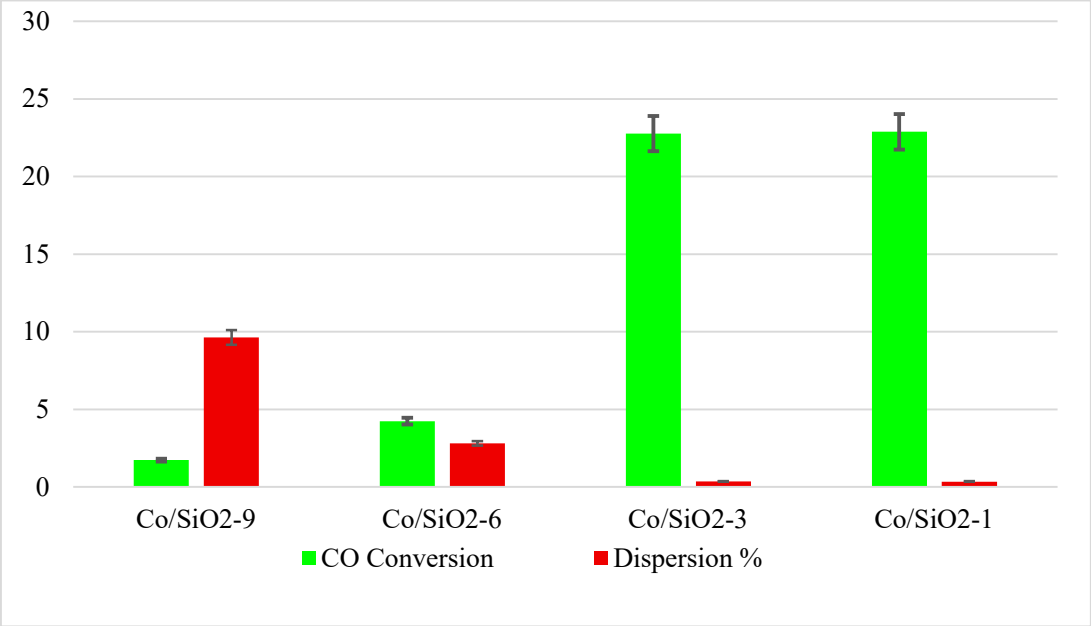



*Figure 5.6. Relationship between CO conversion and dispersion for the four catalysts tested in FT synthesis*

**The product selectivity trends**

Figure 5.7 shows a graphical representation of the trends that were obtained from the selectivity results in relation to the pore diameters of the four catalysts used in the FT synthesis reaction.

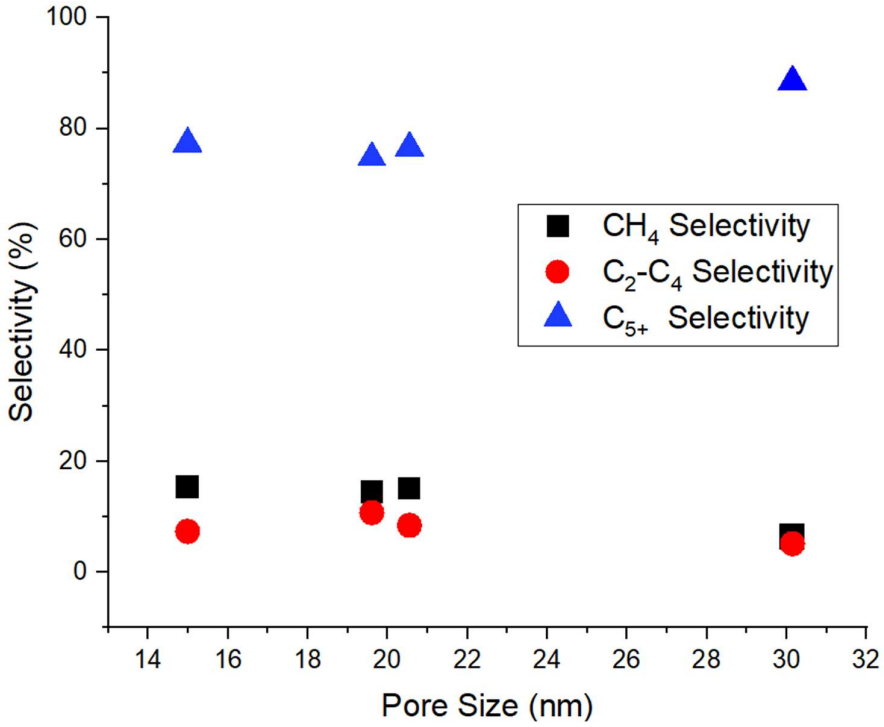



*Figure 5.7. Variation of product selectivity with pore sizes for the four tested catalysts*

Generally, the $CH_4$ selectivity drops significantly as pore size increases, from about 15.4% at 15 nm to just about 6.4% at 30 nm pores. The significance of pore confinement in promoting secondary hydrogenation processes and favouring light hydrocarbons is shown by the significant methane selectivities (~15%) seen at smaller pores (14.98 and 19.6 nm). Reduced secondary reactions that produce methane are shown by lower methane selectivity at bigger pores. The pattern is in line with enhanced pore diffusion and a decreased propensity for hydrogenation on bigger cobalt particles (Okabe et al., 2004).

The light hydrocarbon ($C_2$-$C_4$) selectivity is slightly greater (7–10.7%) at moderate pore sizes (around 15–20 nm), where it peaks, whereas the lowest selectivity (5.15%) is seen for the biggest pores. The relatively low selectivity in the bigger pores is because larger pores favour heavier hydrocarbons by promoting chain development and lowering re-adsorption and breaking (Ghampson et al., 2010).

The $C_{5+}$ hydrocarbon selectivity trend indicates that selectivity for heavier hydrocarbons ($C_5^+$) increases as pore size increases. This is especially true for the biggest pores (30 nm), where $C_5^+$ reaches 88.4%. This suggests that chain development to heavier hydrocarbons is facilitated by bigger pores.

Larger pores tend to allow the formation of larger Co particles with less strong interaction with the support and higher dispersions. This facilitates easier reduction (higher metallic cobalt availability) and favors longer chain growth, resulting in higher $C_5^+$ selectivity and lower methane formation (Cheng et al., 2015; Intarasiri et al., 2017; Song & Li, 2006). From the hydrogen chemisorption studies, $Co/SiO_2$-9 with the biggest pore size of 30.15 nm had the highest $H_2$ uptake of 1.635E-4 moles/g and also the highest dispersion of 9.632% the TPR results also showed the lowest $Co_3O_4$ and CoO reduction temperatures for this catalyst; therefore, the catalytic behaviour also confirms the evidence of an enhanced reduction effect due to the larger pores. By contrast, $Co/SiO_2$-1, has the smaller pore size (14.98 nm), a $H_2$ uptake of 3.596E-6 moles/g, and a dispersion of 0.353%.

$Co/SiO_2$-9 catalyst's low conversion but high $C_5^+$ selectivity indicates that, although there are fewer accessible active sites or originally active particles, those that are active preferentially produce heavy hydrocarbons, perhaps as a result of enhanced re-adsorption and chain development within the larger pores.

**Summary**

Cobalt reducibility and dispersion on $Co/SiO_2$ catalysts can be improved by optimizing pore size to about 30 nm, which increases the active metal surface area. It was also noted that both reducibility and hydrogen adsorption properties, which are correlated with catalytic activity and selectivity, are controlled by the nature of the catalyst pores. The small cobalt particles may be stabilised by strong metal-support interaction in narrower pores, although total reduction is impeded and active surface area is decreased. On the other hand, catalysts with larger pores, and lower CoO reduction and $Co_3O_4$ temperatures require fewer energy-intensive activation steps during catalyst pre-treatment.

From the catalyst pore size range of 15-30 nm, which was tested, high CO conversion is achieved with low to moderate pore diameters of the $Co/SiO_2$ catalysts, whereas the methane and light hydrocarbon selectivity is relatively high in this pore diameter range (~15–20 nm). The largest pore diameter of around 30 nm yielded low conversions and high dispersions

Under these investigated conditions, larger pores (>30 nm) inhibit methane generation and favour heavier hydrocarbon ($C_5^+$) selectivity, although this happens at the cost of reduced CO conversion.

These findings are in line with research that demonstrates how pore size affects cobalt particle size, reducibility, and diffusion phenomena all of which together affect FT synthesis activity and selectivity.

Pore architecture and cobalt active phase dispersion must be carefully tuned to strike a balance between high activity (CO conversion) and good $C_5^+$ selectivity, depending on the desired hydrocarbon product range.

**Discussion**

The results show that bigger pore diameters generally make it easier to reduce cobalt species. This is probably because larger cobalt particles develop with less metal-support interaction. By facilitating longer chain growth, these larger particles increase selectivity towards heavy hydrocarbons ($C_5^+$), whereas smaller pores strengthen cobalt-support contacts, which prevent cobalt reduction and favour the synthesis of lighter hydrocarbons and methane. Furthermore, diffusion inside the catalyst is influenced by pore size; smaller pores may impose diffusion constraints that affect intermediate re-adsorption and product dispersion. The pore structure is also correlated with the growth of cobalt particles and possible sintering effects, which impact the trends in catalytic stability and selectivity over time.

## 5.4 Conclusion

This chapter has thoroughly investigated the influence of pore size on the structural, physicochemical, and catalytic properties of $Co/SiO_2$ catalysts in Fischer–Tropsch synthesis. By varying pore diameters from approximately 15 nm to 30 nm using the Stöber method, clear trends emerged that highlight the pivotal role of pore architecture in governing the unpromoted $Co/SiO_2$ catalyst performance.

The results showed the importance of the study of the catalyst pore sizes and the effects of the pore size in the Fischer Tropsch product. The experimental studies conducted could not entirely manage to keep all the other variables constant as it would require a lot of trials to synthesize the catalysts which would have similar variables such as the surface area and dispersion while only the pore size remaining the varied parameter. However, there was a clear effect of the variable pore sizes in the study with the other parameters affecting the product distribution to a lesser extent. In order to extensively study the pore size effect, the use of ML was found necessary.

Key findings include:

Pore size does a significant contribution to the cobalt reducibility and dispersion. Larger pores (about 30 nm) encourage greater cobalt metal surface area and dispersion and greatly improve cobalt oxide reducibility, as seen by lower reduction temperatures in TPR profiles. In contrast to smaller pores which stabilise cobalt oxides through stronger metal-support interactions.

On the FT synthesis catalytic activity and the resulting product distribution, the best CO conversion rates were shown by catalysts with moderate pore-sizes (~15–20 nm), which also had comparatively higher methane ($CH_4$) and light hydrocarbon ($C_2$–$C_4$) selectivities. On the other hand, catalysts with larger pores showed a significantly higher selectivity for heavier hydrocarbons ($C_5^+$) but a lower conversion of CO. This phenomenon illustrates how cobalt particle size and pore diffusion properties affect the kinetics of chain development while maintaining active site accessibility.

The resulting implications for the product distribution were that as the pore size increases, methane selectivity decreases and heavy hydrocarbon production increases concurrently, indicating that larger pores promote improved chain propagation and restrict secondary hydrogenation processes. In order to maximise the generation of liquid fuels from syngas, understanding these effects is essential.

However, the intricate interactions between pore structure, cobalt particle size, dispersion, and mass transport processes inside the catalyst were highlighted by the fact that the maximum catalytic conversions did not correspond with the biggest metal surface areas, despite the fact that larger pores promote dispersion and reducibility.

These results collectively confirm that pore size tuning is a crucial tactic for managing structure-function connections of cobalt catalysts and adjusting Fischer-Tropsch product distributions to target fuel ranges.

## Recommendations

The following suggestions are put forth to direct future catalyst development and optimisation initiatives in light of the knowledge acquired:

The balance between conversion and selectivity alteration can be accomplished by optimising the pore size range. To optimise cobalt dispersion and reducibility while attaining advantageous selectivity towards heavier hydrocarbons, aim for pore sizes closer to 30 nm.

This range supports longer hydrocarbon chain formation by striking a compromise between diffusion characteristics and active site accessibility.

- Regulate the size of cobalt particles inside pores: create synthesis techniques that regulate cobalt crystallite size and dispersion inside these pores, in addition to pore size tuning. This will make it possible to minimise unwanted methane generation and maximise intrinsic turnover frequency.
- Investigate MSI further: cobalt-silica interactions have a significant impact on reducibility and catalytic behaviour; examine their nature in various pore designs using sophisticated characterisation techniques (such as in situ spectroscopy).
- Carry out pore structure engineering to address diffusion limitations: take into consideration meso- or hierarchical pore structures, which reduce internal diffusion constraints and improve catalyst stability by combining big pores for accommodating cobalt particles with smaller pores for increased surface area.
- Include studies on the stability of the catalysts with different pore sizes for an extended TOS: analyse the long-term catalyst performance under pertinent Fischer-Tropsch operating settings to determine the impact of cobalt particle growth and pore size on deactivation processes, including carbon deposition and sintering.

  Integrate mechanistic studies and computational methods: To help with the logical design of catalysts with specialised selectivity, employ modelling techniques and machine learning studies to forecast how pore size affects reactant and product diffusion and chain growth likelihood.
- Machine learning can be used to isolate and understand the distinct contributions of pore size to catalytic behaviour

By heeding these suggestions, cobalt-based Fischer-Tropsch catalysts that are more selective and efficient will be developed for the generation of clean fuel and valuable hydrocarbon compounds in upcoming sustainable energy processes.

## References


Bambal, A. S., Kugler, E. L., Gardner, T. H., & Dadyburjor, D. B. (2013). Effect of surface modification by chelating agents on fischer-tropsch performance of Co/SiO2 catalysts. *Industrial and Engineering Chemistry Research*, *52*(47), 16675–16688. https://doi.org/10.1021/ie4019676

Barbier, A., Tuel, A., Martin, G. A., Arcon, I., Arcon, I., Kodre, A., & Kodre, A. (2001). Characterization and catalytic behavior of CO/SiO2 catalysts: Influence of dispersion in the Fischer-Tropsch reaction. *Journal of Catalysis*, *200*(1), 106–116. https://doi.org/10.1006/jcat.2001.3204

Beer, M. De, Kunene, A., Nabaho, D., Claeys, M., & Steen, E. Van. (2014). *Technical and economic aspects of promotion of cobalt-based Fischer-Tropsch catalysts by noble metals – a review*. *114*(October 2013), 14–16.

Chen, Y., Wei, J., S. Duyar, M., V. Ordomsky, V., Y. Khodakov, A., & Liu, J. (2021). Carbon based catalysts for Fischer–Tropsch synthesis. *Chemical Society Reviews*, *50*(4), 2337. https://doi.org/10.1039/d0cs00905a

Cheng, K., Virginie, M., Ordomsky, V. V, Cordier, C., Chernavskii, P. A., Ivantsov, M. I., Paul, S., Wang, Y., & Khodakov, A. Y. (2015). Pore size effects in high-temperature Fischer – Tropsch synthesis over supported iron catalysts. *Journal of Catalysis*, *328*, 139–150. https://doi.org/10.1016/j.jcat.2014.12.007

Ghampson, I. T., Newman, C., Kong, L., Pier, E., Hurley, K. D., Pollock, R. A., Walsh, B. R., Goundie, B., Wright, J., Wheeler, M. C., Meulenberg, R. W., Desisto, W. J., Frederick, B. G., & Austin, R. N. (2010). Effects of pore diameter on particle size, phase, and turnover frequency in mesoporous silica supported cobalt Fischer-Tropsch catalysts. *Applied Catalysis A: General*, *388*(1–2), 57–67. https://doi.org/10.1016/j.apcata.2010.08.028

Glebov, L. S., & Kliger, G. A. (1994). The molecular weight distribution of the products of the Fischer-Tropsch synthesis. *Russian Chemical Reviews*, *2*, 185–195.

Gnanamani, M. K., Jacobs, G., Keogh, R. A., Shafer, W. D., Sparks, D. E., Hopps, S. D., Thomas, G. A., & Davis, B. H. (2015). Fischer-Tropsch synthesis: Effect of pretreatment conditions of cobalt on activity and selectivity for hydrogenation of carbon

dioxide. *Applied Catalysis A: General*, *499*, 39–46. https://doi.org/10.1016/j.apcata.2015.03.046

Gorimbo, J., Muvhiiwa, R., Llane, E., & Hildebrandt, D. (2020). Cobalt Catalyst Reduction Thermodynamics in Fischer Tropsch: An Attainable Region Approach. *Reactions*, *1*(2), 115–129. https://doi.org/10.3390/reactions1020010

Intarasiri, S., Ratana, T., Sornchamni, T., Phongaksorn, M., & Tungkamani, S. (2017). Effect of pore size diameter of cobalt supported catalyst on gasoline-diesel selectivity. *Energy Procedia*, *138*, 1035–1040. https://doi.org/10.1016/j.egypro.2017.10.090

Intarasiri, S., Tanakorn, R., Sornchamni, T., Tungkamani, S., & Phongaksorn, M. (2018). Pore size effect of mesoporous support on metal particle size of Co/SiO2 catalyst in Fischer-Tropsch synthesis. *International Journal of Avanced and Applied Sciences*, *5*(11), 80–85. https://doi.org/10.21833/ijaas.2018.11.011

Jacobs, G., Das, T. K., Zhang, Y., Li, J., Racoillet, G., & Davis, B. H. (2002). Fischer-Tropsch synthesis: Support, loading, and promoter effects on the reducibility of cobalt catalysts. *Applied Catalysis A: General*, *233*(1–2), 263–281. https://doi.org/10.1016/S0926-860X(02)00195-3

Jahangiri, H., Bennett, J., Mahjoubi, P., Wilson, K., & Gu, S. (2014). A review of advanced catalyst development for Fischer-Tropsch synthesis of hydrocarbons from biomass derived syn-gas. *Catalysis Science and Technology*, *4*(8), 2210–2229. https://doi.org/10.1039/c4cy00327f

Jakub, Č., & Ochodek, T. (2023). *Long-term performance of Co catalyst and Fischer-Tropsch synthesis setup under realistic conditions Long-term performance of Co catalyst and Fischer-Tropsch synthesis setup under realistic conditions*. 0–15.

Karaca, H., Safonova, O. V, Chambrey, S., Fongarland, P., Roussel, P., Griboval-constant, A., Lacroix, M., & Khodakov, A. Y. (2011). *Structure and catalytic performance of Pt-promoted alumina-supported cobalt catalysts under realistic conditions of Fischer – Tropsch synthesis*. *277*, 14–26. https://doi.org/10.1016/j.jcat.2010.10.007

Khodakov, A. Y., Chu, W., & Fongarland, P. (2007). Advances in the development of novel cobalt Fischer-Tropsch catalysts for synthesis of long-chain hydrocarbons and clean fuels. *Chemical Reviews*, *107*(5), 1692–1744. https://doi.org/10.1021/cr050972v

Khodakov, A. Y., Lynch, J., Bazin, D., Rebours, B., Zanier, N., Moisson, B., & Chaumette, P. (1997). Reducibility of cobalt species in silica-supported Fischer-Tropsch catalysts. *Journal of Catalysis*, *168*(1), 16–25. https://doi.org/10.1006/jcat.1997.1573

Kord-Tamandani, H., Mirzaei, A. A., & Zohdi, S. H. (2023). Significant improvement of catalytic performance for the Fischer–Tropsch synthesis over the cobalt catalysts supported on γ-Al2O3 granules: simultaneous effects of glucose surfactant and promoter. *Chemical Papers*, *77*(12), 7653–7668. https://doi.org/10.1007/s11696-023-03025-6

Li, H., Li, J., Ni, H., & Song, D. (2006). Studies on cobalt catalyst supported on silica with different pore size for Fischer-Tropsch synthesis. *Catalysis Letters*, *110*(1–2), 71–76. https://doi.org/10.1007/s10562-006-0086-y

Li, M., Dong, Y. W., & Li, L. Q. (2015). Pore size-controlled synthesis of molecular sieves and theirs difference in catalytic properties for Fischer – Tropsch synthesis. *Applied Petrochemical Research*, *5*(4), 371–376. https://doi.org/10.1007/s13203-015-0108-z

Maximov, A. L., Kulikova, M. V., & Dementyeva, O. S. (2020). *Cobalt-Containing Dispersion Catalysts for Three-Phase Fischer – Tropsch Synthesis*. *8*(November), 1–14. https://doi.org/10.3389/fchem.2020.567848

Mehmood, A., Ghafar, H., Yaqoob, S., Gohar, U. F., & Ahmad, B. (2017). Mesoporous Silica Nanoparticles: A Review. *Journal of Developing Drugs*, *06*(02). https://doi.org/10.4172/2329-6631.1000174

Merino, D., Pérez-Miqueo, I., Sanz, O., & Montes, M. (2016). On the Way to a More Open Porous Network of a Co-Re/Al2O3 Catalyst for Fischer-Tropsch Synthesis: Pore Size and Particle Size Effects on Its Performance. *Topics in Catalysis*, *59*(2–4), 207–218. https://doi.org/10.1007/s11244-015-0436-3

Mochizuki, T. (2018). Development of Highly Active Co/SiO2 Catalysts with Chelating Agents for Fischer-Tropsch Synthesis. *Journal of the Japan Petroleum Institute*, *61*(6), 332–341. https://doi.org/10.1627/jpi.61.332

Munirathinam, R., Pham Minh, D., & Nzihou, A. (2018). Effect of the Support and Its Surface Modifications in Cobalt-Based Fischer-Tropsch Synthesis. *Industrial and Engineering Chemistry Research*, *57*(48), 16137–16161.

https://doi.org/10.1021/acs.iecr.8b03850

Ning, W., Shen, H., Jin, Y., & Yang, X. (2015). Effects of weak surface modification on Co/SiO2 catalyst for Fischer-Tropsch reaction. *PLoS ONE*, *10*(5), 1–10. https://doi.org/10.1371/journal.pone.0124228

Okabe, K., Li, X., Wei, M., & Arakawa, H. (2004). Fischer-Tropsch synthesis over Co-SiO2 catalysts prepared by the sol-gel method. *Catalysis Today*, *89*(4), 431–438. https://doi.org/10.1016/j.cattod.2004.01.005

Okoye-Chine, C. G., Forbes, R., Gorimbo, J., Moyo, M., Liu, X., & Hildebrandt, D. (2023). The effect of pretreatment on SiO2 for Co-based Fischer-Tropsch synthesis catalysts: a study of the reduction pathway. *Chemical Engineering Communications*, *210*(7), 1097–1107. https://doi.org/10.1080/00986445.2022.2056452

Satterfield, C. N., Huff, G. A., & Longwell, J. P. (1982). Product Distribution from Iron Catalysts in Fischer-Tropsch Slurry Reactors. *Industrial and Engineering Chemistry Process Design and Development*, *21*(3), 465–470. https://doi.org/10.1021/i200018a020

Schulz, H. (1999). Short history and present trends of Fischer-Tropsch synthesis. *Applied Catalysis A: General*, *186*, 3–12.

Song, D., & Li, J. (2006). Effect of catalyst pore size on the catalytic performance of silica supported cobalt Fischer-Tropsch catalysts. *Journal of Molecular Catalysis A: Chemical*, *247*(1–2), 206–212. https://doi.org/10.1016/j.molcata.2005.11.021

Stober, W., Fink, A., & Bohn, E. (1968). Controlled Growth of Monodisperse Silica Spheres in the Micron Size Range. *Journal of Colloid and Interface Science*, *26*(1), 62–69. https://doi.org/10.1589/jpts.29.112

Tian, Z., Wang, C., Si, Z., Wang, Y., Chen, L., Liu, Q., Zhang, Q., Xu, Y., & Ma, L. (2018). Product Distributions of Fischer-Tropsch Synthesis over Core-Shell Catalysts: The Effects of Diverse Shell Thickness. *ChemistrySelect*, *3*(44), 12415–12423. https://doi.org/10.1002/slct.201801515

Wei, L., Zhao, Y., Zhang, Y., Liu, C., Hong, J., Xiong, H., & Li, J. (2016). Fischer-Tropsch synthesis over a 3D foamed MCF silica support: Toward a more open porous network of cobalt catalysts. *Journal of Catalysis*, *340*, 205–218. https://doi.org/10.1016/j.jcat.2016.04.019

Widiatmika, K. P. (2015). Fischer-Tropsch Synthesis. Effect of CO pretreatment on a ruthenium promoted Co/TiO2. *Etika Jurnalisme Pada Koran Kuning : Sebuah Studi Mengenai Koran Lampu Hijau*, *16*(2), 39–55.

Zeng, S., SU, H., DING, N., YU, S., & LIU, K. (2014). Co/SBA-16: Highly selective Fischer-Tropsch synthesis catalyst towards diesel fraction. *Journal of Fuel Chemistry and Technology*, *42*(4), 449–454. https://doi.org/10.1016/s1872-5813(14)60021-9

Zhang, D., Duan, A., Zhao, Z., & Xu, C. (2010). Synthesis, characterization, and catalytic performance of NiMo catalysts supported on hierarchically porous Beta-KIT-6 material in the hydrodesulfurization of dibenzothiophene. *Journal of Catalysis*, *274*(2), 273–286. https://doi.org/10.1016/j.jcat.2010.07.012

# CHAPTER 6: APPLICATION OF MACHINE LEARNING IN STUDYING THE EFFECTS OF CATALYST PORE SIZE ON FISCHER-TROPSCH SYNTHESIS PRODUCTS


## Abstract

Understanding the impact of catalyst pore size on the distribution of hydrocarbon products poses a significant challenge in Fischer–Tropsch (FT) synthesis. This study integrates machine learning with data from published experimental results to elucidate the impact of pore size in $Co/SiO_2$ catalysts on product selectivity. In this study a meticulously curated dataset of 400 experimental results from 60 distinct peer-reviewed studies was compiled, encompassing 79 distinct critical variables such as cobalt loading, reaction temperature, and calcination temperature. Employing the Categorical Boosting (CatBoost) algorithm, the selected model effectively predicted diverse selectivity outcomes, attaining robust predictive performance with $R^2$ values ranging from 0.68 to 0.79. One of the primary conclusions is that pore size is important; pores of about 14 to 18 nm favour the production of longer-chain hydrocarbons ($C_5^+$), which are more desirable for liquid fuels, whereas smaller pores tend to favour the formation of short-chain hydrocarbons($C_1$–$C_4$). Through the integration of various literature data, this study demonstrates how machine learning can reveal significant, quantifiable relationships between catalyst parameters and reaction results. In the end, this method offers a useful, data-driven tool to direct the creation of FT synthesis catalysts that are suited for particular product profiles.


## 6.1 Introduction

The pore size of the silica support is a crucial element influencing the functionality and product selectivity of $Co/SiO_2$ catalysts. The performance of $Co/SiO_2$ catalysts is also impacted by a wide range of other factors, including surface area, particle size, metal loading cobalt dispersion, the reducibility of cobalt oxides, and reaction conditions like pressure, temperature, and the $H_2/CO$ ratio (Bezemer et al., 2006; Prieto et al., 2009; Wu et al., 2015). Moreover, the size and dispersion of cobalt particles generated, the way reactants and

products diffuse through the catalyst, and ultimately the likelihood of hydrocarbon chain formation throughout the reaction are all influenced by the pore structure.

Several deductions have been previously made about the experimental studies on pore size effects on the product distribution, for example, in the previous chapter, longer-chain hydrocarbons ($C_{5^+}$), which are extremely useful as liquid fuels, were found to develop more readily on mesoporous silica supports with comparatively larger pore diameters, usually in the 18 -21 nm range. Conversely, short-chain hydrocarbons like methane and $C_2$–$C_4$ products are frequently produced more readily by catalysts with lower pore diameters (Cheng et al., 2015; Intarasiri et al., 2018; Kim et al., 2023; Mehmood et al., 2017; Osakoo et al., 2014). These results highlight the need to carefully control pore size and mesostructure in addition to the other product distribution influencing parameters when designing a catalyst for FT synthesis. Researchers can affect the cobalt particle size distribution and metal-support interactions, which jointly control catalytic activity and the range of hydrocarbon products produced, by adjusting the pore design (Intarasiri et al., 2017; Kamath et al., 2019; Kutuk, 2021).

### 6.1.1 Application of Machine Learning in Fischer-Tropsch Synthesis and Catalyst Research

The design and optimization of catalysts have improved dramatically as a result of recent developments in Machine Learning (ML), particularly for intricate procedures like FT synthesis (Shafiee, et al., 2025). Large and complex datasets may be analysed with the aid of ML, which also makes it possible to find patterns and connections that are hard to find using conventional experimental or theoretical methods.

In some of the uses of ML in FT Synthesis, Shafiee et al. ( 2024) optimized Co/Fe-supported catalysts designed for jet fuel synthesis ($C_8$–$C_{16}$ hydrocarbons) using a random forest-based machine learning framework. With $R^2$ values of 0.90 for selectivity and 0.92 for CO conversion, their model demonstrated remarkable predictive accuracy by utilizing an extensive dataset that included catalyst structural properties, preparation techniques, and reaction operating parameters Shafiee et al., (2025). In addition to offering a useful tool for directing catalyst design and process optimization to maximize targeted fuel ranges, this work showed how machine learning can successfully identify the critical parameters influencing catalyst performance towards the product distribution.

In support of these initiatives, a new study that was published by Shafiee et al., (2025) offers an additional ML-driven strategy aimed at improving Co/Fe catalysts and reaction parameters for the manufacture of clean fuel through FT synthesis. Faster screening and optimization are made possible by these data-driven frameworks than by traditional experimental studies.

Furthermore, when combined with microkinetic modelling, physics-informed machine learning provides significant computational acceleration (up to 10 000) without sacrificing physical fidelity in catalytic reaction simulations. These hybrid approaches effectively match catalyst parameters and explore reaction mechanisms under a variety of catalyst and reactor circumstances by fusing the predictive ability of machine learning with the accuracy of physical models (Demchuk et al., 2025). These developments collectively represent a new era in Fischer-Tropsch catalyst development, where physics-based modelling, data analytics, and machine learning work together to speed up the discovery and optimization of catalyst formulations and operating strategies, increasing the viability and efficiency of producing clean and sustainable fuels.

### 6.1.2 Advantages and limitations of ML in FT synthesis catalyst modelling

The application of ML in FT synthesis catalyst modelling has the following strengths:

1. Strong Predictive Performance: This study's CatBoost ML model demonstrated the strongest predictive capacity with $R^2$ test values ranging from 0.70 to 0.79.
2. Data Integration Across Studies: By synthesizing experiments and findings from various literature, machine learning (ML) enables thorough analysis that is not achievable through experiments.

3. Feature Interpretability: Partial dependence insights and feature significance metrics are provided by tree-based models, clearly illustrating the most influential parameters statistically and making the analysis much easier.

4. Managing Nonlinear, Multivariable Interactions: Interdependencies between pore size, loading, temperature, calcination, and other factors can be very complex because of the nonlinearity between them. This can be accommodated by contemporary models such as Random Forest, CatBoost, XGBoost.

**The limitations of applying ML to FT synthesis are as follows:**

1. Heterogeneity & quality of data: There is usually a great variation in the completeness and consistency of the literature data, frequently necessitating normalization or imputation (Shafiee, Jafari, et al., 2025).
2. Lack of physical restrictions in statistical models: Purely data-driven models may conflict with the underlying mass and energy balance constraints, chemistry, and laws of microkinetic or physical chemistry (Demchuk et al., 2025).
3. Model Interpretability: Although CatBoost can be easily understood, other machine learning techniques are still unknown in the FT synthesis sector, which makes it difficult to establish trust.
4. Potential overfitting with limited data samples: In high-dimensional spaces, datasets containing hundreds of datapoints may still be at risk of overfitting (Ghojogh & Crowley, 2023; Chen & Qi, 2023).

Although it has some drawbacks, ML still remains a powerful model in analyzing trends in FT synthesis to get a clearer understanding of experimental data and help create future engineered designs and more effective catalysts. In this chapter, six ML models were explored, and the best fit model for the dataset was selected and applied for the analysis of the FT synthesis parameters from experimental data.

## 6.2 Dataset Sampling and ML Model Choice

### 6.2.1 Sampling Method

**Data Pre-Processing and Cleaning**

In the use of ML for the analysis of experimental data, the data pre-processing step is a critical step to ensure that the model to be used will be reliable and efficient during data processing. This is because of the complexity of the experimental data obtained from multiple different sources, as well as that of the FT synthesis process itself. In this study, not all variables could be found in the same publication for all the datasets, and to enable the ML algorithm to be able to read the missing entities, normalization by averaging was used to fill in the points. For collecting the FT process data, for example, for variables such as the Time On Stream (TOS), the steady state values were selected for the entity. For parameters that involved missing variables, where a known equation that connected the variables exists, the relevant calculations connecting the variables were implemented, such as the use of the

Scherrer equation in obtaining the crystallite sizes from the XRD data (Nasiri et al., 2023). In cases that had some incomplete categorical descriptors, such as the catalyst preparation method, techniques like one-hot encoding and frequency-based imputation were implemented. After all the data was collected, data cleaning was done, removing the extreme outliers and sets with too many missing variables. These strategies ensured a robust model fitting, reducing the bias that is introduced by literature inconsistencies thereby improving the interpretability of the data in ML analysis.

**Data Processing**

The experimental results based on work done on cobalt catalysts supported on silica over the past ten years were compiled, and 79 parameters were used. After analysing their importance, their relative contribution towards determining the CO conversion and product selectivities was investigated. This was done in order to establish, using the machine learning method, the range of the pore sizes of the silica-supported cobalt catalysts used can be considered optimal for the maximum selectivities of each of the $C_1$, $C_2$-$C_4$ and $C_{5+}$ hydrocarbons, and also CO conversion in this work.

The data was collected from predominantly $Co/SiO_2$ catalyst-based FT synthesis studies under different experimental conditions. The webplot digitizer software was used to extract the information from graphs in cases where the actual figures were not provided. The sources which were used to select the data are listed in the bibliography section. These were selected based on the most recent FT studies that focused on Co-based FT synthesis, conducted in the past 10 years, with most of the studies considered involving silica-based supports. The use of silica as the basis for the study had some advantages because it can be synthesised in a number of ways (including hydrothermal and sol-gel), enabling researchers to methodically investigate the relationship between surface area and catalytic activity and selectivity (Bezemer et al., 2006).

Furthermore, it is easier to functionalise or alter the morphology of silica to study the function of pore sizes and surface chemistry in CO adsorption and catalytic activity because of its well-known and simple surface chemistry, which is primarily composed of siloxane bridges (Si–O–Si) and silanol groups (Si–OH) (Mu et al., 2021) and the behaviour and influence of the width and shape of the pores during the mass transfer of the reactants and products during the FT reaction (Ghampson et al., 2010; Intarasiri et al., 2017; Kim et al.,

2023; Li et al., 2006). The prediction tool used in this specific investigation was the CatBoost model, which was selected using the procedure explained in the following section.

### 6.2.2 Model selection

The model selection step is a critical part in determining the outcome of the analysis from the use of ML. The relationship between FT synthesis dependent and independent variables is very complex and non-linear, making it difficult to analyze hence the need to use the most effective model that can produce the best interpretation of the data. In this work, six tree-based models were assessed on how they perform in predicting the CO conversion and hydrocarbon product selectivities on the dataset consisting of 400 input parameters. The six advanced tree-based algorithms that were assessed are Random Forest (RF), Gradient Boosting (GB), Categorical Boosting (CatBoost), Extreme Gradient Boosting (XGBoost), Extremely Randomized Trees (Extra Trees) and Histogram–based Gradient Boosting (HistGradientBoosting) model.

The model performances were evaluated based on several parameters, which include the coefficient of determination ($R^2$) test and train metrics, and the Root Mean Square Error (RMSE), after the data had been tuned under k-fold cross validations with three iterations to improve the predictability of the models using hyperparameter tuning to obtain a more optimal performance.

The $R^2$ train generally indicates the way the model fits the experimental data while $R^2$ test shows the ability of the model to learn and generalize and predict unseen data, a best working model should contain a smaller gap between the $R^2$ train and test ($\Delta R^2$) while a bigger difference may indicate the possibility of overfitting or underfitting of the models to the data (Escanciano & Goh, 2019; Ghojogh & Crowley, 2023; Chen & Qi, 2023). The RMSE indicates the degree of deviation of the models predictions from the experimental values so a good model contains a minimum deviation. Table 6.1 shows the target parameters and the evaluation metric values obtained during the model selection process.

Table 6.8. The behaviours of different ML algorithms on the target parameters

| Target | Model | $R^2$ Train | $R^2$ Test | $\Delta R^2$ | RMSE Train | RMSE Test | Best model placing |
|---|---|---|---|---|---|---|---|
| | Random Forest | 0,95 | 0,65 | 0,30 | 5,97 | 14,19 | 3 |
| | Gradient Boosting | 0,99 | 0,58 | 0,41 | 2,83 | 15,50 | 5 |

| | | | | | | | |
|---|---|---|---|---|---|---|---|
| CO Conversion (%) | XGBoost | 0,99 | 0,69 | 0,31 | 1,88 | 13,39 | 2 |
| | CatBoost | 0,99 | 0,71 | 0,28 | 2,41 | 12,91 | 1 |
| | ExtraTrees | 0,97 | 0,65 | 0,31 | 4,59 | 14,07 | 3 |
| | HistGradientBoosting | 0,98 | 0,54 | 0,45 | 3,56 | 16,31 | 6 |
| $C_1$ Selectivity (%) | Random Forest | 0,92 | 0,72 | 0,20 | 2,79 | 6,18 | 2 |
| | Gradient Boosting | 1,00 | 0,70 | 0,30 | 0,48 | 6,39 | 3 |
| | XGBoost | 1,00 | 0,69 | 0,31 | 0,48 | 6,48 | 4 |
| | CatBoost | 0,99 | 0,74 | 0,26 | 0,80 | 5,99 | 1 |
| | ExtraTrees | 0,91 | 0,68 | 0,23 | 2,95 | 6,56 | 5 |
| | HistGradientBoosting | 0,93 | 0,63 | 0,30 | 2,64 | 7,10 | 6 |
| $C_2$-$C_4$ Selectivity (%) | Random Forest | 0,90 | 0,73 | 0,17 | 2,32 | 4,40 | 5 |
| | Gradient Boosting | 0,98 | 0,75 | 0,23 | 1,07 | 4,18 | 4 |
| | XGBoost | 0,98 | 0,79 | 0,19 | 1,08 | 3,90 | 2 |
| | CatBoost | 0,98 | 0,78 | 0,20 | 1,07 | 3,98 | 3 |
| | ExtraTrees | 0,90 | 0,79 | 0,12 | 2,31 | 3,89 | 1 |
| | HistGradientBoosting | 0,96 | 0,72 | 0,24 | 1,50 | 4,49 | 6 |
| $C_{5+}$ Selectivity (%) | Random Forest | 0,89 | 0,75 | 0,15 | 5,40 | 9,27 | 4 |
| | Gradient Boosting | 0,97 | 0,73 | 0,24 | 2,75 | 9,50 | 5 |
| | XGBoost | 0,97 | 0,79 | 0,18 | 2,69 | 8,38 | 1 |
| | CatBoost | 0,98 | 0,78 | 0,20 | 2,39 | 8,67 | 2 |
| | ExtraTrees | 0,89 | 0,75 | 0,14 | 5,51 | 9,18 | 3 |
| | HistGradientBoosting | 0,68 | 0,56 | 0,12 | 9,42 | 12,26 | 6 |

From the table, Cat Boost performance was comparatively the best in the analysis of CO conversion and $CH_4$ selectivity, and the third and second best at predicting the $C_2$-$C_4$

selectivity and $C_{5+}$ selectivities, respectively, where Extra Trees and XGBoost were the best models respectively. Since uniformity is required for comparison, the CatBoost model was selected as the best model overall to do further analysis on the whole data set.

## 6.3 Results and analysis

### 6.3.1 Feature Importance Analysis of the Input Parameters

A detailed understanding of the way the FT synthesis process parameters and catalyst properties affect the ML model predictions is critical for deducing scientific and engineering insights. In this section, after expanding the main categories like catalyst promoters and different forms of the supports (mainly silica based) 79 independent parameters were analyzed and their influence on the dependent variables, namely, CO conversion and hydrocarbon selectivity, was assessed. Feature importance analysis is a critical step that helps identify the most dominant parameters that influence the data interpretability and behaviour of the model towards the target product. Furthermore, ranking the parameters in order of their overall impact on the dependent variables assists in the optimization of the experimental design and identifies the parameters that can be tuned to easily improve the process performance.

The main focus of the feature importance analysis in this chapter was also to be able to determine the relative importance of the catalyst pore size among the 79 different parameters that were used in the study.

Generally, the effects of the catalyst pore size in the FT synthesis product selectivity can be studied differently based on the range of the CO conversion values. Usually at very low CO conversions, around (0 - 20%) the reaction will be still unstable and at too high CO conversions there is usually some readsorption and secondary reactions that influence the selectivity results (Kruit et al., 2013; Schulz, 2006).

The data used in the research was classified into two clusters: one with the CO conversion values between 20 - 60% and the other cluster consisting of all 400 data points in the whole population, with CO conversion values ranging from 0 - 98%. The relative importance of the parameters in these two clusters was then analysed to also study the effects of pore size during these different CO conversion ranges.

The data for CO conversion at < 20% falls in the regime of rate of reaction control, while the data for CO conversion at > 60% falls in the regime of film mass transfer control. The

selectivity data for CO conversions in the range of 20 to 60% are therefore most likely to be affected by pore diffusion limitations. This means that the data in the CO conversion range from 20 to 60% is the most suitable data for analysis to determine whether pore size has an effect on product distribution (Unglaub & Jess, 2023).

Python software was used to analyse the data sets in each case implementing the CatBoost model to analyse the data. Splitting the datasets resulted in seven target product selectivity ranges, these were $C_1$, $C_2$-$C_4$, and $C_{5+}$ selectivities for the two clusters and the CO conversion for the whole population.

After running three iterations under k-fold validation to tune the model and determine the best fit to the data the $R^2$ Test values for the CO conversion, $C_1$, $C_2$-$C_4$, and $C_{5+}$ selectivities were 0.7, 0.74, 0.78 and 0.79 for the whole population and 0.68, 0.73, 0.69 and 0.7 for the 20 – 60 % conversion data set, respectively. It was noted that the $R^2$ values for the 20 - 60% CO conversion data set were generally lower than those obtained from the whole population, this was caused by the relatively fewer points in the data set that resulted from the exclusion of the data for CO conversion < 20% and > 60%. The use of a greater number of values in the ML study generally results in an increase of the $R^2$ value as the algorithm will have more information to learn from. However, there was an improvement in the Mean Absolute Percentage Error (MAPE) and RMSE in the 20 – 60% CO conversion data set. Table 6.2 summarizes the $R^2$, RMSE, and MAPE for the two data sets.

Table 6.2. Metrics for each target variable in the whole population and the 20-60% CO conversion range

| | Whole population | | | 20 – 60% CO conversion data set | | |
|---|---|---|---|---|---|---|
| | $R^2$ Test | RMSE | MAPE | $R^2$ Test | RMSE | MAPE |
| CO Conversion | 0.70 | 12.91 | 0.44 | 0.68 | 8.615 | 0.22 |
| $C_1$ Selectivity | 0.74 | 5.99 | 0.46 | 0.73 | 3.27 | 0.15 |
| $C_2$-$C_4$ Selectivity | 0.78 | 3.98 | 0.43 | 0.69 | 3.08 | 0.25 |
| $C_{5+}$ Selectivity | 0.79 | 8.67 | 0.14 | 0.70 | 6.87 | 0.07 |

The feature importance of the parameters towards each of the target parameters was different on both datasets, with different parameters emerging as the most influential parameters in each set.

Figures A1 to A7 in the appendix section show the schematic representations of the feature importance of the parameters used in this study, presenting the variations observed in the independent parameters in the analysis of each target parameter. In the whole population dataset, catalyst loading was the main influential parameter towards the CO conversion having a relative importance of 18% compared to the other 78 parameters. The calcination time with a relative importance of 10%, calcination temperature with a relative importance of 14%, reaction temperature with relative importance of 15% were found as the most important parameters towards $C_1$, $C_2$-$C_4$ and $C_{5+}$ selectivity respectively as shown in in Figure A1 – A4.

However, the feature importance was not the same after restricting the data set to the values involving 20 - 60 % CO conversion. In this set, although the catalyst loading was still the most influential parameter with a relative importance of 14% for CO conversion, there were notable changes in the relative importance of the other parameters. In particular, the relative importance of the most influential parameter changed: pore size increased to 16% for $C_1$ selectivity (replacing calcination time as the mst important parameter), calcination temperature with a relative importance of 12% for $C_2$-$C_4$ selectivity (replacing calcination temperature), and pore size again with a relative importance of 21% for $C_{5+}$ selectivity (replacing reaction temperature). See Appendix A.1-A.8 for the pie chart representations.

These findings suggest that there is a notable difference in the effects of the independent variables on the product distribution in FT synthesis on the different datasets which correspond to different CO conversion ranges. However, in each case, catalyst loading and calcination temperature were the most important parameters for the CO conversion and the $C_2$-$C_4$ selectivities, respectively.

Looking at the five most influential parameters towards the target variables it is notable that pore size appears among the top five in all the CO conversion and selectivity ranges with varying impacts on each data set. A closer look at the relative importance of pore size in influencing the product distribution will be discussed in the following section.

### 6.3.2 Analysis of the Relative Importance of Catalyst Pore Size Towards the Target Parameters

The five most important parameters were pointed out in each of the clusters towards the influence on the CO conversion and hydrocarbon selectivities among the 79 independent variables that were considered in the study, and the strong influence of catalyst pore size can be noticed in all the ranges as it appears among the top five variables in each case. A plot of these for each cluster are shown in Table 6.3.

By limiting the data set to the values obtained from the CO conversion in the 20 – 60% range, the effect of pore size becomes distinct and generally stronger in each case. In the whole population data set the pore size is the fifth most important parameter in influencing the CO conversion, the third most important parameter towards the $CH_4$ selectivity, the fourth most important parameter towards the $C_2 – C_4$ selectivity and the second most important parameter towards the $C_{5+}$ selectivity.

However, there is a general increase in the relative importance of the pore size upon limiting the data set to the 20 – 60% CO conversion. For the CO conversion, the pore size effect increases in strength from 6% relative importance among the parameters to 10% at which it becomes the second most important parameter. For the $CH_4$ selectivity, the pore size influence rises sharply from the third position with a relative importance of 7% to become the most influential parameter with a relative importance of 15%. For the $C_{5+}$ selectivity, the pore size influence also rises sharply from being the second most important parameter with a relative importance of 10% and becomes the most influential parameter with a relative importance of 21% (more than double) which is the highest relative importance showing that the pore size has the greatest influence towards the production of the long chain hydrocarbons. However, for the influence towards the $C_2$-$C_4$ hydrocarbons selectivity where there is a slight drop from 8% to 6% in the relative importance for pore size at which it becomes the fifth most important parameter in the 20 - 60% CO conversion cluster moving from the fourth position when the whole population is considered.

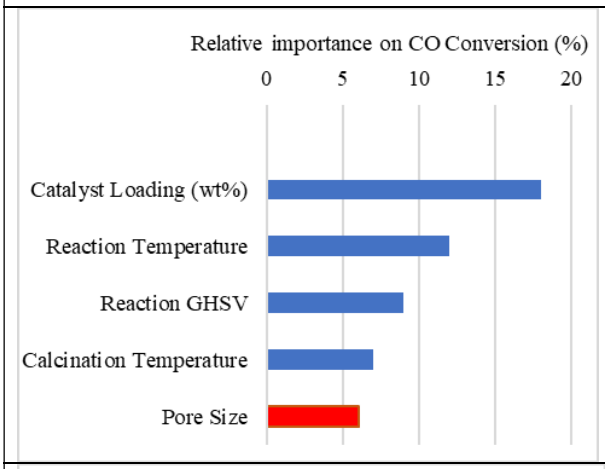
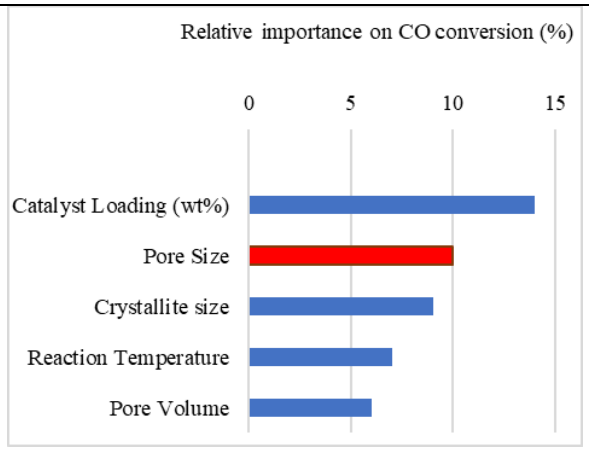
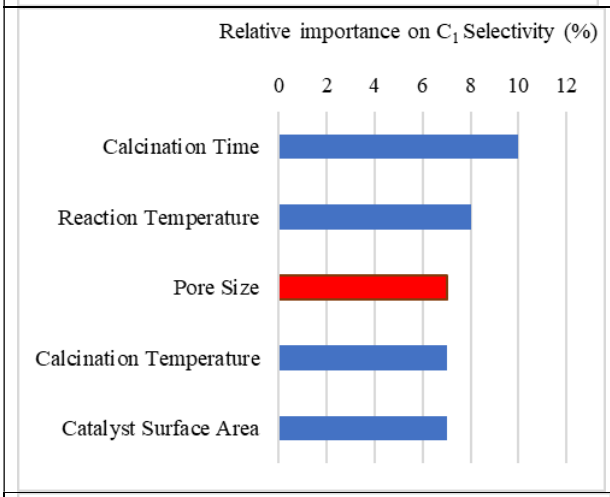
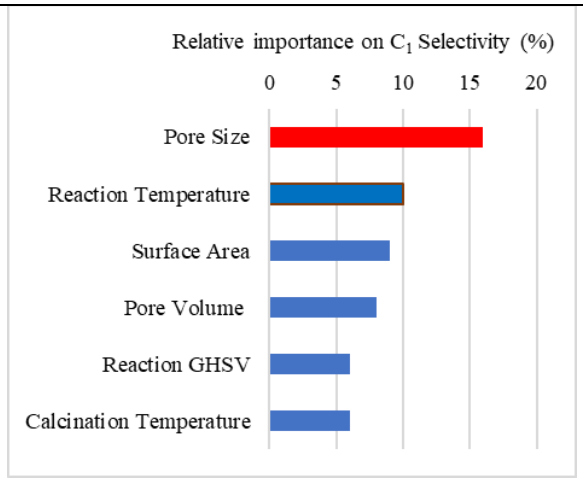
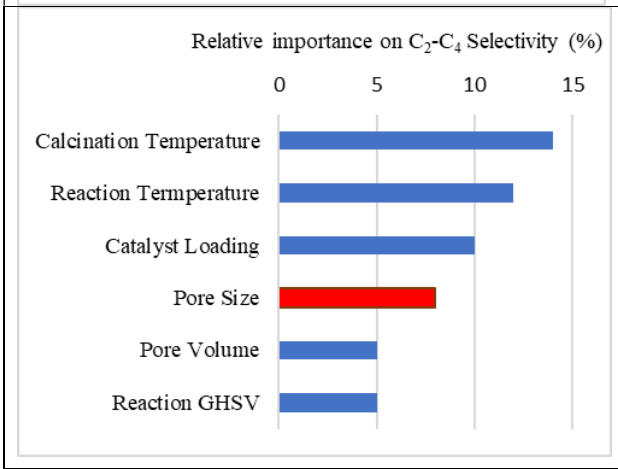
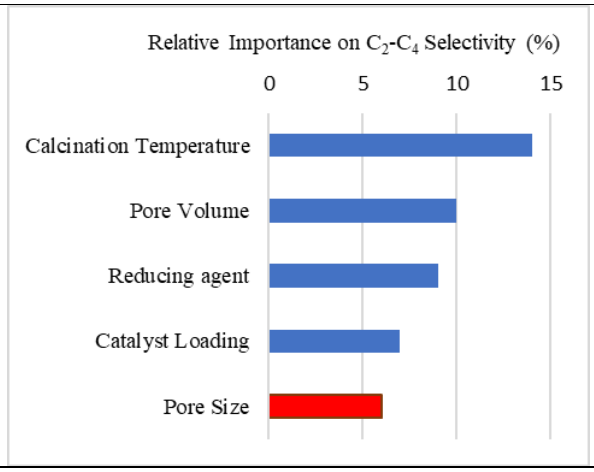
These results generally show that there is a lesser impact of the pore sizes on the FT synthesis product distribution when too low CO conversions or too high CO conversions are included in the study of the pore size effects. Generally, it has been reported that at low CO conversions the reaction will be dominated by the intrinsic reaction kinetics most influenced by parameters, like catalyst loading and reaction temperature, which directly corresponds to the availability of the active sites of the catalyst (Teimouri et al., 2021). This can be seen in

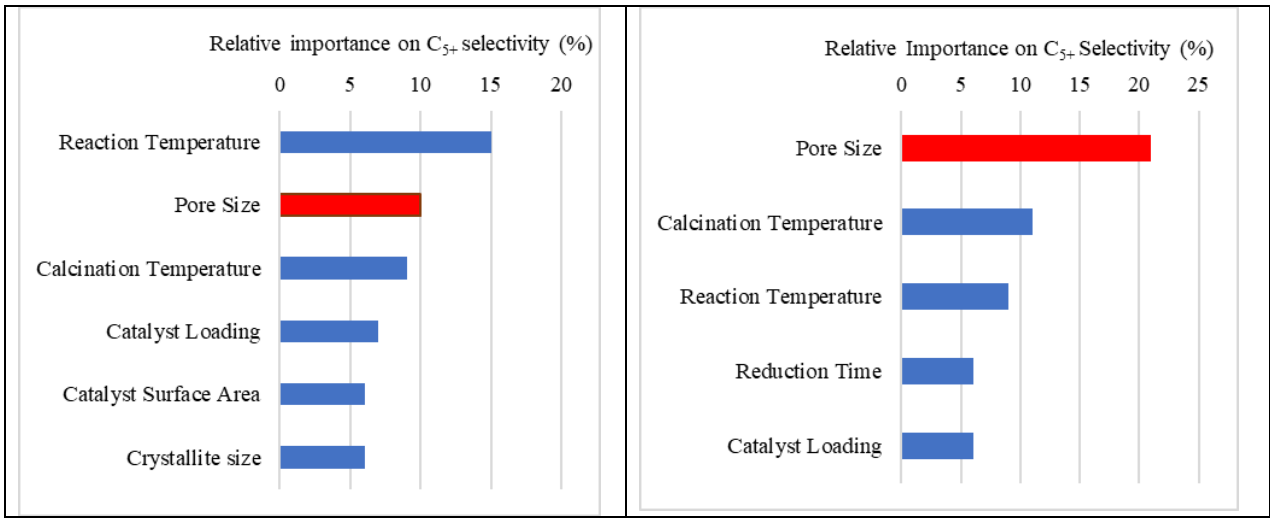
the influence and importance of the catalyst loading and reaction temperature on the product selectivity observed in Table 6.3 on the whole population and 20-60% CO conversion set respectively, it can be observed that the effect of these parameters is more pronounced when the whole population is considered while they become less significant upon considering the 20 – 60% CO conversion range of values. For instance, tracking the behaviour of the reaction temperature, its relative influence is 12%, 8%, 12% and 15% on the whole population towards CO conversion, $C_1$, $C_2$-$C_4$, $C_{5+}$ selectivity and 7%, 10%, less than 6 % and 9% towards CO conversion, $C_1$, $C_{2-4}$, $C_{5+}$ selectivity when CO conversions in the 20-60% range are considered. Catalyst loading also shows a typical decrease in the influence on these parameters in the two data sets, this is perhaps due to there being a large percentage of data points in the whole population set that belong to the 0-20% CO conversion range, compared to those that belong to the > n60% CO conversion range. This is because experimental researchers usually choose a GHSV to achieve a CO conversion that is less than 20% so as to obtain reaction data that is kinetically dependent rather than controlled by film or diffusion mass transfer, so as to be able to study the intrinsic selectivity of the catalyst, rather than that governed by reactor design parameters like catalyst pellet size or GHSV.

When the CO conversions become too high (>60% range), in this region mass transfer limitations due to film diffusion become more prominent in the FT synthesis reaction (Li et al., 2017; Unglaub & Jess, 2023). Under these conditions, secondary reactions are also more prone to occur, thereby contributing towards a shift in hydrocarbon selectivity (Yang et al., 2014). These factors therefore play a bigger role, impacting the relative importance of the effects of the catalyst physical properties such as the pore size. Sometimes wax accumulation also occurs at these conditions causing pore blockage and mass transfer limitations thereby obscuring the effects of pore size (Unglaub & Jess, 2023).

Under intermediate CO conversions in the 20-60 % range the CO conversion and product selectivity is neither dominated by film mass transfer or the reaction kinetics but rather the pore diffusion mass transfer (Li et al, 2017; Becker et al, 2016) thereby making the pore size effect more evident and robust. This explains the more notable relative influence of the pore sizes observed in Table 6.3 in the 20-60% CO conversion range.

Table 6.3. A summary of the comparison of the impact of pore size on the two different data sets analysed

| Whole population | 20-60% CO Conversion |
|---|---|
|  |  |
|  |  |
|  |  |




### 6.3.3 The effects of $Co/SiO_2$ catalyst pore sizes and the five most important parameters on the CO conversion and product distribution.

Unlike using the traditional statistical methods to analyse data, integrating ML in the extraction and analysis of patterns enables the handling of extremely complex non-linear datasets and the ability to easily extract the patterns that govern the catalytic behaviour in FT synthesis. The previous section explained the use of ML to identify and rank the most influential parameters on CO conversion and product selectivity. Among these identified variables, pore size appeared among the top five most influential parameters which makes it important to investigate further, how the FT performance is affected by tailoring the pore size and the other most influential parameters. The pore size has been found in the previous section as a parameter that strongly influences the balance between mass transfer limitations and secondary reactions. However, parameters such as the catalyst loading, reaction and reduction temperature, GHSV, surface area, crystallite sizes and calcination temperature, and pore volume have also been found to play a critical role.

The cluster within the data set that had a CO conversion of 20-60% was selected for the in-depth analysis of the effect of pore size on the product distribution as it had been identified as the range of CO conversion in which the pore size influence is most prominent. Different parameters were found to impact the product distribution differently; however, generally, the five parameters that appeared frequently among the top-ranked parameters on the influence towards CO conversion and product selectivity are catalyst pore size, catalyst loading,

reaction temperature and calcination temperature. For the sake of consistency and ease of comparison, these parameters were chosen as the basis of analysis of interdependence, that is emphasis was placed on how the pore size, in conjunction with these parameters, affects the CO conversion and FT synthesis product distribution when a $Co/SiO_2$-based catalyst is used.

**Dependence of CO conversion on the pore size and the most influential independent variables on the CO conversion**

Figures 6.1 and 6.2 show the outcomes from the ML analysis displaying the effects of pore size on the CO conversion using the data set obtained from the 20-60% CO conversion range. The generalized plots are shown in Figure 6.1. CO conversion generally increases with an increase in pore size from below 4 nm to 11 nm, which appears to be the minimum pore size required for diffusion into and out of the catalyst particles, after which no further notable increase was observed, and a steady average CO conversion of 42 % is observed.

Upon increasing the reaction temperature, there is a steady decrease in the CO conversion from 100 – 240 $^oC$, followed by a steep decrease at 250$^oC$, where the CO conversion levels off at about 39.5 %. For the catalyst loading, there was a steep increase in CO conversion to a steady maximum value of 42% which is obtained at a loading of 12wt%. There was no clear notable change in the CO conversion upon varying the calcination temperature, however there was a small flattish maximum in CO conversion obtained when calcination temperatures of 350 – 450 $^oC$ are used after which a steady decrease was observed to a constant value of around 42.2%. The CO conversion remains steady from the crystallite size in the 5-8 nm range after which there was a sharp decrease, gradually levelling off at higher crystallite sizes.

The 3-D plots in Figure 6.2 give insight into how each of the parameters correlates with the catalyst pore size towards influencing the CO conversion. In Figure 6.2a, a three-way partial dependence plot is shown, illustrating how the CO conversion varies with the pore size and the reaction temperature. Generally, there is no clear trend observed when the pore size increases under constant temperature in the range 190 – 220 °C, but the plot does show that there is a higher CO conversion that is observed at a pore size of around 11nm. However, at higher temperatures in the range above 220 $^oC$, the CO conversion increases sharply and stays high at 42% in the 220-300$^oC$ range, after which it decreases sharply. This trend is observed because at lower temperatures CO activation and adsorption on the catalyst surface are limited by slow reaction kinetics, thereby also reducing the overall CO conversion at very

high temperatures, that is, those above 330°C. Factors such as catalyst sintering, increase of reaction rates of the undesired reaction pathways such as the cleavage of the C-C bond, which hampers the formation of long chain hydrocarbons, and termination reactions become more prominent, lowering the overall CO conversion (Van Santen et al., 2013).

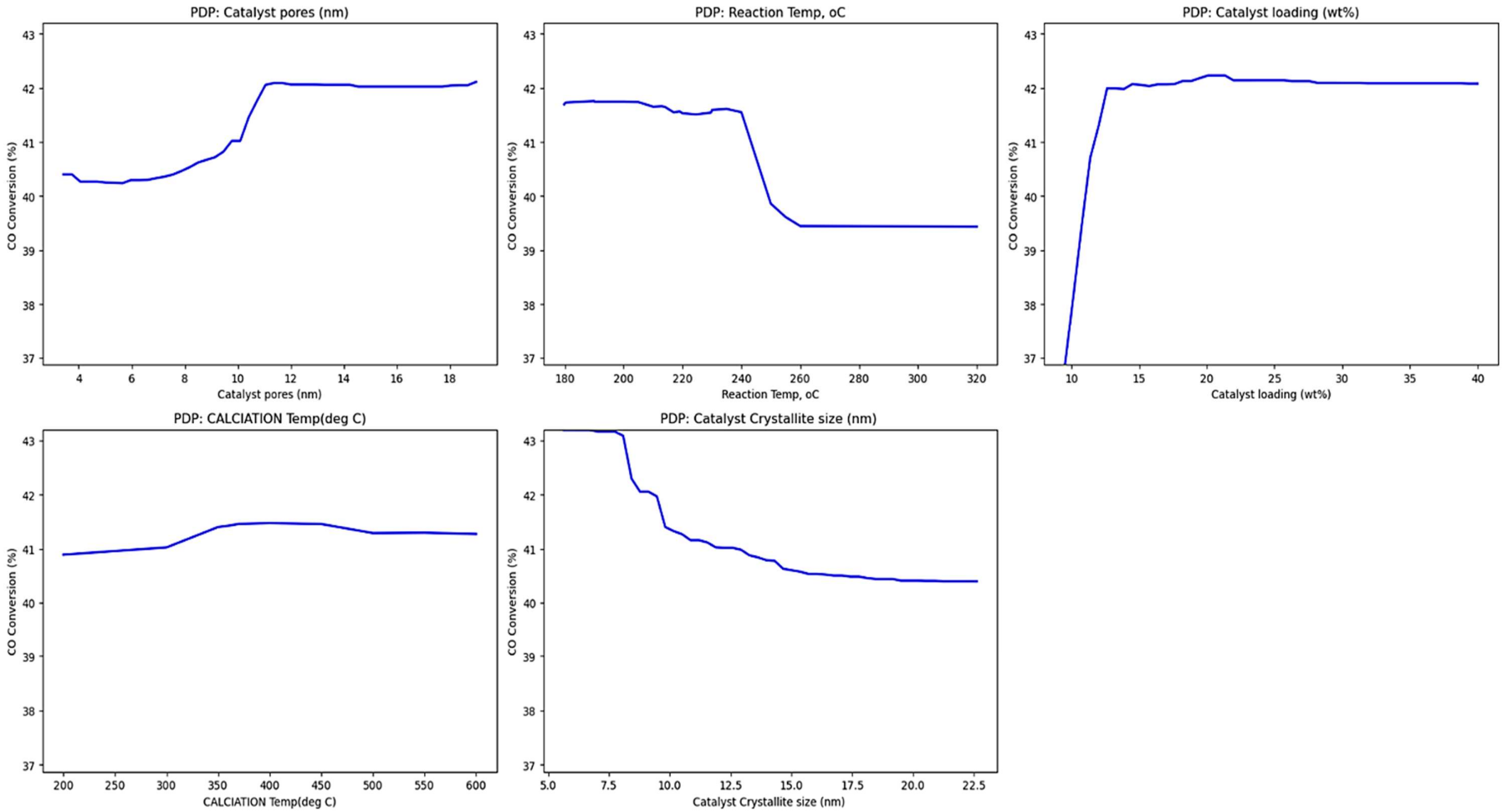



*Figure 6.1. Two-way partial dependence plot of CO conversion against the top five most influential parameters*

In Figure 6.2b, there is generally a sharp increase in the CO conversion as the pore sizes increase from 2 to 5nm at all the catalyst loading values studied. After the pore size of 5 nm there is no observed correlation between the catalyst pore sizes and the catalyst loading, as the CO conversion remains generally constant. As the catalyst loading increases from 10 – 35 wt% a general increase in the CO conversion was observed, with a sharp jump occurring at 20% metal loading, after which the conversions plateau. Taking a closer look at the pore size effect, a small peak in CO conversion could be noticed at around 9 nm especially at high catalyst loading values. This shows that the optimum pore size for obtaining the higher CO conversion is around 9 nm and this is even further enhanced at higher metal loadings, that is above 20%. The higher CO conversion values at elevated cobalt loadings are due to the presence of more active sites that are accessible and also the enhanced reducibility since more metallic cobalt is found when more active metal is loaded onto the support, which in turn increases the CO conversion (Iglesia, 1997; Khodakov et al., 2007; Rytter & Holmen, 2016).

In Figure 6.2 c, there is generally a periodic variation of the pore CO conversion, and as the pore size increases, three peaks were observed at 4-6, 10-12, and 15-17nm. There is no clear correlation between the pore size and the calcination temperature; however, the high CO conversion is generally observed at calcination temperatures of 400$^{o}$C and higher, which is mainly due to the increased reducibility of the catalyst at higher temperatures.

In Figure 6.2d, at pore sizes below 6 nm the CO conversion is generally higher than at pore sizes > 6 nm, with a notable general decrease as the pore size increases. A sharp jump in the CO conversion occurs at 15 nm after which it becomes constant for all pore sizes. In general, lower crystallite sizes correspond to lower CO conversions, while higher crystallite sizes were found to lead to more CO being converted. Overall, high catalyst pore sizes and low crystallite sizes were found to lead to low CO conversion, while lower catalyst pore sizes, less than 6 nm, and higher crystallite sizes above 15 nm resulted in the highest CO conversion. Noting that there is a higher catalyst surface area at smaller pore sizes, this, combined with larger crystallite sizes, leads to an increased density of the active sites, which subsequently increases the probability of higher dispersion of the metal to occur, therefore increasing the degree of reduction and availability of active sites. Larger cobalt crystallites are also easier to reduce than the smaller ones; the latter tend to form oxides or silicates that are more difficult to reduce to the metallic cobalt ( Saib et al., 2010; Iglesia, 1997; Khodakov et al., 2007).

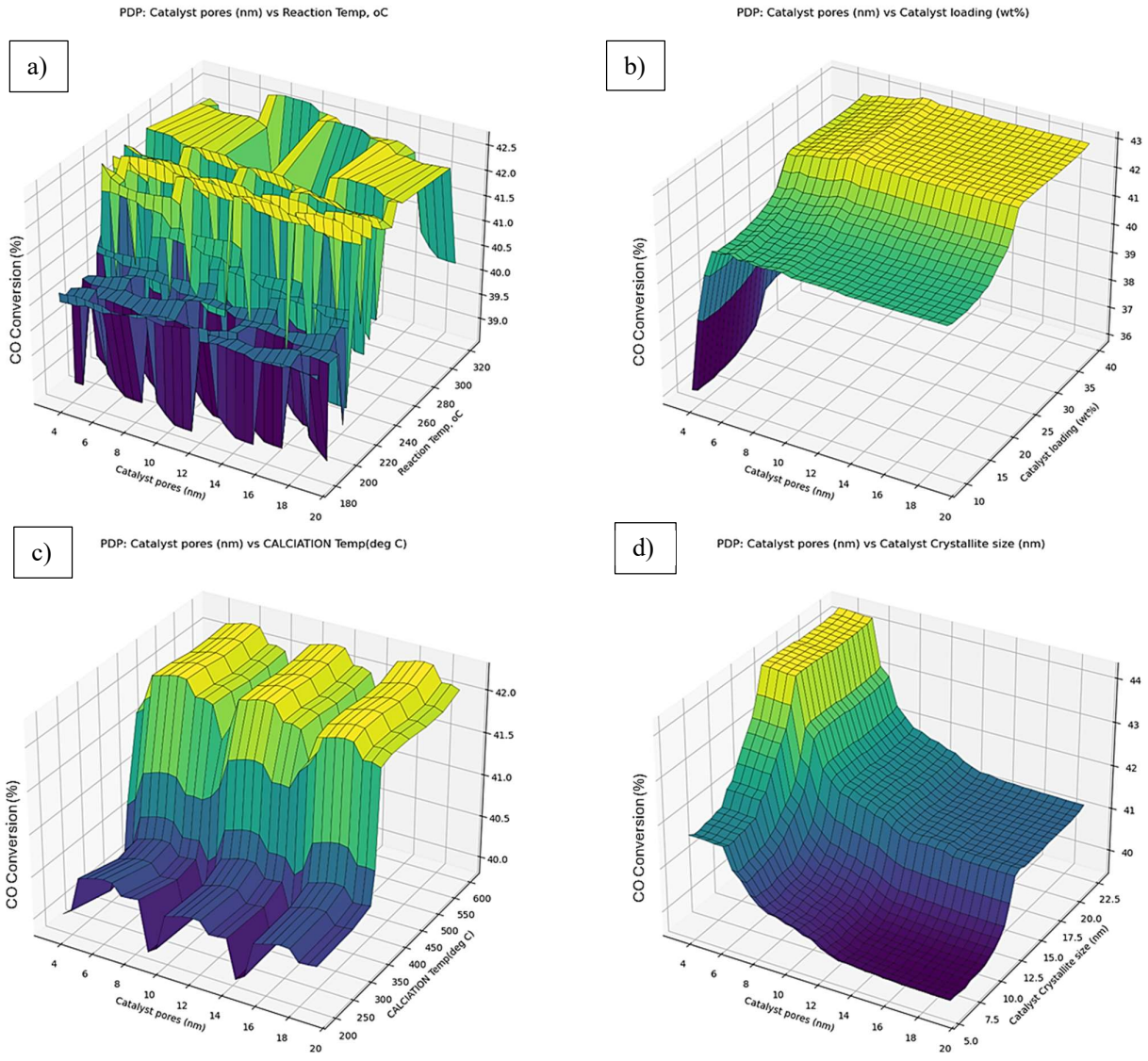



*Figure 6.2. Three-way partial dependence plots of pore sizes and CO conversion against the other top five most influential variables*

**Dependence of $CH_4$ selectivity on the pore size and the most influential independent variables**

The results obtained on the effects of the catalyst pore sizes, coupled with catalyst loading, calcination temperature, reaction temperature, and catalyst crystallite sizes on $CH_4$ selectivity are shown in Figures 6.3 and 6.4.

Figure 6.3 shows the general trends that were obtained from the dependence of $CH_4$ selectivity the above-mentioned parameters. Generally, the $CH_4$ selectivity shows a

decreasing trend as the pore size increases from < 4 nm to > 18 nm at which it becomes minimum; the steps are ascribed to the diverse sources of the data. The effect of reaction temperature on $CH_4$ selectivity shows the opposite general trend to that observed on the CO conversion, as the $CH_4$ selectivity is lower at low temperatures and higher at higher temperatures, reaching a maximum of 14.2% at 230$^oC$ after which it remains relatively constant. On the plot of the $CH_4$ selectivity against catalyst loading, a general decrease in the $CH_4$ selectivity was observed as the catalyst loading is increased above 10%. The $CH_4$ selectivity versus calcination temperature curve is flat at first, with a sharp decrease between 300 $^oC$ and 360$^oC$. The lowest $CH_4$ selectivity is observed in the 360$^oC$ to 500$^oC$ temperature range. The $CH_4$ selectivity appears to be independent of crystallite size; the selectivity generally varies between 13 to 13.6% without any significant change on increase in the crystallite size.

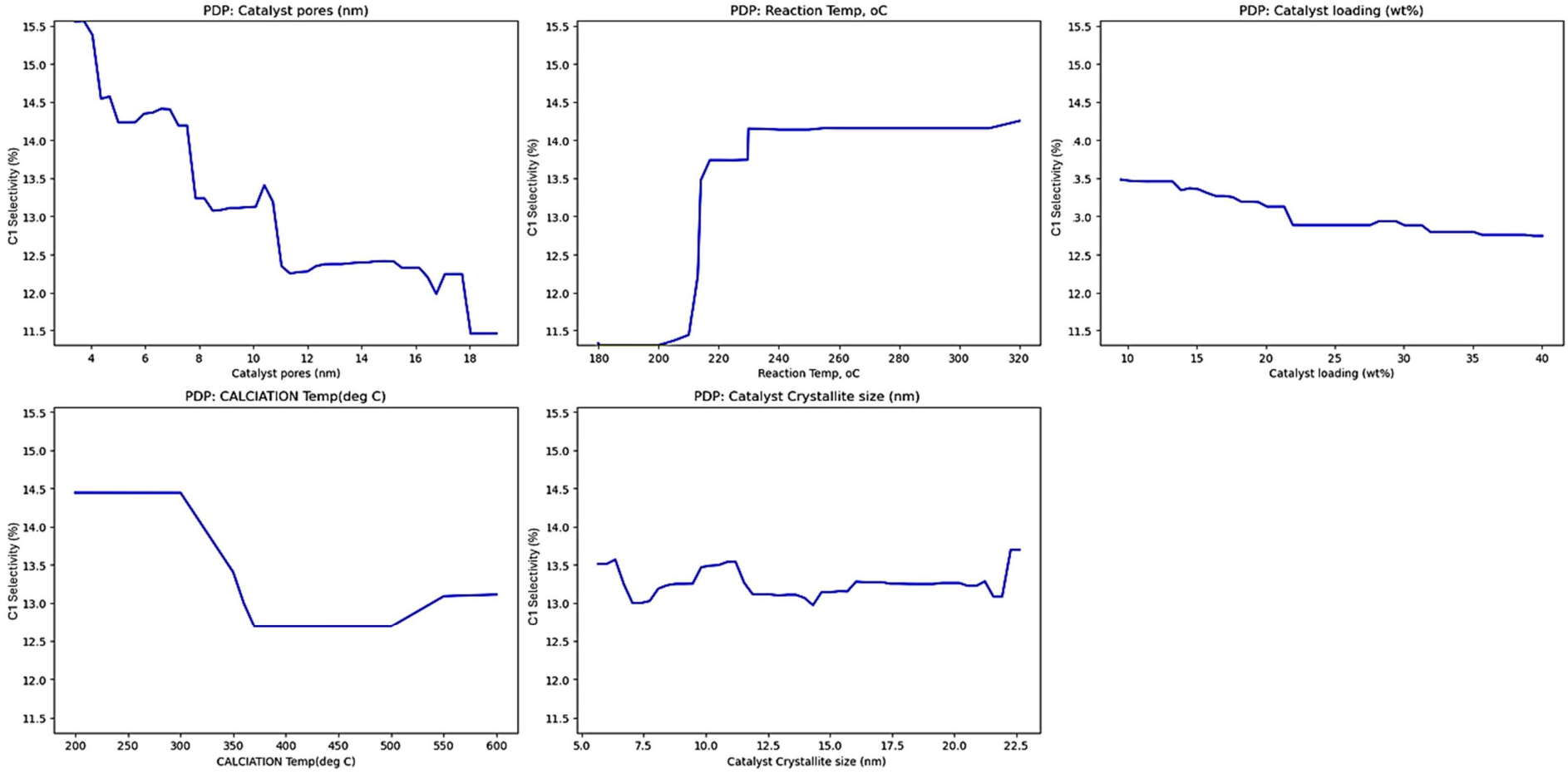



*Figure 6.3. Two-way partial dependence plots of $CH_4$ selectivity against the five most influential parameters*

In Figure 6.4a, a three-way partial dependence plot of pore size, reaction temperature, and $CH_4$ selectivity shows that there is generally a peak observed on the $CH_4$ selectivity in the pore size range of 6-12nm, outside of which dips are observed on either side of the pore size range. Upon the increase in temperature, there is a general decrease in the selectivity from 14% at a temperature range of 200-220$^{o}$C to 12%, a minimum is observed at 270$^{o}$C, and a further slight increase is observed afterwards. The maximum selectivity was observed in the temperature range of 200 - 220$^{o}$C. Overall, the maximum $C_1$ selectivity of 14.8% was found to be obtained between 4 and 7 nm and a temperature of 220$^{o}$C. However, upon increasing the temperature, a new pore size range of 6 to 8 nm was found to give a moderately high selectivity of 12.5% at higher temperatures in the range 250 – 280°C obtained which is the same temperature range that contains the lowest $CH_4$ selectivity values of around 10% when larger pore sizes above 8 nm are considered.

This is because at lower temperatures, the reaction will be kinetically limited as the reactions are slower. Under these circumstances, the larger pores allow easier and faster diffusion of products away from the active sites before further chain growth occurs, favouring the formation of more methane (Khodakov et al., 2007). Anderson, (1984) also supposed that under the mild conditions of temperatures around 220°C the chain growth probability will be lower and this promotes the occurrence of more termination reactions leading to the formation of methane. At elevated temperatures the smaller pores tend to restrict the diffusion of the heavier hydrocarbons, forcing more of the heavier hydrocarbons to be dehydrogenated leading to the formation of more methane (Dry, 2002). This phenomenon is responsible for the peak on $CH_4$ selectivity observed at higher temperatures but lower pore sizes in Figure 6.4a

Figure 6.4b shows a general decrease in the $CH_4$ selectivity as the catalyst loading increases. For the pore sizes, generally, lower catalyst pore sizes are connected with the higher $CH_4$ selectivity. Overall, the lowest $CH_4$ selectivities of 11.5% are observed at very high catalyst loadings of 38-42 wt% and larger pore sizes, while lower catalyst loadings in the range 10-12% and lower pore sizes in the range of 4 to 6 nm result in the greatest $CH_4$ selectivity of 15.2%. The decrease in selectivity at extremely large pore sizes is because better mass transport in the larger pores enhances the desorption and growth of longer chains, hence limiting the $C_1$ selectivity (Intarasiri et al., 2017, 2018). At higher Co loadings on silica, larger metallic crystallites tend to be formed, reducing the fraction of strongly interacting Co-

silicate species, which are difficult to reduce. The larger Co particles lead to lower $CH_4$ selectivity because chain growth probability increases, causing longer chains to be formed, as these particle sizes do not favour over hydrogenation to $CH_4$ (Zepeda, 2025).

In Figure 6.4c, the selectivity oscillates as the catalyst pore size increases, making it difficult to interpret the partial dependence of the pore size and the calcination temperature on the $CH_4$ selectivity, with peaks of the $CH_4$ selectivity of 16% obtained in the ranges: 0 to 4 nm, 6 to 8 nm, and 10 to 12 nm. However, the general trend shows that the highest $CH_4$ selectivity occurs in the 250 - 350°C calcination temperature range, which decreases to a stable value of 13% as the calcination temperature is increased above 400°C. This implies that there are moderate metal-support interactions in the 200 - 350°C calcination temperature range, making the Co species easily accessible for reduction while dispersed enough to form smaller crystallites, which are known to favour the formation of $CH_4$ as explained above (Bezemer et al., 2006). A further increase in the calcination temperatures leads to sintering and the growth of $Co_3O_4$ crystallites, which in turn leads to lower hydrogen coverage, favouring enhanced chain growth and therefore reducing the $CH_4$ selectivity (den Breejen, 2010).

Figure 6.4d shows the same trend observed with cobalt loading when the crystallite sizes are considered, the only notable difference being the peak in the selectivity being observed at a pore size of 8 nm. Overall, a maximum $CH_4$ selectivity of 15.2% was found at smaller crystallite sizes of 7.5 - 10 nm while the lowest $CH_4$ selectivity of 11% was observed at the largest crystallite size above 20 nm for the same reasons explained earlier (Bezemer et al., 2006 ; Zepeda, 2025).

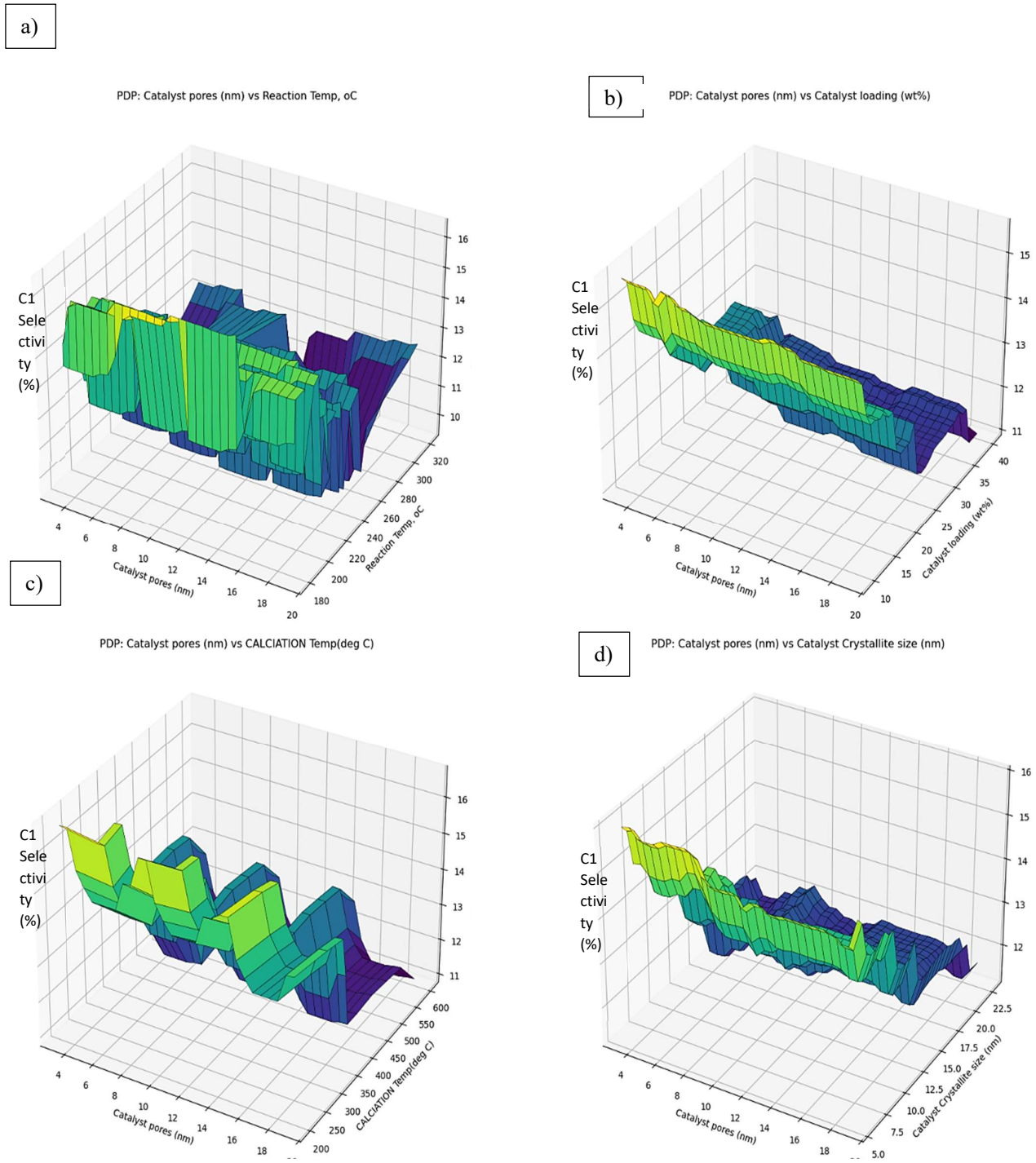



*Figure 6.4. Three-way partial dependence plots of $CH_4$ selectivity and pore size against the other five most influential parameters*

**Dependence of $C_2$-$C_4$ selectivity on the pore size and the most influential independent variables on the $C_2$-$C_4$ selectivity**

Figures 6.5 and 6.6 show the results obtained on the effects of the catalyst pore sizes, and catalyst loading, calcination temperature, reaction temperature, and catalyst crystallite sizes on $C_2$-$C_4$ selectivity.

The two-way partial dependence plots of $C_2$-$C_4$ selectivity against the five most influential parameters in Figure 6.5 show the general trends that were observed in the $C_2$-$C_4$ selectivity as the parameters vary. Generally, the maximum $C_2$ -$C_4$ selectivity observed in this cluster was around 10.5 to 11%, as the catalyst pore size increases, the $C_2$-$C_4$ selectivity decreases sharply from 2 to 9 nm, with slight decrease for pore sizes greater than 9 nm. As the reaction temperature increases, there is initially a slight decrease in the selectivity to a minimum of 9.65% at 215°C after which there is a sharp increase in selectivity observed to a maximum of 10.3% at 250°C, after which it levels off. For $C_2$-$C_4$ selectivity against catalyst loading, higher selectivities are obtained at catalyst loadings below 10% after which a gradual increase is observed until around 20 wt% catalyst loading, after which the selectivity flattens off at about 9.8%. As the calcination temperature increases from 200°C, the selectivity remains at a high value of 11%, followed by a sharp decrease from 300°C to 400°C, reaching a minimum of 9.2% after which a slight increase was observed to 9.4%. Upon analysing the effect of crystallite size, it can be observed that there was a general decrease in the selectivity from a maximum obtained at lower crystallite sizes in the 6 to 7 nm range, after which a sharp decrease was observed to reach a minimum constant selectivity of around 9.6% at a crystallite size of 9 to 12 nm.

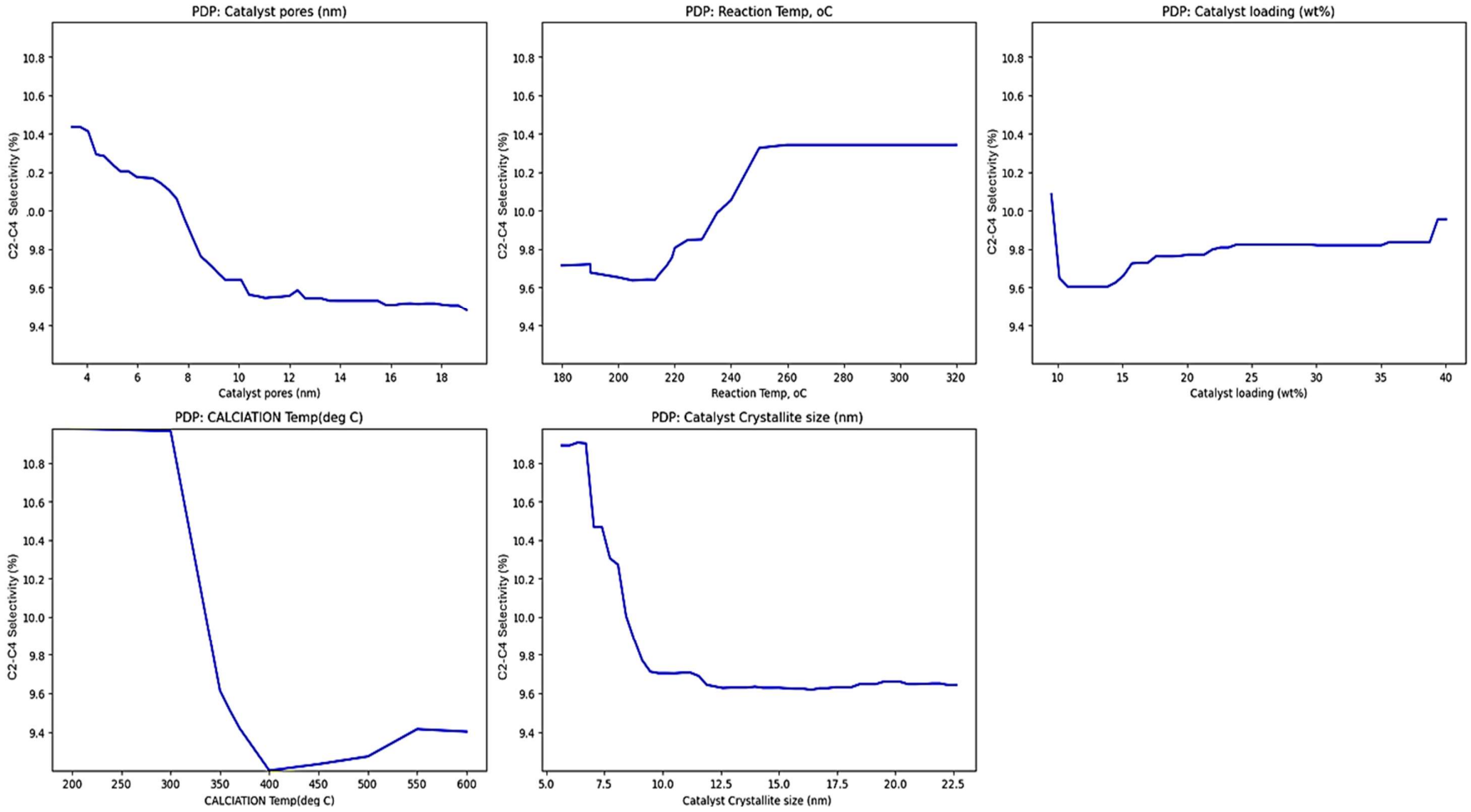



*Figure 6.5. Two-way partial dependence plot of $C_2$-$C_4$ selectivity against the five most influential parameters towards $C_2$-$C_4$ selectivity*

Considering the three-way partial dependence plot shown in Figure 6.6a, there appears to be a maximum selectivity at a pore size range of 6-8 nm, after which a steady decrease in $C_2$-$C_4$ selectivity was observed. Generally, an opposite trend to that observed on the $C_2$-$C_4$ selectivity against the reaction temperature plot was observed when the pore sizes are taken into consideration, with lower reaction temperatures in the range 200-220°C corresponding to the maximum selectivity of 10.6% and a drop in the selectivity to a minimum observed at 240°C after which there was a steady increase to 9.5%. The trend appears to be the same as that observed on $C_1$ selectivity, with a difference in the relative selectivity values where it can be noted that there were lower values for $C_2$-$C_4$ selectivity as compared to $C_1$ selectivity under the same conditions of pore sizes and reaction temperature. This may be because of the existence of chain termination and secondary reactions that are prone to occur on the longer chains to form more methane via readsorption, secondary hydrogenation, and cracking mechanisms (Iglesia, 1997; Bartholomew, 2001).

In Figure 6.6b, the $C_2$-$C_4$ selectivities are generally higher with a maximum of 10.6% observed in the 5 to 7 nm pore size range and 10 to 12wt% catalyst loading, which decreases with an increase in the catalyst loading to a minimum of 9.2% in the same pore size range. There is no significant increase in the $C_2$-$C_4$ selectivity when the pore size is increased for catalyst loadings of 15-35%. The reason for the trend is that at higher Co loadings, this increased amount of the active metal results in an increase in the chain growth probability, causing the products to shift towards long chain hydrocarbons ($C_{5+}$) and the smaller pores of the 5 to 7 nm size range allow secondary hydrogenation and readsorption to occur converting the shorter chains to longer hydrocarbons hence reducing the $C_2$-$C_4$ fraction (Bezemer et al., 2006; Xiong et al., 2008). On the other hand, under the same pore size range, at low Co loadings, dispersion of the metallic cobalt will be higher, and the catalyst active sites increase the probability of forming and releasing lighter hydrocarbons quickly before further propagation or over hydrogenation takes place, leading to the observed maximum selectivity under these conditions (Tavasoli et al., 2007; Herriko, 2012).

In Figure 6.6c, as observed with $C_1$ selectivity, no clear trend is observed when calcination temperature is considered as the third variable. Oscillations in the selectivity are observed with three peaks in the selectivity occurring at 4, 9, and 14 nm at 11.5% and the lowest selectivities are observed at the larger pore sizes of 17-19 nm. However, there is a general

trend observed upon variation of the calcination temperature in that relatively high selectivities are observed in the 200-300°C calcination temperature range and lower $C_2$-$C_4$ selectivities when the calcination temperature goes beyond 400°C. This is ascribed to the same reasons discussed in the previous section.

Considering the three-way partial dependence plot involving the crystallite size as shown in Figure 6.6d, generally, the selectivity decreases from a region of small pore sizes and smaller crystallite size to a region with larger pore sizes and larger crystallite sizes. The maximum $C_2$-$C_4$ selectivity of 11.3% was observed at a pore size range of 3 to 5 nm and crystallite size of 6 to 8 nm, which decreases to 10.5% at crystallite sizes above 9 nm. For pore sizes greater than 5 nm, the $C_2$-$C_4$ selectivity becomes constant at each crystallite size range, having values of 10% at crystallite sizes of 6 to 8 nm, and 9.2% which is the lowest $C_2$-$C_4$ selectivity observed at crystallite sizes from around 9 to 20 nm. Overall, high $C_2$-$C_4$ selectivity is observed at smaller pore sizes and small crystallite sizes, and the higher pore sizes and crystallite sizes result in lower $C_2$-$C_4$ selectivities. This is because of the higher dispersion of cobalt obtained for smaller crystallite sizes, which provides more edge and corner sites, and favours initiation and termination reactions rather than the propagation reactions that are responsible for the long chains. This increases the probability of producing more short-chain hydrocarbons in the $C_2$-$C_4$ range before further growth (Bezemer et al., 2006; Khodakov et al., 2007; Peron et al., 2021). As explained earlier, the smaller pores limit the residence time of the products, thereby reducing the probability of secondary reactions and re-adsorption from taking place due to faster desorption (Iglesia, 1997).

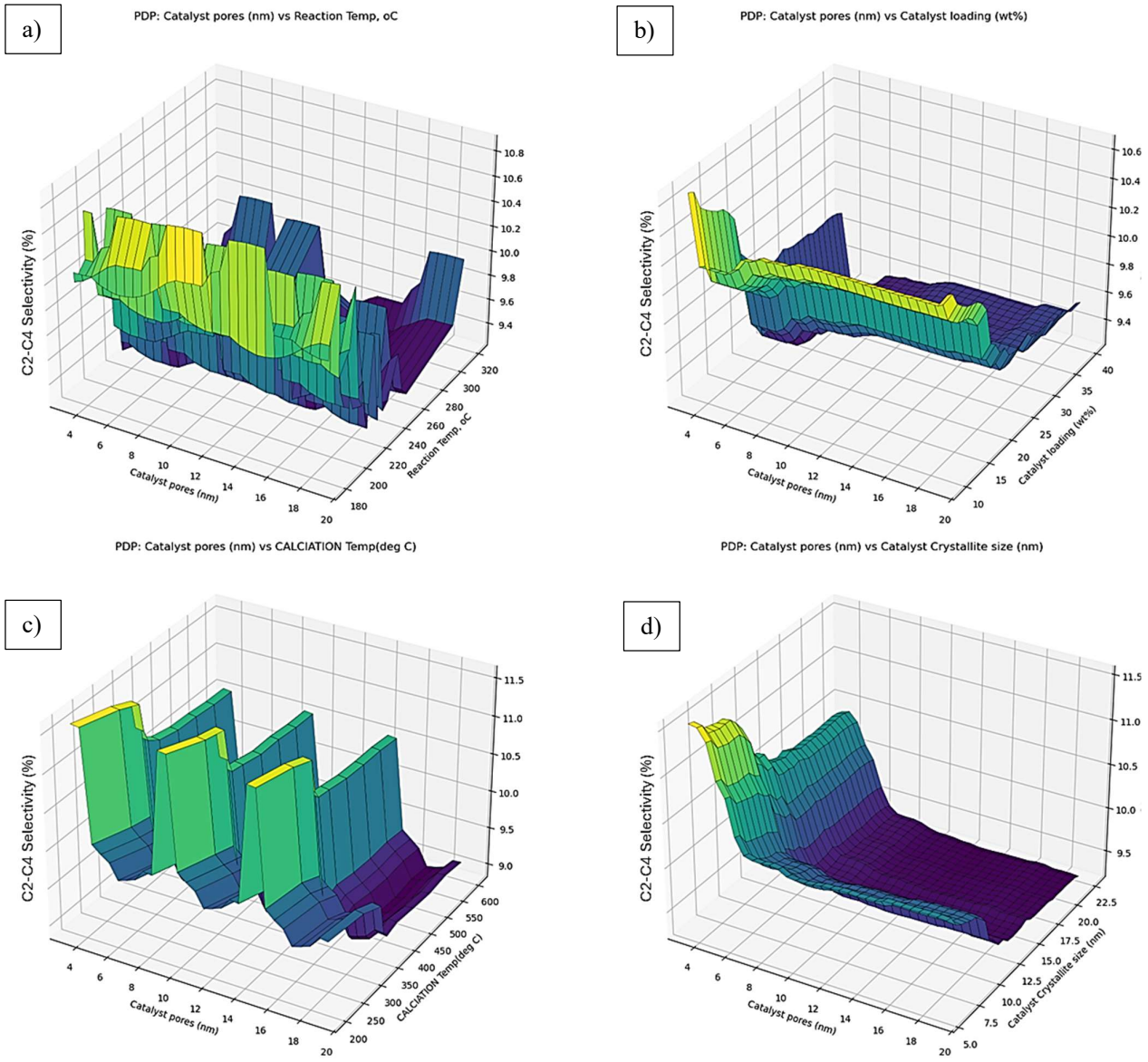



*Figure 6.6. Three-way partial dependence plots of $C_2$-$C_4$ selectivity and pore size against the other five most influential parameters towards $C_2$-$C_4$ selectivity.*

**Dependence of $C_{5+}$ selectivity on the pore size and the most influential independent variables on the $C_{5+}$ selectivity**

Generally, an inverse relationship between the graphs of the partial dependence of the short-chain hydrocarbons and that observed on the $C_{5+}$ hydrocarbons could be deduced from the graphs. Figures 6.7 and 6.8 show the results obtained from the analysis of the dependence of $C_{5+}$ selectivity on catalyst pore sizes, catalyst loading, calcination temperature, reaction temperature, and catalyst crystallite sizes. The two-way partial dependence plots in Figure 6.7

show the general trends that were obtained from the influence of the pore size, reaction temperature, catalyst loading, calcination temperature, and crystallite size.

The $C_{5+}$ selectivity generally increases as the pore size increases. A sharp increase was observed from 3 to 8 nm, after which there was a gradual, slight increase from 8 to 18 nm, where a maximum selectivity of 77.6% was observed. The reaction temperature generally showed the opposite trend to that observed with the pore sizes, as the $C_{5+}$ selectivity decreases as the reaction temperature increases. A constant selectivity was observed in the range of 180 to 210°C for reaction temperature after which a sharp decrease in the selectivity was observed in the 210-250°C temperature range to a minimum $C_{5+}$ selectivity of 74% which remains steady at higher temperatures. Upon varying the catalyst loading, an increase in the selectivity was observed in the catalyst loading range of 10-14% and a small maximum in $C_{5+}$ selectivity was observed at 14% catalyst loading, after which a slight decrease in selectivity was observed. On the plot of calcination temperature against $C_{5+}$ selectivity, the graph generally takes a parabolic shape, with a maximum being observed at 400°C. On the crystallite size plot, the $C_{5+}$ selectivity generally shows little dependence with a slight linear increase as the crystallite size increases.

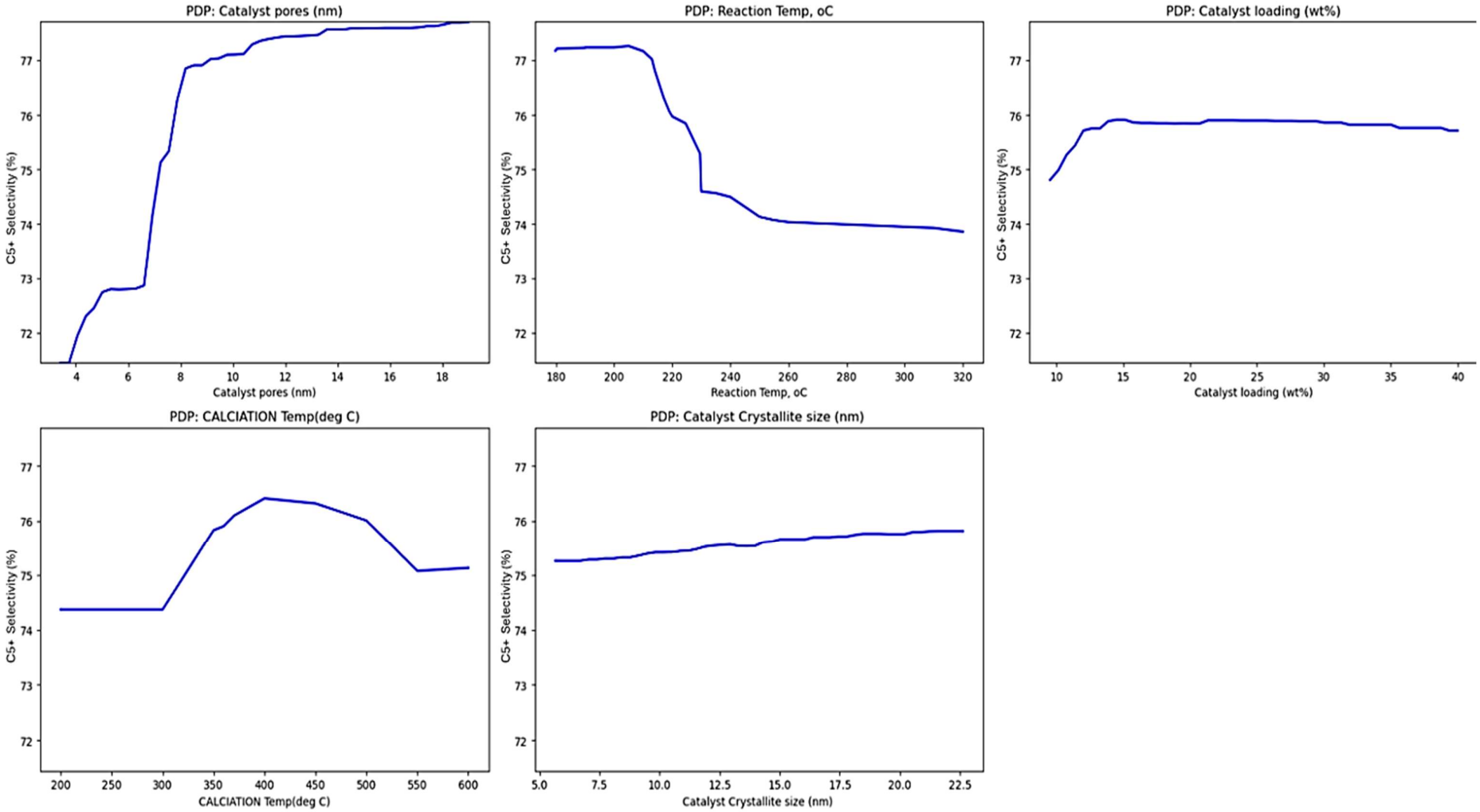



*Figure 6.7. Two-way partial dependence plot of $C_{5+}$ selectivity against the five most influential parameters towards $C_{5+}$ selectivity*

In Figure 6.8a, upon incorporating reaction temperature as the third variable in the pore size vs $C_{5+}$ selectivity graphs resulted in difficulty in clearly visualising the trend that was observed upon increasing the pore size. However, the graph generally shows maximum selectivities in the region corresponding to high temperatures and larger pore sizes. A maximum value of 80% selectivity was observed in the pore size range of 12 to 16 nm and 280 to 300°C reaction temperature and there was a dip in the selectivity at lower temperatures. This is because the larger pores are associated with reduced diffusion limitations and improved mass transport since they allow the longer chain hydrocarbons to diffuse quickly and easily away from the active sites before the secondary reactions take place (Iglesia, 1997; Khodakov et al., 2007). The larger pores also allow for easy of accessibility by the reactants allowing more $H_2$ and CO to be adsorbed, therefore making the propagation reactions more likely (van Steen & Claeys, 2008). Higher temperatures improve the kinetics of the activation of CO and consequently avail more of the surface carbon species that are needed for the propagation (Dry, 2002). Higher temperature also accelerates the diffusion of the carbon species leading to the formation of more $C_{5+}$ hydrocarbons before termination reactions occur (Cheng et al., 2015; Pandey et al., 2021; Wang & Wojciechowski, 1989). However, at very high temperatures, cracking reactions are more prone to occur (Keunecke et al., 2024; Pondini & Ebert, 2013), leading to the formation of the lighter hydrocarbons, causing the maximum selectivity to be observed in this 280-300°C range.

In Figure 6.8b, upon using catalyst loading as the third variable, generally high $C_{5+}$ selectivity was observed at high catalyst loading and larger pore sizes, while the lowest selectivities were obtained in the region of low pore sizes and low catalyst loading. Minimum $C_{5+}$ selectivity of 71% was observed at a small pore size of 3.5 nm and a catalyst loading in the range 9-12% from where there was a sharp increase in selectivity to about 73% at a pore size of 5 nm, after which it remains constant in the same catalyst loading range. A peak in the $C_{5+}$ selectivity, which happened to be the maximum of 78% was observed in the pore size range of 12-18 nm and 30-40% catalyst loading. The findings are explained by the fact that at higher cobalt loading, there are more active sites present and larger crystallite sizes, which are responsible for stronger CO dissociation and reduced secondary reactions, favouring the formation of more $C_{5+}$ hydrocarbons before termination occurs (Dry, 2002; Khodakov et al., 2007). The larger pores in the 12-18 nm range also facilitate better mass transfer, in contrast

to smaller pores, leading to the formation of more $C_{5+}$ hydrocarbons, as explained in the previous paragraph (van Steen & Claeys, 2008).

Figure 6.8c shows the same corrugated trends as in the pore sizes as those observed with $C_1$ and $C_2$-$C_4$ selectivities, where the selectivity tends to oscillate, making it difficult to extract meaning form the variation of the selectivity with pore size when a calcination temperature is the third variable. However, the graph shows that generally low $C_{5+}$ selectivities were obtained at the region of low calcination temperatures, and higher selectivities were obtained at higher calcination temperatures. The maximum $C_{5+}$ selectivity was observed at a calcination temperature higher than or equal to 350°C and pore sizes of 5,7, and 16 nm, and lower selectivities were observed below 350°C. The observation on the calcination temperature is explained by the fact that the higher calcination temperatures often lead to the strengthening of $Co_3O_4$, which can be efficiently reduced to the metallic cobalt during the catalyst activation. Generally, higher reducibility corresponds to a higher active site density, which is a crucial factor in the chain growth probability (Bezemer et al., 2006; Iglesia et al., 1992). The higher calcination temperatures also increase the stability of the silica pores, preventing pore collapse during the reduction stage, which favors the formation of long-chain hydrocarbons as explained above (Gnanamani et al., 2015; Mu et al., 2021; van Steen & Claeys, 2008).

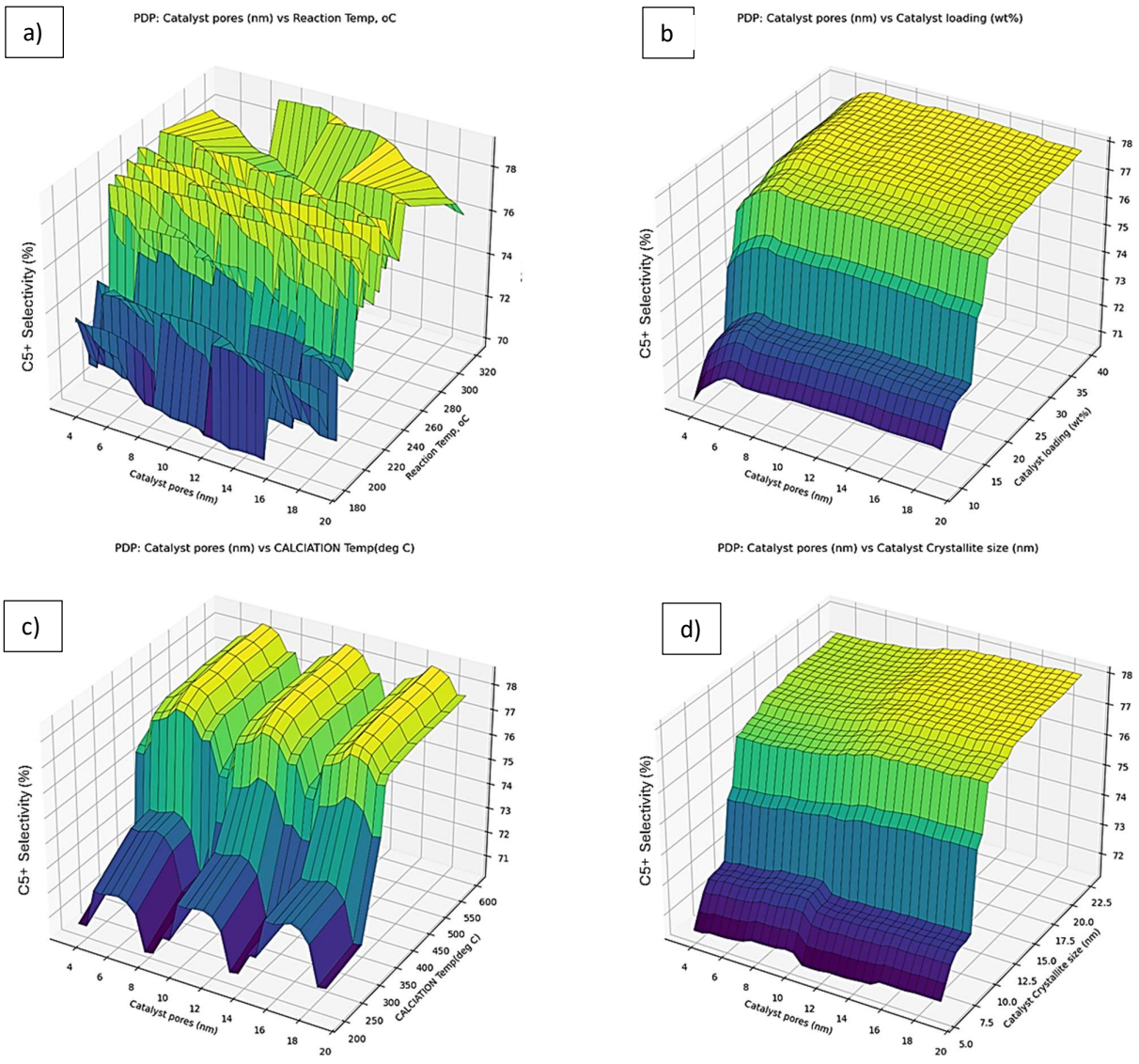



*Figure 6.8. Three-way partial dependence plot of $C_{5+}$ selectivity and pore size against the other five most influential parameters towards $C_{5+}$ selectivity*

Figure 6.8d shows the same trend as that observed with the catalyst loading, where generally, high $C_{5+}$ selectivity was observed at large crystallite sizes and larger pore sizes, while the lowest selectivities were observed in the region of low pore sizes and small crystallite sizes. A $C_{5+}$ selectivity of 78% was observed at the largest crystallite sizes of 22.5 nm and with an average pore size of 18 nm, while a low $C_{5+}$ selectivity of 71.5% was observed at an average pore size of 4 nm and a crystallite size of 6 nm. Generally, the catalyst loading varies directly with the crystallite sizes as an increase in catalyst loading results in larger crystallites; therefore the reasons for the trends observed in Figure 6.8d are the same as those explained in the observations in Figure 6.8b.

## 6.4 Conclusion

ML was successfully applied to the experimental data to gain insight into the effects of pore size and the other important parameters, which are; reaction temperature, catalyst loading, calcination temperature, and crystallite size on the product distribution for the $Co/SiO_2$ FT synthesis catalytic systems. The CatBoost model was chosen as the best applicable method and was implemented to train the model, which involved 400 datasets from 60 different publications and demonstrated a strong predictive performance, reaching a maximum $R^2$ test value of 0.79, demonstrating a strong ability to capture the complex, nonlinear, and multivariable relationships in FT synthesis.

The study also showed that the feature importance is greatly affected by the reaction conditions which are the focus of this study. For instance, it was found that the CO conversion plays a significant role in affecting the feature importance of the input parameters. When the input data was constrained to the 20 to 60% CO conversion range, the effect of pore size on CO conversion, $C_1$, and $C_{5+}$ selectivity was brought to the fore, indicating that the intermediate CO conversions provide a clearer understanding of the structure-function relationships in FT synthesis.

The results revealed distinct parameter values which enable the maximization of the FT process selectivity towards the $C_1$, $C_2$–$C_4$, and $C_5^+$ hydrocarbon fractions, clearly showing the strong interplay between some of the most influential parameters on the $Co/SiO_2$ FT synthesis product distribution.

The maximum $CH_4$ selectivity was observed in the pore size range of 4 to 7 nm, for reaction temperatures between 200 and 220°C, crystallite sizes of approximately 7.5 nm, 10% cobalt loading, and calcination temperatures of 250 to 350°C. This generally showed that high hydrogenation rates take place under these conditions, restricting the chain growth probability due to diffusion limitations within smaller pores as well as less availability of the active sites at lower cobalt loadings/smaller crystallite sizes. The maximum selectivity of $C_2$–$C_4$ hydrocarbons was observed at intermediate pore sizes of 6 to 8 nm, similar reaction temperatures of 200 to 220°C, crystallite sizes of 6 to 8 nm, a cobalt loading of 10-12% and calcination temperature between 200 and 300°C. These range of the parameters facilitate chain growth while avoiding further chain propagation to form heavier hydrocarbons. The maximum selectivity of $C_{5+}$ hydrocarbons was observed ar pore sizes of 6 to 8 nm (which is greater than that observed on both $C_1$ and $C_2$-$C_4$ selectivities), higher reaction temperatures of

280 to 300°C, larger crystallite sizes of approximately 22.5nm, very high cobalt loading of 30-40% and also high calcination temperature (greater than 350°C). These conditions favour an increase in the chain growth probability, due to enhanced density of the active sites and ease of diffusion of the products from the active sites.

These results showed that the smaller pore sizes favoured the production of methane and lighter hydrocarbons due to restricted chain growth, while larger pore sizes lead to the formation of much longer chains in heavy hydrocarbons by improving diffusion and the accessibility of the active sites. This agrees with the experimental results obtained in the previous chapter. The lower temperatures (200 to 220 °C) are associated with limited chain growth, favouring the production of $C_1$ and $C_2$–$C_4$ hydrocarbons, whereas higher temperatures (280 to 300 °C) enhance chain propagation and the production of more $C_5^+$ hydrocarbons. Smaller crystallites were found to favour the formation of lighter hydrocarbons due to better dispersion, whereas larger crystallite sizes (>20 nm) favour the production of heavy hydrocarbons. Higher calcination temperatures and cobalt loading were found to favour the formation of heavier hydrocarbons due to improved reducibility, structural stability and metal dispersion, while the lower range of values conversely favour the production of light hydrocarbons.

Overall, the CatBoost model successfully identifies and ranks key parameters, providing a predictive framework for tailoring $Co/SiO_2$ catalysts in order to achieve desired hydrocarbon distributions from the FT synthesis process. This shows that the use of ML does not only offer predictive insights but it can also provide guidance towards experimental design and strategies for tuning the catalyst properties to achieve desired hydrocarbon distributions in FT synthesis. However, the study only focused on the $Co/SiO_2$ catalysts and the results may differ if other types of FT synthesis catalysts are considered.

Future studies could focus on the other catalyst systems to verify the findings and also consider looking at other datasets based on the CO conversion range to verify the investigation of the pore size behaviour. Three-way partial dependence plots were used to analyse the effect of two parameters at a time. More complex representations can also be incorporated to find the multivariable behaviour of the selectivities. The further studies could also integrate ML with microkinetic modelling and in situ characterization to study, refine and validate mechanistic interpretations.

## References


Anderson, R. B. (1984). Fischer Tropsch Synthesis (pp. 100–160).

Bartholomew, C. H. (2001). Mechanisms of catalyst deactivation. Applied Catalysis A: General, 212(1–2), 17–60. https://doi.org/10.1016/S0926-860X(00)00843-7

Becker, H., Güttel, R., & Turek, T. (2016). Enhancing internal mass transport in Fischer-Tropsch catalyst layers utilizing transport pores. Catalysis Science and Technology, 6(1), 275–287. https://doi.org/10.1039/c5cy00957j

Bezemer, G. L., Bitter, J. H., Kuipers, H. P. C. E., Oosterbeek, H., Holewijn, J. E., Xu, X., Kapteijn, F., Van Diilen, A. J., & De Jong, K. P. (2006). Cobalt particle size effects in the Fischer-Tropsch reaction studied with carbon nanofiber supported catalysts. Journal of the American Chemical Society, 128(12), 3956–3964. https://doi.org/10.1021/ja058282w

Chen, Q., & Qi, J. (2023). How much should we trust R2 and adjusted R2: evidence from regressions in top economics journals and Monte Carlo simulations. Journal of Applied Economics, 26(3). https://doi.org/10.1080/15140326.2023.2207326

Cheng, K., Virginie, M., Ordomsky, V. V, Cordier, C., Chernavskii, P. A., Ivantsov, M. I., Paul, S., Wang, Y., & Khodakov, A. Y. (2015). Pore size effects in high-temperature Fischer – Tropsch synthesis over supported iron catalysts. Journal of Catalysis, 328, 139–150. https://doi.org/10.1016/j.jcat.2014.12.007

Demchuk, T., Nikolaienko, T., Panda, A., Joshi, S. M., Jaso, S., Kalyanaraman, K., Shafiee, P., Jafari, M., Schowarte, J., Dorneanu, B., & Arellano-garcia, H. (2025). ML-based Method for Solving the Microkinetic Model of Fischer-Tropsch Synthesis with Varying Catalyst/Reactor Parameters. 1871(July), 1–19. http://arxiv.org/abs/2503.22304

den Breejen, J. P. (2010). Cobalt particle size effects in catalysis. http://igitur-archive.library.uu.nl/dissertations/2010-0126-200129/UUindex.html

Dry, M. E. (2002). The Fischer-Tropsch process: 1950-2000. Catalysis Today, 71(3–4), 227–241. https://doi.org/10.1016/S0920-5861(01)00453-9

Escanciano, J. C., & Goh, S. C. (2019). Quantile-Regression Inference With Adaptive Control of Size. 1459. https://doi.org/10.1080/01621459.2018.1505624

Ghampson, I. T., Newman, C., Kong, L., Pier, E., Hurley, K. D., Pollock, R. A., Walsh, B. R., Goundie, B., Wright, J., Wheeler, M. C., Meulenberg, R. W., Desisto, W. J., Frederick, B. G., & Austin, R. N. (2010). Effects of pore diameter on particle size, phase, and turnover frequency in mesoporous silica supported cobalt Fischer-Tropsch catalysts. Applied Catalysis A: General, 388(1–2), 57–67. https://doi.org/10.1016/j.apcata.2010.08.028

Ghojogh, B., & Crowley, M. (2023). The Theory Behind Overfitting, Cross Validation, Regularization, Bagging, and Boosting: Tutorial. 3.

Gnanamani, M. K., Jacobs, G., Keogh, R. A., Shafer, W. D., Sparks, D. E., Hopps, S. D., Thomas, G. A., & Davis, B. H. (2015). Fischer-Tropsch synthesis: Effect of pretreatment conditions of cobalt on activity and selectivity for hydrogenation of carbon dioxide. Applied Catalysis A: General, 499, 39–46. https://doi.org/10.1016/j.apcata.2015.03.046

Herriko, E. (2012). Cobalt supported on mesoporous silicas for the Fischer-Tropsch synthesis: Effect of titania grafting and external water (PhD thesis). Chalmers University of Technology, Stockholm, Sweden. June 2012. Available at: http://www.diva-portal.org/smash/get/diva2:776941/FULLTEXT01

Iglesia, E. (1997). Design, synthesis, and use of cobalt-based Fischer-Tropsch synthesis catalysts. Applied Catalysis A: General, 161(1–2), 59–78. https://doi.org/10.1016/S0926-860X(97)00186-5

Iglesia, E., Soled, S. L., & Fiato, R. A. (1992). Fischer-Tropsch Synthesis on Cobalt and Ruthenium. Metal Dispersion and Support Effects on Reaction Rate and Selectivity. In JOURNAL OF CATALYSIS (Vol. 137).

Intarasiri, S., Ratana, T., Sornchamni, T., Phongaksorn, M., & Tungkamani, S. (2017). Effect of pore size diameter of cobalt supported catalyst on gasoline-diesel selectivity. Energy Procedia, 138, 1035–1040. https://doi.org/10.1016/j.egypro.2017.10.090

Intarasiri, S., Tanakorn, R., Sornchamni, T., Tungkamani, S., & Phongaksorn, M. (2018). Pore size effect of mesoporous support on metal particle size of Co/SiO2 catalyst in Fischer-Tropsch synthesis. International Journal of Avanced and Applied Sciences, 5(11), 80–85. https://doi.org/10.21833/ijaas.2018.11.011

Kamath, G., Badoga, S., & Dalai, A. K. (2019). Synthesis and Application of Metallosilicate Supports for Cobalt-Based Fischer-Tropsch Synthesis Catalysts. Energy and Fuels, 33(1), 551–560. https://doi.org/10.1021/acs.energyfuels.8b03209

Keunecke, A., Dossow, M., Dieterich, V., Spliethoff, H., & Fendt, S. (2024). Insights into Fischer–Tropsch catalysis: current perspectives, mechanisms, and emerging trends in energy research. Frontiers in Energy Research, 12(April), 1–11. https://doi.org/10.3389/fenrg.2024.1344179

Khodakov, A. Y., Chu, W., & Fongarland, P. (2007). Advances in the development of novel cobalt Fischer-Tropsch catalysts for synthesis of long-chain hydrocarbons and clean fuels. Chemical Reviews, 107(5), 1692–1744. https://doi.org/10.1021/cr050972v

Kim, J., Kim, S., Ban, M., Lee, D., Kim, S., Lee, J., & Ha, K. S. (2023). Unravelling the effects of short pore on Fischer-Tropsch synthesis and its role as selectivity controller. Chemical Engineering Journal, 475(September), 146039. https://doi.org/10.1016/j.cej.2023.146039

Kruit, K. D., Vervloet, D., Kapteijn, F., & Van Ommen, J. R. (2013). Selectivity of the Fischer-Tropsch process: Deviations from single alpha product distribution explained by gradients in process conditions. Catalysis Science and Technology, 3(9), 2210–2213. https://doi.org/10.1039/c3cy00080j

Kutuk, N. (2021). Mesoporous silica nanoparticles, methods of preparation and use of bone tissue engineering. International Journal of Life Sciences and Biotechnology, 4(3), 507–522. https://doi.org/10.38001/ijlsb.880711

Li, H., Li, J., Ni, H., & Song, D. (2006). Studies on cobalt catalyst supported on silica with different pore size for Fischer-Tropsch synthesis. Catalysis Letters, 110(1–2), 71–76. https://doi.org/10.1007/s10562-006-0086-y

Li, H., Wang, J., Chen, C., Jia, L., Hou, B., & Li, D. (2017). Effects of macropores on reducing internal diffusion limitations in Fischer-Tropsch synthesis using a hierarchical cobalt catalyst. RSC Advances, 7(16), 9436–9445. https://doi.org/10.1039/c6ra27166a

Mehmood, A., Ghafar, H., Yaqoob, S., Gohar, U. F., & Ahmad, B. (2017). Mesoporous Silica Nanoparticles: A Review. Journal of Developing Drugs, 06(02). https://doi.org/10.4172/2329-6631.1000174

Mu, S. F., Shang, R. J., Chen, J. G., & Zhang, J. L. (2021). Pretreating Co/SiO2 to generate highly active Fischer-Tropsch synthesis catalyst with low CH4 selectivity. Ranliao Huaxue Xuebao/Journal of Fuel Chemistry and Technology, 49(11), 1592–1598. https://doi.org/10.1016/S1872-5813(21)60163-9

Nasiri, S., Rabiei, M., Palevicius, A., Janusas, G., Vilkauskas, A., Nutalapati, V., & Monshi, A. (2023). Nano Trends Modified Scherrer equation to calculate crystal size by XRD with high accuracy , examples Fe 2 O 3 , TiO 2 and V 2 O 5. Nano Trends, 3(August), 100015. https://doi.org/10.1016/j.nwnano.2023.100015

Osakoo, N., Henkel, R., Loiha, S., Roessner, F., & Wittayakun, J. (2014). Effect of support morphology and Pd promoter on Co/SBA-15 for Fischer-Tropsch Synthesis. Catalysis Communications, 56(3), 168–173. https://doi.org/10.1016/j.catcom.2014.07.016

Pandey, U., Runningen, A., Gavrilović, L., Jørgensen, E. A., Putta, K. R., Rout, K. R., Rytter, E., Blekkan, E. A., & Hillestad, M. (2021). Modeling Fischer–Tropsch kinetics and product distribution over a cobalt catalyst. AIChE Journal, 67(7), 1–15. https://doi.org/10.1002/aic.17234

Peron, D. V., Barrios, A. J., Taschin, A., Dugulan, I., Marini, C., Gorni, G., Moldovan, S., Koneti, S., Wojcieszak, R., Thybaut, J. W., Virginie, M., & Khodakov, A. Y. (2021). Active phases for high temperature Fischer-Tropsch synthesis in the silica supported iron catalysts promoted with antimony and tin. Applied Catalysis B: Environmental, 292(December 2020), 120141. https://doi.org/10.1016/j.apcatb.2021.120141

Pondini, M., & Ebert, M. (2013). Process synthesis and design of low temperature Fischer-Tropsch crude production from biomass derived syngas. Department of Energy and Environment.

Prieto, G., Martínez, A., Concepción, P., & Moreno-Tost, R. (2009). Cobalt particle size effects in Fischer-Tropsch synthesis: structural and in situ spectroscopic characterisation on reverse micelle-synthesised Co/ITQ-2 model catalysts. Journal of Catalysis, 266(1), 129–144. https://doi.org/10.1016/j.jcat.2009.06.001

Rytter, E., & Holmen, A. (2016). On the support in cobalt Fischer–Tropsch Synthesis—emphasis on alumina and aluminates. Catalysts Today, 275, 11–19. https://doi.org/doi.org/10.1016/j

Saib, A. M., Moodley, D. J., Ciobîc, I. M., Hauman, M. M., Sigwebela, B. H., Weststrate, C. J., Niemantsverdriet, J. W., & Van De Loosdrecht, J. (2010). Fundamental understanding of deactivation and regeneration of cobalt Fischer-Tropsch synthesis catalysts. Catalysis Today, 154(3–4), 271–282. https://doi.org/10.1016/j.cattod.2010.02.008

Schulz, H. (2006). Principles of Selectivity in Fischer-Tropsch Synthesis. DGMK/SCI-Conference "Synthesis Gas Chemistry", Dresden, Germany, 7(1), 85–92.

Shafiee, P., Dorneanu, B., & Arellano-garcia, H. (2024). Towards Machine Learning-driven Catalyst Design and Optimization of Operating Conditions for the Production of Jet Fuel Via Fischer-Tropsch Synthesis. 114(November), 583–588. https://doi.org/10.3303/CET24114098

Shafiee, P., Dorneanu, B., & Arellano-garcia, H. (2025). Improving catalysts and operating conditions using machine learning in Fischer-Tropsch synthesis of jet fuels ( C8-C16 ). Chemical Engineering Journal Advances, 21(January), 100702. https://doi.org/10.1016/j.ceja.2024.100702

Shafiee, P., Dorneanu, B., & Arellano-Garcia, H. (2025). Improving catalysts and operating conditions using machine learning in Fischer-Tropsch synthesis of jet fuels (C8-C16). Chemical Engineering Journal Advances, 21(January), 100702. https://doi.org/10.1016/j.ceja.2024.100702

Shafiee, P., Jafari, M., Schowarte, J., Dorneanu, B., & Arellano-garcia, H. (2025). Streamlining Catalyst Development through Machine Learning : Insights from Heterogeneous Catalysis and Photocatalysis. 1871(July), 1866–1871.

Tavasoli, A., Sadaghiani, K., Nakhaelpour, A., & Ahangari, M. (2007). Cobalt loading effects on the structure and activity for fischer-tropsch and water-gas shift reactions of Co/Al2O3 catalysts. Iranian Journal of Chemistry and Chemical Engineering, 26(1), 9–16.

Teimouri, Z., Abatzoglou, N., & Dalai, A. K. (2021). Kinetics and selectivity study of fischer-tropsch synthesis to c5+ hydrocarbons: A review. In Catalysts (Vol. 11, Issue 3). https://doi.org/10.3390/catal11030330

Unglaub, C., & Jess, A. (2023). Enhancing Kerosene Selectivity of Fischer-Tropsch

Synthesis by Periodical Pore Drainage Via Hydrogenolysis. Catalysis Research, 03(03), 1–19. https://doi.org/10.21926/cr.2303022

Van Santen, R. A., Markvoort, A. J., Filot, I. A. W., Ghouri, M. M., & Hensen, E. J. M. (2013). Mechanism and microkinetics of the Fischer-Tropsch reaction. Physical Chemistry Chemical Physics, 15(40), 17038–17063. https://doi.org/10.1039/c3cp52506f

van Steen, E., & Claeys, M. (2008). Fischer-Tropsch catalysts for the biomass-to-liquid process. Chemical Engineering and Technology, 31(5), 655–666. https://doi.org/10.1002/ceat.200800067

Wang, J., & Wojciechowski, B. . (1989). The Influence of Kinetic Parameters on the Fischer Tropsch Product Distribution. Fuel Science & Technology International, 7(8), 1139–1177. https://doi.org/https://doi.org/10.1080/08843758908962283

Wu, L., Li, Z., Han, D., Wu, J., & Zhang, D. (2015). A preliminary evaluation of ZSM-5 / SBA-15 composite supported Co catalysts for Fischer – Tropsch synthesis. Fuel Processing Technology, 134, 449–455. https://doi.org/10.1016/j.fuproc.2015.02.025

Xiong, H., Zhang, Y., Liew, K., & Li, J. (2008). Fischer-Tropsch synthesis: The role of pore size for Co/SBA-15 catalysts. Journal of Molecular Catalysis A: Chemical, 295(1–2), 68–76. https://doi.org/10.1016/j.molcata.2008.08.017

Yang, J., Ma, W., Chen, D., Holmen, A., & Davis, B. H. (2014). Fischer-Tropsch synthesis: A review of the effect of CO conversion on methane selectivity. Applied Catalysis A: General, 470, 250–260. https://doi.org/10.1016/j.apcata.2013.10.061

Zepeda, T. A. (2025). Selectivity modulation in Fischer-Tropsch synthesis through reducibility control of cobalt-species containing HMS framework. Catalysis Today, 445(October 2024), 115110. https://doi.org/10.1016/j.cattod.2024.115110

## Bibliography


Anderson, R. B. (1984). *Fischer Tropsch Synthesis* (pp. 100–160).

Bartholomew, C. H. (2001). Mechanisms of catalyst deactivation. *Applied Catalysis A: General*, *212*(1–2), 17–60. https://doi.org/10.1016/S0926-860X(00)00843-7

Becker, H., Güttel, R., & Turek, T. (2016). Enhancing internal mass transport in Fischer-Tropsch catalyst layers utilizing transport pores. *Catalysis Science and Technology*, *6*(1), 275–287. https://doi.org/10.1039/c5cy00957j

Bezemer, G. L., Bitter, J. H., Kuipers, H. P. C. E., Oosterbeek, H., Holewijn, J. E., Xu, X., Kapteijn, F., Van Diilen, A. J., & De Jong, K. P. (2006). Cobalt particle size effects in the Fischer-Tropsch reaction studied with carbon nanofiber supported catalysts. *Journal of the American Chemical Society*, *128*(12), 3956–3964. https://doi.org/10.1021/ja058282w

Chen, Q., & Qi, J. (2023). How much should we trust R2 and adjusted R2: evidence from regressions in top economics journals and Monte Carlo simulations. *Journal of Applied Economics*, *26*(3). https://doi.org/10.1080/15140326.2023.2207326

Cheng, K., Virginie, M., Ordomsky, V. V, Cordier, C., Chernavskii, P. A., Ivantsov, M. I., Paul, S., Wang, Y., & Khodakov, A. Y. (2015). Pore size effects in high-temperature Fischer – Tropsch synthesis over supported iron catalysts. *Journal of Catalysis*, *328*, 139–150. https://doi.org/10.1016/j.jcat.2014.12.007

Demchuk, T., Nikolaienko, T., Panda, A., Joshi, S. M., Jaso, S., Kalyanaraman, K., Shafiee, P., Jafari, M., Schowarte, J., Dorneanu, B., & Arellano-garcia, H. (2025). *ML-based Method for Solving the Microkinetic Model of Fischer-Tropsch Synthesis with Varying Catalyst/Reactor Parameters*. *1871*(July), 1–19. http://arxiv.org/abs/2503.22304

den Breejen, J. P. (2010). *Cobalt particle size effects in catalysis*. http://igitur-archive.library.uu.nl/dissertations/2010-0126-200129/UUindex.html

Dry, M. E. (2002). The Fischer-Tropsch process: 1950-2000. *Catalysis Today*, *71*(3–4), 227–241. https://doi.org/10.1016/S0920-5861(01)00453-9

Escanciano, J. C., & Goh, S. C. (2019). *Quantile-Regression Inference With Adaptive Control of Size*. *1459*. https://doi.org/10.1080/01621459.2018.1505624

Ghampson, I. T., Newman, C., Kong, L., Pier, E., Hurley, K. D., Pollock, R. A., Walsh, B. R., Goundie, B., Wright, J., Wheeler, M. C., Meulenberg, R. W., Desisto, W. J., Frederick, B. G., & Austin, R. N. (2010). Effects of pore diameter on particle size, phase, and turnover frequency in mesoporous silica supported cobalt Fischer-Tropsch catalysts. *Applied Catalysis A: General*, *388*(1–2), 57–67. https://doi.org/10.1016/j.apcata.2010.08.028

Ghojogh, B., & Crowley, M. (2023). *The Theory Behind Overfitting, Cross Validation, Regularization, Bagging, and Boosting: Tutorial*. *3*.

Gnanamani, M. K., Jacobs, G., Keogh, R. A., Shafer, W. D., Sparks, D. E., Hopps, S. D., Thomas, G. A., & Davis, B. H. (2015). Fischer-Tropsch synthesis: Effect of pretreatment conditions of cobalt on activity and selectivity for hydrogenation of carbon dioxide. *Applied Catalysis A: General*, *499*, 39–46. https://doi.org/10.1016/j.apcata.2015.03.046

Herriko, E. (2012). *Cobalt supported on mesoporous silicas for the Fischer-Tropsch synthesis Effect of titania grafting and external water*. *June*.

Iglesia, E. (1997). Design, synthesis, and use of cobalt-based Fischer-Tropsch synthesis catalysts. *Applied Catalysis A: General*, *161*(1–2), 59–78. https://doi.org/10.1016/S0926-860X(97)00186-5

Iglesia, E., Soled, S. L., & Fiato, R. A. (1992). Fischer-Tropsch Synthesis on Cobalt and Ruthenium. Metal Dispersion and Support Effects on Reaction Rate and Selectivity. In *JOURNAL OF CATALYSIS* (Vol. 137).

Intarasiri, S., Ratana, T., Sornchamni, T., Phongaksorn, M., & Tungkamani, S. (2017). Effect of pore size diameter of cobalt supported catalyst on gasoline-diesel selectivity. *Energy Procedia*, *138*, 1035–1040. https://doi.org/10.1016/j.egypro.2017.10.090

Intarasiri, S., Tanakorn, R., Sornchamni, T., Tungkamani, S., & Phongaksorn, M. (2018). Pore size effect of mesoporous support on metal particle size of Co/SiO2 catalyst in Fischer-Tropsch synthesis. *International Journal of Avanced and Applied Sciences*, *5*(11), 80–85. https://doi.org/10.21833/ijaas.2018.11.011

Kamath, G., Badoga, S., & Dalai, A. K. (2019). Synthesis and Application of Metallosilicate Supports for Cobalt-Based Fischer-Tropsch Synthesis Catalysts. *Energy and Fuels*,

*33*(1), 551–560. https://doi.org/10.1021/acs.energyfuels.8b03209

Keunecke, A., Dossow, M., Dieterich, V., Spliethoff, H., & Fendt, S. (2024). Insights into Fischer–Tropsch catalysis: current perspectives, mechanisms, and emerging trends in energy research. *Frontiers in Energy Research*, *12*(April), 1–11. https://doi.org/10.3389/fenrg.2024.1344179

Khodakov, A. Y., Chu, W., & Fongarland, P. (2007). Advances in the development of novel cobalt Fischer-Tropsch catalysts for synthesis of long-chain hydrocarbons and clean fuels. *Chemical Reviews*, *107*(5), 1692–1744. https://doi.org/10.1021/cr050972v

Kim, J., Kim, S., Ban, M., Lee, D., Kim, S., Lee, J., & Ha, K. S. (2023). Unravelling the effects of short pore on Fischer-Tropsch synthesis and its role as selectivity controller. *Chemical Engineering Journal*, *475*(September), 146039. https://doi.org/10.1016/j.cej.2023.146039

Kruit, K. D., Vervloet, D., Kapteijn, F., & Van Ommen, J. R. (2013). Selectivity of the Fischer-Tropsch process: Deviations from single alpha product distribution explained by gradients in process conditions. *Catalysis Science and Technology*, *3*(9), 2210–2213. https://doi.org/10.1039/c3cy00080j

Kutuk, N. (2021). Mesoporous silica nanoparticles, methods of preparation and use of bone tissue engineering. *International Journal of Life Sciences and Biotechnology*, *4*(3), 507–522. https://doi.org/10.38001/ijlsb.880711

Li, H., Li, J., Ni, H., & Song, D. (2006). Studies on cobalt catalyst supported on silica with different pore size for Fischer-Tropsch synthesis. *Catalysis Letters*, *110*(1–2), 71–76. https://doi.org/10.1007/s10562-006-0086-y

Li, H., Wang, J., Chen, C., Jia, L., Hou, B., & Li, D. (2017). Effects of macropores on reducing internal diffusion limitations in Fischer-Tropsch synthesis using a hierarchical cobalt catalyst. *RSC Advances*, *7*(16), 9436–9445. https://doi.org/10.1039/c6ra27166a

Mehmood, A., Ghafar, H., Yaqoob, S., Gohar, U. F., & Ahmad, B. (2017). Mesoporous Silica Nanoparticles: A Review. *Journal of Developing Drugs*, *06*(02). https://doi.org/10.4172/2329-6631.1000174

Mu, S. F., Shang, R. J., Chen, J. G., & Zhang, J. L. (2021). Pretreating Co/SiO2 to generate highly active Fischer-Tropsch synthesis catalyst with low CH4 selectivity. *Ranliao*

*Huaxue Xuebao/Journal of Fuel Chemistry and Technology*, *49*(11), 1592–1598. https://doi.org/10.1016/S1872-5813(21)60163-9

Nasiri, S., Rabiei, M., Palevicius, A., Janusas, G., Vilkauskas, A., Nutalapati, V., & Monshi, A. (2023). Nano Trends Modified Scherrer equation to calculate crystal size by XRD with high accuracy , examples Fe 2 O 3 , TiO 2 and V 2 O 5. *Nano Trends*, *3*(August), 100015. https://doi.org/10.1016/j.nwnano.2023.100015

Osakoo, N., Henkel, R., Loiha, S., Roessner, F., & Wittayakun, J. (2014). Effect of support morphology and Pd promoter on Co/SBA-15 for Fischer-Tropsch Synthesis. *Catalysis Communications*, *56*(3), 168–173. https://doi.org/10.1016/j.catcom.2014.07.016

Pandey, U., Runningen, A., Gavrilović, L., Jørgensen, E. A., Putta, K. R., Rout, K. R., Rytter, E., Blekkan, E. A., & Hillestad, M. (2021). Modeling Fischer–Tropsch kinetics and product distribution over a cobalt catalyst. *AIChE Journal*, *67*(7), 1–15. https://doi.org/10.1002/aic.17234

Peron, D. V., Barrios, A. J., Taschin, A., Dugulan, I., Marini, C., Gorni, G., Moldovan, S., Koneti, S., Wojcieszak, R., Thybaut, J. W., Virginie, M., & Khodakov, A. Y. (2021). Active phases for high temperature Fischer-Tropsch synthesis in the silica supported iron catalysts promoted with antimony and tin. *Applied Catalysis B: Environmental*, *292*(December 2020), 120141. https://doi.org/10.1016/j.apcatb.2021.120141

Pondini, M., & Ebert, M. (2013). Process synthesis and design of low temperature Fischer-Tropsch crude production from biomass derived syngas. *Department of Energy and Environment*.

Prieto, G., Martínez, A., Concepción, P., & Moreno-Tost, R. (2009). Cobalt particle size effects in Fischer-Tropsch synthesis: structural and in situ spectroscopic characterisation on reverse micelle-synthesised Co/ITQ-2 model catalysts. *Journal of Catalysis*, *266*(1), 129–144. https://doi.org/10.1016/j.jcat.2009.06.001

Rytter, E., & Holmen, A. (2016). On the support in cobalt Fischer–Tropsch Synthesis—emphasis on alumina and aluminates. *Catalysts Today*, *275*, 11–19. https://doi.org/doi.org/10.1016/j

Saib, A. M., Moodley, D. J., Ciobîc, I. M., Hauman, M. M., Sigwebela, B. H., Weststrate, C. J., Niemantsverdriet, J. W., & Van De Loosdrecht, J. (2010). Fundamental

understanding of deactivation and regeneration of cobalt Fischer-Tropsch synthesis catalysts. *Catalysis Today*, *154*(3–4), 271–282. https://doi.org/10.1016/j.cattod.2010.02.008

Schulz, H. (2006). Principles of Selectivity in Fischer-Tropsch Synthesis. *DGMK/SCI-Conference "Synthesis Gas Chemistry", Dresden, Germany*, *7*(1), 85–92.

Shafiee, P., Dorneanu, B., & Arellano-garcia, H. (2024). *Towards Machine Learning-driven Catalyst Design and Optimization of Operating Conditions for the Production of Jet Fuel Via Fischer-Tropsch Synthesis*. *114*(November), 583–588. https://doi.org/10.3303/CET24114098

Shafiee, P., Dorneanu, B., & Arellano-garcia, H. (2025). Improving catalysts and operating conditions using machine learning in Fischer-Tropsch synthesis of jet fuels ( C8-C16 ). *Chemical Engineering Journal Advances*, *21*(January), 100702. https://doi.org/10.1016/j.ceja.2024.100702

Shafiee, P., Dorneanu, B., & Arellano-Garcia, H. (2025). Improving catalysts and operating conditions using machine learning in Fischer-Tropsch synthesis of jet fuels (C8-C16). *Chemical Engineering Journal Advances*, *21*(January), 100702. https://doi.org/10.1016/j.ceja.2024.100702

Shafiee, P., Jafari, M., Schowarte, J., Dorneanu, B., & Arellano-garcia, H. (2025). *Streamlining Catalyst Development through Machine Learning : Insights from Heterogeneous Catalysis and Photocatalysis*. *1871*(July), 1866–1871.

Tavasoli, A., Sadaghiani, K., Nakhaelpour, A., & Ahangari, M. (2007). Cobalt loading effects on the structure and activity for fischer-tropsch and water-gas shift reactions of Co/Al2O3 catalysts. *Iranian Journal of Chemistry and Chemical Engineering*, *26*(1), 9–16.

Teimouri, Z., Abatzoglou, N., & Dalai, A. K. (2021). Kinetics and selectivity study of fischer-tropsch synthesis to c5+ hydrocarbons: A review. In *Catalysts* (Vol. 11, Issue 3). https://doi.org/10.3390/catal11030330

Unglaub, C., & Jess, A. (2023). Enhancing Kerosene Selectivity of Fischer-Tropsch Synthesis by Periodical Pore Drainage Via Hydrogenolysis. *Catalysis Research*, *03*(03), 1–19. https://doi.org/10.21926/cr.2303022

Van Santen, R. A., Markvoort, A. J., Filot, I. A. W., Ghouri, M. M., & Hensen, E. J. M. (2013). Mechanism and microkinetics of the Fischer-Tropsch reaction. *Physical Chemistry Chemical Physics*, *15*(40), 17038–17063. https://doi.org/10.1039/c3cp52506f

van Steen, E., & Claeys, M. (2008). Fischer-Tropsch catalysts for the biomass-to-liquid process. *Chemical Engineering and Technology*, *31*(5), 655–666. https://doi.org/10.1002/ceat.200800067

Wang, J., & Wojciechowski, B. . (1989). The Influence of Kinetic Parameters on the Fischer Tropsch Product Distribution. *Fuel Science & Technology International*, *7*(8), 1139–1177. https://doi.org/https://doi.org/10.1080/08843758908962283

Wu, L., Li, Z., Han, D., Wu, J., & Zhang, D. (2015). A preliminary evaluation of ZSM-5 / SBA-15 composite supported Co catalysts for Fischer – Tropsch synthesis. *Fuel Processing Technology*, *134*, 449–455. https://doi.org/10.1016/j.fuproc.2015.02.025

Xiong, H., Zhang, Y., Liew, K., & Li, J. (2008). Fischer-Tropsch synthesis: The role of pore size for Co/SBA-15 catalysts. *Journal of Molecular Catalysis A: Chemical*, *295*(1–2), 68–76. https://doi.org/10.1016/j.molcata.2008.08.017

Yang, J., Ma, W., Chen, D., Holmen, A., & Davis, B. H. (2014). Fischer-Tropsch synthesis: A review of the effect of CO conversion on methane selectivity. *Applied Catalysis A: General*, *470*, 250–260. https://doi.org/10.1016/j.apcata.2013.10.061

Zepeda, T. A. (2025). Selectivity modulation in Fischer-Tropsch synthesis through reducibility control of cobalt-species containing HMS framework. *Catalysis Today*, *445*(October 2024), 115110. https://doi.org/10.1016/j.cattod.2024.115110

# CHAPTER 7: CONCLUSION

In this chapter, the overall conclusions from this work and recommendations for future work are discussed.

## 7.1 Introduction

This study provides a framework and a systematic approach for synthesizing catalysts of different pore sizes for use in FT synthesis. The analysis of the impact of the pore size and other important parameters on the product distribution was also done. FT synthesis has potential to address the currently existing energy insecurities by utilizing greenhouse gases for the production of useful hydrocarbons. Nevertheless, the typical constraints of FT synthesis are low activity and lack of control over the product selectivity, which may be brought on by outside variables such as the catalyst properties, like the pore size, and the active metal's interaction with the support or catalyst pre-treatments. With that being the case, in this study, Stöber spheres with 10 different $SiO_2$ pore sizes, ranging from 11 to 29 nm, were synthesized, and the role of four of them towards the product distribution was analysed experimentally. Furthermore, hundreds of experiments from the literature were also analysed using machine learning. SEM, XRD, TEM, BET, and TGA analysed the catalysts' physicochemical characteristics (Chapter 4), and TPR and $H_2$-chemisorption studies were done to examine the dispersion and reducibility during catalyst activation. The use of ML also enabled the analysis of the effects of other parameters, such as reaction temperature, calcination temperature, metal loading, and crystallite size. Based on the results obtained from the characterisation and experimental data and the performance of the catalysts in the FT synthesis process obtained from ML, insight was gained into possible new $Co/SiO_2$ catalyst designs for the production of specific hydrocarbon ranges using FT synthesis.

## 7.2 Conclusions and recommendations

### 7.2.1 Experimental approach

The Stöber process was used to synthesize silica supports with different pore sizes, ranging from 11 to 29 nm, where 10% of cobalt metal was loaded on the supports by using wet impregnation, and the resulting composite was calcined at 400°C (Chapter 4).

- The investigations confirmed the ability of the method to successfully tailor the pore sizes and other physical properties, such as the particle size, surface areas, and density. The ability of the Stöber process to manipulate these parameters is crucial in tailoring and optimizing the catalyst's performance in FT synthesis.
- The catalysts were activated and used for the FT synthesis reaction at 20 bar and 220°C in a fixed-bed reactor, where it was observed that the catalyst pore size affected the reducibility and the product selectivity in the process.
- A general decrease in the $CH_4$ selectivity was observed from a pore size of 15 nm where it was 15.4% to 6.4% at 30 nm.
- For $C_2$-$C_4$ hydrocarbons, the lowest selectivities were observed, which are less that 10% and also showed a general decrease from moderate sizes of catalyst pores (≈15 nm) to the largest pore sizes of ≈ 30 nm.
- For $C_{5+}$ hydrocarbons, the selectivities were the highest and increased as the pore sizes increased. The lowest selectivity of 75% was observed at 19.6 nm while the maximum selectivity of 88.4 % was observed at 30.1 nm.

Catalysts with larger pores of approximately 30 nm were found to be more easily reducible and also showed a significantly higher $C_{5+}$ hydrocarbon selectivity; on the contrary, the catalysts with smaller pore sizes around 15 nm showed a contrasting behaviour with a higher selectivity towards the lighter hydrocarbons and were more difficult to reduce.

Future work can be conducted on the topic, including smaller pore size ranges and analysing the trends observed on pore sizes below 15 nm. The study can also be expanded to investigate the effect of the differences in the surface areas at similar pore size ranges. The inclusion of the catalyst promoters on the $Co/SiO_2$ catalyst could also be investigated on the different support pore sizes.

### 7.2.2 Machine learning approach

400 datasets with 79 distinct descriptors were compiled from FT synthesis-based publications focusing on Co-catalysed reactions in this study. After the model selection process, the CatBoost model was found as the most accurate and the best predictive model based on the higher $R^2$ test values and the smallest differences between the $R^2$ test and $R^2$ train values.

- After analysis of the impact of pore sizes on the product distribution, the results showed that the smaller pore sizes of around 5-6 nm favoured the production of light hydrocarbons due to restricted chain growth.
- larger pore sizes of around 18 nm were found to be the sizes that yielded a maximum selectivity of the longer hydrocarbon chains by improving diffusion and the accessibility of the active site.
- The maximum selectivities of $CH_4$, $C_2$-$C_4$, and $C_{5+}$ hydrocarbons were observed within the pore size ranges of 4-7 nm, 6-8 nm, and 19 nm, respectively.
- The pore size was found to have the most significant impact on the CO conversion, within the 20-60% range

The trends in these findings were the same as those obtained from the experimental section of the study, confirming the experimental results that were obtained in Chapter 5. However, the experimental results do indicate that the maximum $C_{5+}$ selectivity was obtained at a pore size of around 30nm whereas ML studies showed it as occurring at 19nm, this is because of the limited number of the samples used for the investigation in the experimental work where this was the best pore size range obtained for the studied range. Other parameters, including the crystallite size, cobalt metal loading, calcination temperature, and reaction temperature, were also found to be the top influencing parameters of the product selectivity in Co–based FT synthesis.

The future work on ML can be done on the other types of catalysts as well as looking deeper into the reaction mechanisms with specific catalyst physicochemical characteristics to assess the impact on product selectivity. For the Co catalyst-based studies, further studies can also be done on the other datasets involving CO conversion ranges less than 20% and greater than 60% to obtain a more accurate trend observed on the effects of the catalyst properties on the FT-synthesis product distribution. ML can also be used as a tool in analyzing the behavior of existing catalysts as well as for a predictive tool to design or suggest new catalysts that can give the desired products in FT synthesis.

# APPENDIX

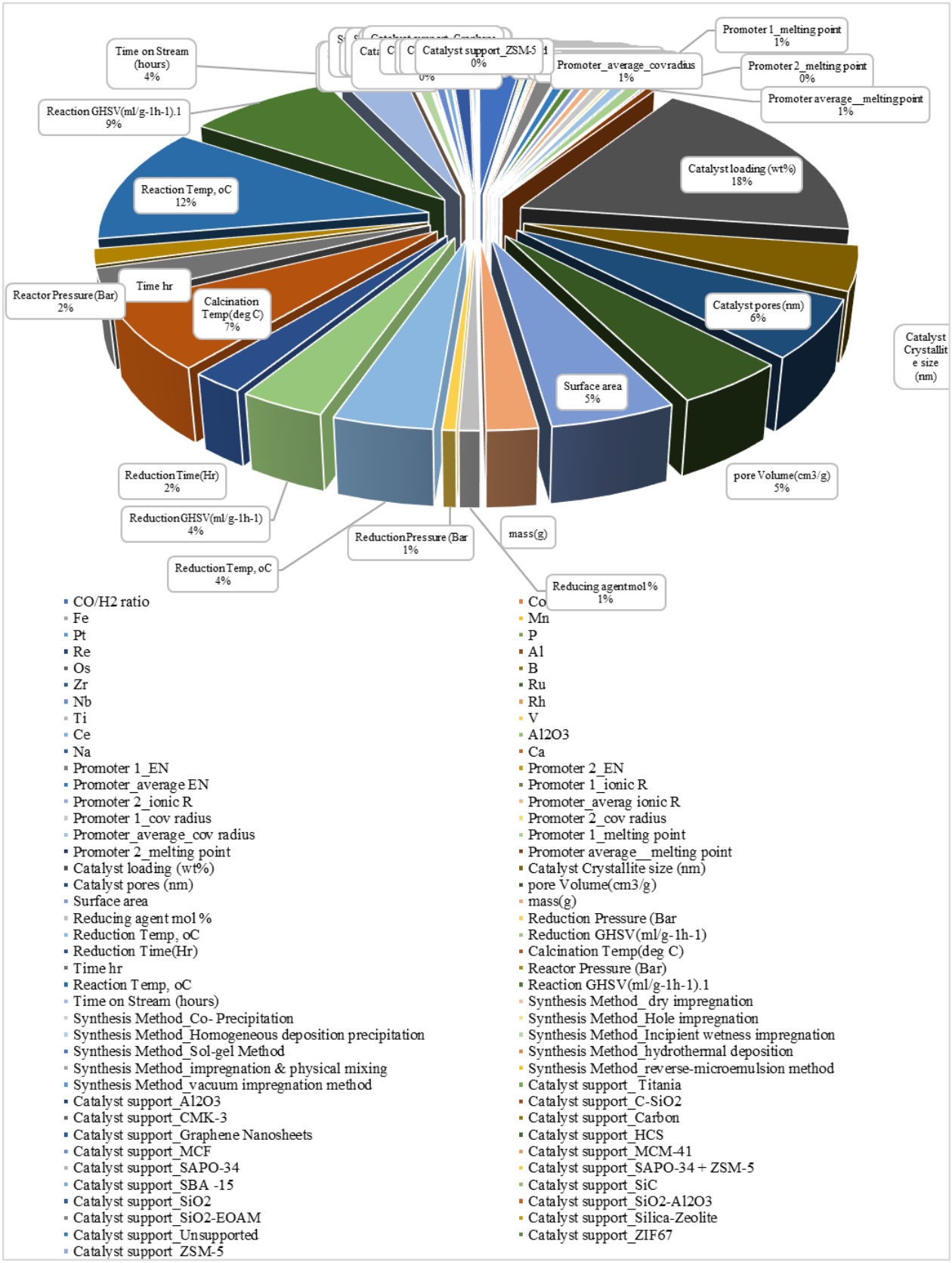



*Figure A.62. Feature importance towards the CO conversion in the whole population*

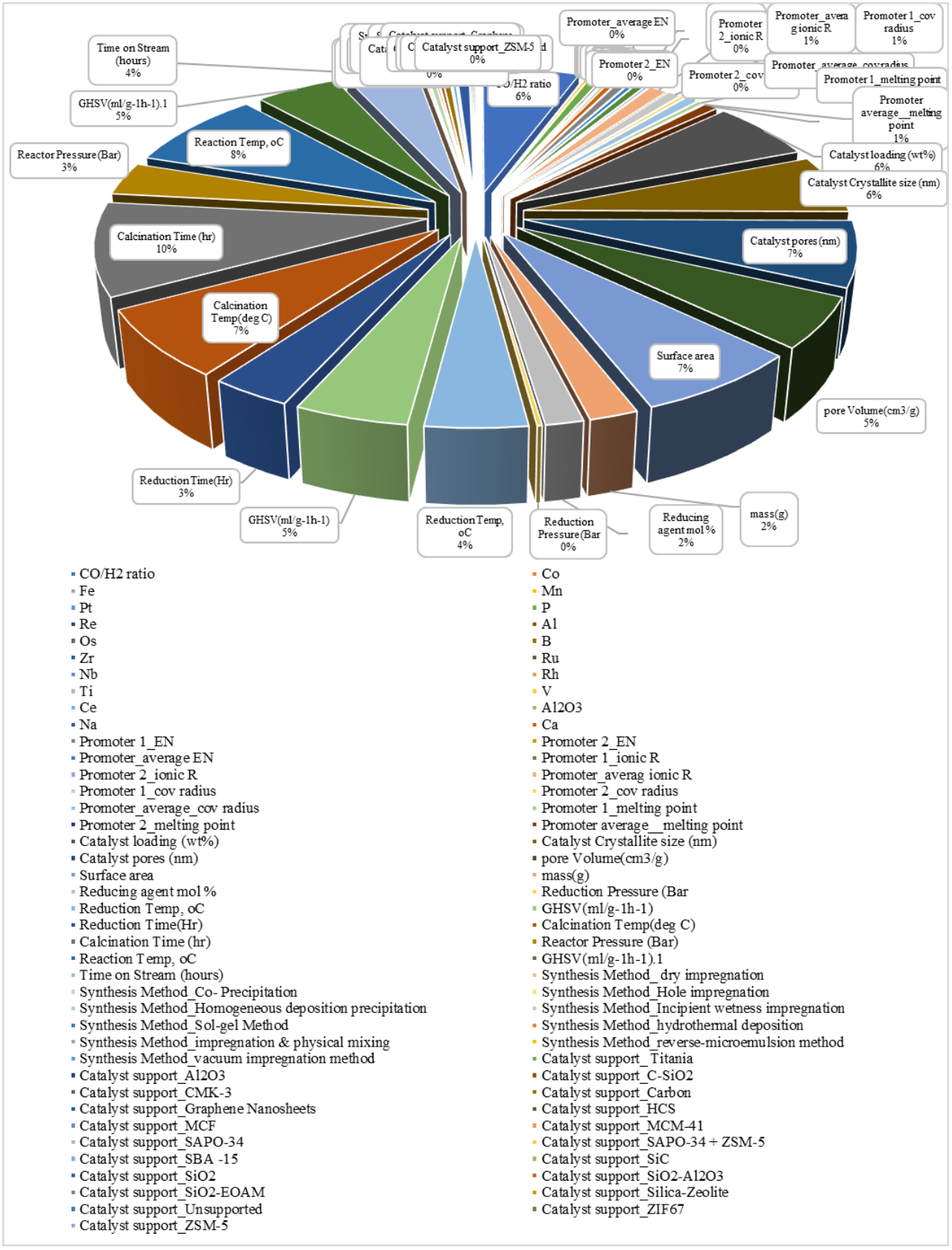



*Figure A.63. Feature importance towards $C_1$ selectivity in the whole population*

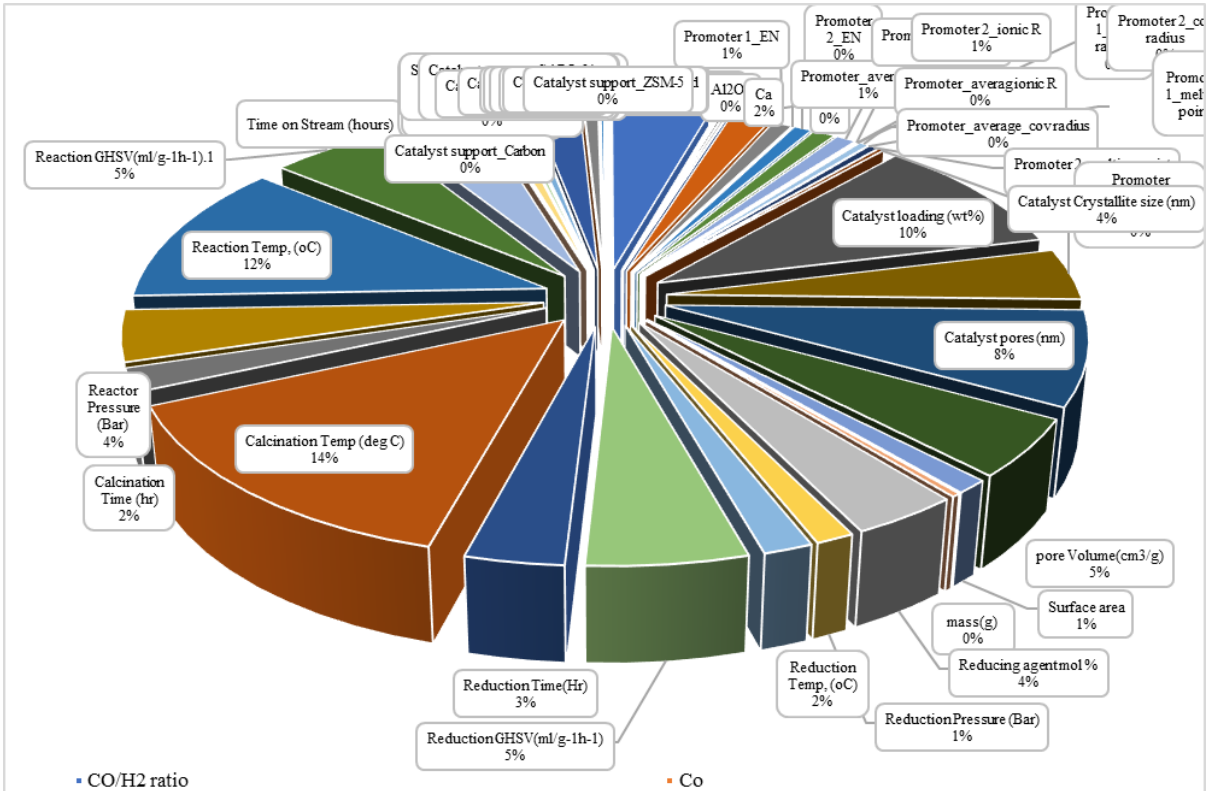



*Figure A.64. Feature importance towards $C_2$-$C_4$ selectivity in the whole population*

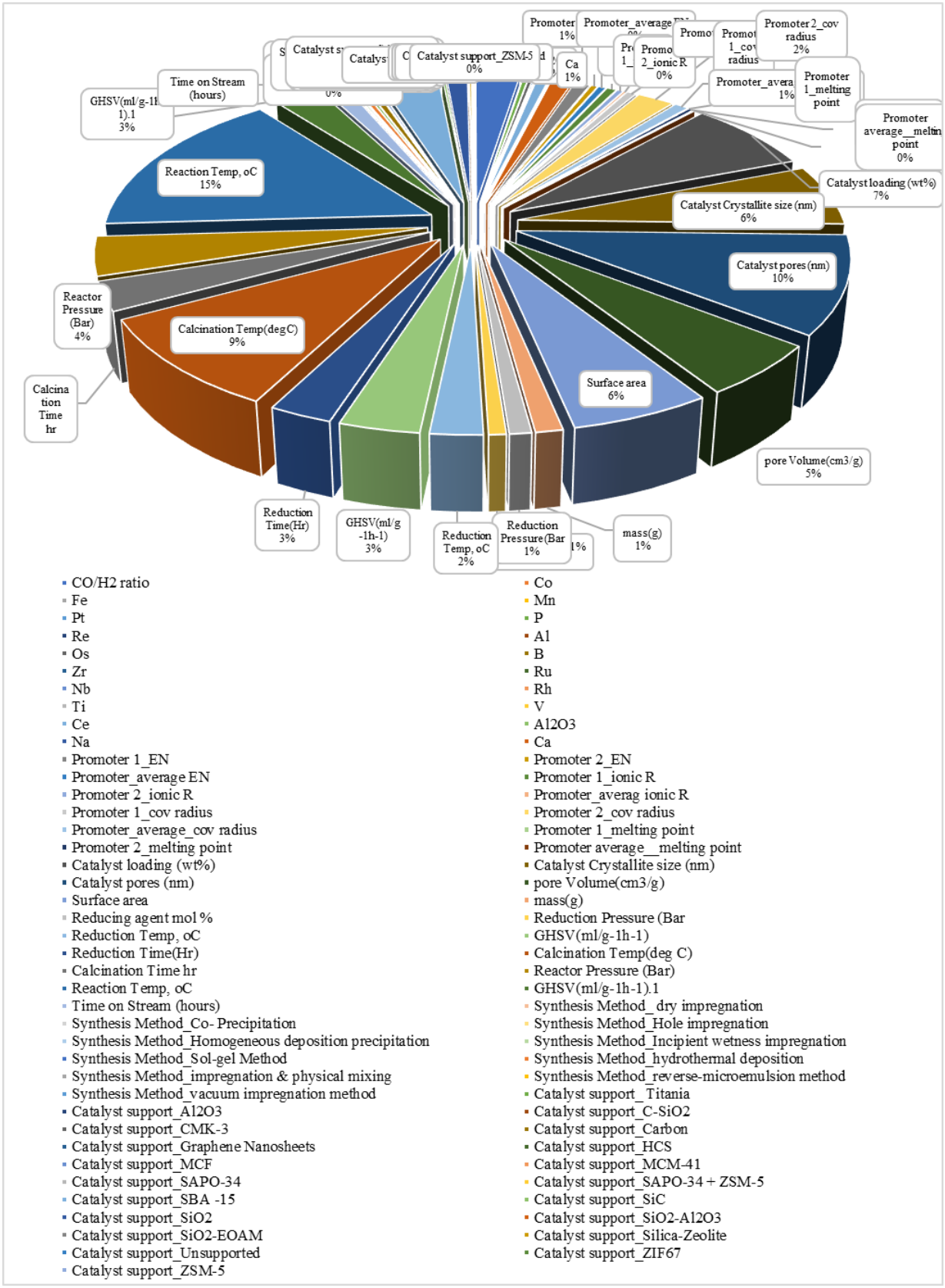



*Figure A.65. Feature importance towards $C_{5+}$ selectivity from the whole population*

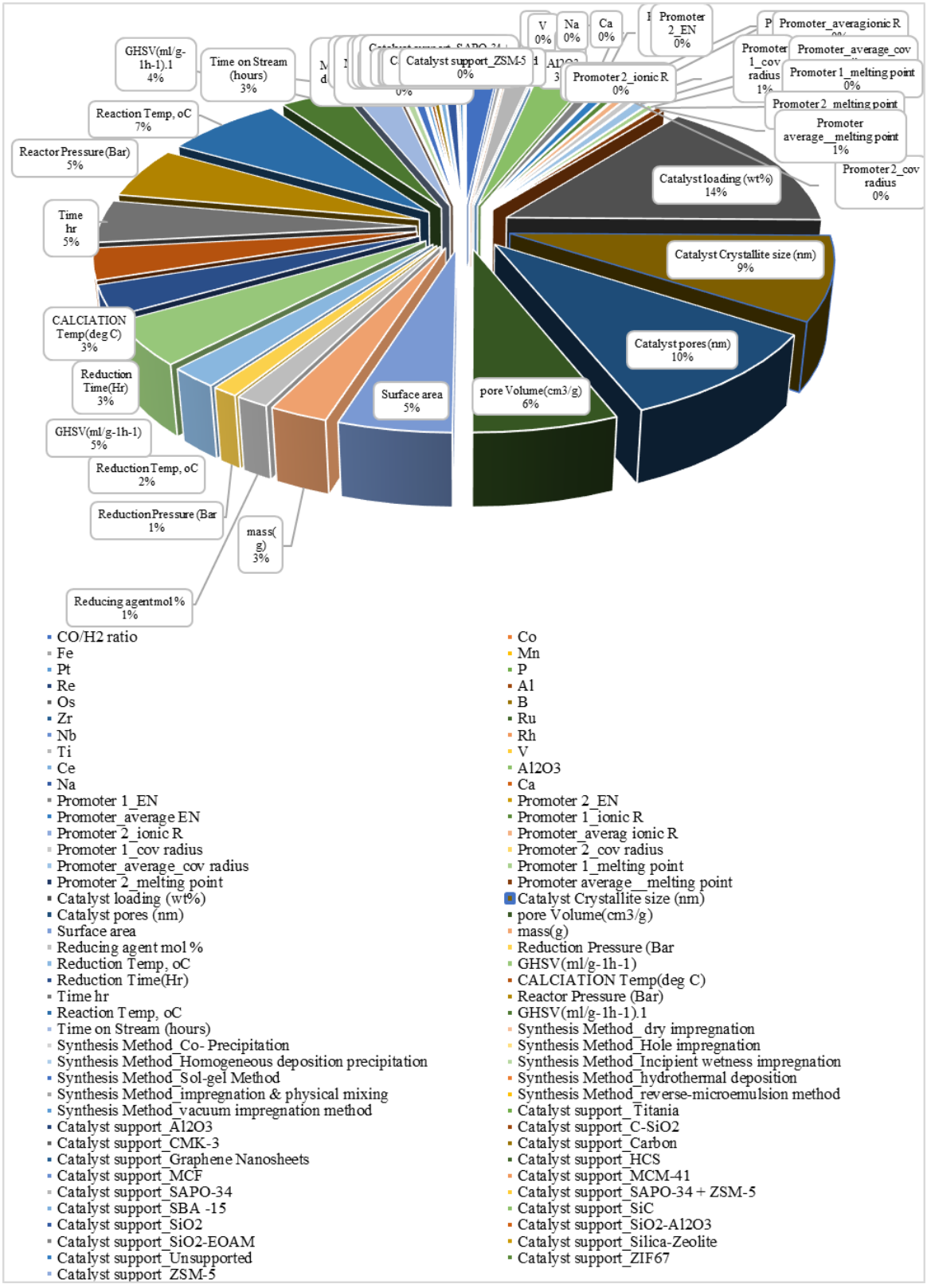



*Figure A.66. Feature importance towards CO conversion for the 20 - 60 % CO conversion data set*

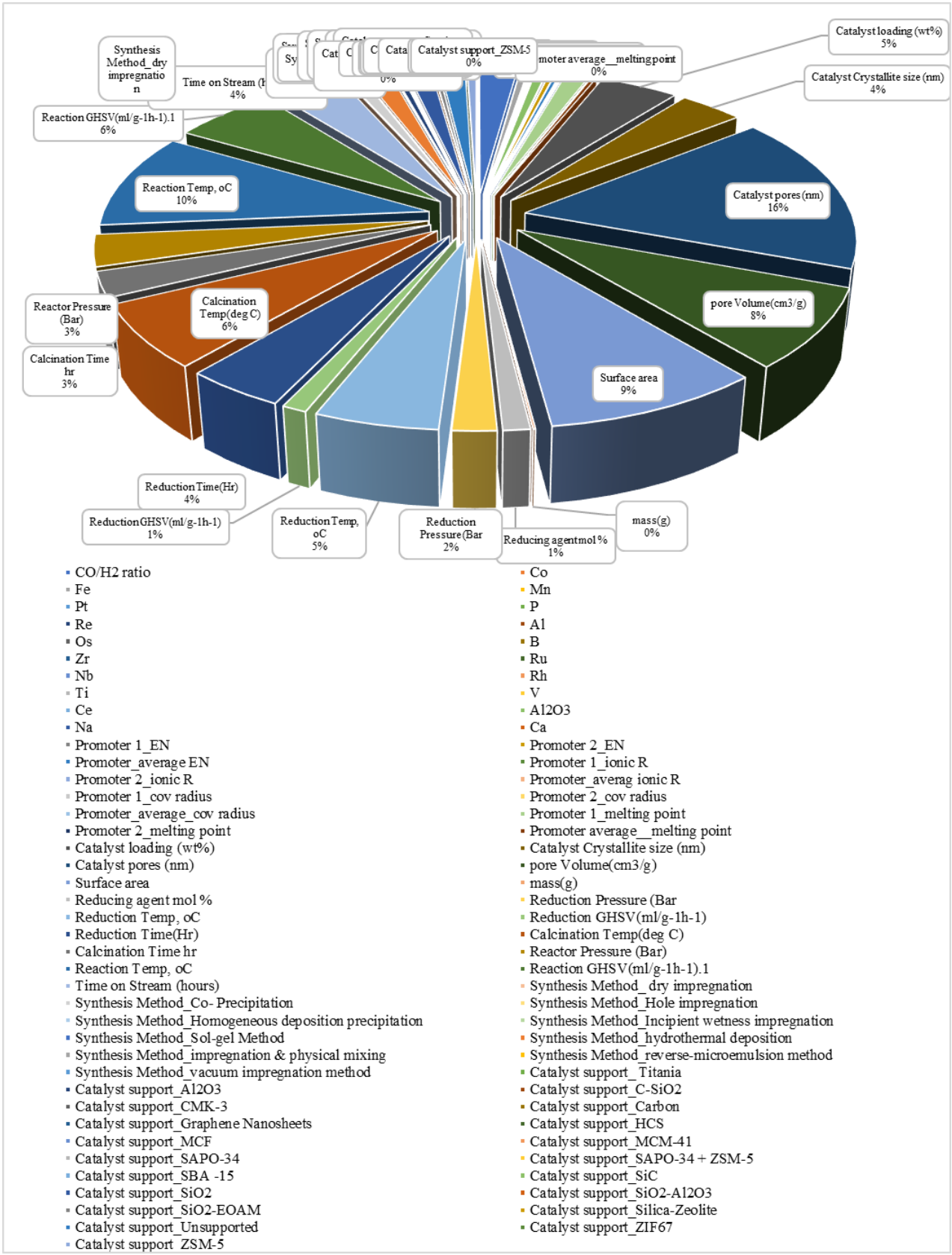



*Figure A.67. Feature importance towards $C_1$ selectivity for the 20-60% CO conversion cluster*

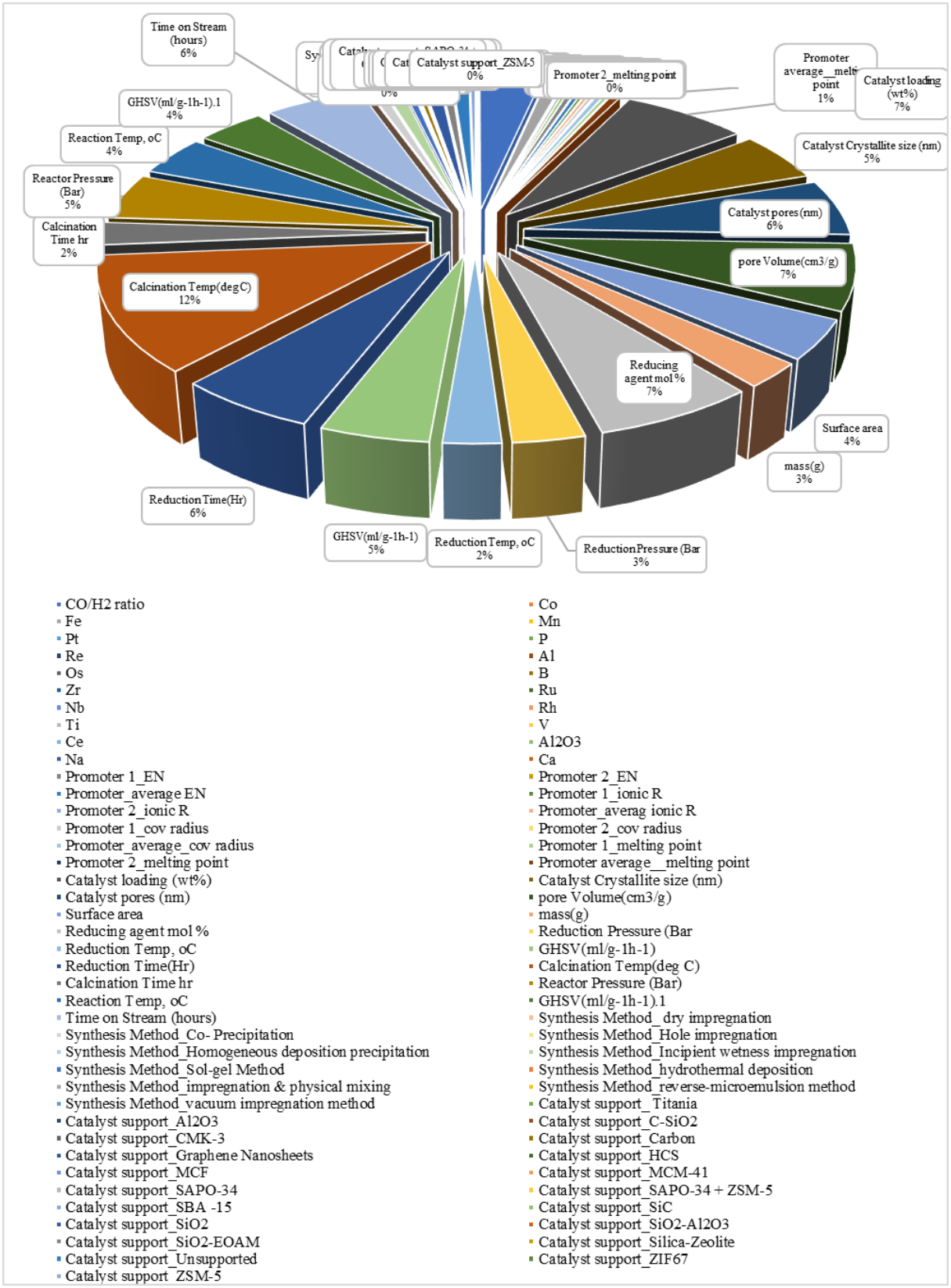



*Figure A.68. Feature importance towards $C_2$-$C_4$ Selectivity analysis for the 20-60% CO conversion data set*

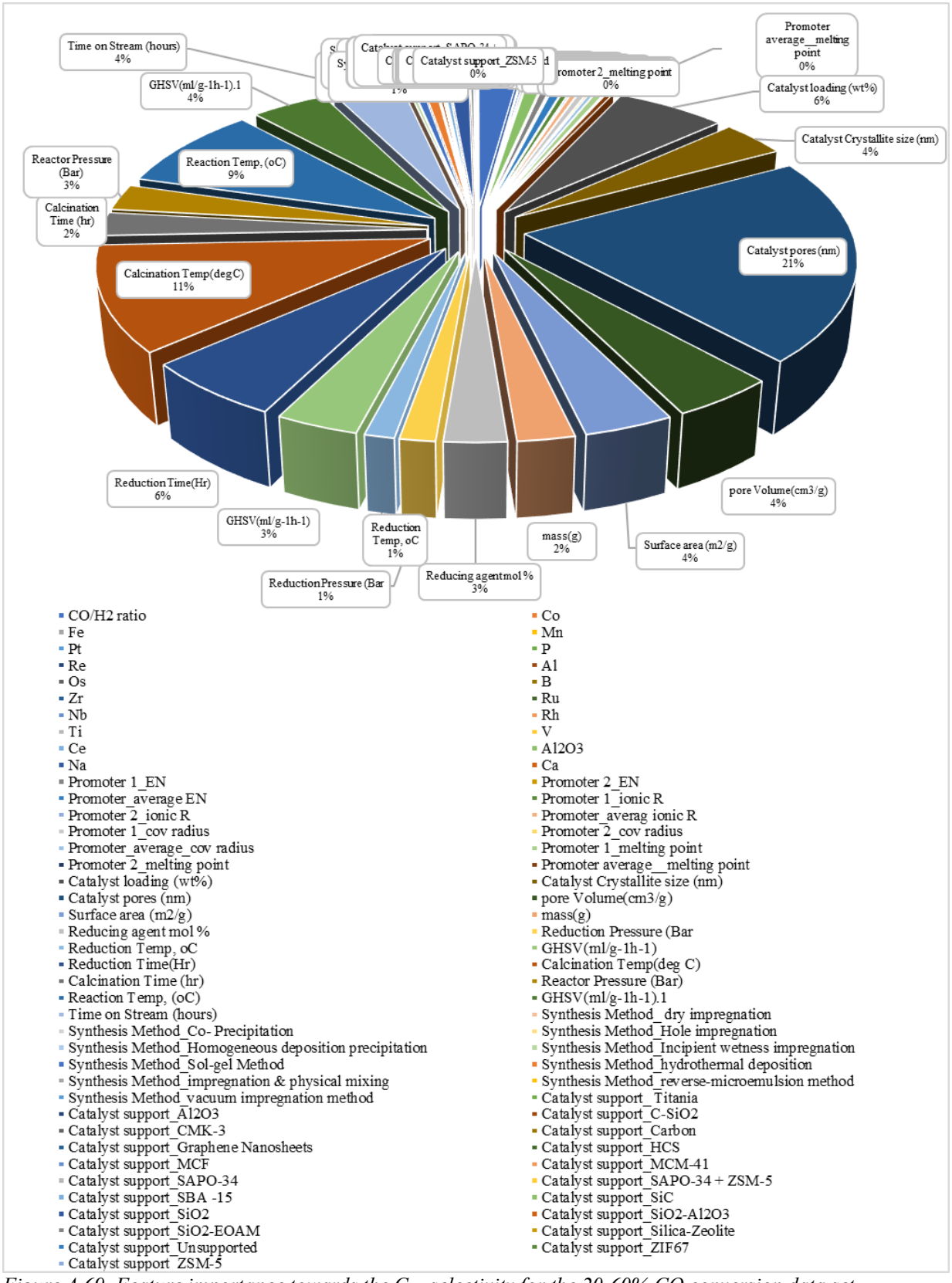



*Figure A.69. Feature importance towards the $C_{5+}$ selectivity for the 20-60% CO conversion data set*